High Temperature Superconducting Magnetic Suspension for Maglev

by

Marc Thomas Thompson

S.B., Massachusetts Institute of Technology, June 1985
S.M., Massachusetts Institute of Technology, August 1992
E.E., Massachusetts Institute of Technology, June 1994

Submitted to the Department of Electrical Engineering and Computer Science
in Partial Fulfillment of the Requirements for the Degree of

DOCTOR OF PHILOSOPHY

at the
Massachusetts Institute of Technology
May 1997

Signature of Author____
Department of Electrical Engineering and Computer Science
May 22, 1997

Certified by____
Professor Richard D. Thornton
Thesis Supervisor

Accepted by____
Professor Arthur C. Smith
Chairman, Committee on Graduate Students
Department of Electrical Engineering and Computer Science

High Temperature Superconducting Magnetic Suspension for Maglev

by

Marc Thomas Thompson

Submitted to the Department of Electrical Engineering and Computer Science
in Partial Fulfillment of the Requirements for the Degree of
Doctor of Philosophy in Electrical Engineering

Abstract

The design and analysis of a 1/5-scale model high-temperature superconducting (HTSC) magnet test facility for Maglev is discussed. Although the science of low-temperature superconducting magnets is well developed, high-temperature superconductors present unique electrical and mechanical design challenges for magnetic suspensions. The design, analysis, and test of a scale-model magnetic suspension suitable for electrodynamic suspensions is the topic of this thesis. The test fixture allows low-friction motion of the levitating magnets, simulating the vertical movement of a Maglev train under external disturbances.

A new low-cost, multiple-loop guideway has been built and tested, and resultant lift, drag, and guidance forces have been measured at operating speeds approaching that of an actual high-speed train. These results are compared to predictions based on simple circuit models with good results. Scaling laws have been derived and the circuit models have been used to size a full-scale system.

The test fixture has also been used to validate the concept of lift generation at zero velocity by AC excitation of the main magnet coils. Scaling laws have been applied and predictions made for a full-scale HTSC suspension. Further work in this area may help overcome one of the fundamental limitations of EDS Maglev --- zero levitation force at zero train velocity, requiring a mechanical suspension for slow speeds.

A novel magnetic secondary suspension has been designed and tested, where vertical position has been monitored and damped in operating conditions that mimic actual Maglev train operating conditions. Results from these tests show that it may be possible to design an active secondary magnetic suspension based on high temperature superconductors, thereby removing the cost and additional complexity of a mechanical secondary suspension from the Maglev train design.

Thesis Supervisor: Professor Richard D. Thornton
Professor of Electrical Engineering
Laboratory for Electromagnetic and Electronic Systems

Thesis Committee: Dr. Yukikazu Iwasa
Francis Bitter Magnet Laboratory

Prof. Steven Leeb
Laboratory for Electromagnetic and Electronic Systems

Acknowledgments

Thanks are due to many people who helped in the successful completion of this project by offering assistance, equipment and support, often on short notice. Research support was provided by the U.S. Department of Transportation administered through the Center for Transportation Studies at M.I.T. The Maglev test facility was constructed with support from the Charles Stark Draper Laboratory.

First and foremost, I must acknowledge the support of my thesis advisor, Professor Richard Thornton. His guidance and good humor throughout the length of the project have been invaluable. He is truly the master of the back-of-the-envelope approximation, and I have learned much from him.

My thesis readers were Dr. Yukikazu Iwasa of the Francis Bitter Magnet Laboratory, and Professor Steven Leeb of the Laboratory for Electromagnetic and Electronic Systems. Both provided valuable technical (and moral !) support throughout the course of the thesis work.

Corporate sponsors include: Ansoft Corporation which donated the finite-element software which was used to simulate the copper and superconducting magnet designs; Mr. Drew Devitt at Devitt Machinery Corporation who donated materials used in assembly of the air bearing; and Polaroid Corporation, which donated electrical components and equipment.

Thanks are also due to:

- Mr. George Anagnostopoulous, Volpe Center, Department of Transportation
- Mr. Tony Kondoleon and Mr. Don Zickefoose, Charles Stark Draper Laboratory
- Prof. John Brisson, Mr. Bob Gertzen, Prof. Joe Smith, MIT Cryogenics Laboratory
- Prof. Louis Bucciarelli, Prof. Zaichun Feng, Prof. Alex Slocum, Mr. Gerald Wentworth, MIT Department of Mechanical Engineering
- Prof. J. Kim Vandiver, MIT Department of Ocean Engineering
- Prof. Markus Zahn and Prof. Jeff Lang, L.E.E.S. Laboratory
- Mr. Al Cook, Parker's Boat Yard, Cotumit, MA
- Dr. Jeff Roblee, Polaroid Corporation, who provided assistance in the design and evaluation of the rotating test wheel and air bearing assemblies
- Mr. Michael Chiu, MIT Department of Mechanical Engineering who loaned several mechanical assemblies and assisted in the construction and analysis of the air bearing
- Mr. Ron Roscoe, Department of Electrical Engineering, MIT
- Vivian Mizuno, L.E.E.S. laboratory, MIT
- Students from the M.I.T. Undergraduate Research Opportunity Program, including Ben Haid, Brian Pellegrini, Damian Megna, Charline Hao, Eric Fong, and Jason Melvin
- The faculty, administration, staff, and students of LEES

For Lisa,

whose patience and love

guide me.

Table of Contents

List of Figures

List of Tables

"Our life are frittered away by detail .... Simplify, simplify."
--- *Henry David. Thoreau*

"Man is a tool-making animal."
--- *Benjamin Franklin*

"There is something fascinating about science. One gets such wholesale return of conjecture out of such trifling investments of fact."
--- *Samuel L. Clemens*

"A devotee of Truth may not do anything in deference to convention."
--- *Mohandas K. Gandhi*

1. Introduction

Magnetic levitation for high speed ground transportation (Maglev) has been an active area of research and development for over 30 years. This new transportation mode has been proposed as an alternative to air, automobile, and high-speed train travel. Various experimental and a large number of theoretical studies have been done. Work has been continuous in Japan and Germany, while U.S. research support has been sporadic. The development in the past 10 years of high-temperature superconductors may alter the economics of high-speed ground transportation for the better. The goal of this thesis has been to design and test a novel prototype electrodynamic magnetic suspension using high-temperature superconductors and an iron core.

High-speed Maglev systems have been designed and tested with cruising speeds of up to 500 km/hour (~300 miles/hour). By comparison, commercial high speed rails such as the German I.C.E., the French T.G.V. and the Japanese Shinkansen which use standard wheel-on-rail technology reach approximately 200 miles/hour. Furthermore, Maglev systems offer higher acceleration rates and a smaller curve radius, which provides the potential for significantly higher point-to-point speeds than high-speed rail.

Maglev systems may be classified into two types, depending on the details of the magnetic suspension. The attractive type Maglev (called the electromagnetic suspension, or EMS), uses electromagnets on the train which are attracted to an iron rail (*Figure 1-1*). The vehicle magnets wrap around the iron guideway, and the attractive force in the +z direction lifts the train. The repulsive system (electrodynamic suspension, or EDS) is levitated by reaction forces caused by induced circulating currents in a passive conductive guideway. In either case, the levitating magnets are mounted to a number of "bogies" which in most Maglev systems are connected to the main train body by a secondary suspension consisting of springs and dampers. The secondary suspension maintains acceptable ride quality in response to external disturbances such as guideway imperfections and aerodynamic forces.

The EMS system was first commercially implemented for the Birmingham International Airport shuttle with two vehicles on line on a 900 meter run at 48 km/hour. The Birmingham system was operated from 1985-1995 with high reliability.

Research on high-speed long distance EMS systems has been done primarily in Germany by the Konsortium Magnetbahn Transrapid. The Transrapid TR07 is a train that has on-board iron-core copper coils with a pole pitch of approximately 0.25 meters. The vehicle wraps around a T-shaped guideway of steel and concrete beams constructed to a very tight tolerance. Propulsion is provided by a long-stator linear synchronous motor, and primary braking is accomplished by regeneration through the linear synchronous motor. Emergency braking is provided by eddy current braking and high-friction skids. Power limitations in the copper levitation coils limit the height of the air gap as doubling the air gap requires doubling the magnet current, quadrupling the magnet power. Therefore, this system operates with a small air gap (~ 1 centimeter), and is unstable if operated with constant current in the levitation coils. Therefore the system requires an active control system with redundancy to meet safety standards.

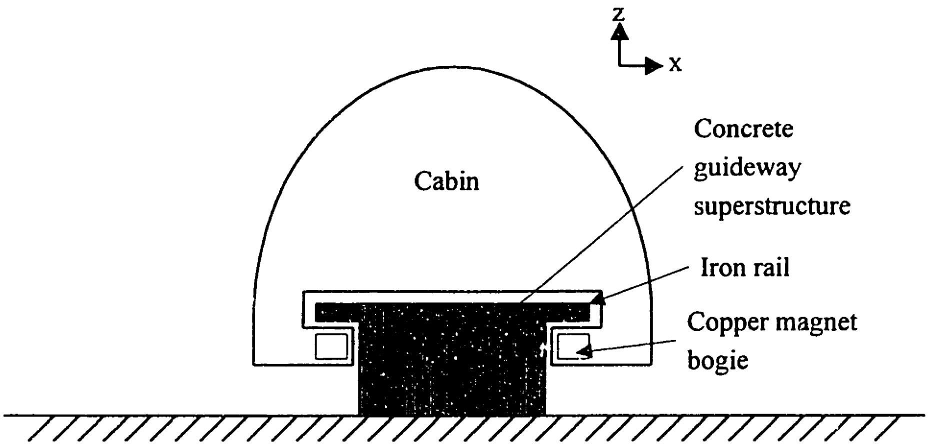

(a) Electromagnetic suspension Maglev train, end view (not to scale)

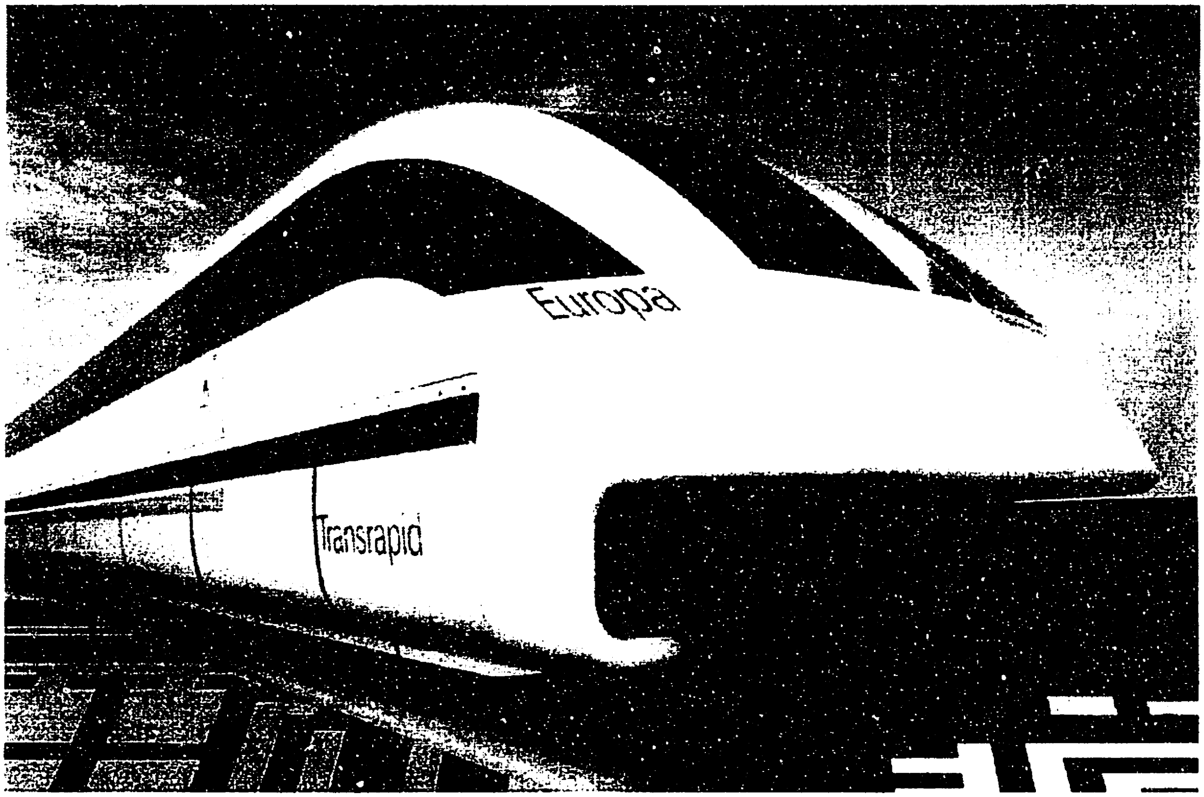

(b) German Transrapid TR07 vehicle

Figure 1-1. EMS Maglev vehicle.

A 40 kilometer test loop is in operation in Emsland, Germany [219, pp. 2]. In 1988, the Transrapid TR06 test vehicle was operated at 257 miles per hour with 8-10 minute transits of the Emsland loop. Intensive testing on the TR07 prototype revenue service vehicle has resulted in the accumulation of more than 100,000 kilometers of tests by 1990. Revenue-producing operation is scheduled to begin in 2004 from Hamburg to Berlin.

The electrodynamic superconducting magnetic suspension (EDS) is a repulsive suspension invented in the United States in the 1960's and has been actively researched in the United States, Japan, and to a lesser extent Germany. Superconducting coils on bogies mounted to a moving train induce circulating currents in a conducting guideway, with resultant levitation and guidance forces. The currents in the guideway also result in a drag force which in addition to aerodynamic drag must be overcome by the train propulsion system. At low speeds, the drag force increases with increasing train speed until the "drag peak" velocity is reached. A unique feature of the EDS system is that at speeds higher than the drag peak, the drag force decreases. Aerodynamic forces, on the other hand, increase as velocity squared.

The EDS suspension is stable without an active control system. At normal cruising speed, the levitation and guidance forces are weakly dependent on train velocity. The dynamics of motion of the train in multiple degrees-of-freedom is underdamped, and must be controlled to achieve acceptable ride quality. However, there is no levitation force at zero velocity, so rubber wheels or some other low-speed suspension is required.

An example discrete-coil EDS Maglev vehicle described as part of the National Maglev Initiative by a team at M.I.T. [178] is shown in *Figure 1-2a,b*. The train shown (not to scale) has two superconducting magnet bogies attached to each side of the train. A propulsive force F_p propels the train at velocity v in the $+y$ direction. This force is provided by a linear synchronous motor. The high field (~ 1 Tesla at the guideway conductors) generated by the superconducting coils in the bogie induces currents in the guideway conductors. The high field also allows operation of the full-scale EDS Maglev train at a significantly higher airgap than the EMS system (~ 10-25 cm). The interaction of the field and the induced current produces a shear levitating force in the z direction. At the "lift-off" speed, the levitation force is sufficient to lift the weight of the train and the passengers. There is a sideways guidance force in the x direction acting on the bogies which tends to center the vehicle on the track. The circulating currents in the guideway coils also produce a drag force F_d in the $-y$ direction which is overcome by the propulsion force.

The forces acting on the guideway coils are transmitted to the guideway superstructure (*Figure 1-2b*). The guideway must be sufficiently stiff to handle the dynamic mechanical load without significant flexure. Mechanical design of guideway structures is discussed in the thesis by Phelan [118], and mitigating strategies for reducing eddy current stresses in guideways is discussed in the paper by Zahn [120].

Research effort in the U.S. focused initially on the EDS system using conductive aluminum sheets, suggested by Guderjahn, Wipf, Coffey and others [154, 158, 159]. Other geometries have been developed since the mid-1970's, with significant work being done on discrete coil and ladder guideway designs. The null-flux suspension, first proposed in 1966 by Powell and Danby [168 - 171] at the Brookhaven National Laboratory, has coils arranged in a differential geometry with a high magnetic field gradient. This suspension has high stiffness and low magnetic drag, and the advantage that there are hold-down forces.

The first scale-model demonstration of EDS Maglev was the Magneplane of Kolm, Thornton, Iwasa, Brown and others at M.I.T [183, 188, 189]. A 1/25 scale model was demonstrated with superconducting magnets and a linear synchronous motor. The motor was used for active heave damping.

The first full-scale system using superconducting magnets was the Japanese National Railways' ML-100, a 3.5 ton vehicle propelled tested on a 500 meter track by a linear induction motor [51]. This full-scale null-flux EDS system has evolved from the Powell and Danby concept and has been further developed and tested at the Miyazaki test site. The Japanese Maglev design uses niobium-titanium low temperature superconductors operating at 700 kA-turns and cooled by liquid helium at 4.2 K. The superconducting coils have a pole pitch of 2.1 meters. The ML500 test vehicle, based on an inverted-T guideway, was tested at 517 km/hour in December 1979. Since then, construction has begun on a new test line at Yamanashi. The new test track will include some gradient sections and other sections with tunnels [51, pp. 16]. The MLU-series test vehicles are based on a U-shaped guideway with separate levitation and guidance loops, operating with an air gap of approximately 20 centimeters. The levitation force is provided by sidewall levitation coils in a shear force arrangement. The target maximum commercial speed of the Maglev vehicle will be approximately 500 km/hour, almost twice the maximum speed of the Shinkansen high speed train.

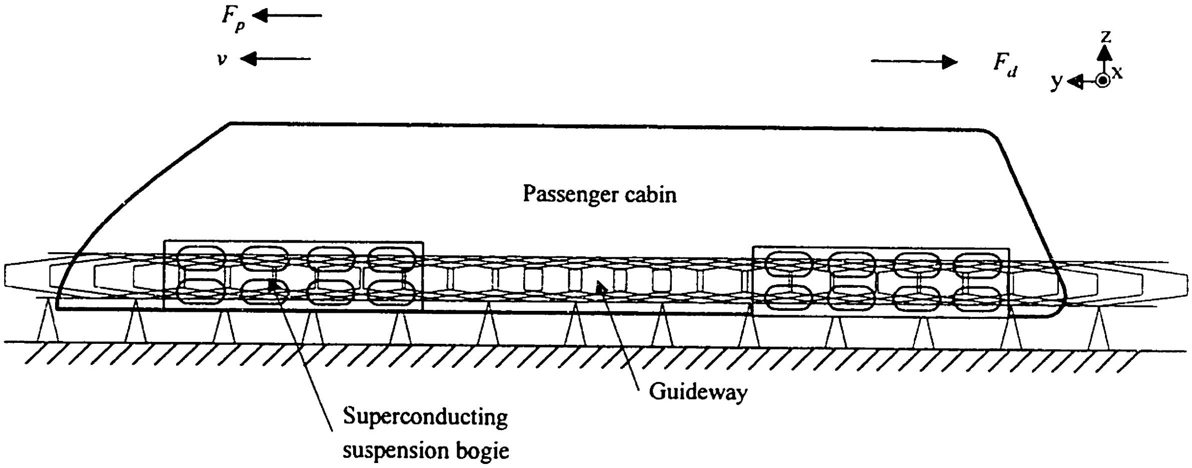

(a) Side view (not to scale)

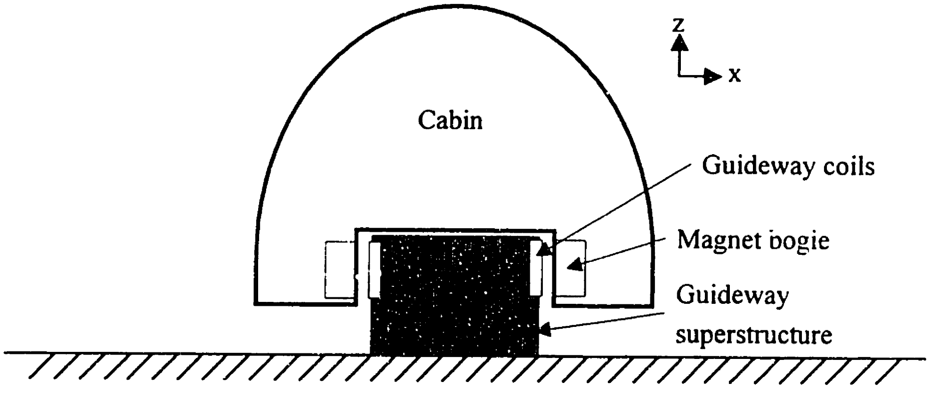

(b) End view (not to scale)

Aero-wedge Style

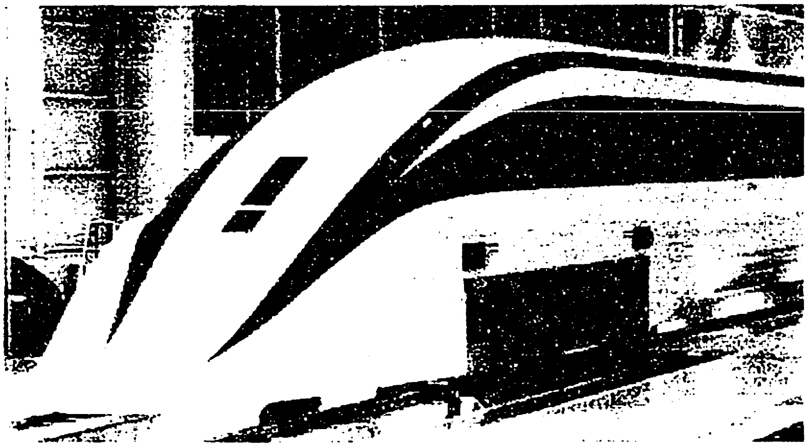

Double Cusp Style

(c) Japanese MLU-series vehicles, showing two different aerodynamic nose cone designs

Figure 1-2. EDS Maglev vehicle

The German and Japanese Maglev development programs, and a variety of results from other test fixtures and theoretical studies have proven the technical viability of Maglev as reliable high speed transportation mode. The prospects for German EMS Maglev look good, with significant government and private research support and a timetable in place for revenue service. The future of Japanese EDS Maglev is less clear, but significant resources are being focused on the development of an air core, low temperature superconducting Maglev system.

The focus of this thesis project has been the design and test of a new magnetic suspension suitable for EDS Maglev using high temperature superconductors and an iron core. The suspension is based on a "flux-canceling" geometry and a new low-cost guideway design. We take advantage of the electro-thermal stability of high-temperature superconductors by implementing an active secondary suspension control system with dynamic control of the current in the superconducting coils. Suspension models have been developed which capture the details of the electrodynamic interactions without being overly complicated.

1.1. Issues Related to EDS Maglev Using High Temperature Superconductors

The discovery in 1987 of the first high-temperature ceramic superconductor (HTSC) with a transition temperature above 77K [29] was promising for Maglev applications, for several reasons. The economics of using low-temperature superconductors is affected by the cost and weight of the liquid helium cryostat. Size scaling also come into play; in general, the power rating of a magnet is proportional to its volume and the heat leak is proportional to surface area, so a larger refrigerator is more efficient. For electric motors, it was shown that low-temperature superconductors were cost-effective only for larger machines [3].

The critical field is the maximum externally applied field for which the superconductor will conduct without loss. This parameter varies with operating temperature and current density inside the superconductor. High-temperature superconductors offer very attractive electrical properties when operated at low temperatures; several materials have a very high critical field at 4.2K (*Table 1-1*). Several materials have been found which have critical fields higher than 100 T, which is much higher than conventional low-T_c superconductors. For this reason, high-T_c materials have been used as inserts in high field magnets, operating at 4.2K, where their properties are very advantageous for magnet designs. One such NMR magnet design, using high-T_c superconductors, operated in a background field higher than 17 Tesla at 4.2K [7].

Table 1-1. Properties of some commonly-used superconductors at 4.2K showing transition temperature (T_c), critical field at zero current and self-field (B_c), and critical current density at zero field (J_c). Values for Jc are approximate, since this value depends strongly on sample preparation

Material	T_c *(K)*	B_c *(T)*	J_c *(A/cm²)*
Nb-Ti	9.5	13	10^6 @ zero field
Nb_3Sn	18	38	10^7 @ zero field
$YBa_2Cu_3O_7$ (YBCO)	95	> 50	
$Bi_2Sr_2Ca_2Cu_3O_{10}$ (BSSCO)	110	> 50	2×10^5 @ zero field

High temperature superconductors may extend the range of cost-effective solutions to smaller machines and magnet designs with a relatively simple cooler. A further benefit is the cost of refrigeration. Separate analyses by American Superconductor Corporation [19] and Iwasa [8] (*Table 1-2*) shows an energy cost comparison, in terms of refrigeration energy needed per Watt of power dissipation, of cooling a refrigerator to various temperatures. These numbers are for a closed system, with boil-off not allowed, and show that much less energy is needed for refrigeration at 77K than at 4.2K. The values are approximate, and change with refrigerator size.

Table 1-2. Approximate refrigeration power required per Watt of dissipation in a cryostat at various refrigerator operating temperatures

	4.2K	***20K***	***50K***	***77K***
Refrigeration energy needed, Watts/Watt	1400	140	25	10

A prototype high-temperature superconducting magnet may be operated inside a simple insulated vessel. The low cost of the liquid nitrogen allows boil-off; re-liquefaction is not required. Furthermore, the latent heat of evaporation for liquid nitrogen ($h_L \approx 161$ J/cm^3) is much higher than that of liquid helium ($h_L \approx 2.6$ J/cm^3) so the volume rate of evaporation of liquid nitrogen per Watt of dissipation will be much less. Liquid nitrogen is relatively cheap (approximately $0.10/liter in quantity) compared to liquid helium (approximately $10/liter). Giese [270] approximates Maglev magnet coolant boil-off costs of $50,000 annually for a liquid helium cooled magnet, and significantly less for a liquid nitrogen cooled magnet, based on two cryostat designs with similar geometries.

Material properties also favor operation of a superconducting magnet at a higher temperature in terms of stability against magnet quenching. The specific heat of metals approaches a constant at temperatures above the Debye temperature (approximately 315K for copper, and 395K for aluminum) [203]. Below the Debye temperature and at cryogenic temperatures, the variation of heat capacity with temperature is as:

$$C_v = \gamma T + AT^3 \qquad \text{[Eq. 1-1]}$$

where γ and A are material constants. At very low temperatures and for most materials the T^3 term dominates. so an increase in operating temperature can result in a drastic increase in heat capacity. At 4.2K, the heat capacity of Nb-Ti is $C_v \approx 5.76\times10^3$ J/m^3 K, while the heat capacity of a silver-clad high-temperature superconductor at 77K is approximately 10^6 J/m^3 K [8]. Therefore, it takes much more energy to raise the temperature of the high-T_c superconductor than a low-T_c superconductor, for a given temperature change, and an HTSC coil is less prone to quenching due to magnetic and mechanical disturbances.

The difficulties associated with using high-T_c material for magnet designs are also numerous. The high-T_c materials discovered so far are oxide ceramics; the materials are brittle. Nb-Ti, on the other hand, is ductile and may be handled similarly to copper magnet wire using standard coil winding processes. Due to the chemical properties of the high-T_c ceramic material, a costly process to sheath the ceramic in a silver matrix is necessary. The resultant high-T_c superconductor is not a wire (as in the case of Nb-Ti) but a flat superconducting tape. The tape geometry requires subtleties in the details of the magnet winding, such as the use of the pancake winding.[1]

The resulting high-temperature superconducting tape exhibits anisotropic electrical characteristics. At a given temperature and operating current, the tape can withstand a much higher field parallel to the tape flat surface than perpendicular to the same surface, before it becomes normal [23]. Therefore, conventional winding geometries designed for copper wire and low-T_c magnets may not work in a high temperature superconducting magnet, since their performance is not dependent on the direction of the field impinging on the conductor.

Also, the critical current density and critical field in the high-T_c material are degraded significantly when operating at 77K as compared to lower temperatures. Data for Intermagnetics General Corporation's silver-sheathed Bi-2223 superconductor is given in *Table 1-3* [6]. Performance at 77K with a 1 Tesla field perpendicular to the flat surface of the tape results in very poor performance, even compared to copper wire.

Table 1-3. Properties of Bi-2223 high-T_c superconductor, operating at 77K, 1 Tesla applied field

J_c (A/cm^2)	***Test condition***
30,000	Zero field
5,000	1T field parallel to tape
300	1T field perp. to tape

The high-T_c materials are also fragile; a tensile strain of 0.2% or greater is sufficient to degrade the superconductor's properties [21, 26]. As compared to Nb-Ti, (where bending strains of 1% are easily handled), much more care must be taken in the winding of the magnet coils with high-T_c material. High-T_c magnet designs have been cited with wire bending radii of a few centimeters [1, 2, 5, 6, 7, 9, 10, 11, 18, 122, 123, 124, 125].

The science of large-scale high-T_c superconducting magnet design is still in its infancy. However, it is possible to make some intelligent approximations, if not to define the exact properties, of a high-T_c magnet for Maglev. For a practical full-scale EDS Maglev magnet design, the following specifications for superconducting wire performance must be met [3, 126]:

- Critical current density greater than 10^5 A/cm^2. Special care must be taken in this specification as the tape is anisotropic with regard to fields parallel and perpendicular to the wide tape surface.
- Critical magnetic field of greater than 1 T at 77K.
- Long wire lengths (> 100 m) so that windings need not be formed in multiple sections.

---

[1] At the time of this writing (1997) Bi-2212 HTSC in round wire format has been developed.

- High strength to withstand Lorentz forces and forces due to thermal expansion.
- Robustness with regard to AC losses, wire uniformity, and quenching.
- Wire must be ductile, and able to withstand significant strain due to bending during the coil winding process.

While critical temperature and critical field in a superconductor are dependent on the chemical structure of the superconductor, the critical current density achievable is primarily dependent on details of the material processing. Steady progress has been made to increase the critical current density of high-T_c materials. Experimental magnets using high-T_c superconductors have been built, although most have been run at temperatures significantly lower than 77K (*Table 1-4*).

Table 1-4. Some prototype high-temperature superconducting magnet designs [1, 2, 7, 10, 11, 122-126]

Group	***Operating temperature***	***Test Condition***
University of Oxford	4.2K to 64K	> 0.4 T@ 4.2K
American Superconductor	27K	> 2 T
Oak Ridge	4.2K	1.14 T
Mitsubishi	20K	High-T_c coil for Maglev, air core
Grumman	20K	iron core magnet for Maglev
Intermagnetics General	4.2K	>0.2 T in 17T background field
University of Wollongong, Australia	77K	Bi-2223, wind and react coils, resulting in 15,000-20000 A/cm^2, self field

1.1.1. AC Losses in HTSC

One significant advantage is that high-temperature superconductors have been proven to be much more robust with regard to losses due to AC coil currents and external AC fields than their low-temperature counterparts. HTSC coils have a higher heat capacity than LTSC coils operated at 4.2K, reducing the likelihood of thermal runaway which results in a magnet quench. Various workers have published data which shows that HTSC coils require a higher dissipated energy density by factors of $10^4 \sim 10^6$ (*Table 1-5*). A minute amount of energy is required to quench a LTSC coil, on the order of microJoules [19]. Therefore, LTSC coils subjected to AC background fields and/or mechanical strains must have magnetic shielding and significant mechanical structural integrity to limit dissipation in the windings. Also, magnet driving currents must be limited to DC currents, as AC currents cause loss due to eddy currents, hysteresis effects, and filamentary coupling.

The Japan National Railways has found that a fundamental limitation to maximum Maglev train speed is vibration-induced mechanical losses inside the LTSC magnet winding [200]. The losses were especially pronounced when the coils were excited at structural resonant frequencies in the 100-300 Hz range. Mechanical losses required an expensive re-design of the superconducting levitating coils and support structure.

Wilson [295, pp. 70] offers a further example of mechanically-induced losses in superconducting wire operating in a field of 5T and with a current density of 3×10^4

A/cm^2. A movement of 10 μm will result in 1.5 J/cm^3 work being done on the superconductor. If only a small fraction of this energy is dissipated as heat due to friction, quenching will result.

Assuming that sufficient cooling is provided, it is expected that a HTSC coil will not quench in a Maglev environment. During operation, "hot spots" may sporadically develop due to external disturbances and disappear. These normal regions inside a high-temperature superconducting coil will grow and shrink slowly and the magnet is unlikely to quench. As a result of this slow normal region growth it is difficult to detect a normal region in a HTSC coil. Further research is needed to determine if HTSC coils operated at intermediate temperatures (20-40K) will result in significant performance improvements. However, the fundamental physics shows that HTSC coils will be more useful in AC applications that LTSC coils.

Table 1-5. Approximate energy density required for magnet quenching Comparison of low-T_c and high-T_c materials [3, 19]

Material	***Quench Energy***	***Test Condition***
Nb-Ti	0.01 J/cm^3	4.2K
BSSCO	15 J/cm^3	60K, 1T

1.1.2. Applications of HTSC to Transportation Research

Maglev trains are subjected to mechanical disturbances under normal operating conditions in the 0 - 20 Hz range [148], due to imperfections in the guideway. EDS magnetic suspensions, and especially the flux-canceling topology, have little intrinsic magnetic damping for vertical motion. Therefore, some form of secondary suspension is required to meet necessary ride quality standards. The secondary suspension provides damping which minimizes the effects of external mechanical disturbances.

Economic considerations demand that there be a reasonable tolerance on the alignment of adjacent Maglev guideway sections. For example, misalignments of 25 meter guideway spans with a train operating at 200 meters/second will result in mechanical disturbances with a fundamental frequency of 8 Hz. The disturbance spectrum will change as the vehicle speed changes, and the EDS primary resonant frequency may be excited at select train speeds. Adequate ride quality is achieved with the use of feedback control which maintains stable suspension while keeping the vertical acceleration in the passenger cabin to acceptable levels.

For low temperature superconducting Maglev designs, most proposed designs have a mechanical secondary suspension provides the necessary damping. A mechanical linkage connects the main levitating magnets to the train passenger compartment. The suspension may have shock-absorbers or air-springs. This mechanical suspension adds weight, complexity, and cost to the overall system design.

Our suspension is based on a secondary magnetic suspension concept using high-temperature superconductors, to take advantage of the robustness of HTSC material with regard to AC currents and AC magnetic fields. The necessary damping is provided by a control system which controls the superconducting magnet currents; in order for the control system to maintain the magnet position, transient currents are put through the superconducting coils. This sort of active control is impossible with low temperature superconductors, due to their AC loss characteristics.

With an active secondary magnetic suspension, the necessary ride quality may be achieved without the mechanical secondary suspension, with associated decrease in train weight and complexity. The use of HTSC coils in an active secondary suspension is a significant contribution to the state-of-the-art in Maglev suspensions.

1.2. Test Fixture System Overview

The design and test of a fixture for the evaluation of a new EDS Maglev system is the focus of this thesis. The fixture has been built, and the resultant Maglev test facility has been used to predict behavior of a full-scale flux-canceling Maglev system (*Figure 1-3*), based on a high-temperature superconducting coil. One side of a Maglev octapole has been built and operated with copper coils.

The guideway is composed of multiple conductive copper coils. When the train is in the vertical null position at $z = z_o$ and traveling in the $+y$ direction, there is no net flux through the levitating coils, and no net current induced around the loop. However, if the train's vertical position deviates from equilibrium, the net changing flux through the loop induces currents in the loop. The Lorentz force is a restoring force in this structure, with the magnetic suspension acting as a linear spring with spring constant k_z. The suspension behaves like a mass and a linear spring, with a resulting resonant frequency $\sqrt{k_z / M}$.

Eddy currents and circulating currents create a drag force acting on the train in the $-y$ direction. There is also a sideways force ($+x$) which pushes the train away from the guideway. For an actual Maglev train, there will be another octapole on the other side of the train, and the sideways force will tend to center the train on the track.

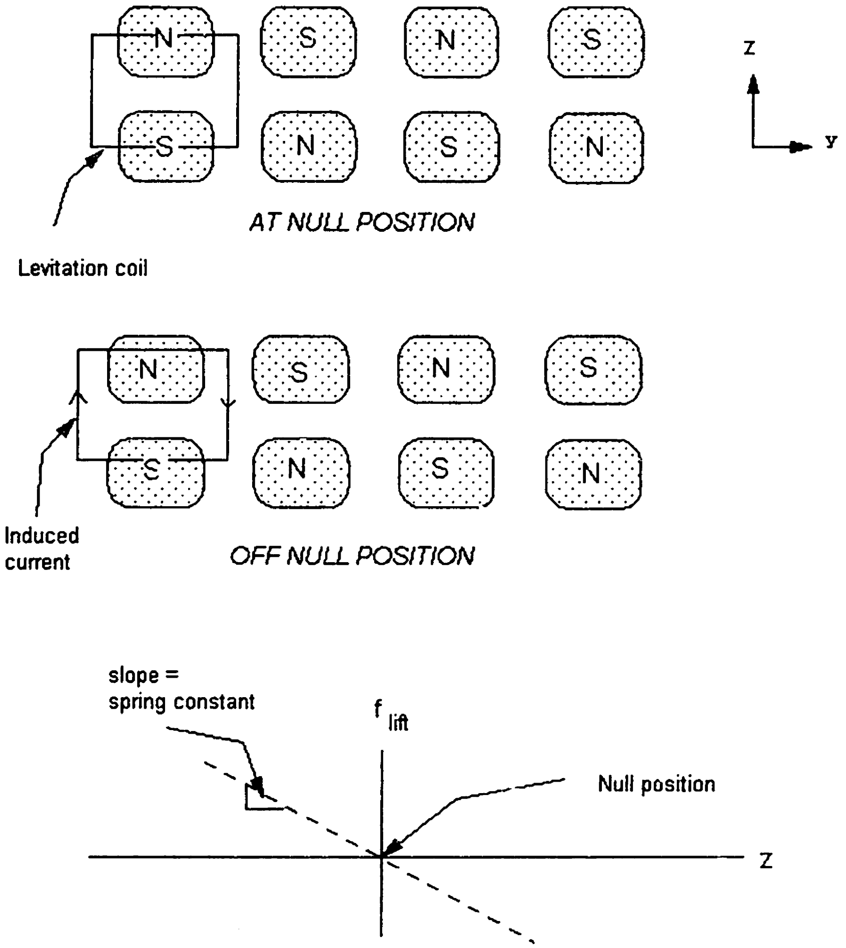

Figure 1-3. Flux-canceling Maglev topology

The rotating test wheel (*Figure 1-4*) is composed of an aluminum hub, with a non-conductive fiberglass/epoxy composite rim. The wheel has a diameter of 1.7 meters, and is designed to operate at a maximum speed of 1000 R.P.M., which corresponds to a linear peripheral speed of approximately 100 meters/sec. The speed of the wheel is regulated by a 10 horsepower motor and speed controller. The magnets are mounted such that the two rows of magnet polefaces line up with the wheel outer radius.

Guideway coils are embedded in the epoxy rim and every effort has been made to reduce the amount of conductive and magnetic material in the vicinity of the magnet pole faces. Furthermore, there is no ferromagnetic material in the vicinity of the guideway conductors. This will allow extrapolation of forces for the full-scale design. The relative motion between the stationary superconducting magnet and the moving guideway coils create the magnetic forces.

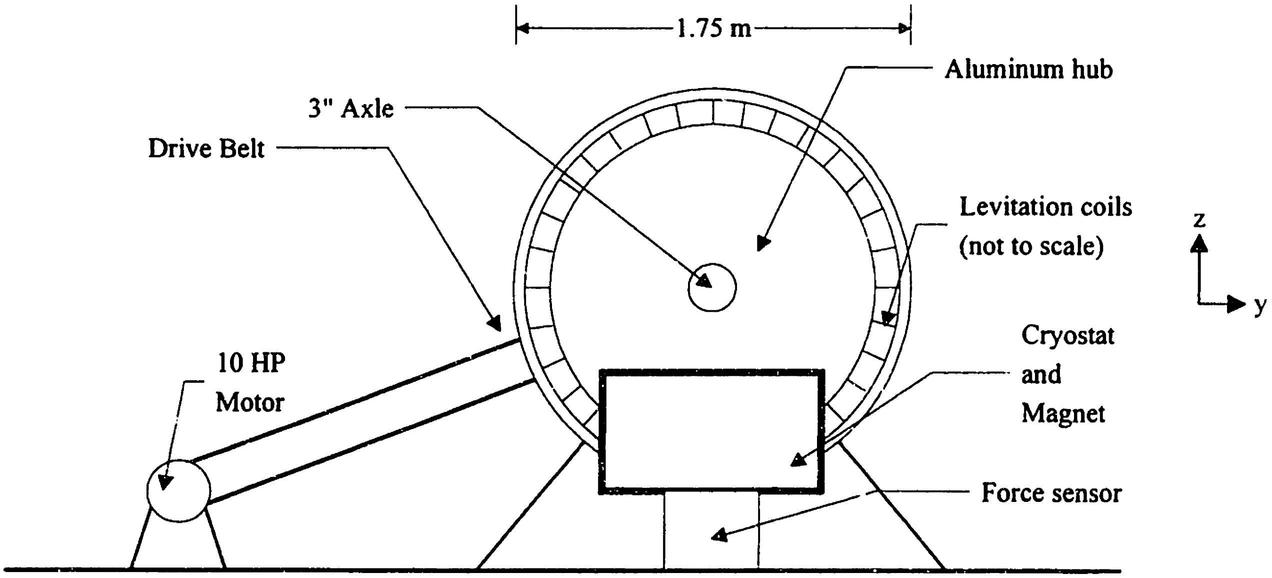

(a) Schematic view of test wheel

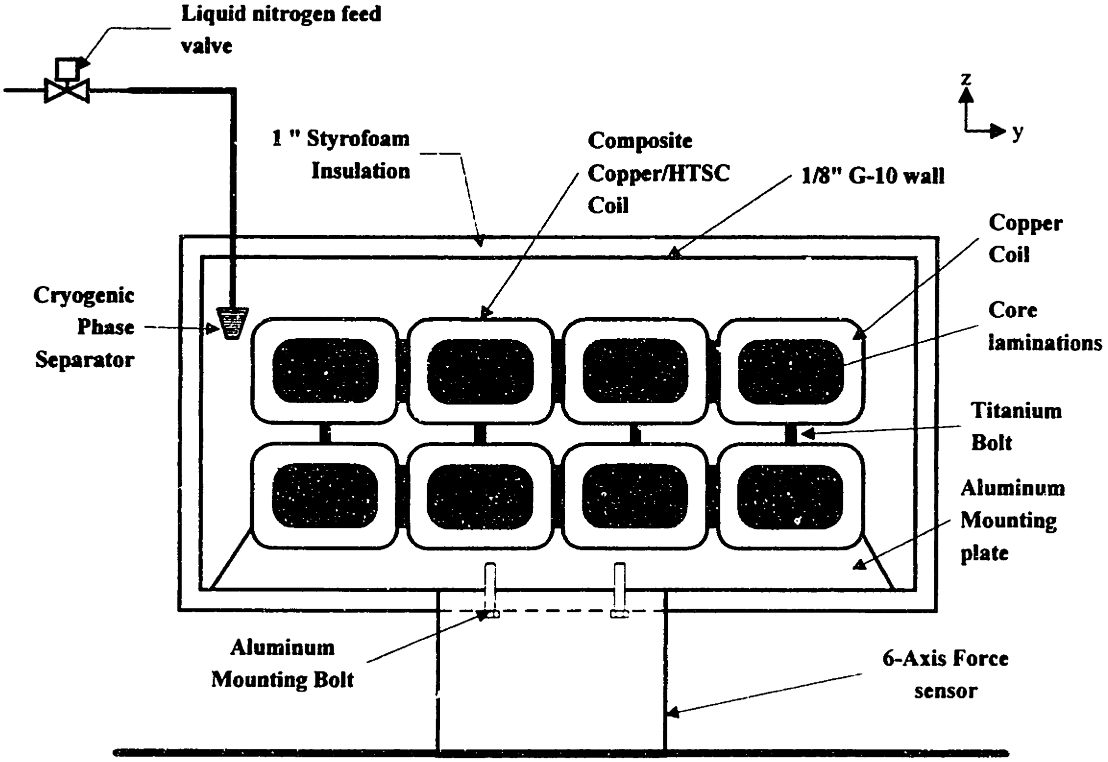

(b) Front view of magnet and cryostat

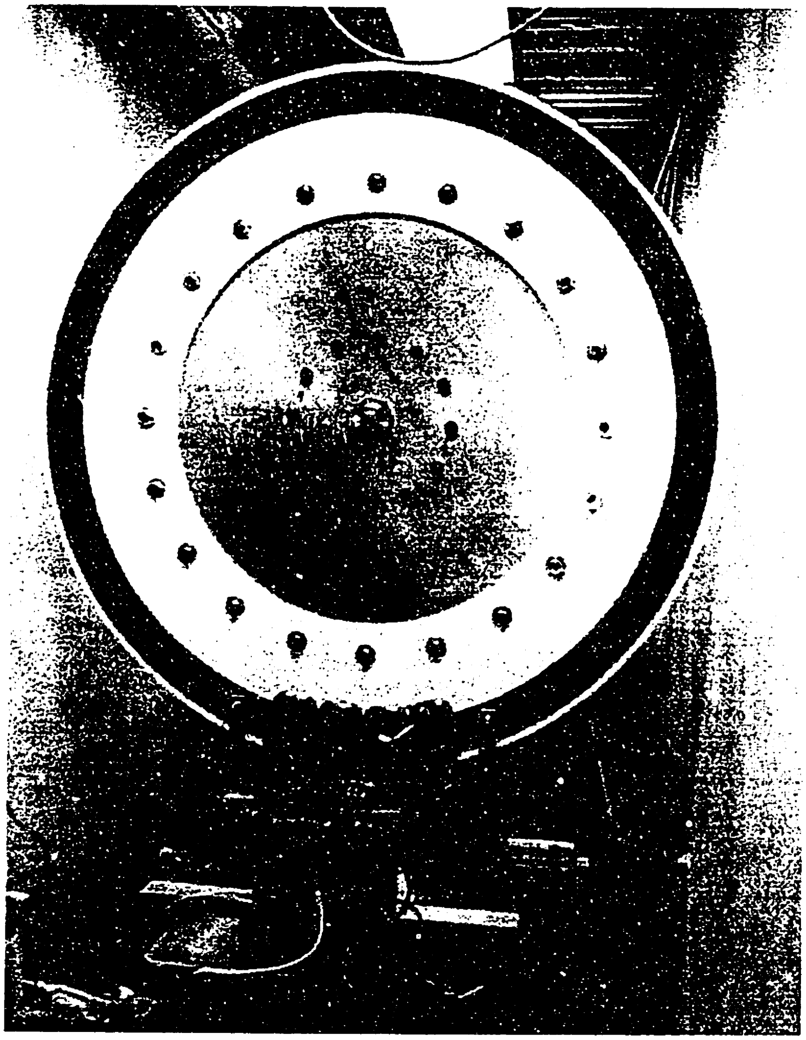

(c) Front view of test wheel

Figure 1-4. Flux-canceling Maglev test fixture

The rotating test wheel has been used to test the viability of using high temperature superconductors for Maglev and linear motors. We compare lift, drag, and guidance forces with calculations derived from simple models. The fixture has been operated in two different modes:

1. For measurement of magnetic forces and torques, and aerodynamic forces, the superconducting magnet assembly is mounted to a 6-axis force sensor. This sensor measures forces and moments in 6 degrees of freedom, with forces 0-200 Newtons and torques 0-100 Newton-meters. The force sensor restricts the translational and rotational motion of the magnet assembly. Forces may be measured for various x, y, and z magnet positions relative to the guideway conductors.
2. For study of vertical dynamics, the magnet is mounted to a one degree-of-freedom air bearing, which allows low friction vertical movement of the magnet. Using this bearing, the vertical motion with and without an active secondary suspension has been studied.

For future tests, it is possible to modify the test wheel and magnets for alternative tests on guideway and/or linear motor topologies.

1.3. Goals of this Thesis

Specific goals of this thesis have been:

- Design, build and test a working model of an iron-core Maglev electrodynamic suspension suitable for use with high temperature superconductors. In the design, low cost construction techniques and materials have been used.
- Design a new low-cost, high-performance loop guideway. Emphasis has been placed on a guideway design which will give an acceptable lift-to-drag ratio for the full-scale design, and which is easy to manufacture.
- Develop hybrid electrodynamic/circuit models for prediction of lift and drag forces. There has been limited use of detailed electrodynamic analysis and finite element analyses; rather, approximate techniques are used which lend themselves as practical design tools.
- Prepare a methodology to collect data for future Maglev electrodynamic stability analyses.

1.4. Organization of Thesis

This thesis covers the design and analysis of a fixture for the testing of candidate Maglev magnet and coil geometries. The Maglev test fixture is of sufficient interest and design complexity that the detail of the design has been presented. Chapter 2 is a literature review, which covers much of the history of Maglev research, including significant works on the development of Maglev circuit and electrodynamic models. Other peripheral Maglev topics, such as guideway design and superconducting coil design are also referenced.

Chapter 3 covers the mechanical design of the test fixture, with details given on the design of the test wheel, cryostat, air bearing, and nitrogen delivery system. Chapter 4 covers the design and construction of the electrical system, including detail of the iron core, copper coil, and superconducting coil designs.

Chapter 5 develops a model for calculation of forces for the magnet and guideway conductor geometries. The approach taken is to produce simple circuit models which may be used as a design aid for a full-scale system. Therefore, the focus has been to utilize available linear circuit-analysis tools without becoming inundated in the detail of the mathematics of the electrodynamic interactions..

Chapter 6 presents the test results and analysis of design models. In this section, measurements of lift force, drag force, and drag peak are compared to predictions based on the circuit models, with good results. Further tests were performed to generate lift force at zero velocity by AC excitation of coil currents.

Chapter 7 concludes the thesis, and summarizes test results and formulates recommendations for future study. Chapter 8 contains appendices covering peripheral topics such as circuit schematics, data on the strength and properties of materials used in the construction of the thesis project, and Matlab programs. Chapter 9 concludes with an extensive indexed bibliography, covering many aspects of the history of Maglev research and details of the thesis design.

2. Literature Review

This thesis project involved the design and analysis of a prototype Maglev systems which incorporate diverse technologies, including high-temperature superconductors, precision electronics, electrodynamics, and highly stressed mechanical structures. Therefore, an extensive review of the literature was performed focusing on many different design case studies. The references are organized in sections indexed in the Chapter 9 of this thesis. Following is a summary of some of the more interesting and/or germane results found.

2.1. HTSC Coil Design and Analysis

Low-temperature superconducting magnet design is a field that has matured, partially through the process of having some spectacular failures [289]. Although the science of HTSC coil design is still in its infancy, there have been several attempts to build prototype HTSC coils to determine how close to design limits these coils may be operated. A literature review was performed prior to the design of our HTSC coils in order to determine the state-of-the-art, and, more importantly, to gain understanding of some design errors that have been made previously.

The papers reviewed focus on many unique features of HTSC coils as compared to their low temperature superconducting (LTSC) counterparts, including:

- The current state-of-the art for HTSC is a silver-sheathed tape form. Therefore, standard coil winding techniques which rely on wires of round or square cross section may not be used. Nb-Ti low temperature superconductor is available in a round wire geometry, and standard coil geometries may be used.
- While all superconductors' critical current densities (J_c) are degraded by applied magnetic field, HTSC is anisotropic in that regard. The J_c is degraded more by an applied field perpendicular to the wide tape surface than a field parallel to the tape. The degradation may be anisotropic by a factor of 10 to 1 or more. The effect is more pronounced at higher temperature than lower temperature [6].
- At cryogenic temperatures, the heat capacity of a metal varies approximately as $C_v \propto T^3$ [19] while the thermal conductivity k varies more slowly [203]. The thermal diffusion time constants depend on the ratio of C_v/k. Therefore, the growth of a normal zone (which in LTSC coils results in a magnet quench) is much slower in HTSC than LTSC, due primarily to the higher heat capacity of the magnet. The thermal time constant, which is proportional to this heat capacity, is $\sim 10^5$-10^6 times larger at 77K than at 4.2K. Also related to this is the energy density required to initiate a magnet quench, which may be $\sim 10^6$ times higher for HTSC [291, pp. 319]. Therefore, HTSC coils are expected to be much more robust with regard to mechanical disturbances.
- HTSC tape is much less prone to degradation in critical current density J_c due to flux jumping because of the higher heat capacity of the material [291, pp. 192].

- While low temperature superconducting magnets may be made self protecting (that is, if the magnet quenches, the normal zone propagates quickly and the magnet energy is dissipated through the whole magnet volume) the slow thermal time constant in HTSC coils precludes self-protection. Therefore, active normal-zone detection and protection is warranted for large coils. Sensing voltage taps may be placed inside the magnet winding to sense normal regions.
- The critical current density J_c is more affected by tensile and compressive strain in HTSC than in LTSC. While Nb-Ti wire may be strained up to 1% with no significant affect on J_c, strains in HTSC must be kept $\varepsilon < 0.2$-0.4% or so [21] or significant degradation occurs. Furthermore, HTSC wire may be irreversibly damaged by strains in excess of a few tenths of a percent. This means that practical HTSC coils must be designed with a minimum bend radius of a few centimeters. If higher strains are necessary, the wind-and-react method may be used where the coil is wound with unreacted superconductor, and heat treated after winding [295, pp. 317].

2.1.1. Prototype Coils and HTSC Design Issues

Since the discovery of high temperature superconducting ceramics in 1987, a number of engineering prototype HTSC magnets have been built. There are new proposed applications for HTSC in Maglev, nuclear magnetic resonance (NMR), superconducting power leads and transmission cable, and superconducting magnetic energy storage (SMES).

In 1988, shortly after the discovery of high-temperature superconductivity, Kirschner et. al. [12] built several high-temperature superconducting magnets using individual yttrium-barium-copper-oxide (YBCO) superconducting ceramic rings. The resulting spiral of YBCO ceramic was a primitive version of today's HTSC solenoid coils. Central fields of ~20 milliTesla were produced when operated in liquid nitrogen.

Later workers have built coils using silver-sheathed HTSC tapes. Aized [1] presents data for coils made from silver-sheathed lead-BSCCO tape, tested in magnetic fields of up to 20 T in the temperature range 1.8K to 77K. Comparisons were made for background fields parallel and perpendicular to the coil axis. Overall current densities of 20,000~30,000 A/cm^2 were achieved at 20T fields and 4.2K. Ariante et. al. [2] present data for silver-clad Bi-2212 coils from 4.2 to 80K, and show that the critical current is on average 50% of the short sample value, reaching 80% in the best case. Degradation is explained by noting that the critical current degrades with bending strain. Since the wind-and-react method was used for these coils, the details of the heat treatment also affect the ultimate performance of the coils. Hazelton et. al. [7] describe the design and test of a prototype Bi-2223 magnet designed as a high-field insert for an NMR application. The coil was operated at 4.2K with a 17 T applied field and produced an additional central field of 0.24 T. The results show that HTSC has very good properties when operated at LTSC temperatures. Jenkins et. al. [9, 10] describe the design of several different HTSC coils from BSCCO-2212 with test data from 4.2 to 77K. It is shown that the anisotropy of the tape response to perpendicular fields is significantly worse at 77K than at the lower temperature. In a later experiment, Jenkins et. al. [11]

describe the design of a small-scale attractive Maglev test fixture, with an HTSC coil operating on an iron core. They describe design criteria that are unique to using HTSC on an iron core, specifically the problem of leakage fields which degrade the performance of the HTSC tape. Vo et. al. [18] built several high temperature superconducting coils made from multifilamentary Bi-2222 tapes. They were able to generate a field of ~0.04T at 77K. They found that by using the wind-and-react technique it was possible to retain ~97% of the short-sample critical current.

Edick [3] presents the case that HTSC windings may be cost effective for large motors from an economic standpoint. He cites data from small prototype motors (< 100 Watts) and predicts a ~ 50% reduction in motor losses and motor size for a 10,000 HP synchronous motor using HTSC, based on a design study. Schoenung et. al. [15, 16] presents a conceptual design for superconducting magnetic energy storage using HTSC. Their results show that for HTSC to be competitive with low temperature superconductors in energy storage that the cost of HTSC material must be reduced and the performance at high fields and moderate strains must be improved. A study of a superconducting magnetic energy storage system using HTSC with 0.5 megaWatt-hour storage capacity with 30 megaWatt discharge power was conducted by Niemann et. al. [28] at Argonne National Lab.

Foner [4] discusses the effects of new material technology on magnet design. He reports results for BSCCO tape with $J_c = 1.5\times10^4$ A/cm^2 at 26T and 4.2K and states that HTSC may be better for large scale applications at 4.2K than low temperature superconductors if the problems of strain tolerance can be solved.

Gamble [5] summarizes the benefits and limitations of HTSC wires. The case is made that while a dissipative energy density inside the magnet winding of ~1-10 kJ/m^3 is sufficient to quench a Nb_3Sn magnet operating at 4.2K, expected quench energies for an HTSC magnet operating at 30-40K is orders of magnitude higher.

Iwasa [8] compares cooling requirements, quench protection, and thermal stability for low temperature superconductor magnets at 4.2K and HTSC magnets at 77K. The results show that HTSC magnets will be much more stable with regard to mechanical disturbances and flux jumping. However, a magnet at 77K will require some sort of active normal-zone detection and protection, since the normal conductor zone will propagate very slowly. Hence, a small normal zone inside an HTSC magnet is likely to heat up significantly if the quench does not propagate through the entire winding. Work has been done to analyze and increase the quench propagation velocity in multifilamentary superconductors [280].

Okada et. al. [13] present a methodology for evaluating the stress in superconducting solenoids. A case study is done for a solenoidal 8T Nb-Ti coil operating at 4.2K. This methodology is useful, especially for HTSC coils where magnetic and thermal strains may significantly degrade coil performance.

Ries [14] concludes that passive quench protection for HTSC coils will not be sufficient, as the energy will be dissipated in a small fraction of the total magnet volume due to the slow velocity of the normal propagating zone. He concludes that in large

HTSC magnets an active quench detection and active dissipation methods must be used, although he offers no methods of detection or protection.

2.1.2. HTSC Material Properties and Test Data

Since the discovery in 1987 that the ceramic material $YBa_2Cu_3O_7$ has a critical temperature of 95K [29], significant progress has been made in producing usable wires, tapes, and coils made from HTSC material. Test data has been compiled on HTSC tapes with regard to critical current density and thermal stability, and the affects of applied field, temperature, and strain.

Murakami [27] tested samples of YBCO crystals. Results showed that J_c exceeded 30,000 A/cm^2 at 77K and 1T. The paper focuses on the chemistry and performance of the raw YBCO crystals and makes no comment on the application of YBCO to practical wire conductors.

Haldar et. al. [6] present data for small coils fabricated in 1993 from silver-clad Bi-2223 which were run at 4.2K and 77K. They found that once the coil was wound there was a difference of 60-80% in J_c between long lengths and short samples due perhaps to the effects of bending strain and self field. They concluded that the HTSC composite tapes show promise for operation in low applied fields at the pumped liquid nitrogen temperature of 64K. Measurements were also made of the temperature dependence of the J_c-B_a measurements for short samples of Bi-2223 over the temperature range 4.2K-90K. Data shows the anisotropy of the J_c degradation, and shows that the anisotropy is especially pronounced for temperatures below ~60K. At 77K the short sample J_c was degraded by 70% for an applied perpendicular field of 0.1T, 75% for a field of 0.2T, and 98% for an applied field of 1T. At 1 T perpendicular to the wide face of the tape and 77K, the short sample J_c was found to be ~500 A/cm^2 compared to ~25,000 at zero field. The performance was significantly better at pumped liquid nitrogen temperature (64K). This anisotropy was verified experimentally by Maley et. al. [25] in 1994

Hazelton [23] says that for the strain for multifilamentary tapes should be limited to 0.2-0.3%. Haken et. al. [21] investigated the effects of tensile and compressive strain on the critical current density of Bi-2212 HTSC tape. It is shown that a compressive strain of ~0.4% and a tensile strain of ~0.5% cause a 10% degradation in J_c at 4.2K and high field. It is unclear from their results what the effects would be at higher temperatures. Montanari et. al. [26] studied the effects of mechanical, thermal, and environmental stresses on multifilamentary HTSC tapes with specific application to superconducting cable design. In an interesting result, it is shown that exposure to high temperature (~100 C) and 97% humidity produces significant degradation of critical current density

Kim et. al. [24] measured the temperature dependence of the normal zone diffusion in Bi-2223 tapes over the range 10-40K. Their results showed that the propagation velocity of the normal zone is several orders of magnitude slower than in low temperature superconducting tapes. The propagation velocity of the normal zone was very slow, on the order of 1 cm/second for a transport current $I_t = 65$ A at 40K.

2.1.3. HTSC Applications to Magnetic Levitation

Various studies have been performed to evaluate the viability of application of HTSC technology to EDS and EMS (attractive Maglev) systems. Several theoretical and experimental studies have been done using high temperature superconducting magnet designs.

Goodall et. al. [123] has concluded that direct control of HTSC magnets in an EMS Maglev environment should be straightforward. Preliminary experimental results show that superconductor losses are minimal and that system power dissipation is dominated by eddy currents in the iron core. They suggest that an overall vehicle weight reduction of 5% may be achieved by replacing copper magnets with HTSC coils. Goodall's group has also demonstrated a magnet used for controlled EMS suspension with a load of 40 kilograms. The results of their Maglev demonstrator test fixture [124] showed that the controlled high-temperature superconducting magnet could be used to provide an EMS suspension of a large load without significant power consumption, and that a significant reduction in the weight of the magnets could be expected by using HTSC coils instead of copper. A later paper by the same group [122] gives test results on an actively controlled HTSC magnet for EMS Maglev applications.

Kalsi [125] considers the application of high temperature superconductors to the Grumman EMS Maglev design. The preliminary analysis suggests that a functional Maglev magnet could be constructed with either Bi-2212 or Bi-2223 and cooled with a cryocooler at 10K or higher.

Scholle and Schwartz [128] have examined the effects of using a high-T_c superconductor in an air-core EDS Maglev configuration. They performed simulations based on the Japanese MLU002 geometry to determine the strains, power dissipation, and temperature rise in the superconducting material. They concluded that vibration-induced strains in the HTSC coils due to ground-coil/superconductor interactions at select vehicle velocities may exceed several percent, hence significantly affecting the critical current density. They also concluded that the power dissipation and heat leak for the Maglev coils will be small enough so that the magnet may be run for extended periods of time before recooling.

Yokoyama et. al. [129] discuss design issues for a high-T_c Maglev magnet for the Japanese Maglev system. The superconducting coil is based on a Bi-2223 tape and is cooled by a refrigerator at 20K and is operated in persistent mode. Each coil is run at 590 kA-turns with a design limit at 20K of 800 kA-turns. They concluded that the temperature rise due to AC losses would be minimal and that the coil would be very stable to external disturbances.

Senba et. al. [127] built an attractive-type magnetic levitation system with the levitated body being a mass of bulk YBCO superconductor cooled with liquid nitrogen. The levitated body is a demonstration of the Meissner effect. The group at the Texas

Center for Superconductivity at the University of Houston [227] has built a superconducting magnetic bearing for flywheel energy storage using a YBCO high-temperature superconductor cooled at 77K. The prototype used permanent magnets for levitation and HTSC coils for control, and a load of 19 kg was levitated and rotated up to 2000 R.P.M. with very little loss.

2.1.4. AC Applications and AC Losses in HTSC

The subject of AC losses in high-temperature superconductors has become of interest due to possible new applications in Maglev, superconducting magnet energy storage (SMES), current leads for low-temperature superconducting magnets, and power distribution. Iwasa [8, 291, pp. 319] has concluded that while total AC losses in a HTSC magnet will be of the same order-of-magnitude as in a comparable LTSC magnet, the effect of AC losses is much reduced due to the increase in the energy density needed to initiate a magnet quench. Furthermore, refrigeration is easier at higher temperatures [19], with an energy cost of the order of 10 Watts of energy for every Watt of energy removed when operated at 77K. This compares to ~1000-2000 Watts/Watt at 4.2K.

Prior art over the past 20 years has focused on calculation and measurement of AC losses in low temperature superconductors. Hlasnik and Ito [274] discuss the use and limitations of low temperature multifilamentary composite superconductors in motors, transformers, and other machines up to 60 Hz. They discuss progress in increasing the critical current densities in AC applications by decreasing the size of the low temperature superconducting filaments.

Gomory [271, 272] discusses methods of measuring magnetization and AC losses in low temperature superconductors. Power loss is calculated by measuring magnet current and voltage and compensating for the reactive impedance of the coil.

Giese [270] discusses the possibility of using HTSC in generators, motors, transmission lines, SMES, transformers, and power electronics. He makes the point that since the energy (and power) of a superconducting machine or motor is proportional to its volume while heat leak is proportional to surface area, the cost of refrigeration favors large machines. If you take this line of thinking to its logical conclusion, it may be that HTSC will be cost effective for smaller machines than their LTSC counterparts.

Boggs [270] evaluated YBCO fiber as a possible candidate for power transmission, and generated scaling laws for AC losses in superconducting wires. Paasi et. al. [282, 283] evaluated AC losses in single layer coils of Bi-2223 at 4.2K and 77K at frequencies up to 100 Hz. At 50 Hz, 77K and with 1 Ampere peak sinusoidal current at 50 Hz, a power density of ~150 Watts/m^3 was measured. It was also found that the AC losses do not have the I^3 dependence on transport current which would be predicted by the critical state model. The losses at 77K were more than two orders of magnitude lower than the losses in a copper coil of similar geometry.

Herrmann et. al. [273] evaluated losses in a 5 kA$_{RMS}$/50kV 50 Hz AC current lead using BSCCO superconductor. It was predicted that a significant refrigeration load reduction could be achieved by using HTSC. Yasukawa et. al. [287] fabricated and tested a 2 kA HTSC current lead system which could carry current at 50 Hz. Ciszek et. al. [268] present the results of measurements on losses in Bi-2223 tapes under various operating conditions of transport current, frequency, and applied AC external field. All measurements were taken at liquid nitrogen temperature (77K). Their results show that the dominant losses are due to magnetic hysteresis.

2.2. Inductance Approximate Calculation Methods

In the design and analysis of our magnet and guideway structures, approximate techniques for the calculation of self and mutual inductances were used. Several early references were used, and the validity of filamentary and other approximations for our structures were verified by finite element analysis. In Maglev guideway design as well as the design of motors and transformers, a figure of merit for a coil is the L/R time constant; for a more efficient coil, it is necessary to maximize the inductance and minimize the winding resistance. Several references were found which allow approximate inductance calculations and derivation of scaling laws.

The works by Campbell in 1908 [32] and Butterworth in 1915-1916 [30, 31] provide useful methodologies for the calculation of mutual inductance of filamentary coils with parallel axes. Although such problems may now be easily solved by numerical integration, their works provide equations from which important design criteria and scaling laws may be derived. A similar problem was solved by Kim et. al. [38] who calculate the restoring force between two noncoaxial circular coils. It is interesting to note that the earlier works by Campbell and Butterworth could have been used to solve the problems in this paper more simply. The methods in these 3 papers have been adopted in the analysis of our prototype guideway.

Lyle [39] developed a method in the early 1913 where the self-inductance of a circular coil of rectangular cross section may be calculated to an arbitrary level of accuracy by calculating the inductance of a filamentary ring with the filament placed at the geometric mean distance (G.M.D.) of the cross section. This method may be used with arbitrary accuracy by breaking up a complicated cross section into multiple filaments placed at the G.M.D.

Grover [34] builds on the seminal works of Maxwell, Lyle, Dwight, Butterworth, and others and presents compiled methods for the approximate calculation of inductors of arbitrary cross section. Although much of the material is dated due to the availability today of computers, there is an abundance of useful approximations, both for low and high frequency inductance calculations. The Radio Engineers' Handbook, by F. Terman [45] also provides inductance calculations for many interesting winding shapes. Electrical Coils and Conductors by H. Dwight [33], Static and Dynamic Electricity by W. Smythe [44], and the skin effect reference by H. Wheeler [46] provide useful information on the calculation of skin and proximity effects in wires, and calculation of inductance in the high-frequency limit.

Hurley and Duffy [36] present a method by which Maxwell's original equation for the mutual inductance of coaxial filamentary rings may be extended to coils with a finite cross section. The geometric mean distance method of Lyle was used to calculate self and mutual inductances. Experimental verification of their method is done for frequencies up to 100 MHz for planar coils above a ferrite substrate.

Murgatroyd [41] performed design studies in order to optimize the Q of toroidal air-core inductors. By using the calculus of variations, he calculated the ideal geometry of coil cross section which maximizes inductance for a given turn length. His methods are limited to toroidal cage coils, but may be extended to coils of other geometries.

2.3. *Maglev System Design and Test Data*

2.3.1. Elementary Theory of Magnetic Levitation

The literature is rich with references evaluating the performance of EDS magnetic suspensions, focusing primarily on problems which may be reduced to simple models with closed-form solutions. Theoretical work has focused on static equilibrium solutions. Boerdijk [205] in 1956 summarized state of the art in levitation technology and reported on an experiment where a piece of diamagnetic graphite was levitated over specially shaped permanent magnets. He also commented on the application of superconductors to levitation, and specifically to magnetic bearings.

Early workers analyzed simplifying cases which give insight into more complicated levitating geometries. Solutions have been calculated for eddy induced currents and resultant forces acting on a long straight wire moving with constant translational velocity over a conductor by Reitz [108] and Davis and Wilkie [136]; a permanent magnet moving over a thin sheet by Davis [102]; and a moving rectangular coil over a conductor by Langerholc [104], Lee and Menendez [105, 106], Ooi [107], Reitz [108], and Reitz and Davis [109].

In a later work, Hill [208] in 1990 considered the special case of a current sheet with a sinusoidal spatial dependence traveling over a conducting sheet. He calculated results in the thin and thick sheet limits. His results were verified by a test fixture consisting of permanent magnets suspended above a circular magnetic plate 88 cm in diameter.

Saslow [213] applied Maxwell's theories to many different situations involving magnets, wires, and continuous sheets. One interesting example which he gives is the drag calculation for a magnet falling down a conducting tube. He shows that the falling time through the tube scales as $\sim m^2$ where m is the magnetic dipole strength. This result is entirely consistent with other Maglev drag force calculations. He also comments that recent advances in high strength rare-earth magnets makes the demonstration much more dramatic.

2.3.2. Maglev Early Works

Following is the summary of the early investigators of Maglev, including Powell and Danby, Davis and Wilkie, Coffey, Guderjahn and Wipf, Kolm and Thornton, Coffey, Atherton, Borcherts and others. A useful history of electromagnetic levitation research in the years 1910-80 is provided by Jayawant [162, 210, 215]. An exhaustive bibliography of magnetic suspension research and patents applied to bearings is provided by Geary [214]. This reference covers electrodynamic, electromagnetic, and superconducting magnetic suspension research through 1963. A thorough bibliography of electrodynamic and electromagnetic Maglev and linear motor research through 1975 is provided by Thornton [174, 175].

Magnetic levitation using eddy currents was first proposed in 1914 by the French scientist Bachelet who proposed using coils excited with AC currents by magnetic induction for levitation [217, pp. 15]. He built a prototype vehicle which carried a conducting aluminum plate on its bottom surface, and was levitated above a row of electromagnets. He found that for this system the power dissipation was prohibitive, requiring 15 kiloWatts to levitate a 15 kg mass at a height of 1 centimeter.

The first recorded demonstration of magnetic levitation using superconductors was by Arkadiev in 1945 who levitated a 15 millimeter wide bar over a superconducting lead plate [215, pp. 35]. Subsequent research in the 1950's was done on levitated superconducting rotors for gyroscope applications. A method for levitating a moving vehicle over superconducting rails was proposed by Powell in 1963. This scheme was modified later and by Powell and Danby in 1966 [163] who first proposed placing superconducting magnets on a moving vehicle, levitating the vehicle above a passive guideway where there are induced currents.

Guderjahn et. al. [138, 158, 159] and Coffey et. al. [154] in 1969 proposed using similar technology to levitate and propel high speed rockets. The Guderjahn design consisted of null-flux coils levitated over a thick aluminum sheet. The calculated lift/drag ratio of 10/1 at cruising speed was sufficient for a test rocket sled, but is not practical for a high-speed train.

Studies of baseline specifications for Maglev vehicles using low temperature superconductors were done by Borcherts et. al. [153] and Thornton [175] in 1973 who proposed specifications for vehicles capable of 300 miles/hour. Pioneering Japanese work was done by Ichikawa and Ogiwara [161] who in 1974 proposed a Maglev train with Nb-Ti suspension coils operating at 250 kA-turns. Continuous sheet guideways were considered plausible until the mid 1970s, when it was shown in several studies that significantly higher efficiency could be achieved with ladder or discrete-coil guideways.

2.3.3. Maglev System Specification and Design

In the heyday of Maglev EDS research in the 1970's, a number of studies were done which specified Maglev system requirements and performance. Borcherts, Davis, Reitz, and Wilkie [153] in 1973 presented a baseline specification for an EDS train, with a cruising speed of 300 miles/hour. In this design, the train travels in a U-shaped guideway with separate lift and guidance magnets. Details of the cryostat design, as well as heat load were given.

Miericke and Urankar [210, 211] in 1973-74 developed exact analytical expressions for an EDS system utilizing null flux coils and a continuous sheet track.

Results are compared to normal flux systems. They conclude that the continuous sheet track is superior with regard to construction costs and safety as compared to the closed loop guideway proposed by Powell and Danby.

Andriollo et. al. [149] present a method for the design optimization of the coil configurations for an EDS Maglev system. A number of design criteria were considered in the design study, including the amount of the levitation coil conductor, the levitation transient stability, ride comfort, and others. Over 700 different designs were considered and evaluated by computer, and designs were optimized for a given cost function.

Papers from workers at the Japanese National Railway [156, 157] discuss the design of the MLU002 prototypes, designed to operate up to 500 km/hour. The Japanese system has a non-linear vertical spring constant, and a nominal operating gap of approximately 20 cm. The papers give significant detail on the primary suspension, but secondary suspension and control is not discussed.

The United States Department of Transportation funded 4 system concept definition reports [178] in 1992. The separate studies considered baseline designs for Maglev vehicles, including suspension, guidance, guideway, and propulsion systems.

2.3.4. Maglev Circuit Modeling Techniques

The impedance-modeling technique is a method by which the electrodynamic effects in Maglev coils and guideway structures are reduced to lumped circuit models. The simplest circuit models allow calculation of average forces. Although the circuit modeling tends to obscure the details of the electrodynamic interactions, it is a powerful technique for evaluating Maglev systems.

The technique was first introduced by Guderjahn et. al. [138] in 1969 in an analysis of the use of magnetic levitation for a rocket sleds in an evacuated tube. In this technique, the energy of the entire levitated system is evaluated by measuring the inductance of the excited coils as position is varied. The force on the coils can be calculated if the gradient of the mutual inductance is found. Image methods were used to predict Maglev lift forces at high train speed.

Iwasa [52] applied the technique to the Magneplane Maglev system in 1972. The technique was extended to study the static stability of pitch and roll. The method was used by Ohno et. al. [57] in 1973 to predict pulsating forces in discrete-coil Maglev guideway geometries. The method was applied in 1974 by Atherton and Eastham [134] to Maglev geometries for various levitation and guidance schemes. In 1975, Howell et. al. [91] applied similar techniques to the Wolfson experimental Maglev vehicle, and evaluated dynamic stability, ignoring aerodynamic damping. They found that dynamic stability could be greatly improved by adding passive copper damping windings. In 1976, Atherton et. al. [61] applied the impedance modeling technique to Maglev systems with passive secondary suspensions. They claim that passive aluminum damper coils mounted on the underside of the sprung mass are an attractive alternative to mechanical or hydraulic dampers. Wong, Mulhall, and Rhodes [59] summarized the results of previous workers and further explained the use of transformer models for evaluating Maglev forces.

The technique was further expanded to include multiple-loop coils and guideways, with works by He, Rote and Coffey [48 - 50] and Ooi [58], among others. Methods of guideway inductance calculation were discussed by Mills [54 - 56], who summarizes some of the inductance calculation methods of Grover [34]. An important simplification that is made when evaluating the null-flux topology is that the guideway conductors are large enough and far enough apart that the mutual inductance with adjacent coils is ignored. Multiple-loop structures require the computation of inductance and resistance matrices. The computations are simplified if a single-harmonic excitation is assumed.

Jain and Ooi [53] discuss the limitations of the impedance modeling technique. They show that the technique is valid in the high speed limit, but that the fundamental approximations break down in the low speed limit.

2.3.5. EDS Maglev Electromechanical Stability

Early studies of Maglev suspensions focused on the calculation and measurement of static forces and torques, rather than the dynamics of vehicle motion. The stability of Maglev train motion is of considerable interest due to its effects on passenger safety and structural requirements. The subject is very complicated and there is not as yet a definitive reference covering all aspects of Maglev stability. Many theoretical studies have been performed on simplified limiting cases.

Woods et. al. [98] considered the stability of a levitated superconducting current ring and evaluated passive damping techniques as well as active stabilization. In a related topic, Holmes [90] studied the stability of levitating forces on metal spheres suspended in A.C. magnetic fields, with application to induction heating of molten metals.

Davis and Wilkie [87] and Fink and Hobrecht [88] analyzed the motion of a long wire over a thin conducting plate, and found vertical and translational instabilities in the absence of air drag. They found that for a Maglev system the unstable longitudinal time constant is very long (~ several minutes) and that there is an underdamped vertical mode at approximately 2 Hz. These studies further showed that the vertical oscillation of the moving wire can produce a negative damping force depending on the wire speed.

Yamada et. al. [99] built an experimental facility to test the dynamics of EDS Maglev in 1973. A ferrite magnet was suspended and allowed to vibrate near a rotating aluminum drum. The damping behavior of the system was observed at various operating speeds, and it was found that negative damping exists for linear velocities above a critical velocity. For a full-scale train traveling over a sheet guideway, these results extrapolated to negative damping for train speeds higher than ~60 km/hour.

Iwasa [52] and later Iwamoto et. al. [92] and Ohsaki [97] applied the inductance-modeling method to the study of Maglev stability. Iwamoto predicts a negative damping coefficient for train speed over ~50 m/sec traveling over a trace with discrete loops.

Iwamoto recommends using passive damping to achieve good ride quality. Nguyen et. al. [96] describe the design of a passive magnetic damper.

Chu and Moon [86], demonstrated instabilities in a 2 D.O.F. electrodynamic Maglev model, showing limit cycle oscillations at operating speeds near the Maglev drag peak. Due to the small scale of their model, aerodynamics significantly affected their results. In other experiments, Moon reports results from a rotating wheel test facility for study of lateral, heave, roll, yaw, and pitch motions [95, pp. 140]. A yaw-roll instability was observed.

The most detailed study of instabilities in EDS Maglev has been performed by the Cai and Chen and the Maglev group at Argonne National Laboratories [84]. Suspension instabilities of EDS systems with 3 and 5 degrees-of-freedom (D.O.F.) have been evaluated by computer simulation. Their results show that coupling effects among the 5 D.O.F. play an important role and that there are several potential instabilities. The instabilities depend on the equilibrium air gap, which in turn is determined by the vehicle mass, passenger load, and guideway design.

2.3.6. Maglev Control Systems

Several different schemes for active and passive control of vertical dynamics have been proposed. They include active secondary air suspensions [65], passive damping using aluminum or copper damping coils [61], and hydraulic dampers [74]. Active control of magnet currents is proposed for EMS systems, where copper coils are used and superconducting magnet quenching is not an issue General discussions of EMS control systems were done by Goodall's group in England [72, 73]. Other EMS secondary suspension studies were done by Fruechte et. al. [71] at General Motors Corporation, and by Gran and Proise [75] at Grumman Corporation. Another method for EMS control involves using a phase-locked loop [79] for the stabilization of vertical position. In this scheme, the levitating coil is a tuning element in a phase locked loop. Secondary mechanical suspensions are discussed in Abe and Tsunashima [60] for EMS systems, and in [80] for EDS systems.

For EDS systems using low temperature superconductors, active control of the magnet currents has not been implemented due to the deleterious effects of AC losses. Several studies show that the intrinsic damping of vertical dynamics is very low. Atherton, Eastham, and Sturgess [61] proposed secondary magnetic damping using short-circuited aluminum coils coupled to the linear synchronous motor. The use of the linear synchronous motor for active heave damping was demonstrated by Brown [183] in 1975 for the M.I.T. Magneplane project. Nagai, Mori, and Nakadai [65] built a small scale one degree-of-freedom EDS Maglev test fixture, with a resultant damping ratio without control of 0.5%. With active control, the damping ratio was increased to 20%.

Boldea [83] performed an analysis where it is shown that an EDS system with active control of magnet currents can theoretically provide good ride comfort at 100 m/sec without a secondary suspension system. Secondary control coils are allowed to have transient currents under active control. Performance of the discrete ladder and continuous-sheet guideways are compared. It was found that for the continuous sheet, for a full-scale Maglev system the drag peak will occur at approximately 40 m/sec, and a high speed lift-drag ratio of 14 is predicted. This is compared to a ladder guideway, where the drag peak occurs at 15 m/sec and a lift/drag ratio of 29 is predicted at cruising speed. Also, for the continuous sheet, skin effect is more pronounced due to the wide geometry of the sheet.

Modern control systems with control of multiple degrees of freedom for EDS systems are discussed by Nakadai, Nagai, Nonami, He, and Nishimura [67, 68].

2.3.7. Maglev Thermal Stability

Low temperature superconducting coils are susceptible to quenching due to AC losses from magnetic, electrical, and mechanical disturbances. Pioneering work on mechanical disturbances and its effect on LTSC coils was done by Wilson [295] in the 1970's. Since the discovery of mechanically-induced quenching in the Japanese Maglev program, several studies were done [197, 198, 204] discussing mechanical requirements for air-core LTSC magnets suitable for Maglev. A later study [199] shows the effects of a magnet quench on the levitation and guidance forces in a running Maglev train. This is of particular interest, since the low temperature superconducting coils on the MLU002 train run at 95% of the design limit.

2.3.8. Maglev Scale-Model Test Results

Several programs have been implemented to evaluate Maglev scale model systems. With the notable exception of a test fixture for evaluation of linear synchronous motors and null-flux suspension built by the Japanese National Railways in 1975 [187], work has concentrated on models of discrete-coil systems.

One of the earliest model tests was performed by Borcherts and Davis at Ford [182] in 1972. A 4.24 centimeter diameter low temperature superconducting coil was suspended in a cryostat above a rotating 61 centimeter diameter aluminum cylinder. The cylinder was rotated up to linear peripheral speeds of 483 kilometers/hour. The experimental results were used to compare to analytic results for a loop coil traveling over a continuous sheet guideway. A lift/drag ratio at high speed of 30-50 was predicted for a full scale train. Other early tests were done by the Siemens group in the early 1970s [185, 211, 212].

At M.I.T., 1/25 scale tests of the Magneplane system of Kolm, Thornton, Iwasa, Brown [183, 188, 189] and others was carried out in 1972-75. The 1 meter long, 14 kilogram test vehicle was propelled by a linear synchronous motor at 25 meters/second on a 116 meter long guideway. Active heave damping was provided by the linear synchronous motor. It was shown that the superconducting magnet vehicle was lighter than a similar design with permanent magnets, and that the linear synchronous motor could be used to damp heave oscillations.

A 550 meter test track was built and operated at the University of Warwick by Rhodes and Mulhall [194]. A scale model vehicle was tested, towed by a rope up to speeds of 35 meters/second. The vehicle was 3 meters long and weighed 150 kilograms.

Canadian Maglev studies have been carried out at the Universities of Toronto, Queens, and McGill. Electrodynamic forces and moments have been measured on a 7.6 meter diameter, 1 centimeter thick rotating aluminum test wheel [180]. Test in the mid-1970's simulated continuous sheet guideways.

Later rotating test fixtures have been operated at Argonne National Laboratories by Mulcahy, He, Rote and Rossing [192], at Siemens Corporation [185] and a smaller scale test at the University of Budapest [181]. A test fixture for EMS low speed people movers has been built by Japan Air Lines [186].

2.3.9. Other Issues Related to Maglev System Design

2.3.9.1.Magnetic Shielding

Magnetic shielding is of special importance in air-core Maglev designs such as the Japanese MLU-series. The German EMS system has lower guideway field, and the iron core design and iron rails guide the flux away from the passenger cabin. Significant work has been done in Japan to reduce stray fields. Passive and active shielding have been discussed.

Passive shielding for Maglev was first discussed by Iwasa [131] in 1973. He found that a heavy iron plate 2 cm thick must be placed in the floor of the passenger cabin, adding 10,000 kg to the weight of a 100 passenger vehicle. An aluminum shield was recommended to attenuate A.C. fields due to propulsion windings. Later works [130, 132] result in designs which may be lighter.

An analysis of stray magnetic fields from a linear synchronous motor was done by Thornton et. al. for the Department of Transportation in 1993 [176, pp. 85]. The study developed approximate models for the far field due to an array of magnets, and included end effects. Mitigating strategies for reducing the stray field were offered. Although the study was done in the context of linear synchronous motors, the results are applicable to iron-core and air-core Maglev magnets.

2.3.9.2.Guideway Design and Ride Comfort

The study of guideway design and ride comfort are important because of safety and system cost issues. The cost of a guideway structure is expected to be 60-80% of the overall initial capital investment [145]. A more flexible guideway can be built at a lower cost, but there are complications due to vehicle/guideway interactions which may impact safety and ride quality. A Ph.D. thesis by Phelan [118] at M.I.T. discusses Maglev guideway structures.

Fearnsides et. al. [146] reviewed ride quality specifications. They used railroads as their test case, but the results are applicable to Maglev vehicles. Later, Jayawant and

Sinha [148] studied low speed vehicle dynamics with specific application to EMS Maglev systems operating up to 50-70 km/hour. They built an experimental suspension test rig and determined that the optimum operating air gap for an attractive suspension is around 15 mm, if the passenger acceleration level was not to exceed 0.04g. This could be achieved without a secondary suspension.

In 1972, Yamada et. al. [112] performed a study comparing guideways with independent coils with a proposed ladder guideway systems. It was found that the ladder system has a higher lift-drag ratio at cruising speed, and that it is desirable to increase the number of guideway coils in order to reduce the pulsating forces acting on the train.

Cai. et. al. [145] and the group at Argonne National Laboratories have developed a model which consists of a rigid train consisting of multiple magnetic loads traveling over a flexible guideway. Their results show that less guideway deflections occur if the levitation magnets are distributed over the length of a vehicle. Although this is an intuitive result, their results are important as they quantitatively evaluate expected guideway deflections, which can be kept to a fraction of a centimeter by proper design.

In a U.S. Department of Transportation supported work, Zahn [120] discussed heating effects in steel rebars in Maglev guideways. In this study, transient electromagnetic effects due to the field from the passing train are analyzed for representative guideway structure.

2.4. Test Wheel Mechanical Design Issues

A short review of the literature in flywheel design was performed prior to the design of our Maglev test wheel. Of specific interest are material parameters of composite materials such as strength, cost, and thermal properties found in [228-231, 236]. Basic stress analysis for rotating discs is found in reference [255], and rotordynamics and calculation of rotating wheel resonances is found in references [245, 256].

3. Test Fixture Design and Construction

This chapter discusses in detail the mechanical design of the MAGLEV test fixture, including details of the test wheel, guideway conductor pattern, cryostat, air bearing, and liquid nitrogen delivery system.

3.1. Guideway and Test Wheel Mechanical Design

The test wheel was designed with the following goals and specifications:

- The guideway pattern was designed for low manufacturing cost and good electrical performance. Copper sheets were cut with a high pressure water jet cutter. The resultant conductor pattern was brazed to ensure a good electrical joint along the inner and outer rims.
- The test wheel rim will not deflect axially greater than 1 millimeter under magnetic loads. This insures that magnetic measurements will not be significantly affected by deflections under magnetic loading, and that axial wheel resonant frequencies will not be significantly excited.
- Wheel will not yield for speeds up to 1000 RPM, with an acceptable safety margin. Detailed stress analyses were not performed; however, a conservative design approach was used. Stresses due to rotation, magnetic forces, and thermal expansion were calculated and accounted for.
- Wheel was constructed using low cost materials and fabrication techniques.
- Lowest wheel resonant frequencies and mode shapes were calculated and measured in order to determine flywheel critical speeds. These resonances will be excited if there is any imbalance in the test wheel. The wheel response at these critical speeds was monitored during operation. Disk flexure resonances were measured using two accelerometers.

Under magnetic load, an order of magnitude estimate for the maximum levitation force can be found by evaluating the magnetic pressure. It is expected that during normal operation of the test fixture that the magnetic field at the polefaces will be 0.1 Tesla or less. This approximation is a useful order-of-magnitude estimate for the magnitude of the magnetic force. Given 8 polefaces, each of area A_p approximately 4 cm × 8 cm,

$$f_{z,\max} \approx \frac{B_o^2 A_p}{2\mu_o} \approx \frac{(0.1)^2(8)(0.04)(0.08)}{2(4\pi \times 10^{-7})} \approx 100 \; Newtons \qquad [Eq.\ 3\text{-}1]$$

Therefore, there will be a maximum levitation force of 0-100 Newtons. The maximum drag force for EDS MAGLEV is 50% of the maximum lift force, so the design will result in a drag force of 0-50 Newtons. The resultant force acting on the test wheel is distributed over many levitation coils inside the test wheel.

3.1.1. Selection of Construction Materials for Wheel

The design of the test wheel involves selecting proper materials for the guideway conductors and wheel substrate. This selection process requires the analysis of cost, ease of construction, and mechanical properties. For the guideway conductors (*Table 3-1)* copper and aluminum were considered. Aluminum is lighter, with a comparable yield stress to copper, but is more difficult to electrically connect, requiring a welding operation. Copper has the advantage of higher electrical conductivity and ease of brazing but has a higher cost per unit volume. Therefore, copper was chosen for the guideway conductors.

Table 3-1. Test wheel guideway material parameters

Material	***E, modulus (GPa)***	***Density (g/cm^3)***	***Yield stress (MPa)***	***Cost, $/kg***
Copper	118	8.95	260	~2
Aluminum	69	2.75	250-400	~2

Several substrate materials were considered (*Table 3-2*). Carbon fiber and aramid are attractive because of their high modulus of elasticity, high yield stress, and low density. However, the cost per unit mass is much higher than fiberglass. Therefore, fiberglass was chosen for the final wheel design, resulting in the lowest material cost design.

Table 3-2. Test wheel rim structural material parameters

Material	***E, modulus (GPa)***	***Density (g/cm^3)***	***Yield stress (GPa)***	***Cost, $/kg***	***Estimated wheel mass***	***Material cost***
Fiberglass	50~85	2.5	3.4~4.5	~1	66 kg	~$70
Polyethylene	120	0.97	2.59	-	27 kg	-
Aramid (Kevlar)	120	1.44	4.5	~10-20	40 kg	~$400-800
Carbon fiber	300~500	1.5	2~6	~20-50`	42 kg	~$840-2100

The final specifications for the test wheel are shown in *Table 3-3* and *Figure 3-1.*

Table 3-3. Test wheel geometry specification

	Minimum	***Maximum***
Rim outer radius, R	34.10" (86.6 cm)	34.40" (87.4 cm)
Rim inner radius, r_i	19.985" (50.75 cm)	20.015" (50.84 cm)
Rim thickness, h	0.625" (1.59 cm)	0.650" (1.65 cm)
Copper conductor inner radius	29.5" nominal (74.9 cm)	
Copper conductor outer radius	33.5" nominal (85.1 cm)	
Copper conductor nominal radius	31.5" (80 cm)	
Wheel front face runout	+0.030" (0.05 cm)	-0.030"
Aluminum hub diameter	50" (127 cm)	
Aluminum hub thickness	1" (2.54 cm)	
Bolt circle	20 holes for 0.765" bolts on a 45.5" diameter	

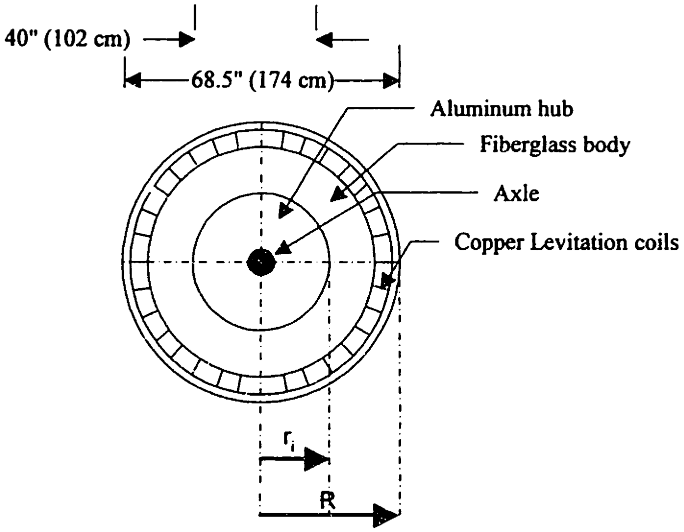

(a) Front view of test wheel

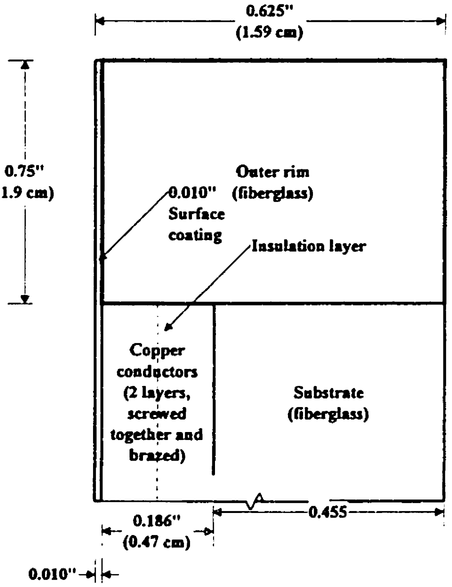

(b) Cross-sectional view of test wheel near outer edge (to scale)

Figure 3-1. Test wheel geometry.

3.1.2. Guideway Mechanical Design and Metal Cutting

The guideway conductor pattern was constructed from 0.093" thick sheets of 1/2 hard #110 copper. The repeating conductor pattern was cut with an Omax high-pressure numerically-controlled water jet cutter, from 35"×12" sections of copper (*Figure 3-3a*) in a 60^0 section. The water jet cutter has a high-pressure jet 0.030" in diameter and garnet dust is injected into the water stream as an abrasive to increase cutting speed and efficiency. The originally-designed guideway geometry was adjusted to accommodate a minimum cutting line width of 0.030."

The water jet cutting proved to be a more economical method than other methods. The thin slot width does not allow an efficient milling operation. Laser cutting for thick sheets is difficult due to the high thermal conductivity and reflectivity of copper. Wire-EDM is a precision process, but is costly and slow. The water cutting resulted in an acceptable mechanical tolerances of a few thousandths of an inch. Each 60° section took approximately 1 hour to cut. For a production operation, the conductor pattern could be punched out of sheets of copper.

The dimensions of the guideway conductors are shown in *Figure 3-3b*. The dimensions were chosen with attention to electrical performance and mechanical integrity. For instance, the 0.2" rim width was designed with attention to the hoop tension caused by test wheel rotation. The width of the individual ladder rungs was maximized in order to reduce the resistance of the loops.

A free-body diagram of the guideway rungs is shown in *Figure 3-3c*. The inertial force due to wheel revolution (F_r) acts at point *C*, the center of mass of the guideway rungs. The magnetic levitating force (F_m) is distributed over the horizontal sections of the ladder rungs and rim, and is modeled as acting at point *B*. The combined inertial and magnetic forces act as a shear load on the copper/fiberglass interface, with maximum compressive stress on the fiberglass at point *C*. Therefore these forces are transmitted to the rim and contribute to the hoop tension acting on the rim. Therefore the rim was designed with high tensile strength in mind.

Each section was terminated with an end joint which was mated in a lap joint with the next copper section. This joint was designed with maximum mechanical strength in mind, as the hoop tension during test wheel rotation is significant. The end joint is shown in *Figure 3-2*.

Figure 3-2. Prototype single guideway layer

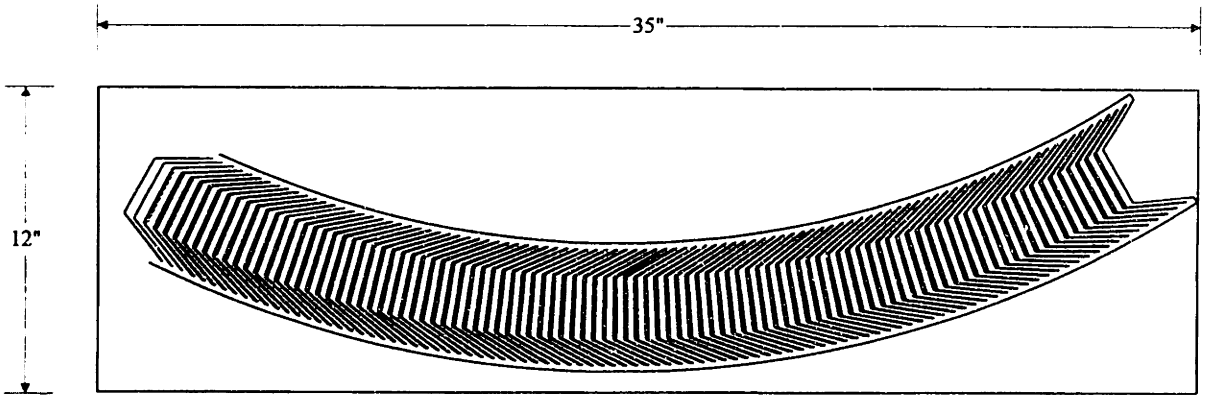

(a) 60° wheel section cut from sheet of copper

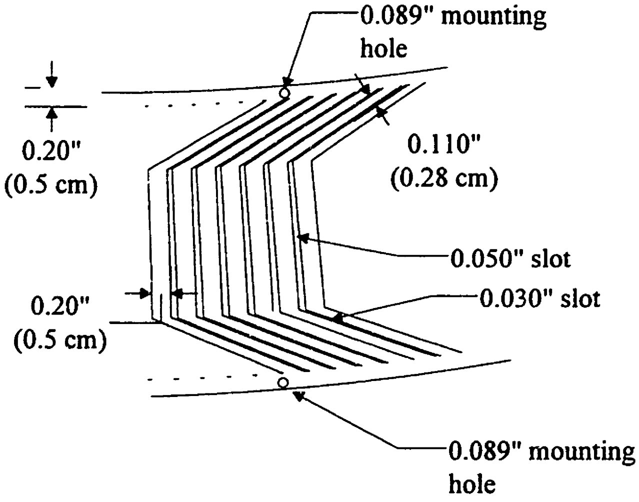

(b) Dimensioned detail of guideway conductors

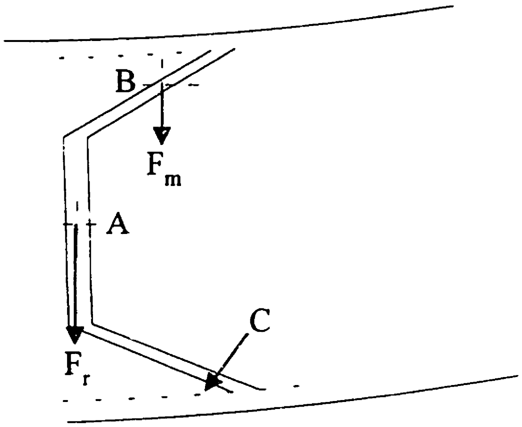

(c) Free-body diagram of guideway rung

Figure 3-3. Detail of guideway conductors

3.1.3. Test Wheel Static Deflections and Stresses

The state of stress and deflections in the wheel are analyzed assuming plane stress only. That is, the wheel thickness is much smaller than its radius, and the variation of stress with thickness can be assumed to be negligible, and the axial stress is small compared to the radial and azimuthal stresses. Therefore, the tensile stress ($\sigma_{\theta\theta}$) and the radial shear stress ($\sigma_{\theta r}$) are the dominant stress components (*Figure 3-4a*).

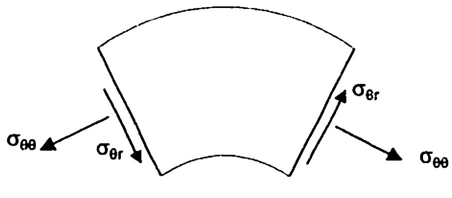

(a) Geometry for determining stress in flywheel section

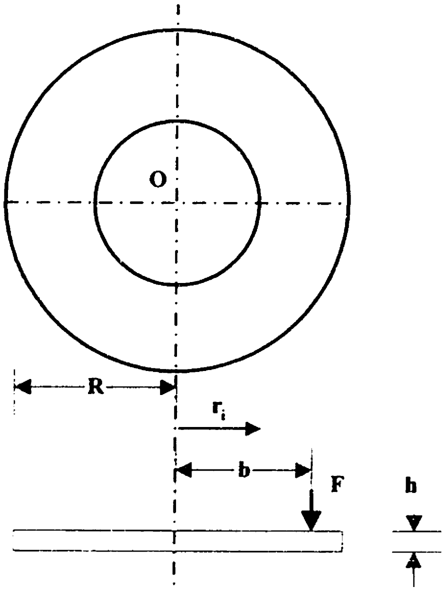

(b) Disk with applied magnetic point load F

Figure 3-4. Geometry for determining wheel deflection under magnetic load

It is assumed that the forces act normal to the surface of the test wheel. The geometry of the wheel is shown in *Figure 3-4b*, where the magnetic load is modeled as a point load F acting at a radius of $r = b$. The aluminum hub is modeled as a rigid body which will not deflect under load.

The force acts at a point near the edge of the test wheel. The bending stress at the inner edge of the fiberglass at $r = r_i$ is given by [251, pp. 233]:

$$\sigma_{r,\max} \approx 4.7\frac{F}{h^2} \qquad \text{[Eq. 3-2]}$$

giving for $F = 500$ N, and $h \approx 1.5$ cm a maximum stress $\sigma_{r,max} \approx 10$ MPa, which is well below the yield stress of fiberglass where $\sigma_y \approx 1000$ MPa.

The deflection due to load is more difficult to analyze. However, the deflection has the form:

$$\Delta_{\max} \propto kF\frac{R^2}{Eh^3} \qquad \textit{[Eq. 3-3]}$$

Timoshenko [255] shows that the coefficient $k \approx 0.06$ for the case shown. Therefore, for $F = 500$ N, R = 0.9 meter, $E = 50$ GPa, and $h = 1.6$ cm, the maximum deflection $\Delta_{max} \approx$ 0.1 mm. Therefore, the wheel thickness is sized acceptably for static loads.

3.1.4. Stresses due to Disk Rotation

For stresses due to disk rotation, the design strategy was to calculate several limiting cases of wheel loading, and to build a conservative design. The shear and tensile stresses due to disk rotation [251] assuming plane stress and small deflections are given by:

$$\begin{aligned} \sigma_{\theta r}(r) &= \frac{3+\nu}{8}\rho\omega^2(R^2 + r_i - \frac{R^2 r_i^2}{r^2} - r^2) \\ \sigma_{\theta\theta}(r) &= \frac{3+\nu}{8}\rho\omega^2(R^2 + r_i - \frac{R^2 r_i^2}{r^2}\frac{1+3\nu}{2+\nu}r^2) \end{aligned} \qquad \textit{[Eq. 3-4]}$$

where:

ν = Poisson's ratio ~ 0.3 for fiberglass
ρ = density of material ~ 2500 kg/m^3
R = outer radius of disk (m)
r_i = inner radius of disk (m)
r = radius to point inside wheel (m)
ω = angular speed (radians/sec)

The highest radial (shear) stress occurs at $r = \sqrt{Rr_i}$ [251] and the highest tangential stress occurs at the inner radius. The stresses calculated (*Figure 3-5*) are well below the yield stress for fiberglass composite.

This initial calculation does not take into effect the stress in the copper conductors at the periphery of the wheel. As a starting point, the hoop stress acting a copper ring is calculated. For the thin ring, the tensile stress is found by:

$$\sigma_{\theta\theta,Cu} \approx \rho_{Cu}(\omega R)^2 \qquad \textit{[Eq. 3-5]}$$

The maximum rotation speed for the hoop is given by:

$$\omega_{\max} \approx \frac{1}{R}\sqrt{\frac{\sigma_y}{\rho}} \qquad \textit{[Eq. 3-6]}$$

Therefore, the stress is of more importance using copper conductors than a similar design using aluminum. Equivalently, an aluminum ring may be rotated at a higher speed because the yield stresses of aluminum and copper are comparable and aluminum is 3 times lighter than copper.

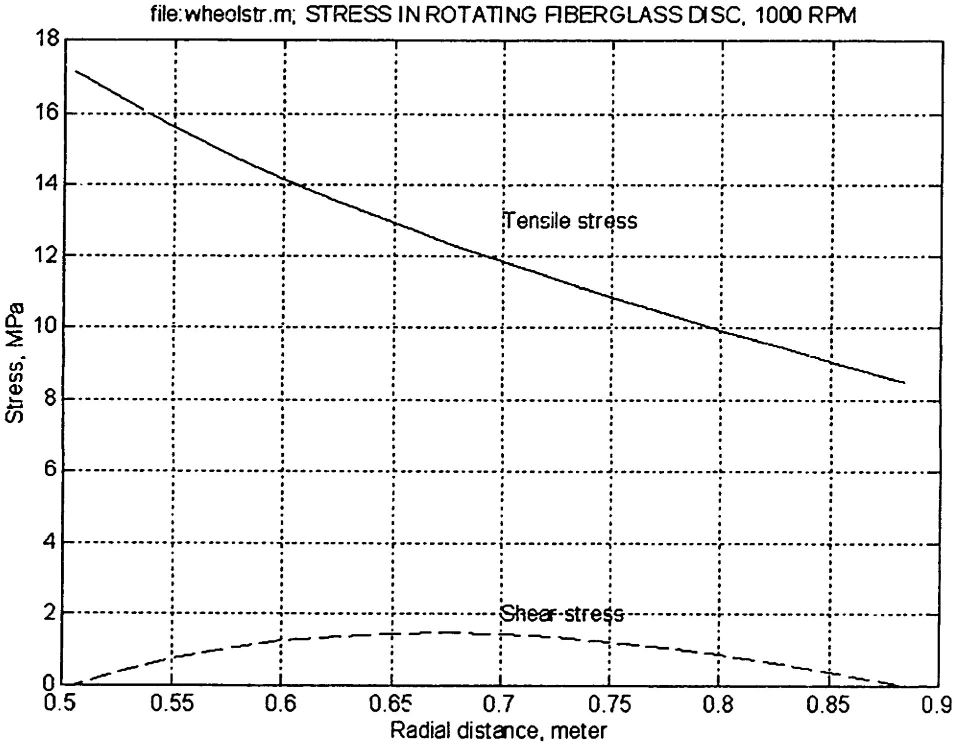

Figure 3-5. Tensile and shear stress in rotating fiberglass disk at 1000 RPM

The bond between the fiberglass substrate and the copper conductor at point *A* (*Figure 3-3c*) is of special importance. Ignoring the effect of the side rung (point *B*), shear stress τ_{zr} is set up at this point on the fiberglass, equal to:

$$\tau_{zr} \approx \frac{2t_c \rho_{Cu} v_{\max}^2}{R} \qquad [Eq.\ 3\text{-}7]$$

The copper plate thickness is t_c and v_{max} is the linear velocity at the outer copper radius R. The factor of 2 is due to the fact that there are two copper plates, one on top of another. An upper bound for the shear stress acting at point A is calculated to be 0.4 MPa, well below the maximum shear stress for fiberglass.

At 1000 RPM, the maximum hoop stress in the copper results in $\sigma_{\theta\theta} \approx 70$ MPa. For a copper yield stress of $\sigma_y \approx 260$ MPa, a maximum wheel speed of 1600 RPM is calculated. When the distributed effect of the coils is taken into effect, the calculated hoop stress will be increased; it is estimated that the hoop stress will be increased by a factor of 6 due to the rungs of the guideway ladder, resulting in a maximum rotation speed of 1100 RPM. Therefore, the fiberglass substrate must be suitably sized so that the stress in the copper is reduced so that an acceptable safety margin is achieved.

The wheel lamination is modeled as in *Figure 3-6*, where the tensile force *F* acts on a section of the laminated wheel. In this idealization, the bond between the copper and the fiberglass is rigid, so that the copper and fiberglass strain together. The weight of the fiberglass is ignored in determining the force due to the hoop stress. The copper and fiberglass sections are modeled as two mechanical springs in parallel. The force due to the hoop stress in the copper conductors is divided up between the two springs in relation to the spring constants; for instance, the force in the copper is given by:

$$F_c \approx F\frac{k_c}{k_c + k_f} = F\frac{E_c t_c}{E_c t_c + E_f t_f} \qquad \textit{[Eq. 3-8]}$$

where E_c is the Young's modulus for copper and E_f is the modulus for fiberglass. Based on the elementary stress analysis, a reasonable design approach would be to make $E_c t_c \approx E_f t_f$, hence reducing the hoop stress by a factor of 2 without adding too much fiberglass weight. Therefore, with $E_c \approx 120$ GPa, $E_f \approx 60$ GPa, and $t_c = 0.186"$, $t_f = 0.372"$. This result is consistent with the earlier analysis for static deflections, and a fiberglass substrate of $t_f = 0.455"$ is sufficient.

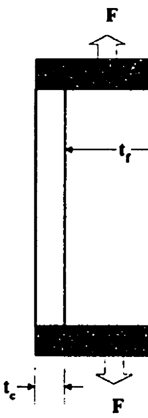

Figure 3-6. Wheel lamination model for determining minimum fiberglass thickness

As shown in *Table 3-4*, at maximum wheel speed the linear peripheral speed is greater than 300 kilometers/hour. The resultant acceleration at the periphery is approximately 1000 g at 1000 RPM.

Table 3-4. Wheel speed and linear peripheral velocity

RPM	***meter/sec***	***km/hour***	***miles/hour***
0	0	0	0
100	8	30	19
200	17	60	37
300	25	90	56
400	34	121	75
500	42	151	94
600	50	181	112
700	59	211	131
800	67	241	150
900	75	271	169
1000	84	302	187

3.1.5. Thermal Expansion

The copper levitation coils embedded in the test wheel have power dissipation due to the induced currents in the loops. The power dissipation may be expressed as:

$$< P_{coils} > = v f_{drag} \qquad [Eq.\ 3\text{-}9]$$

where f_{drag} is the magnetic drag force and v is the linear surface velocity of the magnets over the conductors. The maximum drag force during operation of the wheel is expected to be approximately 100 Newtons at maximum magnetic field at a speed of ~25 meters/second. The total maximum power (2500 Watts) power is dissipated over the 600 individual loops in the test wheel, with a resulting maximum power dissipation of approximately 4 Watts per coil. Each coil has a volume of approximately 2.5 cm^3, and a mass of $M_{coil} \approx$ 22 grams. Given a maximum safe temperature rise, the maximum operating time before the wheel is allowed to cool down is calculated from:

$$t_{op} \approx \frac{C_v M_{coil} \Delta T}{< P_{coil} >} \qquad [Eq.\ 3\text{-}10]$$

where C_v = 385 J/kg-K is the heat capacity of copper and ΔT is the maximum allowable temperature rise. This calculation assumed that the temperature of the copper conductors rises adiabatically, and that there is no heat flow to the surrounding fiberglass. The thermally-induced stress $\sigma_{thermal}$ in the fiberglass is then:

$$\sigma_{thermal} \approx E_f \alpha_c \Delta T \qquad [Eq.\ 3\text{-}11]$$

where $E_f \approx$ 50 MPa is the Young's modulus of the fiberglass-epoxy composite and $\alpha_c \approx$ 17 ppm/°C is the temperature coefficient of thermal expansion of the copper. The yield stress of composite is ~1000 MPa, and for an acceptable safety margin, $\sigma_{thermal}$ was chosen to be 100 MPa, resulting in a maximum temperature rise of 98 °C, and a maximum operating time of 66 seconds. However, fiberglass has a tendency to soften at higher temperatures, so in normal operation the wheel temperature was monitored to keep the temperature rise below 10 °K. The temperature rise will be lower than calculated due to heat conduction to the fiberglass and cooling due to wind flow.

A stress analysis summary (*Table 3-5*) shows that the wheel should operate safely up to speeds of 1000 RPM. The shear stress in the brass screws exceeds the yield stress in this simple analysis, but will be lower due to the forces transferred to the solder joint and fiberglass substrate.

Table 3-5. Summary of maximum calculated stresses in test wheel at 1000 RPM

Cause of stress	***Calculated stress (MPa)***	***Maximum allowable stress (MPa)***
Shear stress in fiberglass, due to wheel	18	~500
Tensile stress in fiberglass	~2	~500
Shear stress in fiberglass, due to copper	0.4	~500
Hoop stress in copper	~210	260
Hoop stress in solder	59	104
Shear stress in solder	17	76
Shear stress in 4-40 brass screws	115	75

3.1.6. Wheel Resonant Frequencies

The wheel resonant frequencies were calculated so that vibration may be monitored during wheel operation. During wheel acceleration, or if there is a static or dynamic unbalance, wheel resonances will be excited. This analysis is for purposes of calculating first-order resonant frequencies only.

In order to calculate various wheel resonant frequencies (or "critical speeds"), a lumped-parameter model is used to calculate the lowest natural frequencies for several different vibration modes. During wheel operation, anomalous wheel responses will be monitored.

3.1.6.1. Torsional Resonance

There is a torsional mode corresponding to the twisting of the disk with moment of inertia $I_{\theta\theta}$ on a flexible shaft with torsional spring constant k_t given in Newtons/radian. When this mode is excited, the wheel will behave as a torsional pendulum (*Figure 3-7*). The torsional stiffness of the axle is found by [256]:

$$k_t = \frac{GJ}{l_t} = \frac{\pi R^4 G}{2l_t} \qquad \text{[Eq. 3-12]}$$

where G is the shear modulus of the aluminum shaft ($\approx$ 26 GPa) [230, pp. 286], J is the polar moment of the cross sectional area, and l_t is the shaft length between the wheel and the motor coupling. The shaft acts as a torsional spring, with resultant resonance of the torsional pendulum given by:

$$\omega_t \approx \sqrt{\frac{k_t}{I_{\theta\theta}}} \qquad \text{[Eq. 3-13]}$$

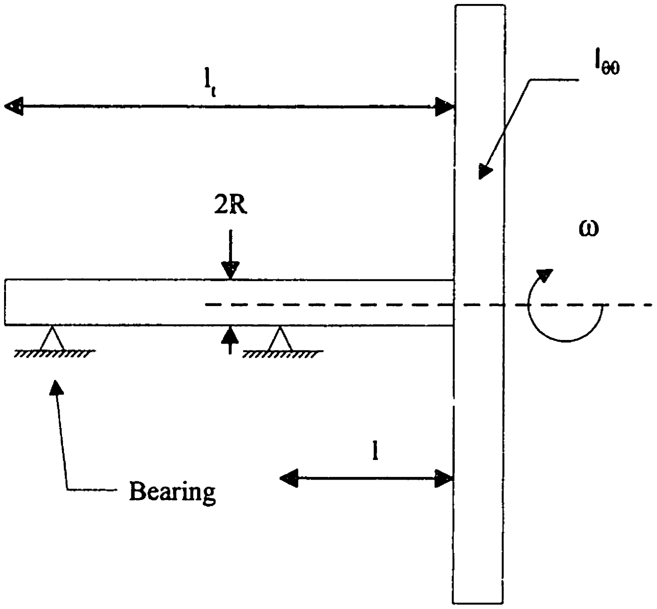

Figure 3-7. Model for determining torsional resonance

The moment of inertia $I_{\theta\theta}$ is comprised of 3 components, due to the aluminum hub, the fiberglass wheel, and the copper conductors in the periphery. The first moment of inertia of a disk of thickness h, mass density ρ, and radius R is:

$$I_{disk} = \frac{1}{2}\rho\pi R^4 h = \frac{1}{2} MR^2 \qquad \text{[Eq. 3-14]}$$

The moment of inertia of the copper guideway may be approximated by the moment of a thin ring of mass M and radius R where $M = 15.6$ kg and $R \approx 0.8$ meter:

$$I_{ring} = \frac{1}{2} MR^2 \qquad \text{[Eq. 3-15]}$$

Table 3-6. Test wheel components of moments of inertia

Source	***Calculated rotational moment of inertia about axle axis***
Copper coils	$I_{copper} = 5.0$ kg-m^2
Aluminum hub	$I_{Al} = 17.5$ kg-m^2
Fiberglass rim	$I_f = 34.6$ kg-m^2

These results show that modification of the guideway design will not significantly affect the wheel resonant frequencies.

3.1.6.2.Bending Resonance

The bending resonance can be approximated by calculating the bending spring constant of the axle and assuming that the wheel is a point mass. Although this method is not strictly correct [250, pp. 254] it is a useful approximation technique. The bending resonance is given by:

$$\omega_b \approx \sqrt{\frac{k_b}{M}} \qquad \textit{[Eq. 3-16]}$$

where $M \approx 170$ kg is the total mass of the test wheel, including conductor, fiberglass, and aluminum hub. The bending stiffness of the circular axle is given by:

$$k_b = \frac{3EI_{axle}}{l^3} = \frac{3E\pi R^4}{4l^3} \qquad \textit{[Eq. 3-17]}$$

This calculation assumes that the bearing has infinite stiffness. The actual resonant frequency will be lower due to the finite stiffness of the bearing.

3.1.6.3. Disk Flexure

For disk flexure, a vibration mode when the disk itself deforms similarly to the vibration of a drum head, the frequencies of vibration may be found by assuming that the disk behaves as a circular plate (*Figure 3-8*) [245, pp. 240] with appropriate boundary conditions. For a disk with a free outer edge, the resonant frequencies are given by:

$$f_{ij} = \frac{\lambda_{ij}^2}{2\pi a^2}\sqrt{\frac{Et^3}{12\gamma(1-\nu^2)}} \qquad \textit{[Eq. 3-18]}$$

where a is the radius of the disk, E is the Young's modulus of the material in the disk, t is disk thickness, γ is mass per unit area of disk, and ν is the Poisson's ratio. The 3 lowest-frequency natural modes are found from λ_{ij}^2 = 5.253, 9.084 and 12.23. The constants λ_{ij}^2 depend on the natural mode shape of interest.

This calculation assumes that the disk is of homogeneous material and of constant thickness and is freely supported. The test wheel as built is comprised of fiberglass, copper, and aluminum of varying thickness and is supported by the 3" diameter aluminum axle. Therefore, this method for calculating disk flexure resonant modes is a crude approximation at best. In order to calculate resonant modes for disk flexure, average values were used for disk thickness, density, Young's modulus, and Poisson's ratio.

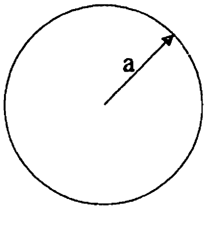

Figure 3-8. Circular plate geometry for calculation of flexural resonant modes

Calculated resonant frequencies (*Table 3-7*) show that the mode corresponding to the mass of the wheel bending on a flexible shaft is likely to be unimportant, since it is at a high frequency. The torsional mode may be excited during normal wheel operation at speeds near 230 RPM. Disk flexure modes should not be excited as they are at frequencies higher than maximum operating frequency.

Table 3-7. Test wheel resonant frequencies

Resonance	***Calculated mode***	***Measured***	***Wheel speed (RPM)***
Torsional	3.85 Hz	---	231
Bending	76.3	---	4580
Disk flexure modes	29.6 Hz	21.9 Hz	1314
	51.2 Hz	49.6 Hz	2976
	69.0	68.6	4116

3.2. Test Wheel Assembly

3.2.1. Guideway Conductors

After the individual guideway sections were cut, the inner face of the copper conductor pattern was painted with an electrically-insulating Krylon ColorWorks 8102 High Temperature Stove Paint. This paint is specified to maintain its integrity to temperatures of 1000 F intermittently, 800F continuous. The 12 guideway sections were then screwed together with brass, round-head #2-58 screws (*Figure 3-9b*) spaced approximately 5 inches apart along the outer and inner rim edges. The resulting ring of copper conductors was brazed along the inner and outer diameters, using a 50% lap joint for additional shear strength. The edge of each section was beveled approximately 0.030" (*Figure 3-9a*) so that the solder joint would have higher strength to withstand the shear force due to hoop tension. After the soldering operation, the heads of the screws were ground off.

Harris Corporation Stay-Brite 8™ silver bearing solder (94% tin, 6% silver) was used. The solder has high strength and a relatively low melting temperature of 535 °F. Its yield strength is approximately 3 times higher than low cost lead/tin solder. This solder was chosen over a higher-temperature silver-bearing braze joint (where the melting temperature is ~1000-1500 °F) as there was significantly less thermal stress on the copper conductors during assembly. An assembled prototype guideway section is shown in *Figure 3-9c*. Steps in the final assembly process of the guideway conductors are shown in *Figure 3-10*.

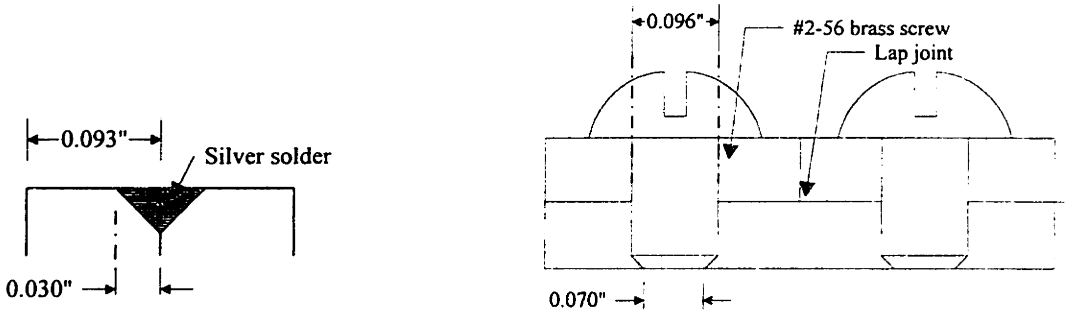

(a) Detail of edge beveling and brazing

(b) Screw mounting specification

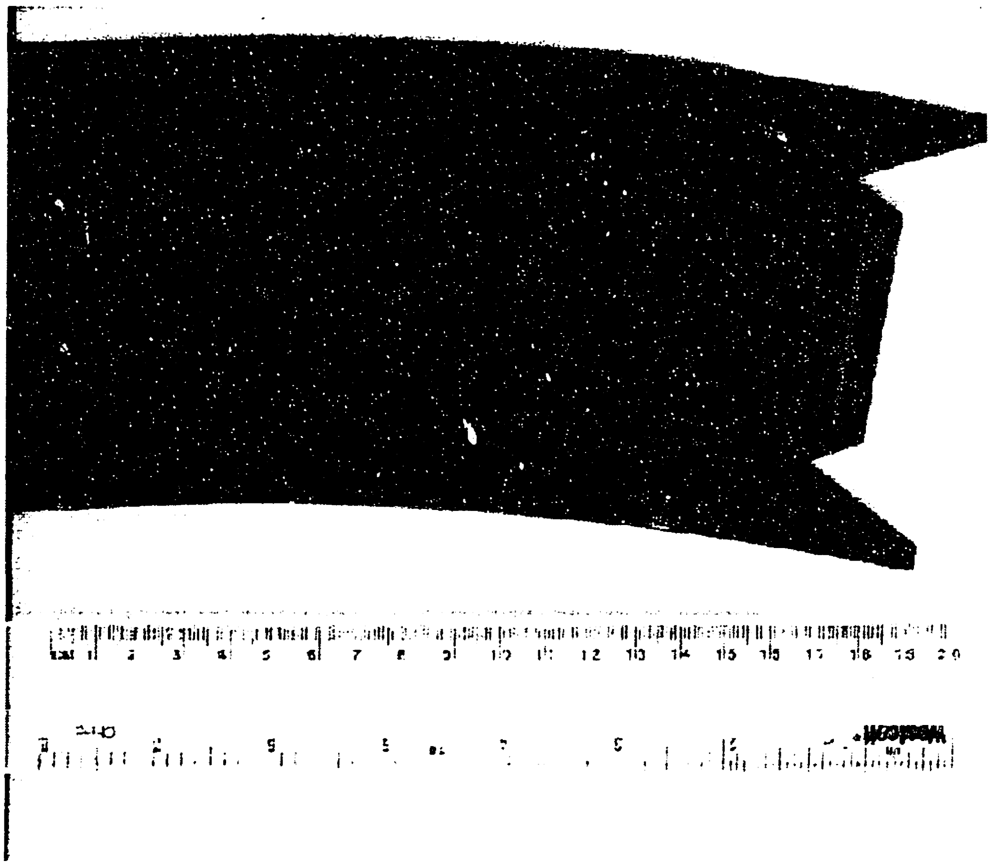

(c) Prototype assembled, showing end section

Figure 3-9. Assembled prototype guideway

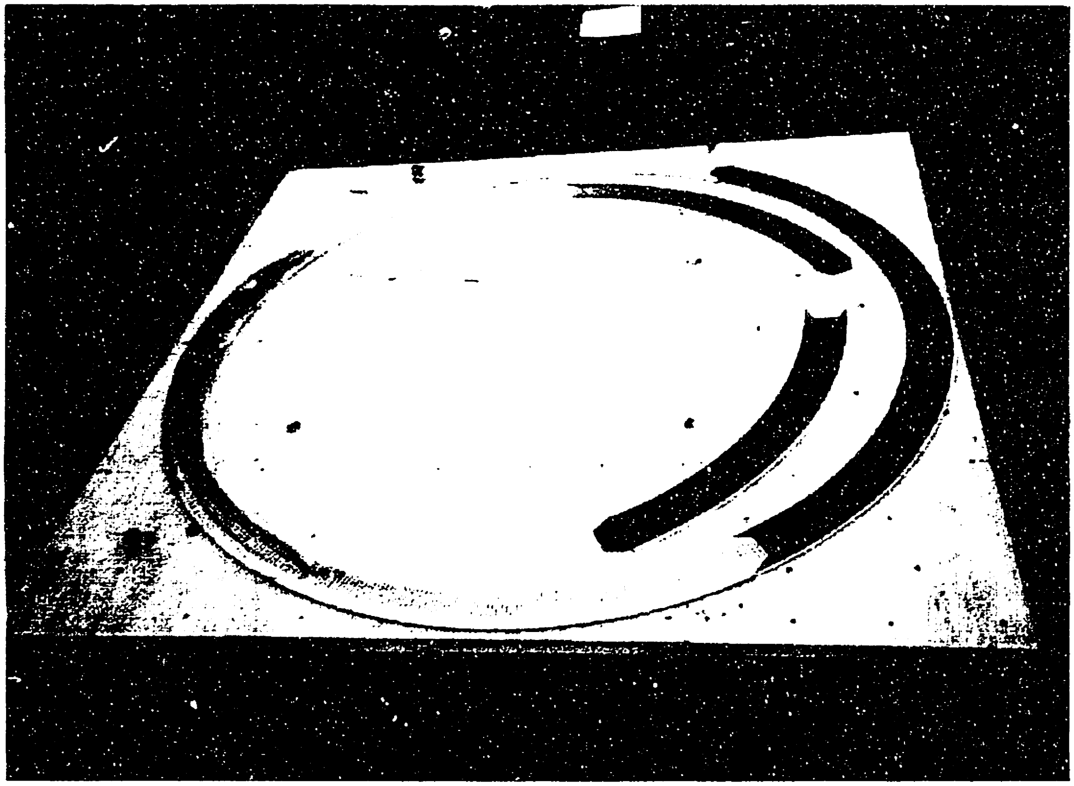

(a) Laying out painted guideway sections

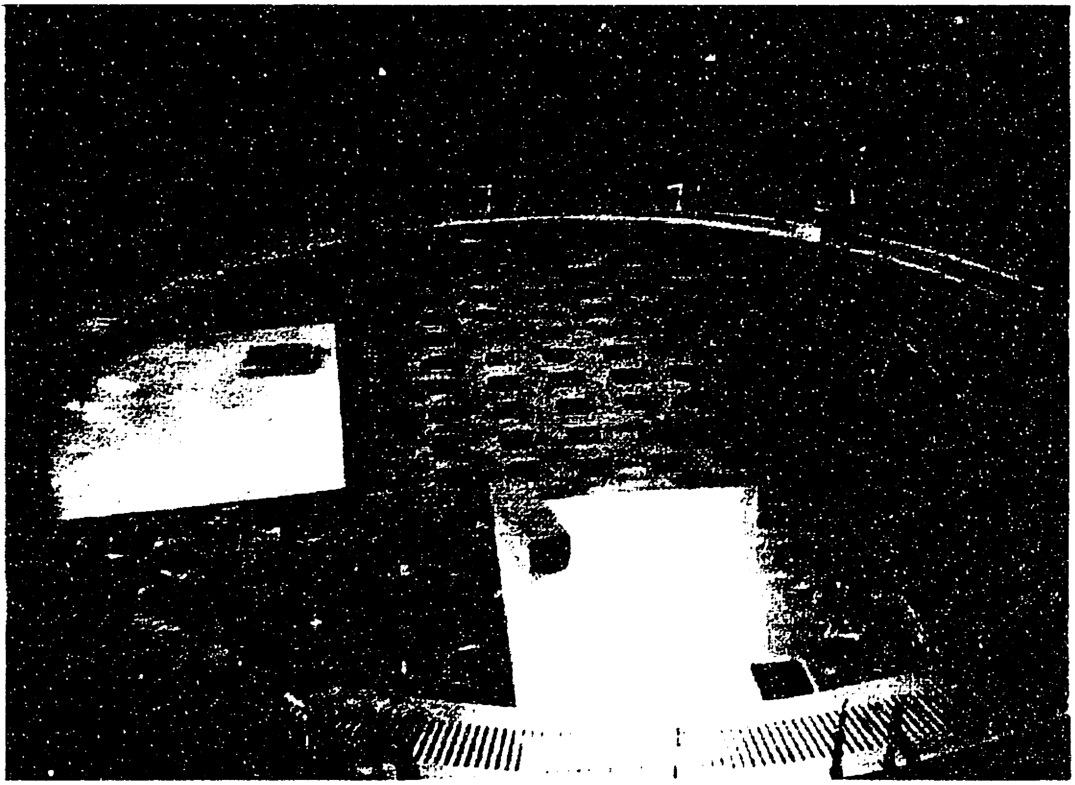

(b) Alignment prior to bolting

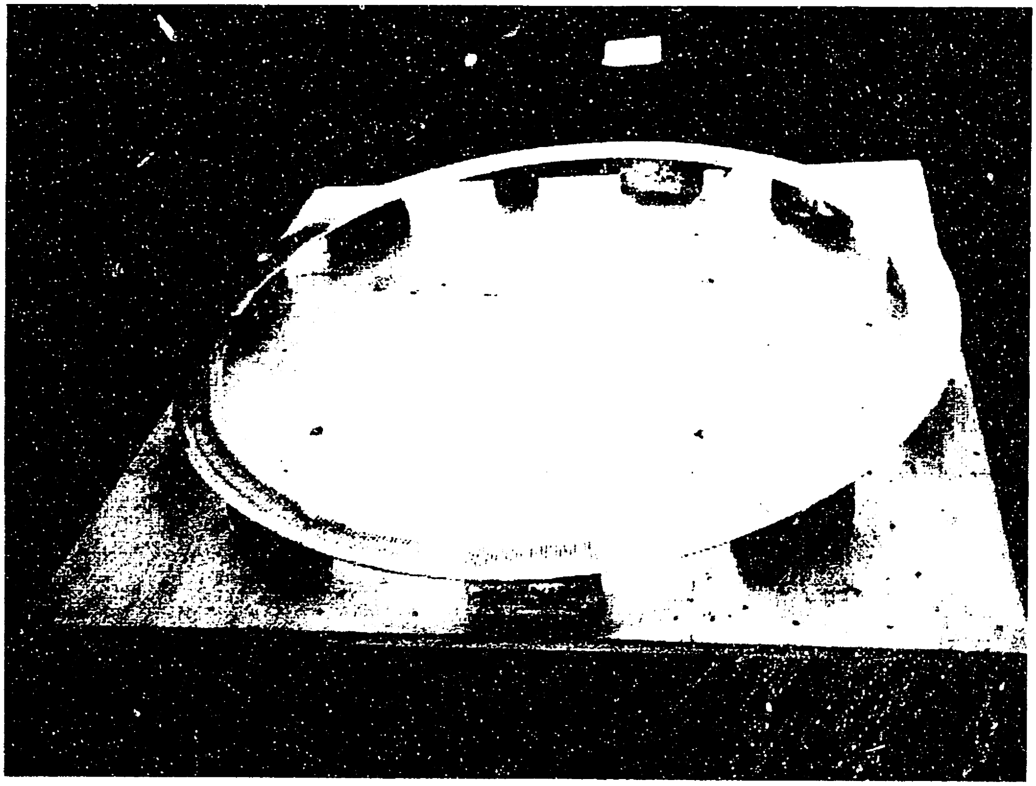

(c) Bolted sections aligned and ready for brazing

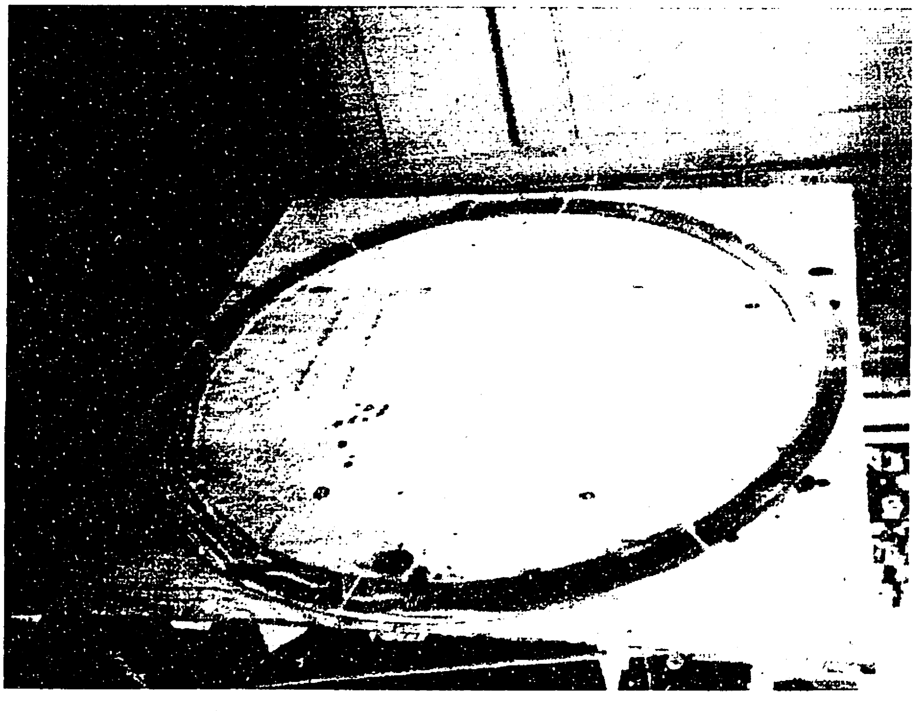

(d) Completed guideway prepared for transport

Figure 3-10. Assembly of guideway conductors

3.2.2. Disk Construction

After brazing, the eccentricity of the copper ring was measured, and found to be true within 1/16 of an inch. The completed copper guideway ring was mounted to a wooden frame and carefully transported to a vendor. A precision mold was constructed, and a composite disk of fiberglass cloth and epoxy was constructed over the copper conductors. Steps in the disk construction process are shown in *Figure 3-11*, with the finished test wheel shown mounted and ready for operation in *Figure 3-12*. A transparent coating of epoxy was used on the front face of the wheel so that the copper conductor pattern is visible.

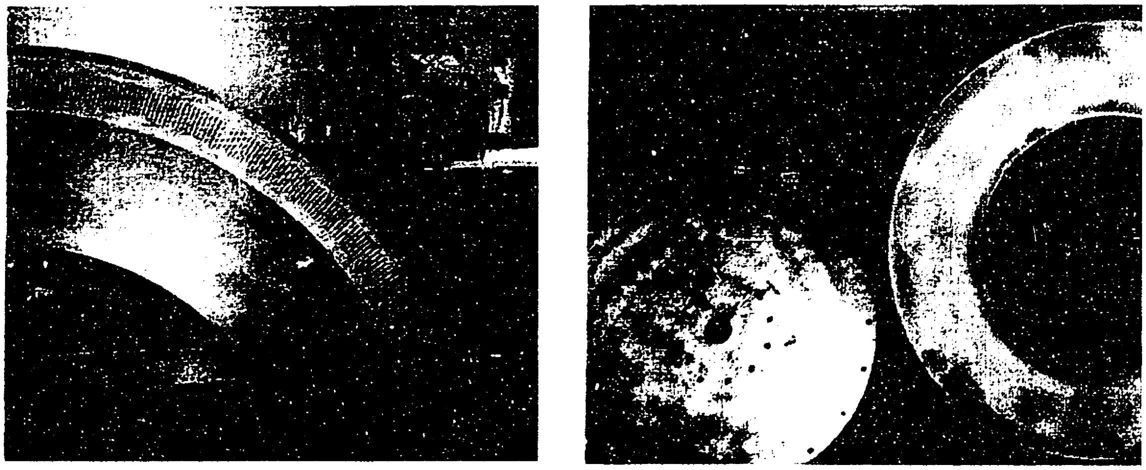

(a) Conductors embedded in fiberglass rim

(b) Rear view of aluminum hub and fiberglass rim prior to mounting

(c) Mounting hub to rim, view of bolt holes

Figure 3-11. Test wheel construction

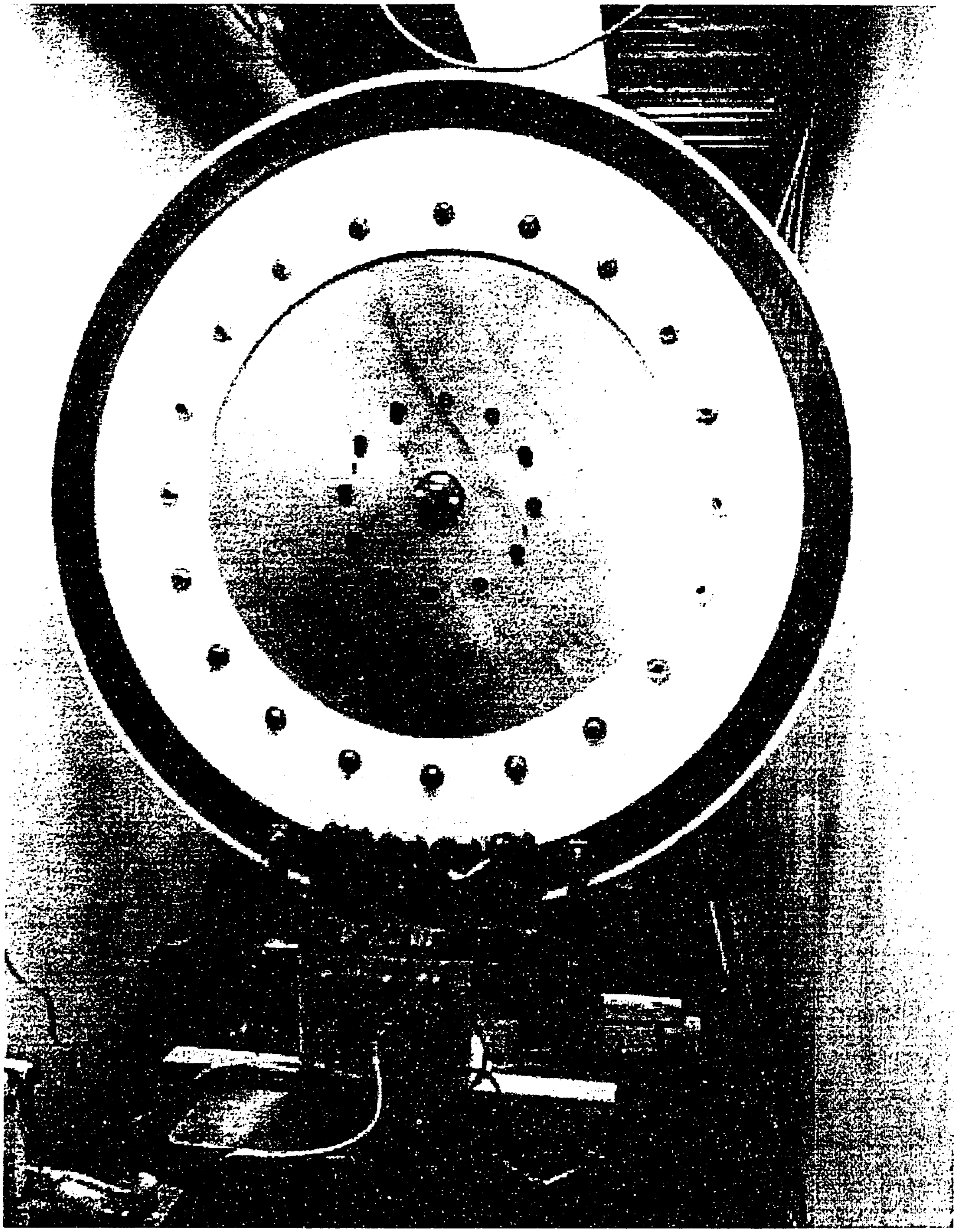

(a) New test wheel mounted to axle, ready for testing

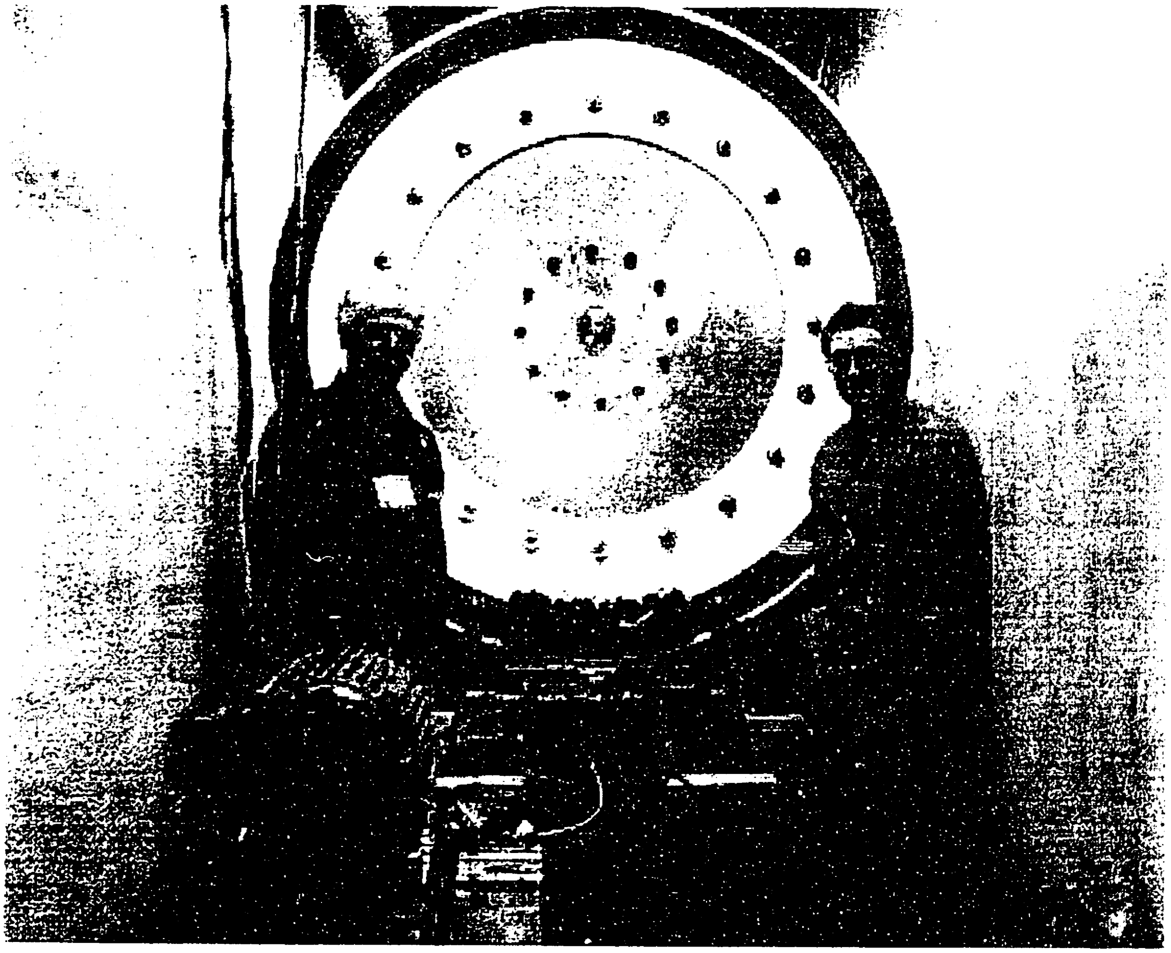

(b) The author with Prof. R. D. Thornton
Figure 3-12. Completed test wheel

3.3. Air Bearing

The air bearing system (*Figure 3-13*) allows low friction, one degree of freedom motion of the magnet in the vertical direction in order to test dynamic performance of the suspension. The bearing is under load due to magnetic guidance (x) and drag (y) forces and associated torques. The bearing allows free motion of the magnet assembly vertically, while constraining the magnet in the other 5 degrees-of-freedom. Theoretical aspects of air bearings are discussed in [243] and the design of our air bearing is discussed in more detail in [238].

Due to the small scale of the magnet, the suspension cannot levitate its own weight. Therefore, the vertical magnetic suspension was assisted by a long steel spring. The spring constant of the mechanical steel spring was designed to be small compared to the effective magnetic spring constant, so that dynamics are dominated by magnetic effects.

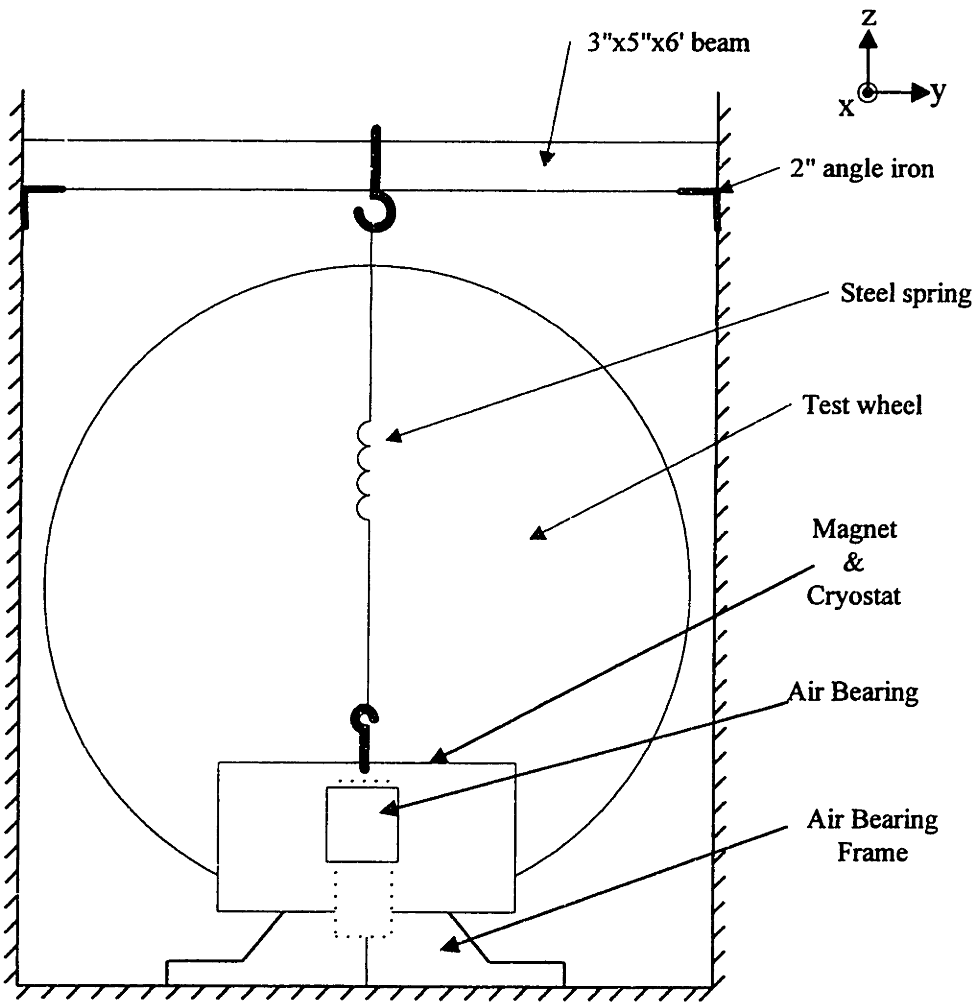

(a) Setup of air bearing in relation to magnet and test wheel

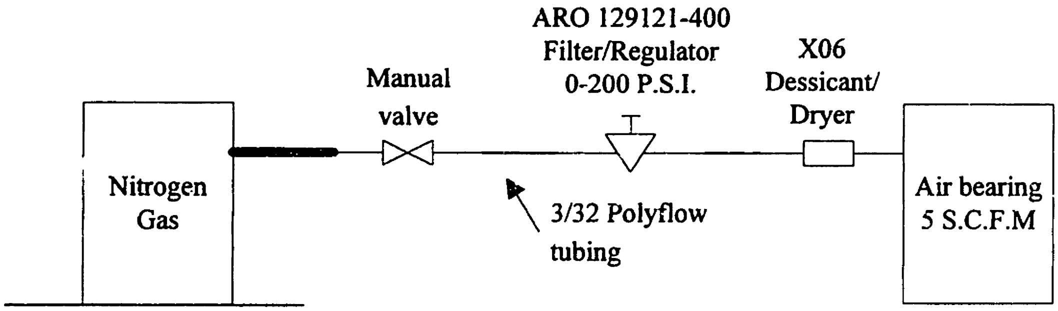

(b) Air bearing piping

Figure 3-13. Schematic view of air bearing system

The bearing housings were designed to slide on an alumina shaft 4”×1.36”×30” (10cm×3.5cm×76cm) (*Figure 3-14 a,b*). The shafts are machined with a very smooth surface finish. Before assembly, the alumina shafts were cleaned with sulfuric acid in order to remove any contaminants.

A tank of compressed pre-purified nitrogen gas was used as the air supply for the bearings. The air supply was cleaned and dried with a Wilkerson Model X06 desiccant dryer and an ARO 129121-400 Filter/Regulator Unit. The bearings are designed to operate with a nominal air gap of 5-15 μm (0.2-0.6 mils) and misalignments and torques can cause the bearing pads to contact the alumina shafts, with corresponding increase in damping. After initial assembly it was found that the main bearing would ground out with a z-torque of ~ 6 Newton-meters or greater. Therefore, a secondary outrigger bearing was added to compensate for this torque. Test data shows good performance of the two bearing system when the bearing is operated at 140 P.S.I (*Figure 3-15a*) with *z*-torques less than 16 Newton-meters. Some preloading was required to assist in load bearing for torques due to the magnetic drag force and imbalance in the alignment of the vertical spring mount with regards to magnet center-of-gravity.

During setup the air bearing was aligned with the magnets not energized. It was realized that some damping is tolerable, as the damping of the entire system will be less when the magnets are energized due to the effective magnetic spring. The equation of motion in the vertical (z) direction is:

$$M\ddot{z} + c\dot{z} + (k_{mech} + k_{mag})z = 0 \qquad \textit{[Eq. 3-19]}$$

where z is the deviation from the equilibrium magnet position, M is total mass (including the air bearing, cryostat, and magnet), c is a damping term associated with mechanical losses in the air bearing and mechanical spring, k_{mech} is the mechanical steel spring constant, and k_{mag} is the magnetic spring constant evaluated at the operating point. The resonant frequency and damping ratio are given by:

$$\omega_o = \sqrt{\frac{k_{mech} + k_{mag}}{M}}$$
$$\zeta = \frac{c}{2M\omega_o} = \frac{c}{2\sqrt{M(k_{mech} + k_{mag})}} \qquad \textit{[Eq. 3-20]}$$

This result shows that the damping ratio will decrease when the magnets are energized due to an increase in the magnetic spring constant. This assumes that the damping term c does not change (perhaps due to magnetically-induced torques on the air bearing). Damping test results of the fully assembled magnet and air (*Figure 3-15b*) show a resonant frequency of 0.66 Hz and a damping ratio of ~1%. The resonant frequency increased when the magnets were energized, in tests described in Chapter 6.

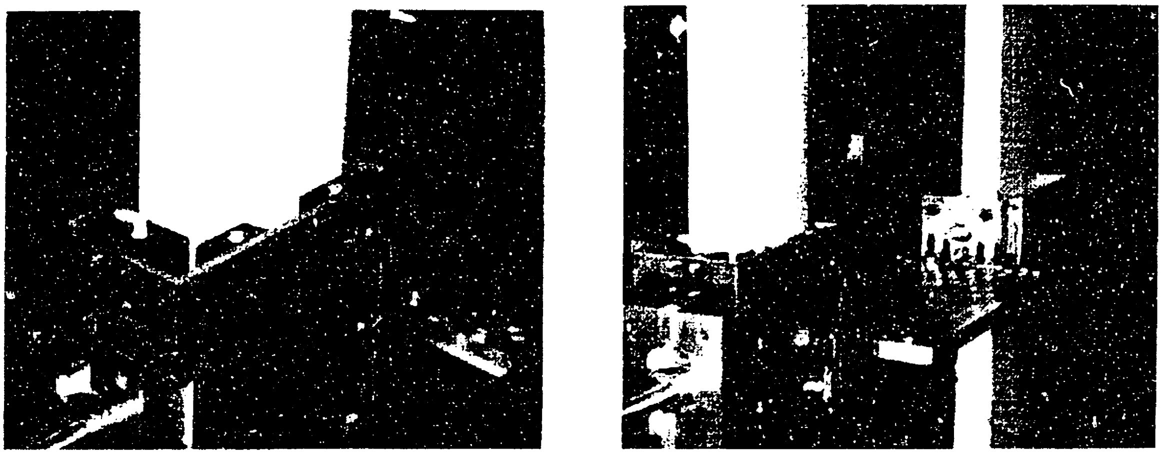

(a) Main air bearing

(b) Main and outrigger bearings

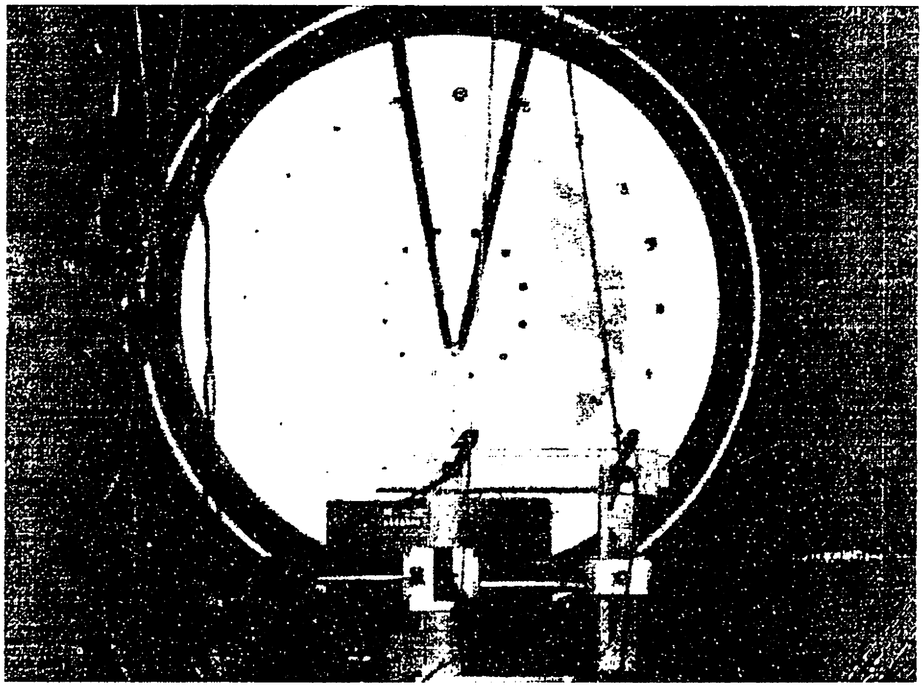

(c) Complete air bearing and magnet assembly

Figure 3-14. Air bearing assembly

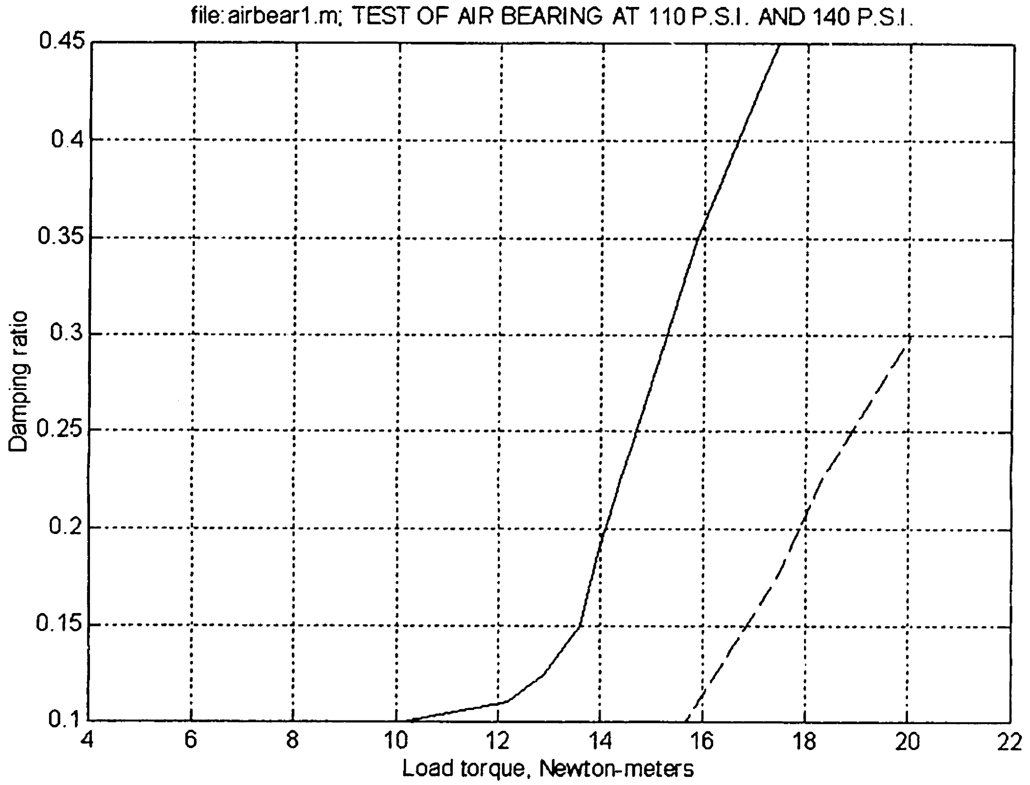

(a) Damping test data vs. torque at 100 P.S.I. and 140 P.S.I.

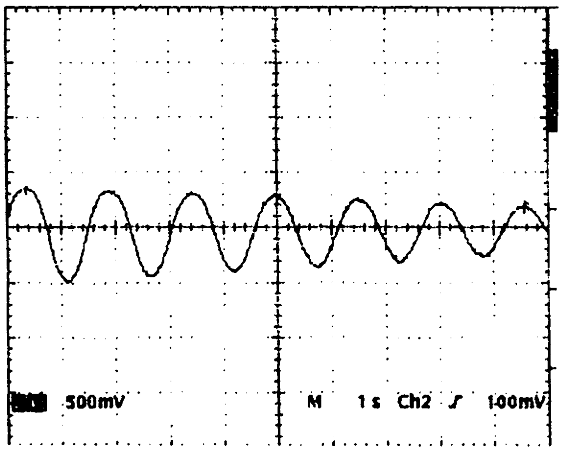

(b) Performance of air bearing for 1 cm magnet vertical deflection
Measured resonant frequency, 0.66 Hz; damping ratio ~1%

Figure 3-15. Air bearing test data

3.4. Cryostat and Liquid Nitrogen Delivery System

The cryostat (*Figure 3-16*) was designed to hold the iron-core magnet in a liquid nitrogen bath. Level sensors were installed in the cryostat so a nitrogen delivery system can maintain a constant level of coolant over the magnets.

The vessel was constructed from sheets of 1/8" thick G-10 fiberglass/epoxy composite, with the corner seams sealed with 2" wide strips of fiberglass boat tape and Emerson and Cuming Stycast™ 2850-GT epoxy. 5 outer walls of the cryostat were insulated with 1" thick Styrofoam. The front face of the cryostat, where the magnetic polefaces are flush, was milled out to a 1/16" thickness, with the magnet polefaces fitting into the groove. The necessary tight spacing between the magnet pole faces and the test wheel did not allow insulation on this face. The aluminum support braces keep the front face of the vessel flush when differential thermal expansion occurs. An outer layer of 1/16" phenolic on 5 faces of the vessel protects the styrofoam insulation from damage.

The capacity of the cryostat is approximately 8 liters of liquid nitrogen. The latent heat of evaporation of nitrogen at 77 K is $h_L = 161$ J/cm^3. The total cooling requirement includes heat leak from the cryostat and power dissipation from the copper coils. Heat flux leak through the G-10 and styrofoam insulation was calculated to be $q_{leak,cond.} \approx 150$ W/m^2, corresponding to a heat leak due to conduction of approximately 30 Watts. Radiative heat transfer is a few Watts.. The fill rate was measured with the magnets not operating, and was approximately 0.8 liters/hour corresponding to a cryostat heat leak of ~35 Watts.

During test fixture operation, this power may exceed 1-2 kiloWatts when all copper coils are energized and the test wheel is rotating. A significant portion of the total heat transfer is heat leak through the un-insulated face of the cryostat facing the test wheel. Therefore, a nitrogen flow rate of $Q = P_{diss}/h_L \approx 0.8$ liters/minute is expected. The bath of 8 liters was sufficient so that all coils were fully immersed over all operating conditions.

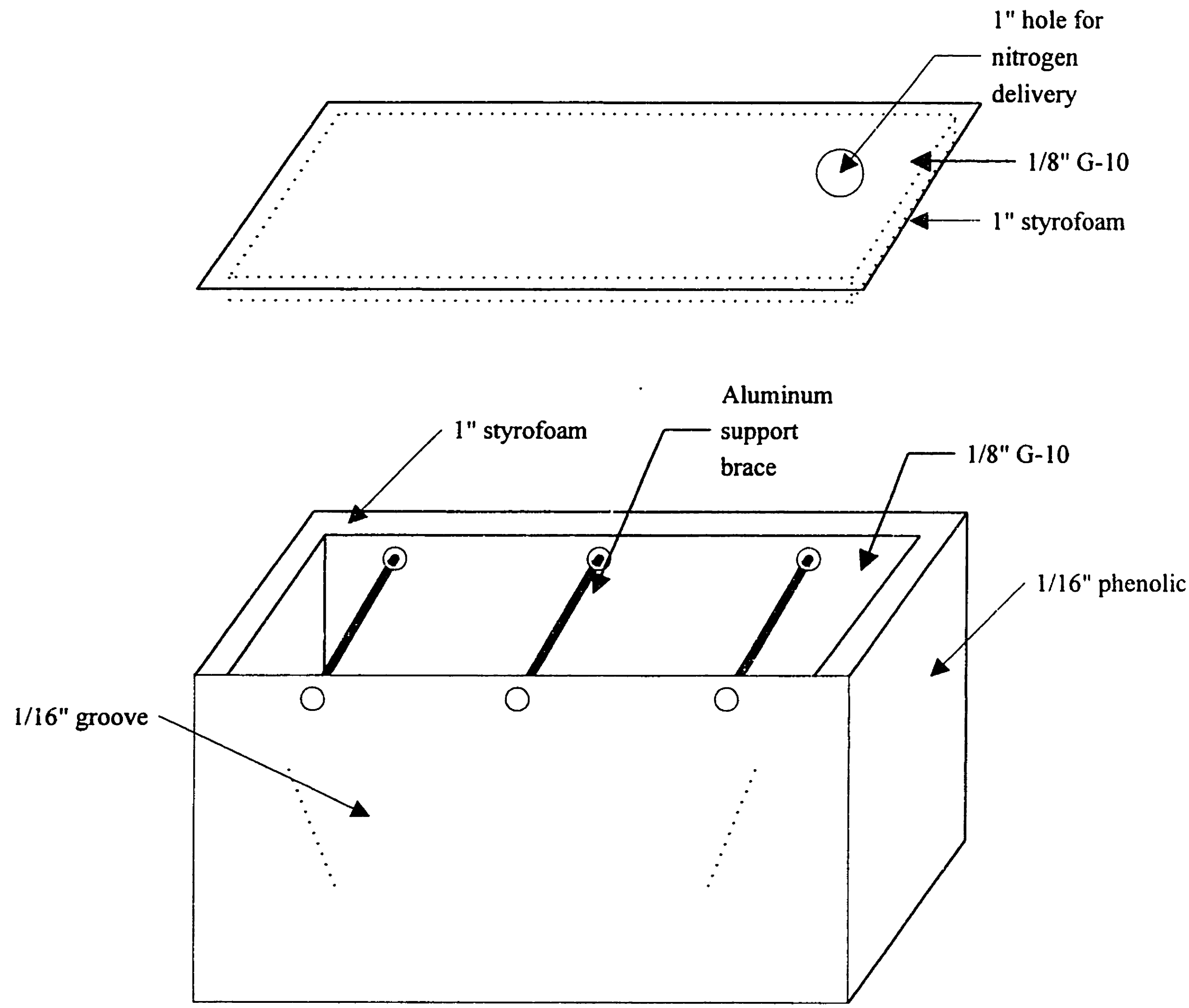

Figure 3-16. Cryostat design

The liquid nitrogen delivery system (*Figure 3-17*) was designed to maintain a constant level of liquid nitrogen in the cryostat under all operating conditions. An Avco 40 PSI cryogenic valve controls the nitrogen flow to the cryostat. A parallel manual valve provides a constant minimal flow which keeps the pipe cools when the valve is off. Level sensors inside the cryostat monitor the level of liquid nitrogen and activate the cryogenic valve when needed. Using this system, the level of liquid nitrogen was kept level to within a few millimeters.

To limit excessive splashing inside the cryostat due to the liquid nitrogen shooting into the bath, a cryogenic phase separator was added to the end of the copper feed pipe. The phase separator creates a back pressure which allows the nitrogen vapor to be vented from the side of the separator, and the liquid drips from the bottom. This eliminated a significant "belching" when the cryogenic valve was activated. A mechanical baffle was also added to reduce the nitrogen waves from falsely triggering the sensor. The baffle consisted of a 1/2" diameter G-10 tube open at both ends. The main level sensor is fixed to a G-10 insert with a cryogenic epoxy.

The design and construction of the initial prototype liquid nitrogen delivery system is described in more detail in a thesis built and tested in the Laboratory for Electromagnetic and Electronic Systems at M.I.T. [240]. Schematics and a circuit description are given in the Appendix (chapter 8) of this thesis.

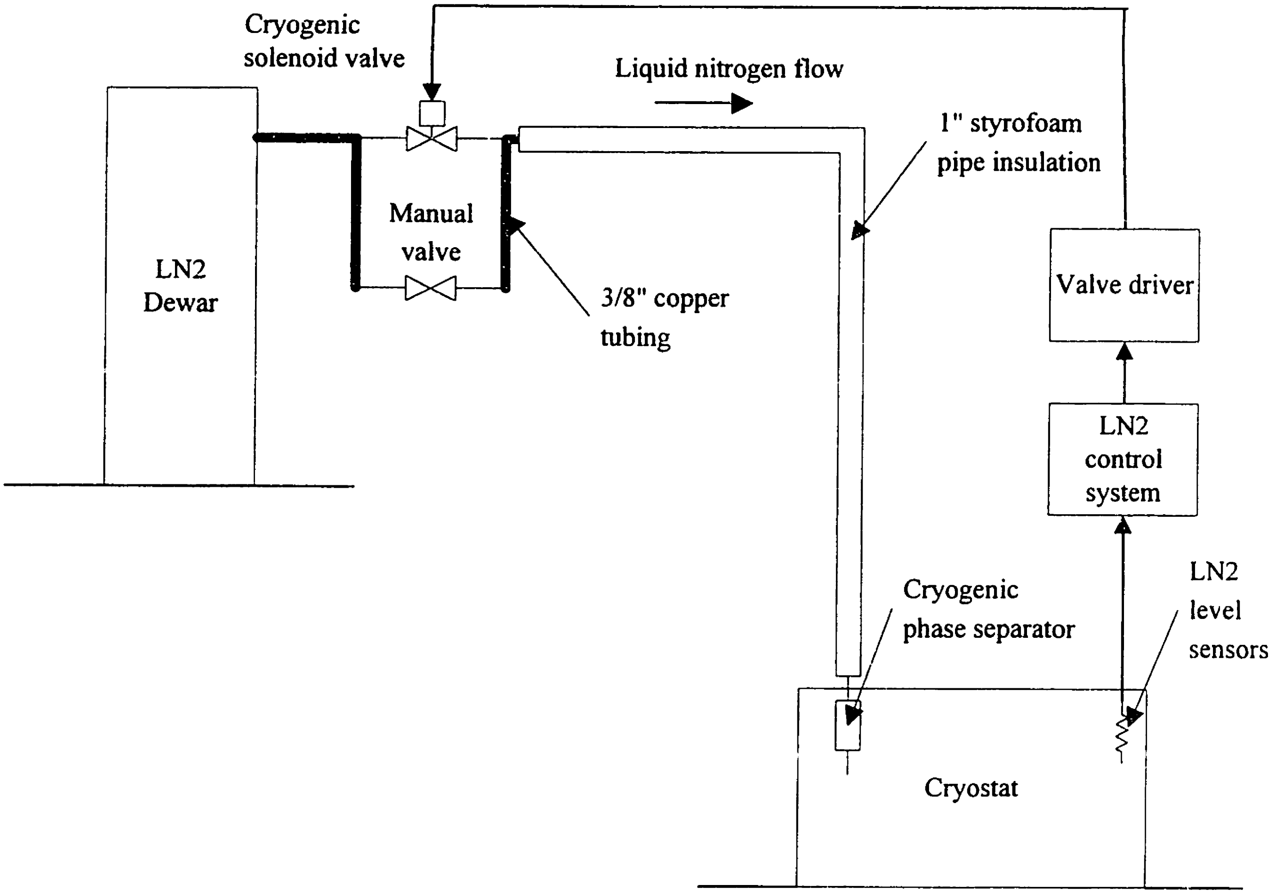

Figure 3-17. Liquid nitrogen delivery system

4. Magnet and Control Electronics Design

This chapter covers the design and construction techniques for the copper coils, prototype superconducting coils, iron core, and control electronics.

4.1. Magnet Design

4.1.1. Iron Core and Copper Coils

A linearized view of the magnet with copper coils is shown in *Figure 4-1*. The magnet core is constructed with laser-cut laminations of 0.9 mm thick M19 transformer steel. The core laminations were bonded together with National Starch and Chemical Corporation's Bondmaster E-645 epoxy, which was thinned with ketone. The epoxy was thinned so that it would not take up a significant fraction of the core volume. A thin layer of epoxy was sprayed on each lamination. The laminations were then stacked and the structure was pre-cured at 50C for 1 hour. After pre-curing, the structure was then cured at 180 C for 1 hour.

The total mass of the core material is approximately 21 kg. The laminations for the pole faces were cut so that the poleface has a bend radius of 1 centimeter to meet a minimum practical superconducting coil bend radius. A sample of the lamination stack-up was tested at room temperature, at elevated temperature, and at 77K in a liquid nitrogen bath. There was no damage evident due to differential thermal expansion under repeated testing.

Eight copper coils were wound with 18 gauge copper magnet wire on an arbor with the same geometry as the magnet polefaces. The final copper coil design had 550 turns in a winding window of 5 cm x 2 cm. The design limit of the copper coils is 8 amps in still air (with current density $J \approx 1000$ A/cm^2 which exceeds the recommended maximum operating value [19]) and 20 amps when operating in the liquid nitrogen bath ($J \approx 2500$ A/cm^2). The measured resistance of each coil is 3.4 Ω at 300K and 0.442 Ω when cooled to 77K, corresponding to a maximum copper power dissipation per coil of 220 Watts at 300 K, and 180 Watts at 77 K.

The power dissipation per unit length in a section of the core made up of N laminations (*Figure 4-1c*) is calculated to be [47]:

$$P \approx \frac{\sigma L W^3 (^{dB}/_{dt})^2}{16 N_L^2} \qquad \text{[Eq. 4-1]}$$

The power loss may be made arbitrarily small by reducing the thickness of the lamination. With a core design with $\sigma \approx 10^6$ $(\Omega\text{m})^{-1}$, $N_L = 40$ and expected AC fields of $\Delta B < 0.5$ Tesla at frequencies $f < 10$ Hz, the power loss in the core is calculated to be less than a Watt.

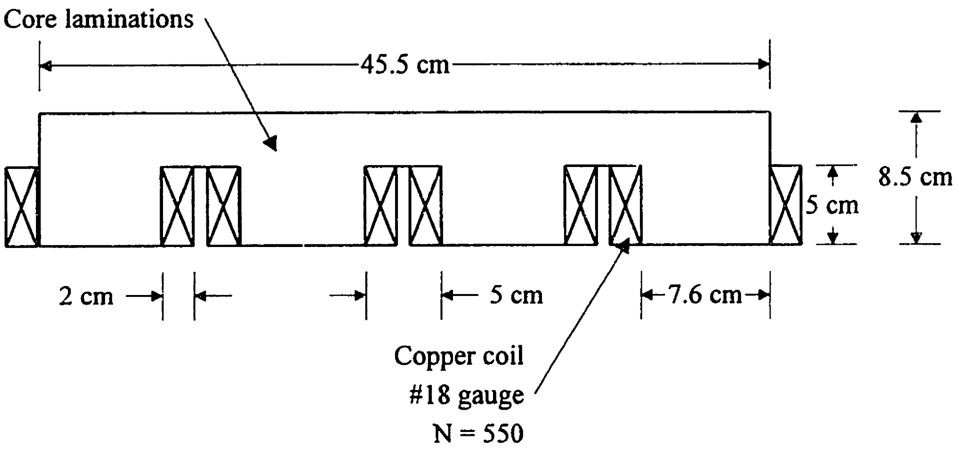

(a) Side view of linearized iron-core magnet with copper coils

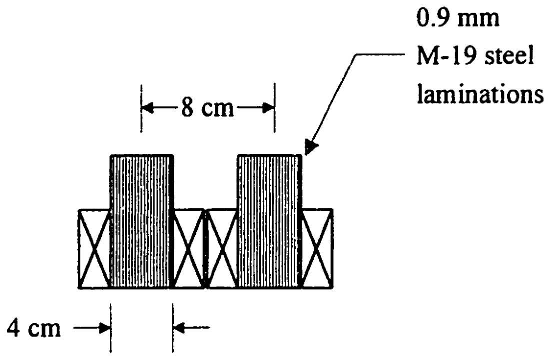

(b) Rear view

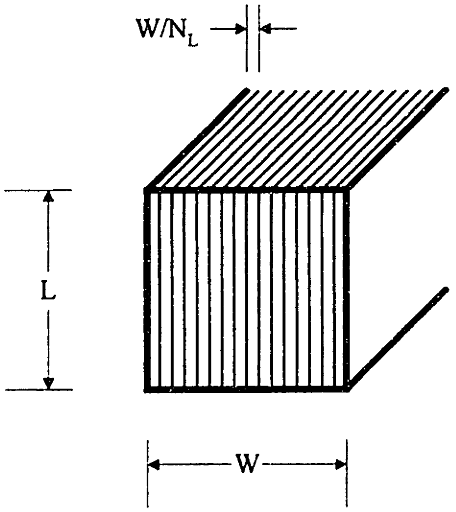

(c) Core laminations

Figure 4-1. Linearized magnet detail, with copper coils

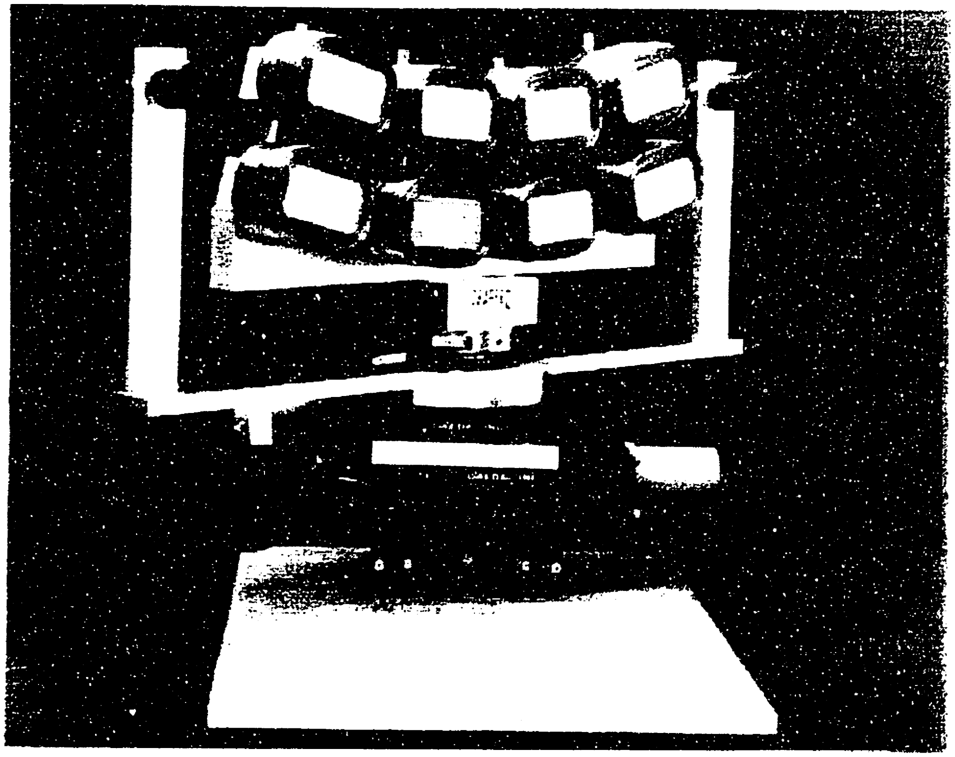

Figure 4-2. Iron-core magnet, mounted to multi-axis force sensor, showing capacitive position sensors

4.1.2. Magnet Wiring

The magnets were designed so that the top row of coils are operated in a North-South-North-South arrangement (*Figure 4-3*), while the bottom row is offset by one half-cycle. The resultant magnet behaves as a magnetic octapole.

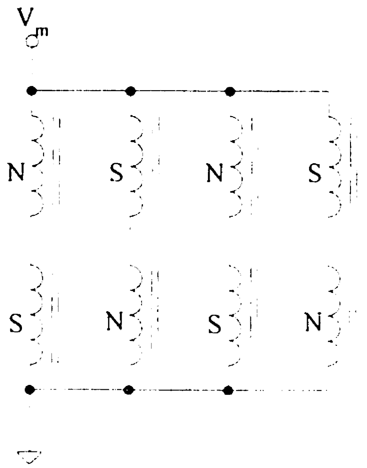

Figure 4-3. Magnet wiring for flux-canceling Maglev

Finite element analyses were run on the non-linear iron core design (*Figure 4-4*). The flux density normal to the guideway (B_x) was calculated at a distance x = 1 cm from the poleface of the magnet, which is the nominal setpoint for guideway-to-poleface setting. This analysis was checked against measurements taken with a Gaussmeter on the magnet operating with copper coils. The measured value at the center of the poleface was $B_x = 0.069$ Tesla, which matches the calculated value to within a few percent. The finite element analysis was also used to scale the thickness of the magnet back-iron, so that the weight of the magnet was minimized while insuring that the iron does not saturate for normal operating levels.

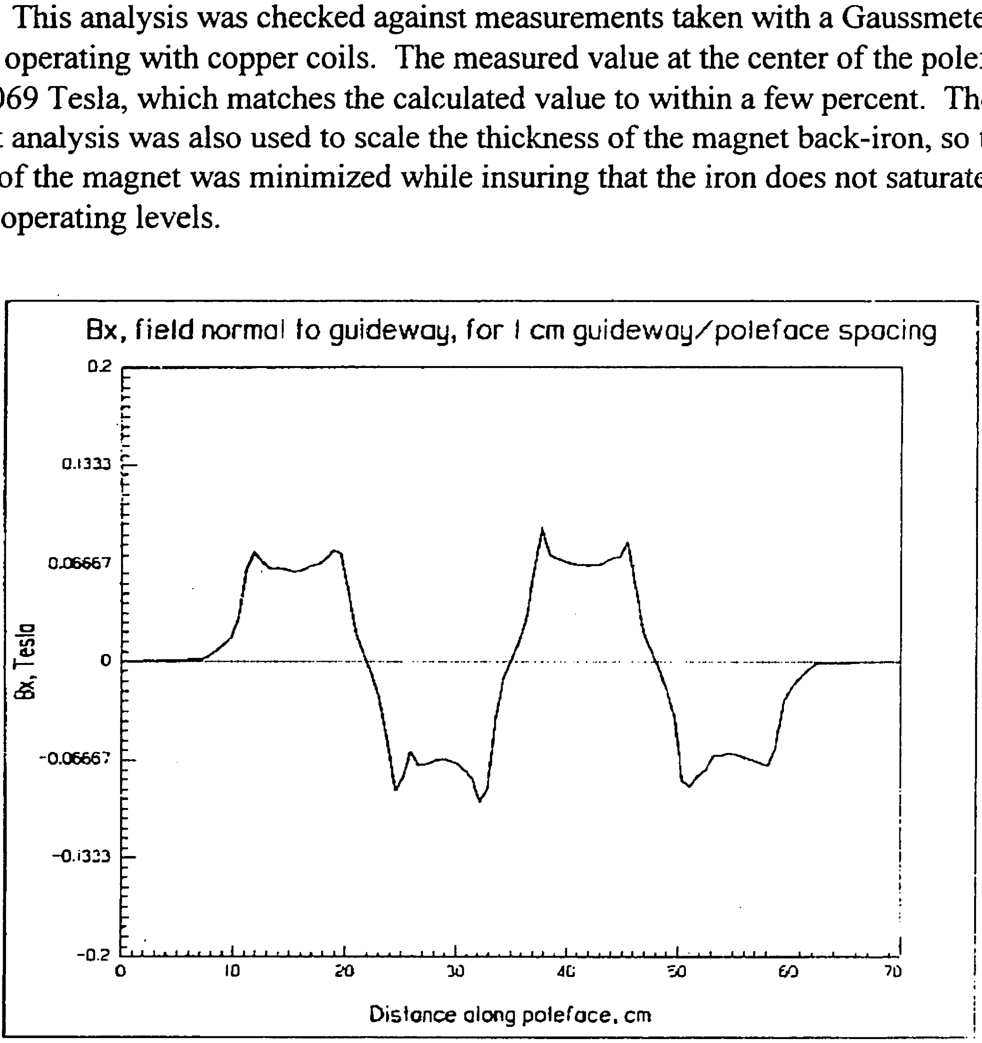

Figure 4-4. Results of finite element analysis, NI = 2200 Ampere-turns per coil

4.1.3. Superconducting Coils

High-temperature superconducting coils were designed which may be used to retrofit the existing magnet. Several prototype pancake coils were constructed from Bi-2223 superconductor, with HTSC tape dimensions as show in *Figure 4-5*. The cross sectional area of the tape is $A_t = 7.4\times10^{-7}$ m^2, and the area of the superconductor is $A_{sc} = 1.8\times10^{-7}$ m^2, or 25% of the total area. Other specifications are shown in *Table 4-1* [6]. In between each turns of the coil, there is an insulator made of polyimide tape (Kapton) 0.0027" (76 μm) in thickness. After winding and before epoxy impregnation, the edges of the Kapton tape were trimmed off with a razor. A winding width of 1 cm was designed. Ideally, this would accommodate $N = 36$ turns per pancake, but due to the bulging of the winding $N = 30$ was wound per coil.

After winding, the coil was impregnated with Stycast 2850-GT low-temperature epoxy. The coil was cured at 70 °C for 24 hours.

Table 4-1. High temperature superconducting tape specification[1]

Tape width	$2a = 3.7$ mm
Tape thickness	$t = 0.2$ mm
I_c at 77K, zero field	11.2 A
Total superconductor area	1.8×10^{-7} m^2
% superconductor	25%
Conductivity of silver at 77K, σ_{Ag}	6×10^{8} $(\Omega\text{-m})^{-1}$
J_c at 77K	6200 A/cm^2
J_{eng} at 77K	1550 A/cm^2
Maximum tensile strain	0.2 %
Maximum bending strain	0.4%

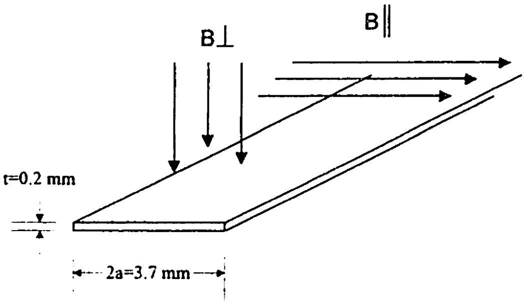

(a) Definition of perpendicular and parallel fields

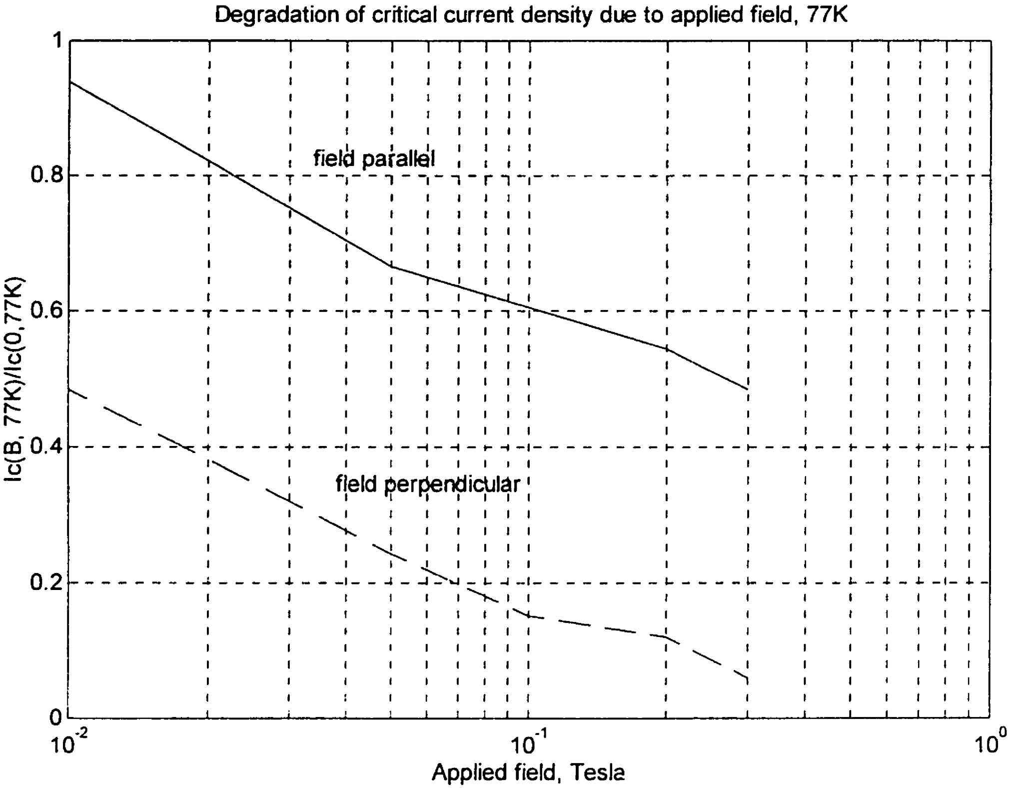

(b) Data from IGC BSCCO-2223 tape [6]

Figure 4-5. Degradation of I_c as a function of applied field orientation for HTSC tape

---

[1] Data from Intermagnetics General Corporation

An approximate value for the self-inductance of each pancake coil can be found by using an expression for the inductance of a rectangle of rectangular wire is [45, pp. 53]:

$$L = 0.921N^2\left\{(s_1+s_2)\log_{10}\left(\frac{2s_1s_2}{w+t}\right) - s_1\log_{10}(s_1+g) - s_2\log_{10}(s_2+g)\right\}$$
$$+0.4N^2\left\{2g - \frac{s_1+s_2}{2} + 0.447(w+t)\right\} \quad \textit{[Eq. 4-2]}$$

where L is in microhenries, N is the number of turns in the rectangular coil, s_1 and s_2 are the mean outer lengths of the rectangle side (in meters), w is the width of the rectangle cross section, t is the thickness of the rectangle cross section, and g is the diagonal length of the coil cross-section. The model shows good agreement with finite-element analysis and measurements on the prototype coil (*Table 4-2*).

Table 4-2. Prototype HTSC coil electrical parameters

	Calculated (Terman method)	***Finite Element Analysis***	***Measurement at 1 kHz***
R @ 300K	0.3206 Ω	---	0.47 Ω
R @ 77K (when normal)	0.0641 Ω	---	---
L	167 μH	166 μH	155 μH

An I/V curve was generated for the prototype pancake coil (*Figure 4-6b*). Results show that the critical current of the coil was degraded by approximately 50% during the winding process, perhaps due to the crude solder connections or the 2 centimeter bend radius[2]. With a tape thickness $t = 0.2$ mm and a minimum bend radius of $\rho = 2$ cm a maximum bending strain of $\varepsilon = t/2\rho = 0.5\%$ is predicted, which is sufficient to degrade the critical current density [6, 21]. However, the coil performs better than a copper coil of identical geometry up to approximately 17 Amperes.

For operation as a Maglev magnet coil, the anisotropy of the tape with regard to degradation of critical current due to perpendicular fields (*Figure 4-5b)* makes it advantageous to keep the HTSC material from the poleface area where leakage flux is of the greatest magnitude. A proposed HTSC-based magnet design based on the tested copper coil magnet is shown in *Figure 4-7.* A copper coil is placed inside the HTSC coil in a composite coil arrangement. The copper coil has a shielding effect and therefore reduces the stray field impinging on the HTSC tape. This also has the advantage of increasing the bend radius in the HTSC coil.

---

[2] In this measurement, the actual critical current density if the 10 μV/cm criterion is used is approximately 2 Amperes.

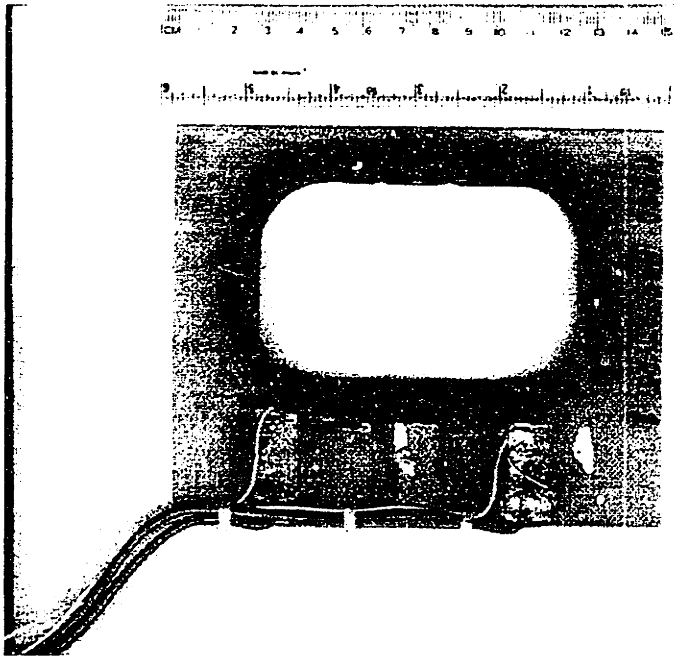

(a) Prototype HTSC coil, mounted and strain-relieved

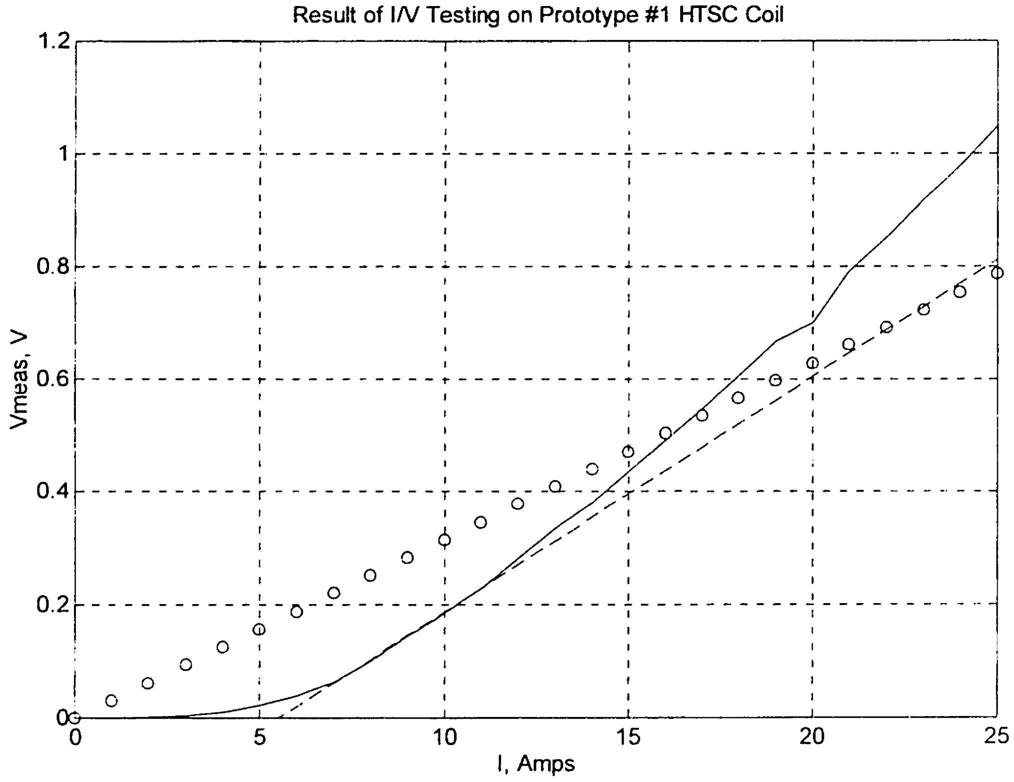

(b) Results of I/V testing with prototype coil
Horizontal axis: coil current; Vertical axis: measured voltage at current taps

Figure 4-6. Tests of prototype HTSC coil, 77K, zero field
Solid line --- measurements. Dotted line, prediction, based on I_c = 5.5 Amps
ooo --- Comparison with copper coil of same geometry

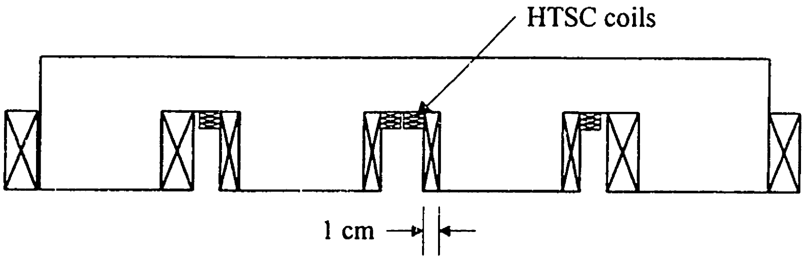

(a) Linearized front view

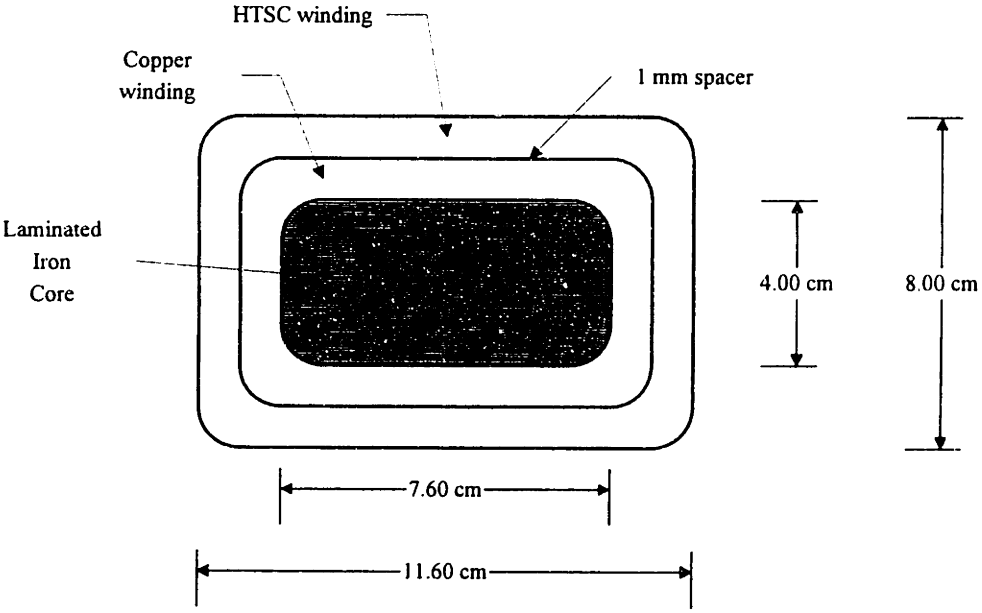

(b) Pole face view

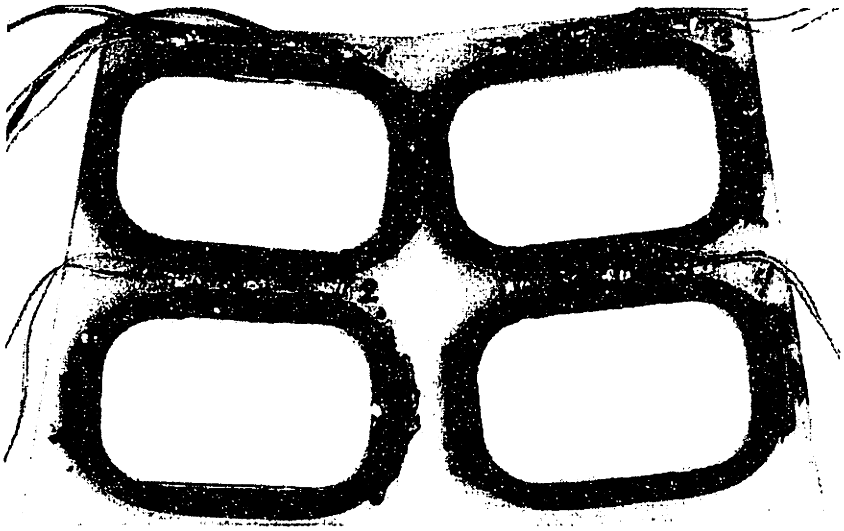

(c) Prototype multiple-HTSC coil fixture

Figure 4-7. High-temperature superconducting magnet design

4.1.4. Prediction of AC Losses

Superconductors permit lossless D.C. current conduction. However, operation of a superconducting coil in the presence of changing fields or AC currents is not lossless. There are 3 main causes of AC losses in multifilamentary superconducting coils: eddy current losses in the metal matrix surrounding the filaments, hysteresis loss, and inter-filament coupling losses. These losses may be approximated by using methods outlined in Wilson [295] and Iwasa [291].

Eddy current losses are the easiest to understand, and may be calculated by normal methods. The eddy current loss per unit length of tape with a sinusoidal applied external field is:

$$< P_{eddy} > \approx \frac{1}{3}\sigma_{Ag}\,\pi^2 a^3 t B_o^2 f^2 \qquad \textit{[Eq. 4-3]}$$

where σ_{Ag} is the electrical conductivity of silver at 77K, t is the tape thickness, B_o is the AC field amplitude normal to the wide surface of the tape, and f is frequency.

Hysteresis loss is caused by the non-linear B/H magnetization curve of the superconductor. In the small field limit, where $B_o << B_p = \mu_o J_c a$, the applied field does not fully penetrate the superconductor, and the power dissipation per unit length of tape due to hysteresis is:

$$< P_{hy} > \approx \frac{4B_o^3}{3\mu_o B_p} atf \qquad \textit{[Eq. 4-4]}$$

This approximation is valid for $B_o < 0.14$ T for our tape.

The coupling loss in generic superconducting tapes is strongly dependent on the tape internal geometry, in particular, the winding pitch of the superconducting filaments. The power per unit conductor length due to coupling loss is [291, pp. 264]:

$$< P_{cp} > \approx \frac{2B_o^2}{\mu_o}\frac{\tau_{cp}}{\tau_{cp}^2 f^2 + 1} atf^2 \qquad \textit{[Eq. 4-5]}$$

with the coupling time constant τ_{cp} given by:

$$\tau_{cp} \approx \frac{\sigma_{Ag}\mu_o l_p^2}{4\pi^2} \qquad \textit{[Eq. 4-6]}$$

The coupling time constant is a measure of the L/R time constant of the filamentary loops. Currently available HTSC tapes do not have twisted filaments, (equivalently, the winding pitch $l_p \rightarrow \infty$). Therefore, there is no coupling loss in this HTSC tape.

Predicted power loss for the prototype HTSC coil is shown in *Figure 4-8*. Scaling laws may be used to predict losses for the full-scale system. Results show that losses will be small at frequencies of expected Maglev disturbances (0 ~10 Hz).

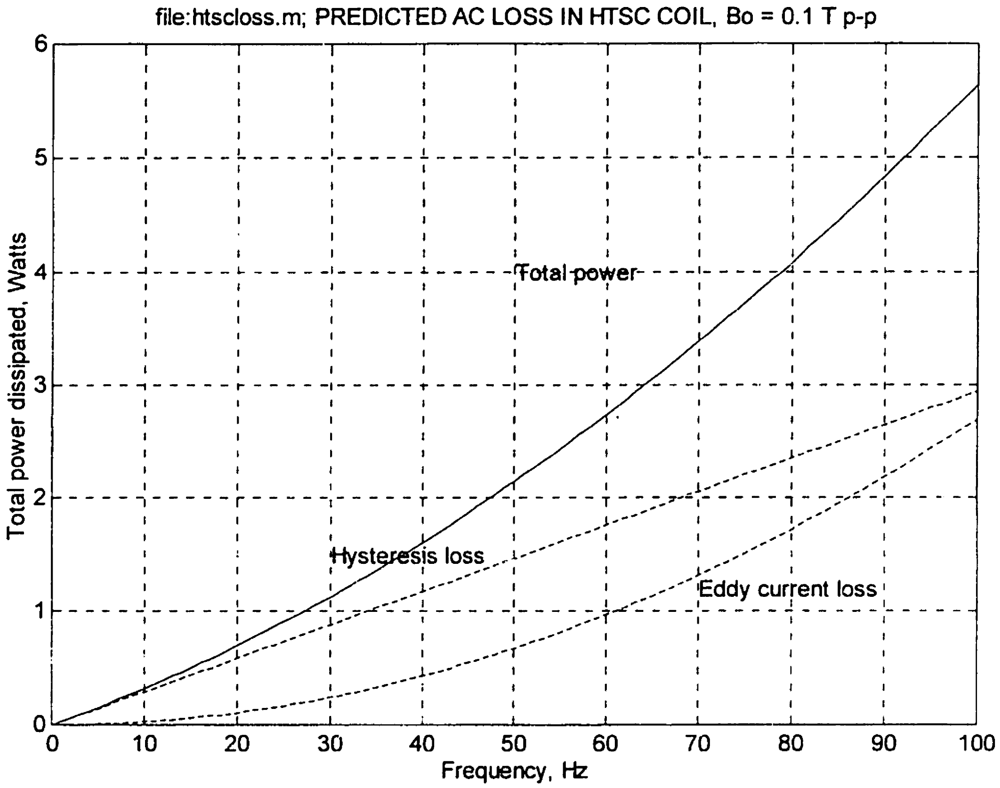

Figure 4-8. Predicted AC loss in prototype HTSC Coil

4.2. Control Current Source

For control of magnet vertical position, the currents in the coils must be actively controlled. *Figure 4-9* shows the control current source configuration and the measured impedance of the coil load measured at the control terminals The low frequency load impedance is approximately 66 milliHenries, 3.4 Ω at room temperature. A high-power current source was designed to drive the test coils differentially for vertical position control of the levitation magnets. A full set of schematics for the current source is given in the Appendix in Chapter 8.

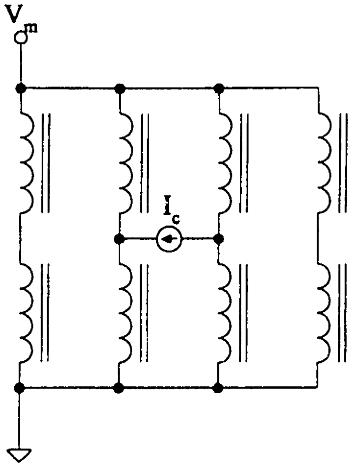

(a) Magnet wiring for differential control

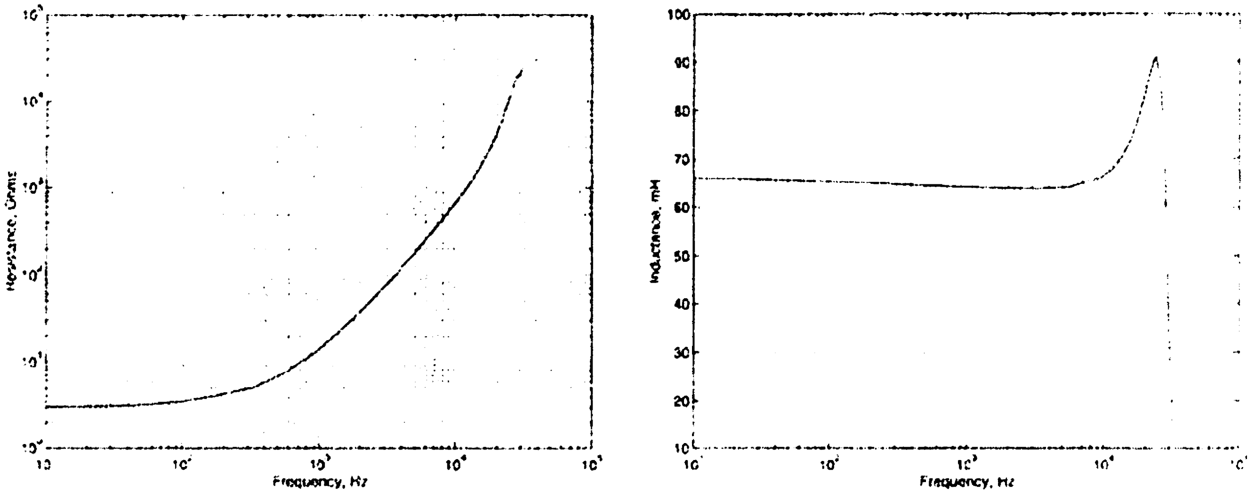

(b) Terminal impedance at driven terminals, assuming series L-R model

Figure 4-9. Measured terminal impedance measured at differential driving terminals

5. Electrodynamic Models and Active Secondary Suspension

In this section, the development of an electrodynamic system model and control system for control of the vertical position of the Maglev magnet is discussed. A simple suspension model is developed which predicts lift force, drag force, lift/drag ratio, and velocity of the Maglev drag peak. These models may be used to scale the results for a full-scale system.

5.1. Magnetic Suspension Modeling Techniques

In the evaluation of the performance of magnetic suspensions, several equally valid analysis approaches are available. First, by using a continuum electrodynamic model, the fields and currents can be calculated for a given magnet and coil geometry and magnet speed and position. Equivalently, if the magnetic energy storage E_m is known for all magnet positions x, y, z and time t, the magnetic forces can be found by:

$$\bar{F}_m(x,y,z,t) = -\nabla E_m(x,y,z,t) \qquad [Eq.\ 5\text{-}1]$$

This method is useful when the magnetic field solution is available in closed-form. The approach has been successfully used for continuous-sheet suspension models [136], [208], [213] where a semi-infinite sheet is considered. The task is further simplified if infinite train velocity is assumed and the stored magnetic energy E_m can be found by assuming that the guideway is perfectly conducting. In this case, image methods may be used and depending on the skin depth of the excitation frequency, the lift and drag may be calculated in the high and low frequency limits.. Also, using this approach, the superconducting coils on the moving train are modeled as dipoles, or as idealized single-turn rectangular coils.

In the finite element method, the superconducting coils and guideway are broken into discrete sections, and Maxwell's equations are solved in each section, meeting appropriate boundary conditions. However, when there are changing magnetic fields and induced currents, the finite element method becomes difficult because a great amount of computing time and memory is required. Furthermore, commercially-available codes do not address the problems of moving conductors.

These approaches are not well suited to second-generation MAGLEV geometries, such as ladder structures, the null-flux geometry, and the new "flux-canceling" geometry where induced currents are artificially confined to geometrically-repeating discrete coils. In this instance, the use of a fully developed electrodynamic model tends to obscure the underlying physics. Therefore, an approximate circuit model has been developed which is used to predict forces and the velocity of the Maglev drag peak.

5.1.1. Ideal EDS System

For a simplified EDS system (for instance, the case of a long current-carrying wire traveling over an infinitely wide, thin conducting plate with velocity v) the lift and drag forces may be expressed as [136]:

$$f_L = F_o \frac{v^2}{v^2 + v_p^2}$$

$$f_D = \frac{v_p}{v} f_L = F_o \frac{v_p v}{v^2 + v_p^2} \qquad \textit{[Eq. 5-2]}$$

The velocity v_p is the "drag peak" velocity and is given by:

$$v_p = \frac{2}{\mu_o \sigma t} \qquad \textit{[Eq. 5-3]}$$

where σ is the electrical conductivity of the plate and t is its thickness.

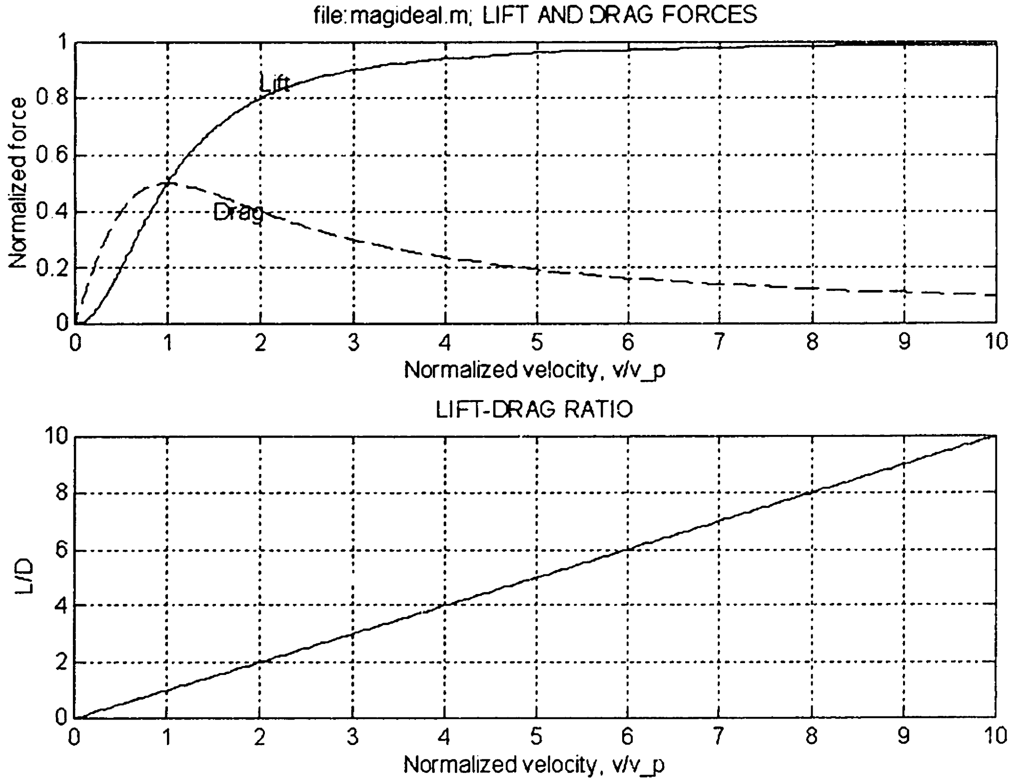

Figure 5-1. Ideal EDS Maglev lift and drag forces, and lift-to-drag ratio

Operation above the drag peak results in a drag force decreasing as $1/v$. Other important functional dependencies to note are:

- At low velocity, lift force increases as v^2 and drag force increases as v.
- At the drag peak velocity, lift force and drag force are equal.
- The maximum drag force is 50% of the maximum lift force.

- Above the drag peak velocity, the lift force approaches an asymptotic maximum value, and drag force decreases as $1/v$.
- The lift-to-drag ratio is given by the ratio of v/v_p, and increases linearly with operating speed. This is easily understood by considering the power dissipated in the guideway coil which reaches a constant value at high speed.

It is desirable to reduce the drag peak velocity as much as possible so that significant lift will be generated at low speeds and the train "lift-off" velocity is minimized. This may be accomplished by using a guideway with higher electrical conductivity (σ larger) or a guideway with more material (t larger). Equivalently, we want to minimize the resistance of the path in which the induced currents flow.

The drag peak evaluation of our multiple-loop guideway is not as straightforward. In order to calculate dominant time constants, approximated equivalent lumped circuit models have been developed.

5.2. Circuit Modeling of EDS Maglev

Significantly higher lift-drag ratios may be achieved by using a guideway comprised of discrete loops. An electrical model of the guideway which captures the functional dependence of lift and drag forces is shown in *Figure 5-2*. In this simplified model, a single guideway loop is shown, and the case will be solved for a loop which does not interact with any other loops.

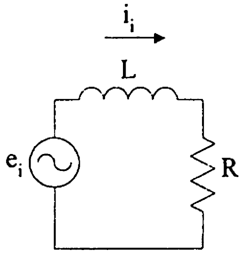

Figure 5-2. Model of single isolated guideway loop

The guideway loop is modeled by a self-inductance L and self-resistance R. The voltage around the loop is induced by the superconducting magnet traveling over the guideway coil. Assuming that the applied magnetic field is dominated by the first harmonic of the spatial frequency, the applied magnetic field is time-varying due to the velocity of the magnet over the guideway, or:

$$B(t) = B_o e^{j\frac{\pi}{p}(y-vt)} \qquad \text{[Eq. 5-4]}$$

where B_o is the average flux density, p is magnet pole pitch, and v is train velocity. The applied voltage around the guideway loop is:

$$e_i = \frac{d\lambda}{dt} = -j\left(\frac{\pi v}{p}\right)B_o A \qquad \textit{[Eq. 5-5]}$$

where A is the loop area and λ is the flux linkage through the loop. Assuming that the magnetic field is dominated by the fundamental spatial mode, the effective frequency seen by the loop due to the magnet traveling over the guideway is:

$$\omega = 2\pi f = \frac{\pi v}{p} \qquad \textit{[Eq. 5-6]}$$

The induced current in the loop is:

$$i_i(\omega) = \frac{e_i}{j\omega L + R} = \frac{j\omega B_o A e^{j\omega t}}{R\left[\frac{j\omega L}{R} + 1\right]} \qquad \textit{[Eq. 5-7]}$$

This agrees with an intuitive analysis, where in the low frequency limit, the loop current is resistance limited, or:

$$i_i(\omega \to 0) \approx \frac{j\omega B_o A e^{j\omega t}}{R} \qquad \textit{[Eq. 5-8]}$$

and in the high frequency limit, the current is inductance-limited:

$$i_i(\omega \to \infty) \approx \frac{B_o A e^{j\omega t}}{L} \qquad \textit{[Eq. 5-9]}$$

The time-average lift force is:

$$< f_z(\omega) > = \frac{l}{2}\mathrm{Re}\left\{i_i(j\omega)B^*(j\omega)\right\} = \frac{lB_o^2 A}{2R}\frac{\omega^2\frac{L}{R}}{1+\left[\frac{\omega L}{R}\right]^2} = \frac{lB_o^2 A}{2R}\frac{\left(\frac{\pi v}{p}\right)^2\frac{L}{R}}{1+\left[\frac{\pi v L}{pR}\right]^2} \qquad \textit{[Eq. 5-10]}$$

where l is the horizontal length of the loop where induced currents travel through the high-field region, generating lift. The drag force can be found from the drag power:

$$f_D = \frac{|i_i|^2}{2Rv} = \frac{(B_o A)^2 v}{4(pR)^2\left[\left(\frac{L\pi}{Rp}v\right)^2 + 1\right]} \qquad \textit{[Eq. 5-11]}$$

For this model, the drag peak velocity is predicted as:

$$v_p = \frac{pR}{\pi L} = \frac{\lambda/2\pi}{L/R} \qquad [Eq.\ 5\text{-}12]$$

where λ is the fundamental wavelength. It is important to note that the equations for lift and drag have the same functional dependency for frequency (and hence for velocity) as the lift and drag force profiles presented earlier.

5.2.1. Inductance Modeling of Multiple-Loop Guideway

For our flux-canceling geometry, the guideway pattern is significantly more complicated due to the fact that there are multiple overlapping loops, with resulting mutual inductances and mutual resistances. In this case, a matrix approach is warranted for the solution of loop currents. The induced currents in the guideway conductors may be found by evaluating the matrix problem

$$\{j\omega[L] + [R]\}\{i\} = -\frac{d}{dt}\{\phi\} = -\{v\} \qquad [Eq.\ 5\text{-}13]$$

where *[L]* and *[R]* are N-by-N vectors which take into account the self and mutual inductance and resistance terms of the guideway and *{i}* and *{v}* are column vectors corresponding to the induced loop currents and voltages. For the fully distributed system, N → ∞, but for approximate results the solution may be truncated as the mutual resistance and mutual inductance terms fall off with distance.

The right-hand side of this expression is due to the excitation of the magnet, and depends on velocity and position of the guideway loops. In the case of our guideway, the resistance matrix is complicated by the fact that there are mutual resistance terms for adjacent loops. In comparison, the Japanese null-flux system uses individual coils, so the resistance matrix *[R]* is diagonal with no mutual resistance terms.

5.2.2. Note on Approximate Techniques and Scaling Laws

For the purposes of calculating guideway coil self and mutual inductances to fill the inductance matrix, approximate models were developed for our geometry. Although the inductances can be calculated easily by finite element analysis, this method gives little insight into scaling laws. Therefore, wherever possible approximate techniques were used with good results.

Solutions exist for various inductor geometries, including disk coils, filamentary loops, and more complicated geometries. A realizable geometry for which tabulated results exist is the round loop with rectangular cross section, with mean radius a, axial thickness b, and trace width c (*Figure 5-3*). The self-inductance of this single loop may be calculated using techniques outlined in Grover [34, pp. 94], where the inductance is found to be:

$$L = 0.1aPF \qquad [Eq.\ 5\text{-}14]$$

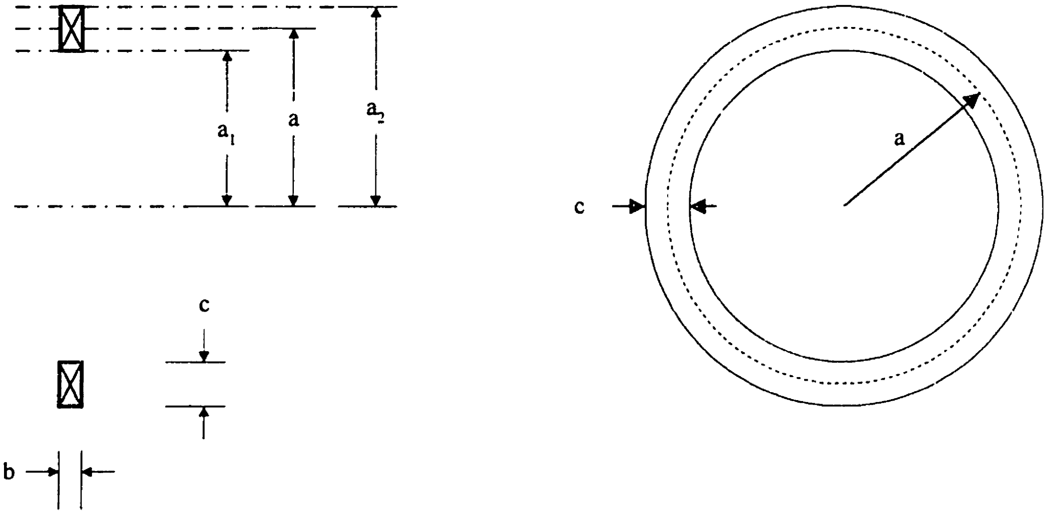

(a) Cross sectional view

(b) Top view

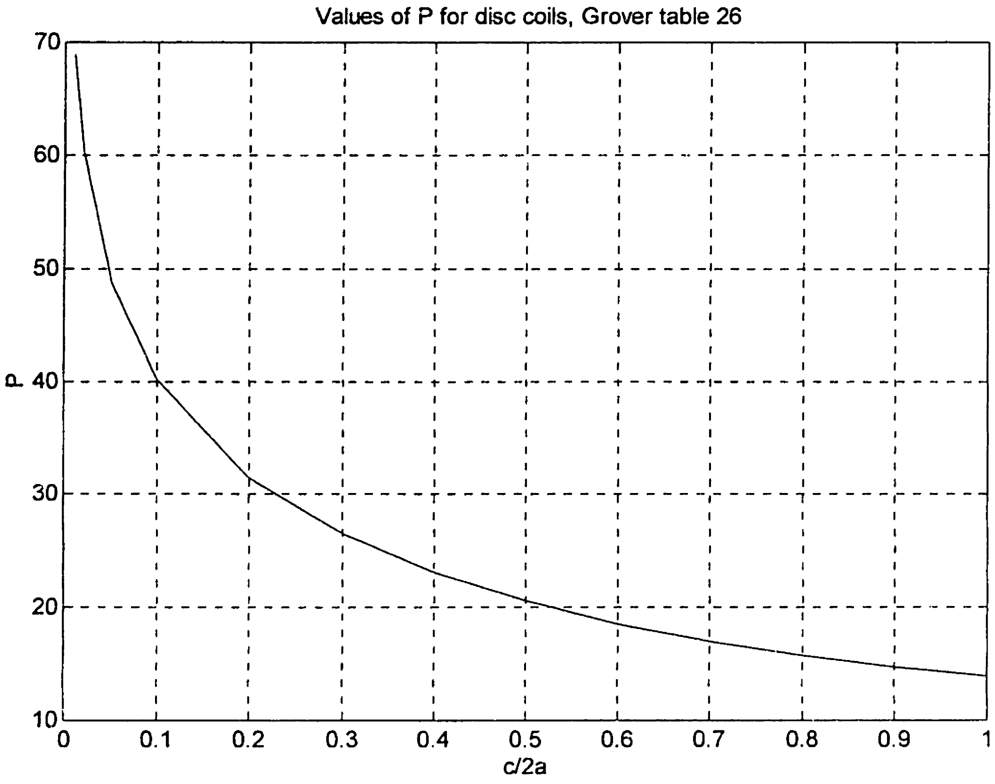

(c) Function P, for disk coils

From Grover [34], Table 26, pp. 113

Figure 5-3. Circular coil with rectangular cross section

For this calculation, a is in meters and L is in μH. P is a function of the coil normalized radial thickness $c/2a$ (*Figure 5-3c*) and applies to a coil of zero axial thickness ($b = 0$), and F accounts for the finite axial length of the coil. For $b << c$ and $c << a$ (coils resembling thin disks) the factor $F \approx 1$, an important limiting case. Therefore, for a coil with double the mean radius, there will be a doubling of the inductance.

The circular disk coil resistance and quality factor Q may be approximated as well. For a current loop with applied voltage V the current density in the loop has a radial dependence given by [291, pp. 54]:

$$J(r) = J_o \frac{a_1}{r} = \frac{\sigma V}{2\pi r} \qquad \text{[Eq. 5-15]}$$

The total current in the loop is:

$$I = b \int_{a_1}^{a_2} \frac{\sigma V}{2\pi r} dr = \frac{b\sigma V}{2\pi} \ln\left(\frac{a_2}{a_1}\right) \qquad \text{[Eq. 5-16]}$$

Therefore, the DC resistance of the loop is:

$$R_{DC} = \frac{2\pi}{b\sigma \ln\left(\frac{a_2}{a_1}\right)} \qquad \text{[Eq. 5-17]}$$

This interesting result shows that rings with the same aspect ratio (ratio of a_2 to a_1) will have the same DC resistance, no matter what the average coil radius a is. For a thin loop where $c << a$, the resistance reduces to:

$$R_{DC} \approx \frac{2\pi a}{bc\sigma} \qquad \text{[Eq. 5-18]}$$

Higher inductance results for a narrow trace ($c << a$). The resultant low frequency Q_{LF} for a thin loop with $c << a$ is:

$$Q_{LF} \approx 0.1PFbc\sigma f \qquad \text{[Eq. 5-19]}$$

and resulting time constant:

$$\tau = \frac{L}{R_{DC}} \approx \frac{0.1PFbc\sigma}{2\pi} \qquad \text{[Eq. 5-20]}$$

At high frequencies the coil Q will be degraded due to the increase in resistance due to the skin effect.

The goal of this exercise was to approximate the complicated guideway loop geometry by a geometry where analytic expressions are available. The results for the circular disk coil with rectangular cross section were applied to a single loop of the guideway with good results. Shown in *Figure 5-4a* is the actual geometry of one guideway loop coil which spans one pole pitch $p = 12.6$ cm. The procedure for finding an approximate equivalent disk coil (*Figure 5-4b*) is as follows:

- Calculate the area enclosed by the actual coil. To find the circumference of the coil use the mean distance to each coil element. $A_{total} = 103.75$ cm^2
- Find the mean radius of a circular coil which has the same perimeter. $a = 5.75$ cm
- Calculate the mean radial thickness of the coil. $c = 0.39$ cm
- Find P as a function of $c/2a = 0.0337$, interpolating from <u>Grover</u> Table 26, pp. 113 $P = 53.87$
- Find F as a function of $c/2a$ and $b/c = 0.6082$, using <u>Grover</u> Table 24, pp. 108 $F = 0.9182$

This methodology is designed to match the self-inductance of the actual guideway coil with a circular coil. In further calculations, the self-resistance of the actual guideway coil ($R_s \approx 0.0007\ \Omega$) is used in the evaluation of natural frequencies. Results (*Table 5-1*) show good agreement between measurements made using an actual coil, finite element analysis on the coil, and the approximate calculation.

Table 5-1. Comparison of calculations on coil geometries

Measured inductance @ 10 kHz	***Grover Calculation (using circular disk coil with rectangular cross section)***	***Finite Element Analysis (using actual guideway coil geometry)***
259 nH	276 nH (see above)	280 nH

Further approximations can be made by modeling the circular disk coil by a thin filament near the center of the cross-section of the disk. An approximate formula for the calculation of the self-inductance of a filamentary loop was first given by J.C. Maxwell [40], where:

$$L = \mu_o a N^2 \left\{ \ln\left(\frac{8a}{r}\right) - 2 \right\} \qquad [Eq.\ 5\text{-}21]$$

where a is the radius of the loop in meters and r is the radius of the wire. A paper by T. R. Lyle [39] in 1913 shows that the filament approximation will give the self-inductance of any circular coil with rectangular cross section to any degree of accuracy when the mean coil radius is substituted for a and the geometric mean distance (G.M.D.) is substituted for r. The values of mean radius and G.M.D. are adjusted depending on the mean radius and the cross-section profile of the coil. The same reasoning can be applied to find the mutual inductance between filamentary loops, as in the early papers by S. Butterworth [30, 31] and A. Campbell [32].

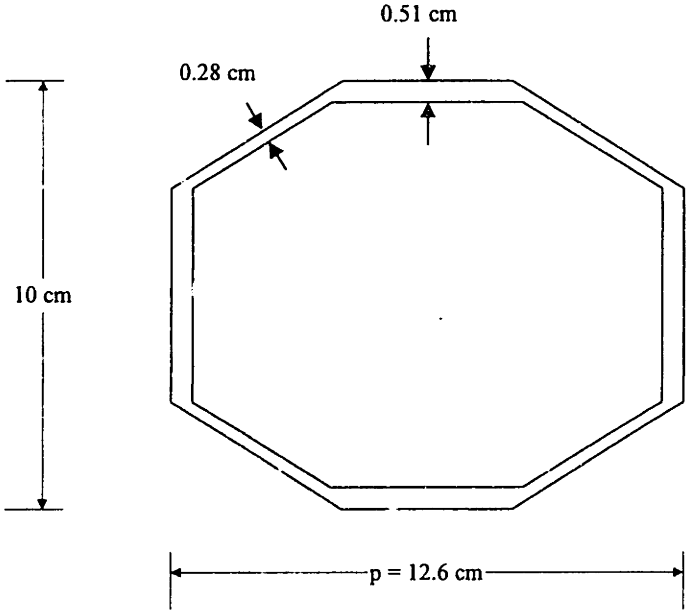

(a) Actual linearized geometry of one pole-pitch wide primitive guideway loop

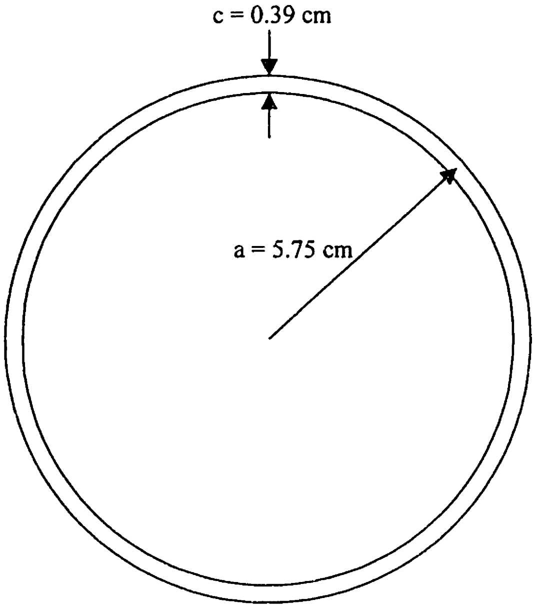

(b) Approximate model, using disk coil

Figure 5-4. Coil model

5.2.3. Semi-Infinite Distributed Model

Simple models may be used to demonstrate the effects of mutual coupling between guideway loops on the Maglev drag peak. Using a 3-coil model (*Figure 5-5b*), the transfer ration between loop current and voltage in the sinusoidal steady state is:

$$sL\begin{bmatrix} 1 & k_{12} & k_{13} \\ k_{12} & 1 & k_{12} \\ k_{13} & k_{12} & 1 \end{bmatrix} + R\begin{bmatrix} 1 & r_{12} & r_{13} \\ r_{12} & 1 & r_{12} \\ r_{13} & r_{12} & 1 \end{bmatrix} = \begin{Bmatrix} v_1 \\ v_2 \\ v_3 \end{Bmatrix} \qquad \text{[Eq. 5-22]}$$

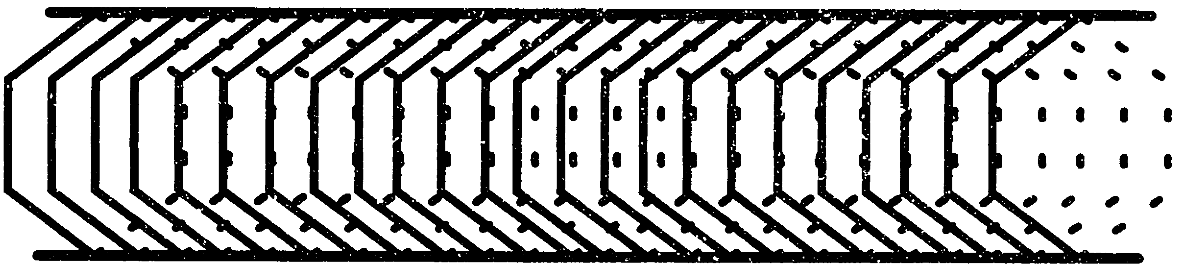

(a) Linearized geometry of guideway coils

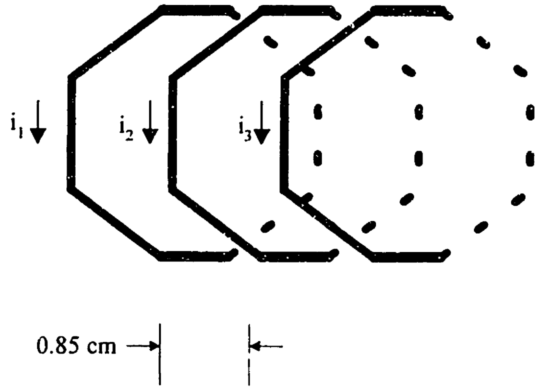

(b) Broken up into non-interacting coils (exploded view)

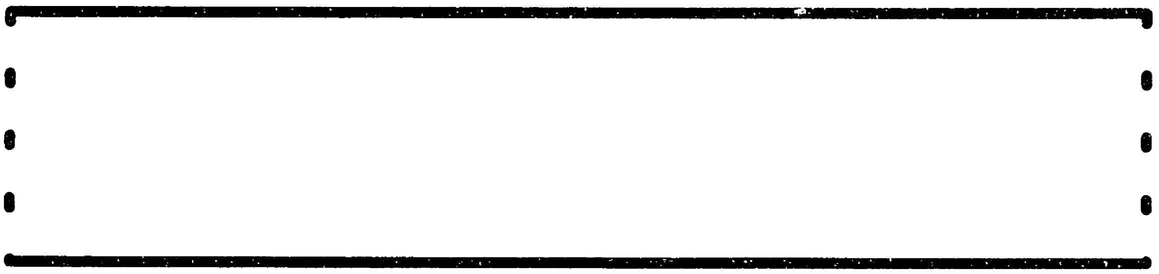

(c) Rim

Figure 5-5. Guideway geometry

The self inductance of each loop is L and the loop-loop mutual inductance $M_{ij} = k_{ij}L$ where k_{ij} is the loop coupling coefficient which is less than 1. The effects of mutual resistance are modeled by the off-diagonal term r_{ij}. The natural frequencies and mode shapes of this structure are found by solving the eigenvalue problem:

$$sL\begin{bmatrix} 1 & k_{12} & k_{13} \\ k_{12} & 1 & k_{12} \\ k_{13} & k_{12} & 1 \end{bmatrix} + R\begin{bmatrix} 1 & r_{12} & r_{13} \\ r_{12} & 1 & r_{12} \\ r_{13} & r_{12} & 1 \end{bmatrix} = \begin{Bmatrix} 0 \\ 0 \\ 0 \end{Bmatrix} \qquad \text{[Eq. 5-23]}$$

The self and mutual inductances may be calculated using approximate methods outlined by F. Grover [34].

The solution for an isolated loop coil was found for $R = 0.0007\ \Omega$ and $L = 300$ nH, values which are approximate for our geometry. For a single isolated coil, a lowest-frequency pole of $\omega_1 = R/L = 3000$ radians/second is calculated corresponding to a critical frequency of 477 Hz and an equivalent drag peak velocity of 120 meters/second. Obviously, this velocity is much too high for a practical Maglev system, so a single loop model is not sufficient. For a system with two interacting coils and coupling coefficient $k = 0.9$, the lowest-frequency pole is $\omega_2 \approx 1580$ radians/second, showing the effects of mutual coupling. The lowest-frequency time constant as the coil-to-coil coupling coefficient $k \rightarrow 1$ is twice as high as the case for the single coil since the inductance increases by a factor of 4 and the resistance increases by a factor of 2.

In order to predict the drag peak frequency, mutual inductances were measured for the interacting guideway loops (*Figure 5-6*). The method for measuring mutual inductance is described in the Appendix (Chapter 8) and there is good agreement between measurements and calculations made on a filamentary approximation based on the formulations of Butterworth and Campbell [30 - 32].

Based on the resultant inductance matrix, and a calculated resistance matrix (including mutual resistance terms) the 15 natural frequencies associated with a 15-loop guideway approximation were calculated (*Table 5-2*). The Matlab program for this calculation is found in the Appendix. Results show that the lowest natural frequency is at 96.5 Hz, corresponding to a linear peripheral speed of 24.3 meters/second, and a test wheel rotation speed of 290 RPM. The second mode is at 174 Hz, and is an odd spatial mode.

Table 5-2. Calculation of natural mode frequencies and equivalent velocity

Mode	*f (Hz)*	*v (meters/sec)*	*Wheel speed (RPM)*
1	96.5	24.3	290
2	174	43.8	523
3	316	79.6	950
4	387	97	1164
5	589	148	1772

The eigenvectors of the two lowest-frequency modes are shown in *Figure 5-7.* It is important to note the following:

- The mode shapes are in approximately the same shape as the excitation, as the model covers one pole-pitch, or one half cycle of a spatial sinusoid.
- Since the mode shapes are in the same shape as the excitation, the dominant modes excited will be the low frequency modes.
- From this, a drag peak velocity of 24 - 44 meters/second is predicted.
- Since the 15-loop guideway is a truncated version of the actual distributed guideway, it is likely that the lowest-frequency mode will dominate due to the smoothing effect of the infinite structure.

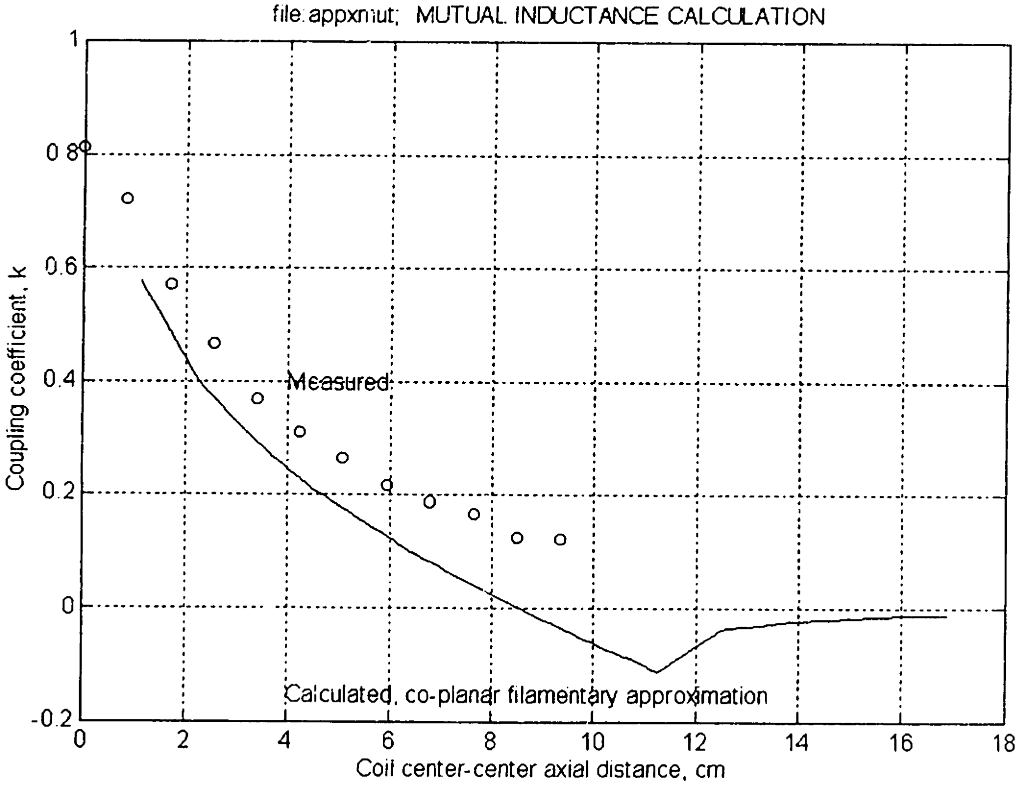

Figure 5-6. Comparison of calculated (solid line) to measured guideway coil-coil mutual inductance

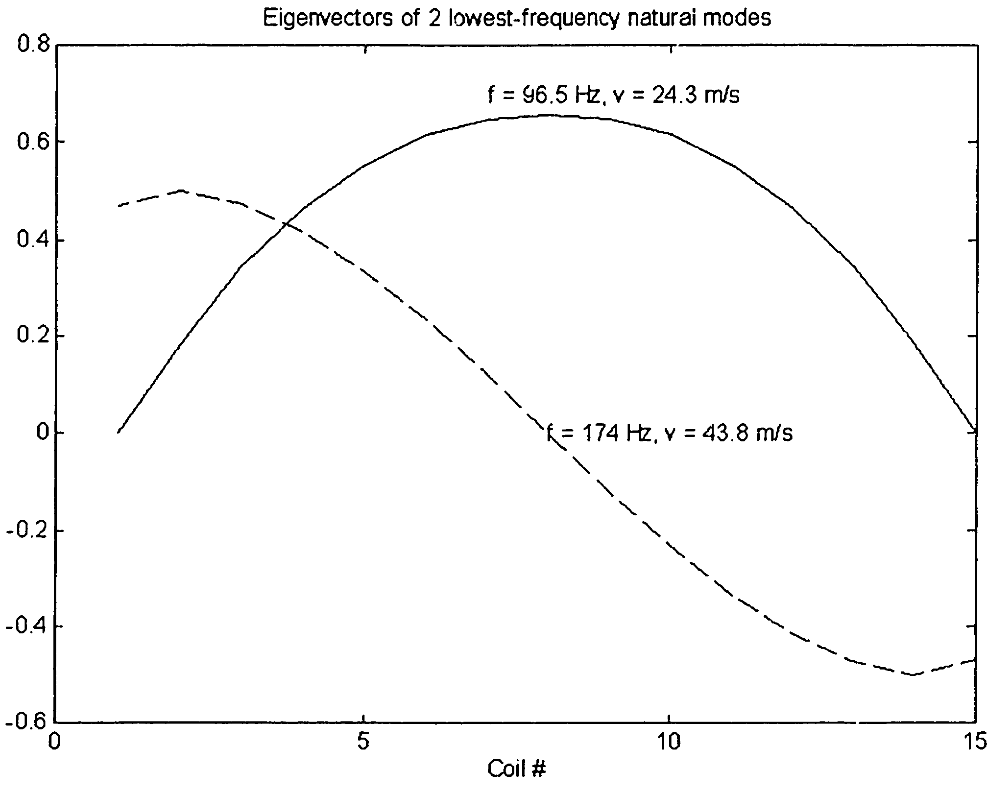

Figure 5-7. Mode shapes associated with two lowest natural frequencies for guideway model

Calculation of the lift and drag forces for different velocities requires solving the full matrices with excitation due to the induced voltages. The problem can be posed as:

$$\left[j\omega[L]+[R]\right]\{i\}e^{j\omega t}=j\omega A_l\{B_o\}e^{j\omega t} \qquad \text{[Eq. 5-24]}$$

where *[L]* and *[R]* are the same matrices as found before and the excitation vector is on the right hand side. The left hand side is the impedance matrix

$$\left[Z(j\omega)\right]\{i\}=j\omega A_l\{B_o\} \qquad \text{[Eq. 5-25]}$$

The solution for the loop currents *{i}* can be found by inverting the impedance matrix.

$$\{i\}=j\omega A_l\left[Z(j\omega)\right]^{-1}\{B_o\} \qquad \text{[Eq. 5-26]}$$

Once the loop current vector is known, the lift and drag force can be directly calculated by normal methods. Results of these calculations and comparison to test results is given in Chapter 6.

5.3. Active Secondary Control System

EDS Maglev systems using superconducting magnets have low damping. Furthermore, it has been demonstrated that an electrodynamic suspension may have slightly negative damping under certain operating conditions [64], [92], [99]. Therefore, a control system is needed to prevent underdamped or unstable vertical oscillations.

In order to suspend the magnet statically, the downward gravitational pull is canceled by an upward magnetic force. One characteristic of the EDS suspension is that the magnet is levitated stably; that is, a deviation from the equilibrium position results in a restoring force, similar to a mass and a spring. In an electromagnetic suspension (such as a steel ball suspended in a magnetic field) there is no stable equilibrium for DC excitation of the magnet.

The magnetic levitating force acting on the magnet is given by:

$$f_Z = -k_m z = -Ci_M^2 z \qquad [Eq.\ 5\text{-}27]$$

where k_m is the equivalent spring constant, z is the vertical distance with reference to the magnet "null position," i_M is magnet current, and C is a constant which accounts for magnet and coil geometry and relative velocity between the magnet and levitating coils. At $z = 0$, the magnet is operating at the null position, where there is no net time-varying flux through the levitating coils, and ideally there is no levitating force.

Assuming that there are incremental changes in forces, magnet vertical position, and magnet currents, a linearized model can be generated relating incremental changes in magnet vertical position to changes in incremental magnet current. Vertical force, vertical position and magnet current are given as the sum of a DC component and an incremental component:

$$\begin{aligned} f_Z &= F_Z + \tilde{f}_z \\ z &= Z_o + \tilde{z} \\ i_M &= I_M + \tilde{i}_m \end{aligned} \qquad [Eq.\ 5\text{-}28]$$

Resulting in:

$$f_Z \approx -CI_M^2 Z_o - CI_M^2 \tilde{z} - 2CI_M Z_o \tilde{i}_m \qquad [Eq.\ 5\text{-}29]$$

where second-order and higher terms have been neglected. At equilibrium, the magnet will be in a rest position slightly below the null position, so that there will be a resultant magnetic force which balances the force of gravity:

$$F_Z = Mg = -CI_M^2 Z_o \qquad [Eq.\ 5\text{-}30]$$

resulting in the equilibrium magnet position:

$$Z_o = -\frac{Mg}{CI_M^2} = -\frac{Mg}{k_m} \qquad [Eq.\ 5\text{-}31]$$

As expected, this result shows that the equilibrium position will be below the null position, at a position dictated by the equivalent spring constant, so that there will be a restoring force to balance the weight of the magnet.

Newton's law applied to the magnet results in:

$$M\frac{d^2\tilde{z}}{dt^2} = f_M - Mg = -CI_M^2\tilde{z} - 2CI_M Z_o\tilde{i} \qquad \text{[Eq. 5-32]}$$

resulting in :

$$\frac{M}{CI_M^2}\frac{d^2\tilde{z}}{dt^2} + \tilde{z} = \frac{2Mg}{k_m I_M}\tilde{i}_m \qquad \text{[Eq. 5-33]}$$

Using the spring constant k, and converting the equation to the frequency domain results in:

$$\left(\frac{M}{k_m}s^2 + 1\right)z(s) = \frac{2Mg}{k_m I_M} i_m(s) \qquad \text{[Eq. 5-34]}$$

resulting in the transfer function between magnet position and magnet control current:

$$\frac{z(s)}{i_m(s)} = \frac{2Mg}{k_m I_M\left(\frac{M}{k_m}s^2 + 1\right)} \qquad \text{[Eq. 5-35]}$$

This result shows that this suspension will have two jω axis poles, as in a simple, lossless mass-spring system:

$$s_{p1,2} = \pm j\sqrt{\frac{k_m}{M}} \qquad \text{[Eq. 5-36]}$$

In reality, the poles will be slightly in the left-half or right-half planes due to the details of the system.

Such a system can have the closed-loop poles arbitrarily adjusted by applying position-velocity feedback (*Figure 5-9*). By adjusting the parameters K_f, K_v, and K_p the poles can be placed in the left-half plane with sufficient damping to achieve good ride quality. Results of testing of the control system are given in Chapter 6.

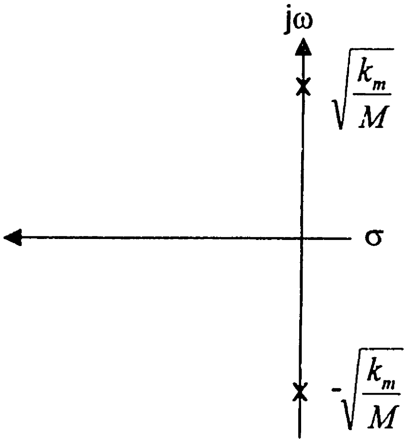

Figure 5-8. Pole plot of vertical dynamics of flux-canceling EDS

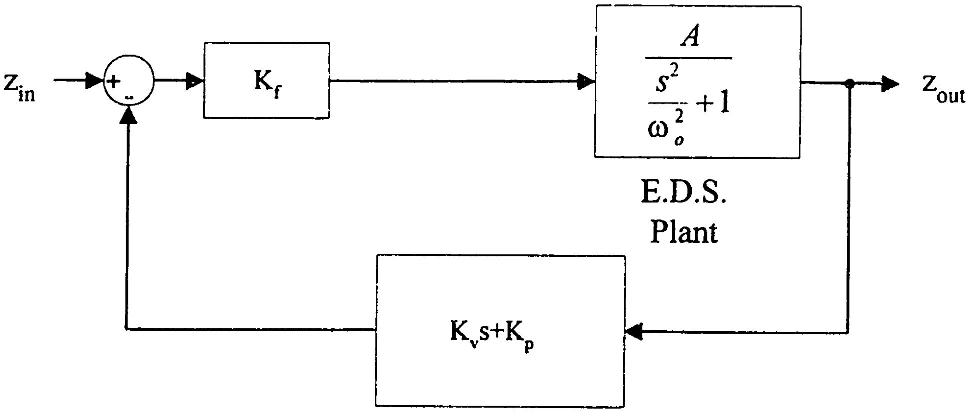

Figure 5-9. Control system block diagram

6. Maglev Test Program

Details of the test fixture including speed control of the test wheel and operation of the data acquisition system are discussed in [190]. The goals of the test program were to:

- Verify that the test wheel operates safely and with sufficient mechanical tolerance over normal operating conditions.
- Measure forces and moments for the magnets in different equilibrium positions and for different linear velocities using the 6 degree-of-freedom force sensor.
- Test the viability of using AC excitation of the magnet coils to achieve significant lift force at zero train velocity.
- Test the viability of actively controlled high temperature superconducting magnets in a magnetic secondary suspension by testing the magnet with copper coils and a low-friction air bearing.

The relationship between wheel speed setting (in RPM) and velocity is given in *Table 6-1.*

Table 6-1. Relation between wheel speed setting and peripheral velocity

Speed, RPM	***v, meters/sec***	***v, km/hour***	***v, miles/hour***	f_{eff}
0	0	0	0	0
100	8.4	30	19	33
200	16.8	60	38	67
300	25	90	57	100
400	33	121	77	133
500	42	151	96	166
600	50	181	115	199
700	59	211	134	233
800	67	241	153	266
900	75	271	172	299
1000	84	302	189	332

6.1. Test Wheel Evaluation

Prior to testing, runout and natural frequency measurements were done on the test wheel after mounting it to the aluminum hub of the test fixture. The runout test was done to determine the amount of rotating imbalance which will add a periodic torque to the main bearings. Runout also limits the minimum magnet to guideway coil spacing that may be tested. Several different test wheel resonances were measured to determine if natural modes would cause wheel vibration during operation.

6.1.1. Runout

The axial runout was measured with capacitive sensors which sense the distance from a known reference location to the guideway coils. A runout of ±0.9 mm was measured for the finished test wheel (*Figure 6-1*) after mounting on the aluminum hub. In a second measurement, runout was measured on the front face of the wheel with a dial indicator. The resultant runout to the front fiberglass coating of the wheel is less than that measured with the capacitive sensor, indicating that the copper coils slightly shifted inside the fiberglass during the manufacturing process. This small amount of runout is not expected to affect magnetic measurements.

6.1.2. Test Wheel Mechanical Resonant Modes

The lowest-frequency natural modes of the test wheel were measured by mounting 2 accelerometers to the test wheel in two separate configurations (*Figure 6-2*). By moving the accelerometers information about the mode shapes of oscillation can be inferred. The three lowest modes of oscillation were measured at 21.9 Hz, 49.6 Hz, and 68.6 Hz. These measured natural frequencies compare well with calculated frequencies of 29.6, 51.2 and 69.0 Hz, given in Chapter 3. These frequencies are high enough so that they will not be excited during normal wheel operation up to 1000 RPM.

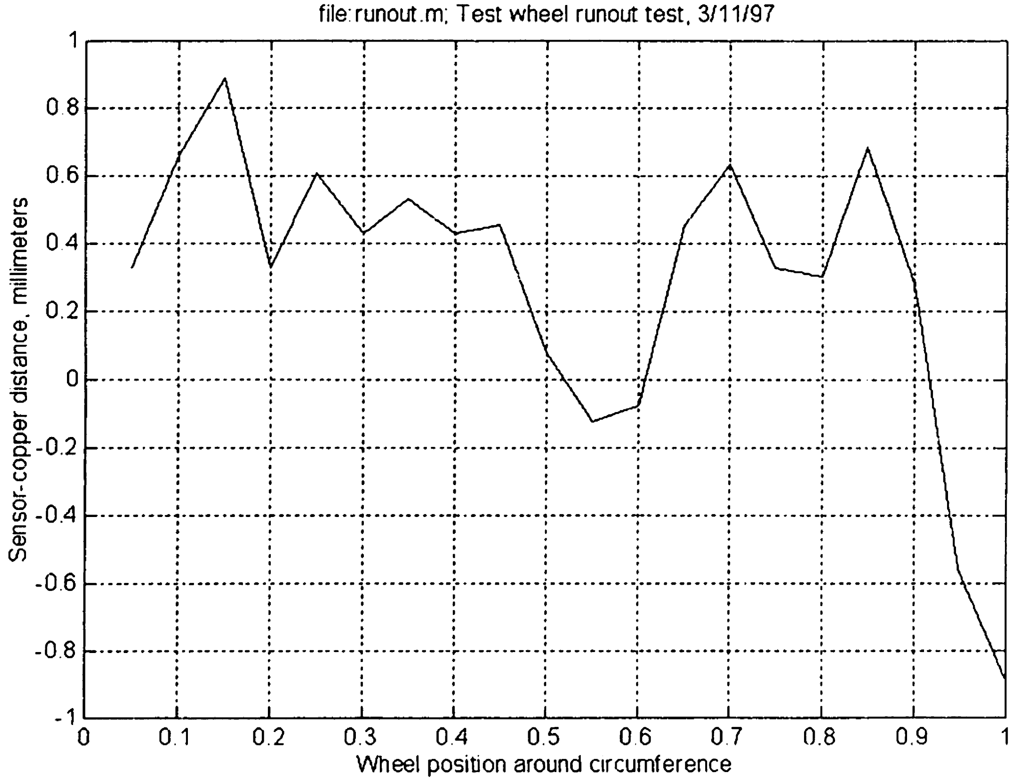

Figure 6-1. Measured test wheel runout.
Measurements made with two capacitive sensors. Sensing was done to the front surface of the copper conductors

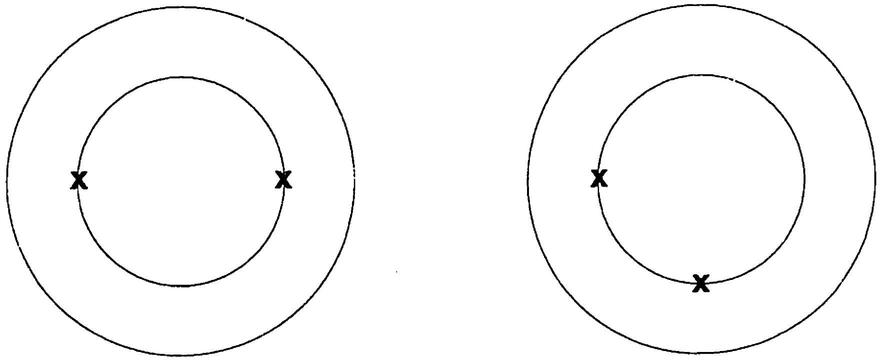

Figure 6-2. Accelerometer mounting locations
2 different mounting locations were used to determine the phasing of the accelerations in order to identify odd and even flexure modes.

6.1.3. Preliminary Wheel Tests

In initial testing, the wheel speed was slowly increased from 0 to 625 RPM. Vibration was monitored during the initial spin-up, as was temperature of the main bearings. At 600 RPM an acceleration of 0.067 g peak-to-peak was measured near the main bearing on the bearing table, indicating that rotating imbalance is not significantly stressing the test fixture.

6.2. Basic Maglev Measurements Using Force Sensor

The procedure for making basic measurements of forces and moments was as follows:

- The magnet was wired in the flux-canceling configuration (*Figure 6-3a*).
- The magnet was positioned near the test wheel in the desired vertical (z) and horizontal (x) positions.
- The test wheel was run at the speed corresponding to the desired linear velocity.
- The data acquisition system was activated, beginning a 4 second sampling of force and torque data from the force sensor.
- In the middle of the sampling period, the power supply driving the coils was turned on, and the resulting force transient was measured (*Figure 6-3b*).

In the example shown (*Figure 6-3b*) the magnet was set above the null position at $z = 1.45$ cm and each coil was energized with 5 Amperes corresponding to $NI = 2750$ Ampere-turns per coil. Therefore, it is expected that the "lift" force be in the $-z$ direction for this case. For a wheel speed of 350 RPM ($v \approx 29$ meters/second) a lift force of approximately -50 Newtons and a drag force of approximately 20 Newtons was measured.

By repeating the measurements at different wheel speed and vertical positions, the Maglev force profiles for lift (z force), drag (y force) and guidance (x force) were generated. Results can be scaled for different magnet currents by realizing that all magnetic forces scale as $(NI)^2$.

The result of several test wheel runs is shown in *Figure 6-4*. In *Figure 6-4a*, the magnet was set below the null position, and a positive lift force is measured. In *Figure 6-4b*, the magnet was set +1.25 cm above the null position and a negative lift force is measured. The drag force shows a peak at approximately 20-25 meters/second. Also of note is the guidance force, which is a significant fraction of the lift force. In *Figure 6-4c*, the magnet was set near the null position, and the forces are reduced accordingly.

The important results from this test are:

- The drag peak velocity is approximately 20-25 meters per second. This critical velocity will decrease significantly for a full-scale Maglev magnet. The dependence of drag peak velocity with magnet size can be predicted with scaling laws developed later in this chapter.
- The guidance force for this configuration is a significant fraction of the lift force.

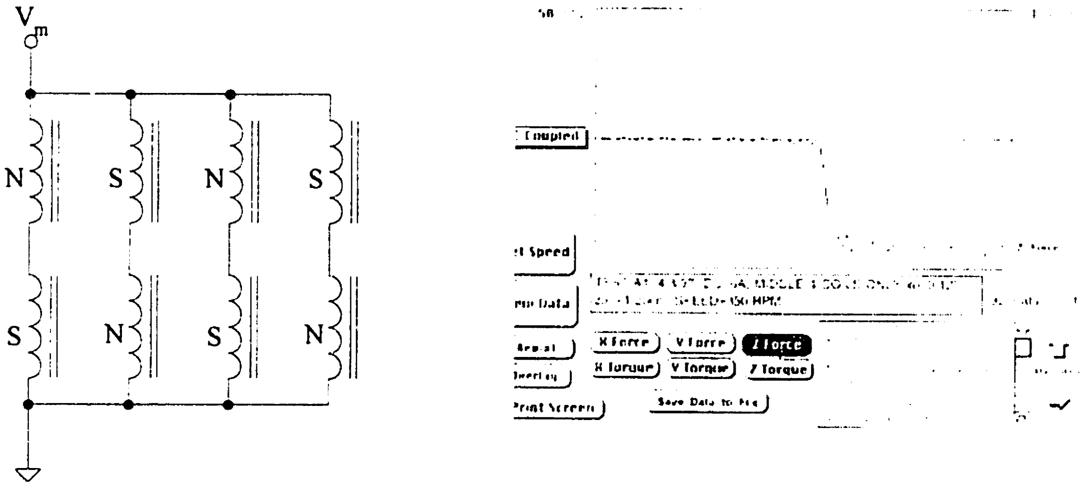

(a) Magnet wiring for basic lift measurements

(b) Lift measurement
Data stream 4 seconds long; magnet energized after 2 seconds

Figure 6-3. Magnetic lift measurement, showing approximately -50 Newtons of lift at 350 RPM

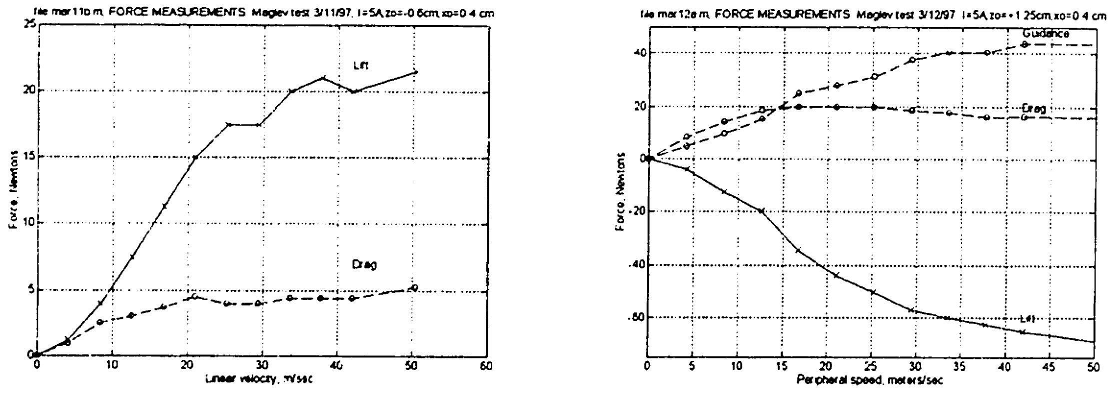

(a) Magnet below null position at z = -0.4 cm

(b) Magnet above null position at z = 1.45 cm

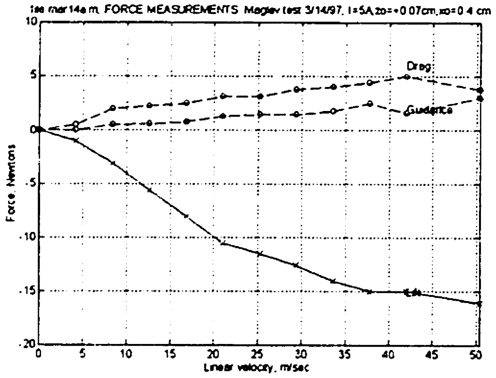

(c) Magnet slightly above null position at z = 0.27 cm

Figure 6-4. Lift, drag, and guidance force measurements at different vertical (z) displacements Results for test wheel speeds 0 - 600 RPM (v = 0 - 50 meters/second) I = 5A per coil, NI = 2,750 A-turns per coil, all 8 coils energized

The drag force shows a more pronounced peak when the effects of eddy currents on the guideway rim are calculated. The power loss in the guideway rim is calculated assuming the width of the guideway rim $w = 0.5$ cm, the thickness $t = 0.5$ cm, the length in which the eddy currents travel $L = 10$ cm and average field at the guideway $B_o = 0.05$ Tesla, resulting in a power loss [47, pp. 402]:

$$\langle P\rangle = \frac{(8)wtL^3\sigma\left(\frac{dB}{dt}\right)^2}{16} \approx \frac{wtL^3\sigma\left(\frac{\pi v B_o}{p}\right)^2}{2} \qquad \text{[Eq. 6-1]}$$

The factor of 8 in Eq. 1 is due to the 8 pole faces of the magnet, each with length 8 centimeters. The power loss is due to eddy currents circulating along the length of the rim. The extra drag force due to the eddy currents is $f_{eddy} = \langle P\rangle/v$ where v is the linear velocity, or:

$$\left\langle f_{y,eddy} \right\rangle \approx \frac{wtL^3\sigma \left(\frac{\pi B_o}{p} \right)^2 v}{2} \qquad \text{[Eq. 6-2]}$$

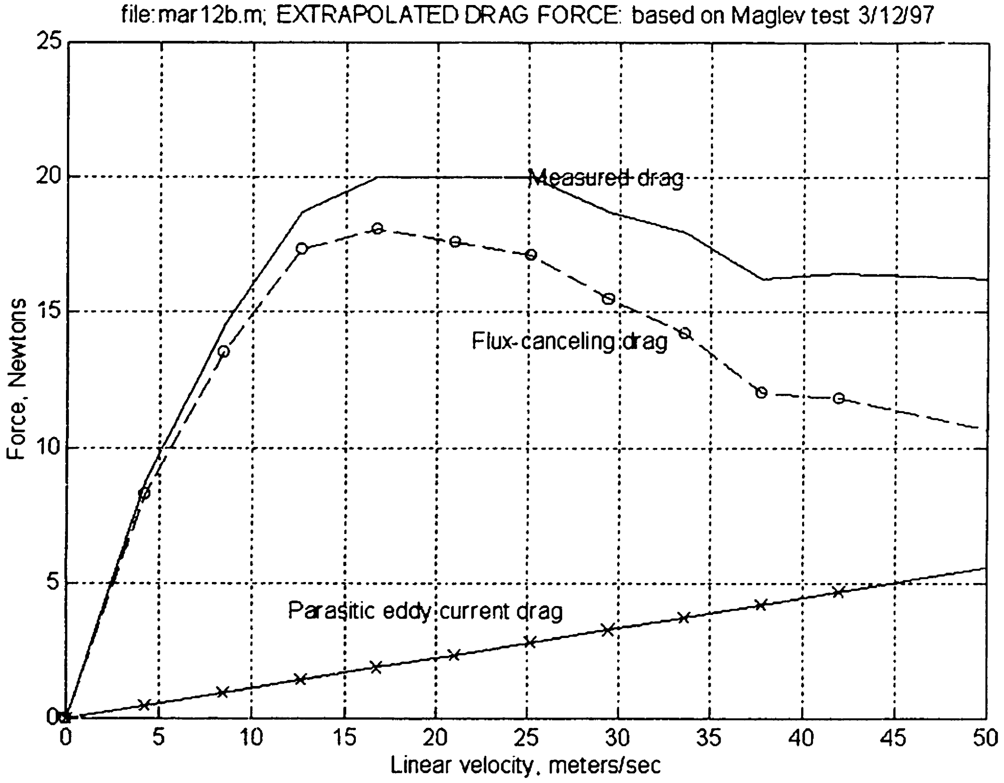

Figure 6-5. Extrapolated Maglev drag force profile
Effects of parasitic eddy current drag is estimated for magnet above null position at z = + 1.45 cm.

The lift force vs. displacement is plotted in *Figure 6-6*. The slopes of the lines may be interpreted as the magnetic spring constant, the change in magnetic lift force with vertical position. It is of note that the lift force profile is more linear than that of other EDS suspensions, such as the null-flux system. The linearity has important ramifications for control system design.

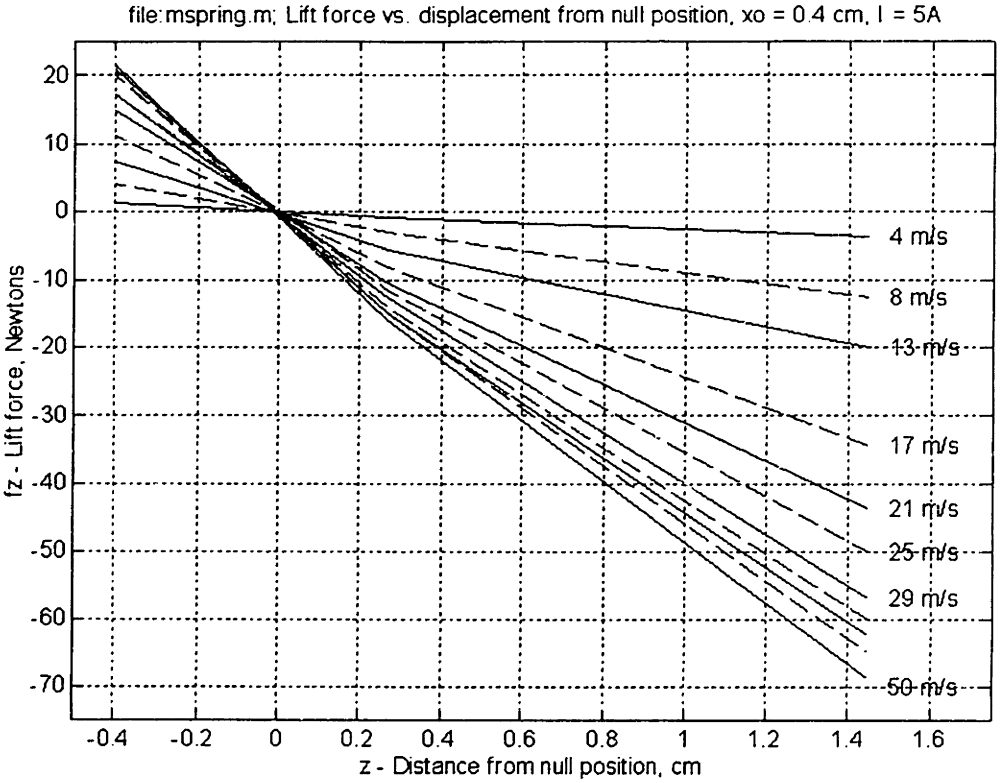

Figure 6-6. Lift force vs. vertical displacement

The result of a calculation based on the electrodynamic model in Chapter 5 is shown in *Figure 6-7*, and compared to measured data taken with the test wheel in the range 0 - 600 RPM (0 - 50 meters/second). There is good agreement for the 15-coil model for the lift force f_z.

The excitation vector (top left) is approximately a half-sinusoid, corresponding to the applied magnetic field integrated over the area of the guideway loops. The shape of this vector insures that only first and second modes will be excited, due to the orthogonality of natural modes. Measurements on drag force (bottom right) bear this out, as the measured drag peak velocity was approximately 25 meters/second and the electrodynamic model predicts ~40 meters/second. Higher-order modes are at significantly higher natural frequencies.

The vectors corresponding to loop currents (top right) is used to calculate lift and drag forces. Lift force is found by:

$$<f_z(\omega)> = \frac{l}{2}\sum_{j=1}^{15} \operatorname{Re}\left\{i_j(j\omega)B_j^{*}(j\omega)\right\} \qquad [Eq.\ 6\text{-}3]$$

where l is a length scale associated with the horizontal length of the coil, i_j is the induced current in the j_{th} coil, and B_j is the average field acting on the induced current.

The lift force model shows good agreement with experiment in the 0-50 meter/second range, although there may be divergence at higher velocities. This may be due to the effects of higher-order modes at higher frequencies, but further study is warranted.

The drag force is found by evaluating the power dissipated in the guideway coils, or:

$$< f_y(v) > = \sum_{j=1}^{15} \frac{\left|i_j\right|^2}{2Rv} \qquad \text{[Eq. 6-4]}$$

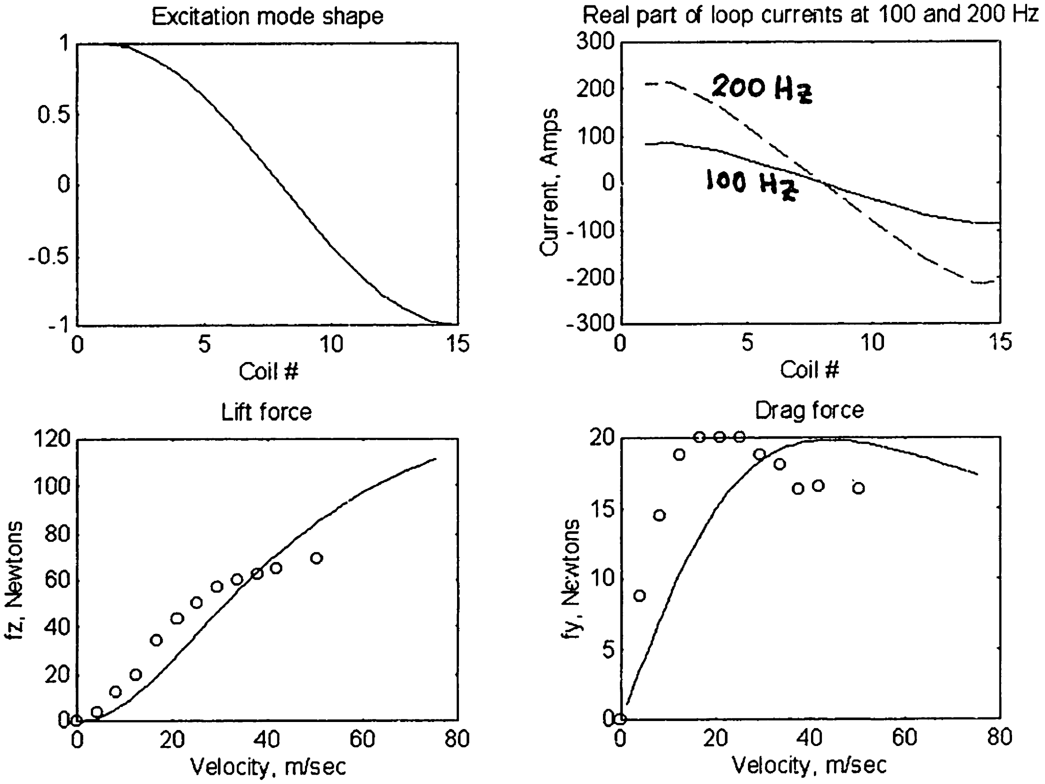

Figure 6-7. Predictions of electrodynamic model
Magnet +1.25 cm above null position
Upper left, coil excitation vector {v}
Upper right, induced loop currents {I} at 100 Hz and 200 Hz
Lower left, comparison of measured to calculated lift force vs. velocity
Lower right, comparison of measured to calculated drag force vs. velocity

6.2.1. Scaling Laws for Full-Scale System

The goal of this section is to predict performance of a full-scale Maglev system based on scaling laws, simple guideway coil geometries, and test results from the scale-model magnet. The Maglev test fixture described in this thesis is a 1/5 scale geometry. The results from approximate calculations and measurements on the scale-model system may be used to predict performance of the full-scale train. Results may be extrapolated from calculations on simple resistance-inductance circuits, as the previously mentioned measurements have proven this approximate technique to be valid. It is assumed that in scaling up the system, every linear dimension in the guideway and magnet is scaled by the factor l.

As shown previously, the inductance of a disk inductor (*Figure 6-8*) has the form:

$$L \propto aPF \qquad [Eq.\ 6\text{-}5]$$

where a is the mean radius, P is a function of normalized radial thickness $c/2a$ and F is a function of normalized axial thickness b/c. If all dimensions of the inductor are scaled by the factor l, the inductance also scales by the same factor as P and F remain constant.

The self-resistance of the loop is given by:

$$R \approx \frac{2\pi a}{\sigma bc} \qquad [Eq.\ 6\text{-}6]$$

and this resistance scales as $1/l$. The resultant time constant of the loop (given by L/R) scales as l^2, and shows that large scale inductors will be more efficient than small ones. Given this scaling, the EDS drag peak velocity is expected to scale as $1/l$, although the effects of parasitic eddy currents will modify this somewhat.

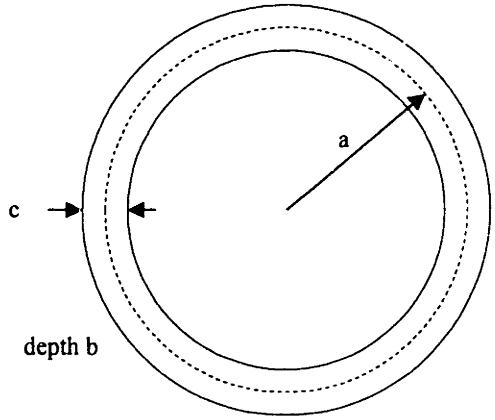

Figure 6-8. Model for development of scaling laws for EDS Maglev
Scaling laws for circular disk inductors may be calculated by using the Grover formulation.

The maximum number of coil turns scales with the winding area, or as l^2. The average guideway field scales as l, due to the l^2 factor increase in turns, and the l increase in pole pitch. The induced voltage V_i around a guideway loop may be expressed as:

$$V_i = j\omega B_o A \propto l^3 \qquad [Eq.\ 6\text{-}7]$$

where B_o is the average magnetic field, and A is the area of the guideway loop. In the high-speed limit, the induced current is limited by the inductance of the coil, as:

$$I_i \approx \frac{V_i}{j\omega L} \propto l^2 \qquad [Eq.\ 6\text{-}8]$$

The lift force is due to the product of the induced current, the applied magnetic field, and the length scale, or:

$$f_z \propto I_i B_o l \propto l^4 \qquad [Eq.\ 6\text{-}9]$$

The maximum lift force scales as ℓ^4, which also could be inferred from evaluating the magnetic pressure acting on the iron polefaces. The drag force scales as I_i^2R, or as ℓ^3 and hence the lift/drag ratio at cruising speed scales as ℓ. Other parameters such as scaling of lift/drag and lift-to-weight ratio may also be inferred from the test results. A summary of the scaling laws is shown in *Table 6-2.*

Table 6-2. Scaling law summary for EDS Maglev scaled by factor ℓ
Primed coordinates are for the scaled-up system

Parameter	***Constitutive Relation***	***Scaling law***
Guideway loop self-inductance, L	$L \propto \ell PF$	$L' = \ell L$
Guideway loop self-resistance, R	$R \propto 1/\sigma\ell$	$R' = R/\ell$
Guideway dominant time constant, τ	$= L/R \propto 1/\ell^2$	$\tau' = \tau/\ell^2$
Effective frequency at guideway, ω		$\omega' = \omega/\ell$
Drag peak velocity		$v_{pk}' = v_{pk}/\ell$
N, turns	$\propto \ell^2$	$N' = \ell^2 N$
Average field normal to guideway, B_o	$\propto NI/\ell \propto \ell$	$B_o' = \ell B_o$
Induced guideway loop voltage, V_i	$\propto j\omega B_o\ell^2 \propto \ell^2$	$V_i' = \ell^2 V_i$
Max. induced loop current, I_i	$\propto V_i/j\omega L \propto \ell^2$	$I_i' = \ell^2 I_i$
Lift force at cruising speed, f_z	$\propto B_o I_i \ell \propto \ell^4$	$\propto B_o I_i \ell \propto \ell^4$
Drag force at cruising speed, f_y	$\propto I_i^2 R \propto \ell^3$	$\propto I_i^2 R \propto \ell^3$
Lift/drag ratio at cruising speed	$= f_z/f_y$	$\propto \ell$

Using these same scaling laws, performance of full-scale trains based on copper magnets and on HTSC operating at 40K has been predicted (*Table 6-3*). The extrapolation from 1/5-scale test results to 1.0 scale copper and for copper operating at 77K is straightforward if limitations imposed by air cooling of the copper magnets are not considered. It is unlikely that the number of Ampere-turns shown for the full-scale copper magnet would be achieved in practice due to the heat transfer limitations of air or water cooling.

It is assumed that the copper coils operating at 77K have the same power dissipation as 1.0-scale copper coils operating at room temperature. Therefore, a higher coil current is possible at 77K since the conductivity of copper at liquid nitrogen temperature is only 13% of the room temperature value. This assumes that there is sufficient copper area exposed to the boiling liquid nitrogen. An upper limitation[1] for allowable power dissipation in the copper coil is the peak nucleate boiling heat transfer flux, which for liquid nitrogen is $q_{pk} \sim 15$ Watts/cm^2 [291, pp. 113].

---

[1] Assuming that the winding has sufficient ventilation space for LN2

The performance of a silver-sheathed HTSC magnet operating at 40K is extrapolated from the copper coil results and from available data taken from tests on HTSC coils and samples of HTSC tape [*Figure 6-9*]. The achievable current density in HTSC at 40K is much higher than that in HTSC at 77K (approximately by a factor of 2-6 from published data). For the same number of Ampere-turns, less material will be needed for the HTSC design, resulting in a lighter coil. Current HTSC tapes are available with critical current $I_c = 40$ Amperes at 77K corresponding to a critical current density significantly higher than that supported by copper at 77K. A value of $I = 100$ Amperes or higher seems reasonable for an HTSC coil design at 40K given current technology. Further improvement may be made by adjusting the dimensions of the core, as the full winding area will not be needed.

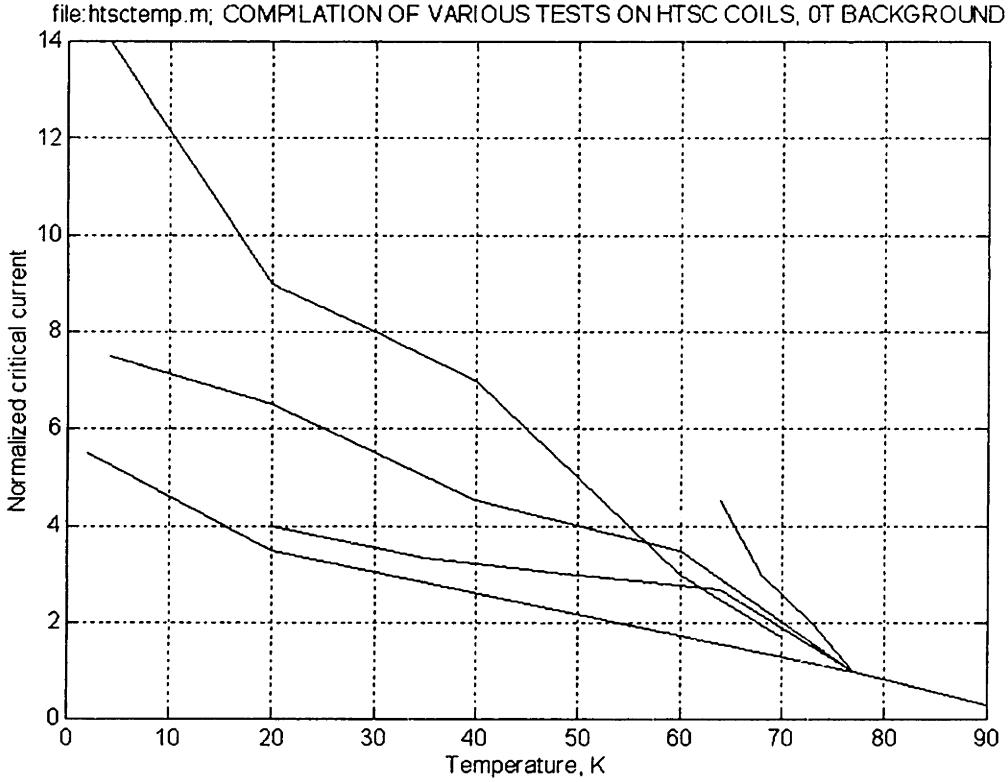

Figure 6-9. Variation in HTSC critical current for various designs
Data normalized to values at 77K [1, 2, 5, 6, 10]

The performance of the predicted 1.0-scale HTSC magnet at 40K is comparable to that of the Japanese MLU002 test vehicle, which operates with an MMF of 700 kA-turns while generating a levitating force of 196 kiloNewtons [51, pp. 7]. The advantage to the iron-core HTSC design is that less Ampere-turns and less superconducting material is needed, and there is the possibility of actively controlling the magnet currents to achieve acceptable ride quality. AC control of the magnet currents and active secondary magnetic suspension is the focus of the next section of this thesis.

Table 6-3. Scaling law summary for EDS Maglev

Comparison between 1/5 scale suspension test results, 1.0-scale copper magnet operating at room temperature, 1.0 scale copper at 77K, and HTSC at 40K (Cooling weight not included)

Parameter	***1/5-scale model***	***1.0 scale copper***	***1.0 scale copper, 77K***	***HTSC @ 40K***
Guideway loop self-inductance, L	280 nH	280 nH	1.4 μH	1.4 μH
Guideway loop self-resistance, R	0.0007 Ω	0.00014 Ω	0.00014 Ω	0.00014 Ω
Loop time constant, τ	0.4 msec	10 msec	10 msec	10 msec
Levitation coil turns, N	550 turns	13750	13750	1500
Levitating coil operating current, I	5 Amps	5	14.4	136[1]
Levitation power dissipation	680 Watts	85 kW	85 kW	0
NI, each coil	2750 A-turns	68750	198,450	198,450
Overall current density in winding, λJ	275 A/cm^2	275	800	7500
Average field normal to guideway, B_o	0.067 Tesla	0.335	0.96	0.96
Lift force at v = 100 m/s, f_z	70 Newtons	43.8 kN	365 kN	365 kN
Drag force at drag peak, f_y	20 Newtons	2.5 kN	20.8 kN	20.8 kN
Drag peak velocity v_{pk}	25 m/sec	5 m/sec.	5 m/sec.	5 m/sec.
Extrapolated drag force at v = 100 m/sec	9.4 N	249 N	2.1 kN	2.1 kN
Lift/drag ratio at v = 100 m/s	7.4	175.4	175.4	175.4
Magnet core weight	29 kg	3625	3625	3625
Coil weight	8 kg	1000	1000	106
Total magnet weight[2]	37 kg	4625	4625	3731
Magnetic drag power @ 100 m/sec	0.94 kW	24.9 kW	208 kW	208 kW
Guideway power, kW/ton of lift	120 kW/ton	5.07	5.07	5.07
Lift/weight ratio	0.19	0.97	8.0	10.0

1. Assuming HTSC tape is of same cross sectional area as 18 gauge wire; for comparison only
2. Cryostat weight not included

6.3. AC Coil Excitation and Force Measurements

Further tests were run to determine if significant lift is possible at zero train velocity by exciting the levitation coils with AC currents. It is desirable to remove the requirements for a mechanical suspension (for instance, wheels or air bearings) for low speed operation of the EDS train. The fact that high temperature superconductors are robust with regard to AC losses is a further motivation, and such control is difficult using low temperature superconductors due to quenching. Test results were used to predict performance of a full-scale system using HTSC coils.

For this series of tests, the coils were wired as in *Figure 6-10a*. The coils were wired so that for the first half cycle of the sinewave current excitation, the top two coils are in a North-North arrangement, and the bottom two coils are energized South-South. For this configuration, if the guideway is offset from the null position, there is a net changing flux through the guideway loops and hence a restoring force.

Tests with the force sensor and data acquisition system to measure lift were unsuccessful due to the low sampling rate of the system. Therefore, a simple test fixture for the measurement of the DC component of lift due to AC currents was constructed (*Figure 6-10b*). A section of guideway was suspended by a long steel spring with a measured spring constant k = 0.61 Newtons/meter. By appropriately counterweighting, the horizontal deflections of the guideway were minimized.

The static displacement of the guideway was measured when the magnet coils were energized with sinusoidal AC current., and with a known spring constant the resulting magnetic force is calculated. The transfer function from force to deflection for this mass-spring system is:

$$\left|\frac{z}{f_z}\right| = \frac{\frac{1}{k}}{\sqrt{\left(1-\frac{\omega^2}{\omega_o^2}\right)^2 + \left(\frac{2\zeta\omega}{\omega_o}\right)^2}} \qquad \text{[Eq. 6-10]}$$

where k is the spring constant, ω_o is the undamped resonant frequency of the system, and ς is the damping ratio. The resonant frequency of the mass-spring system, approximately 1 Hz, was much lower than the current excitation frequencies of 10 to 100 Hz. Therefore, the system effectively filters the AC component of the lift force and the static vertical displacement of the guideway is an indication of the magnetic force.

Results of AC lift measurements are shown in *Figure 6-10c* for various equilibrium displacements from the null position, and for excitation frequencies of 10, 20, 50 and 100 Hz. A maximum frequency of 100 Hz[2] was chosen as this is the approximate equivalent frequency of the Maglev drag peak, and higher frequencies will not result in dramatically higher lift. The data shows that lift comparable to that achieved by electromagnetic induction by motion can be achieved, however at the cost of high power delivery from the magnet current source. Scaling laws can be used to show that a full-scale magnet with eight coils each with $NI = 165{,}000$ (corresponding to $N = 2062$ turns and $I = 80$ A p-p) will generate approximately 1 ton of lift with a lift-to-weight ratio of 0.28 at 100 Hz (*Table 6-4*). With $NI = 495{,}000$ A-turns p-p, a magnet lift-to-weight ratio of ~2.5 will be achieved for a full-scale magnet based on an HTSC coil.

The primary losses will be switching losses in the driving electronics, and AC losses in the levitation and guideway coils. The actual lift-to-weight ration will be less due to the weight of the cooling system, and further study is required to determine the extent of power losses in the HTSC coil due to switching.

Table 6-4. Scaling laws applied to AC lift measurements
(Cryostat weight not included)

	1/5-scale copper, I = 12A, 100 Hz	***1.0 scale HTSC @ 40K, I=80A p-p, 100 Hz***	***1.0 scale HTSC @ 40K, I=240A p-p, 100 Hz***
Ampere turns, p-p	6,600	165,000	495,000
Lift force	17 N	10625 N	95,625 N
Magnet lift/weight ratio	0.05	0.28	2.5

---

[2] If the operating frequency is known and does not change, a series capacitor can be added to resonate with the inductive load to reduce the large reactive voltage required to drive the magnet coil.

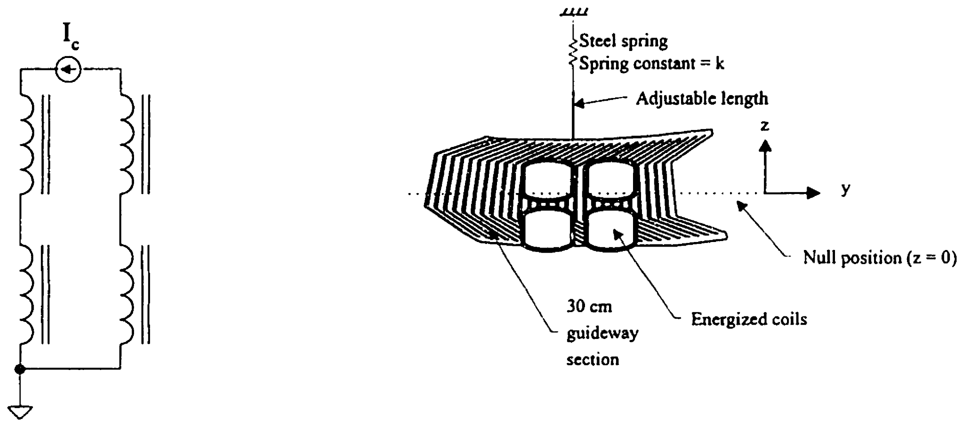

(a) Magnet wiring for AC lift measurements

(b) Test fixture

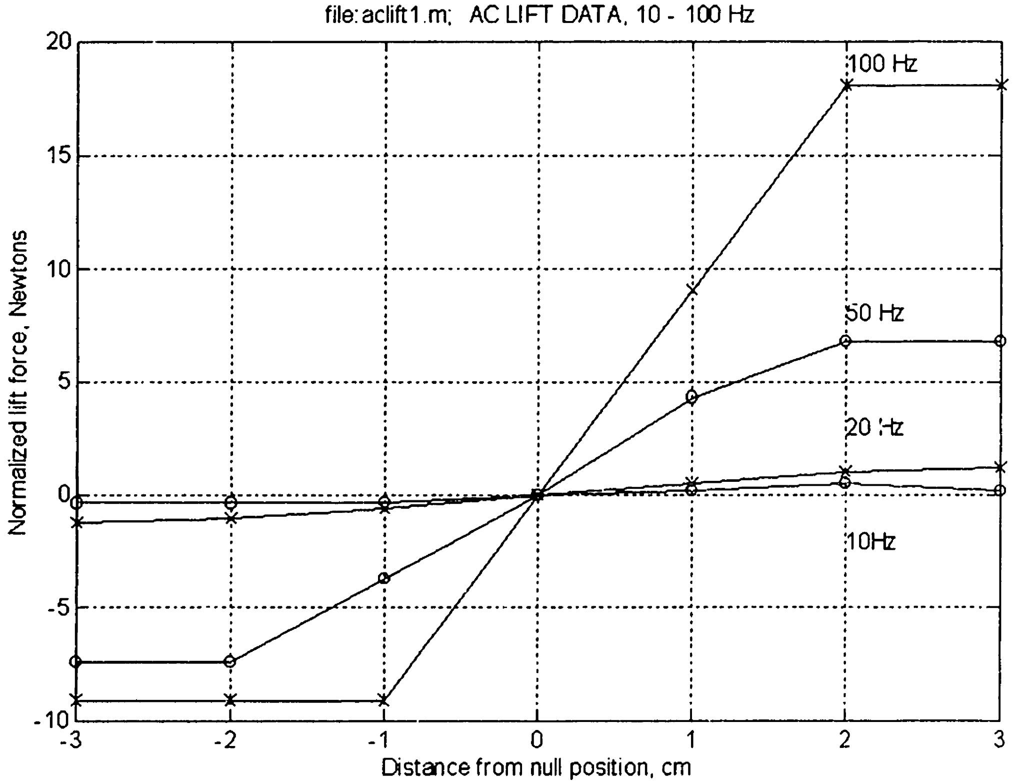

(c) Test results for AC lift

Figure 6-10. AC lift measurements at 10, 20, 50 and 100 Hz

6.4. Tests of Active Secondary Suspension

6.4.1. Differential Lift

In order to test the concept of differential lift, the control current source was connected as in *Figure 6-11a*. Each of the coils was energized with 6 Amps DC by the main power supply V_m. A 12 Amp peak-to-peak square wave driven by the control current source I_c and the resultant measured lift force is shown in *Figure 6-11b*. This test verifies that it is possible to control the vertical force by controlling the magnet nodes shown in the figure. The advantage of driving at these points is that the effective inductance at the coil terminals is decreased by mutual coupling between magnet coils.

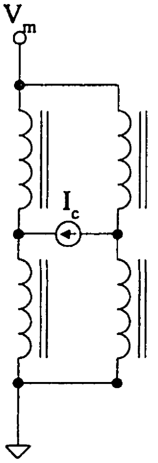

(a) Magnet wiring for differential lift measurement

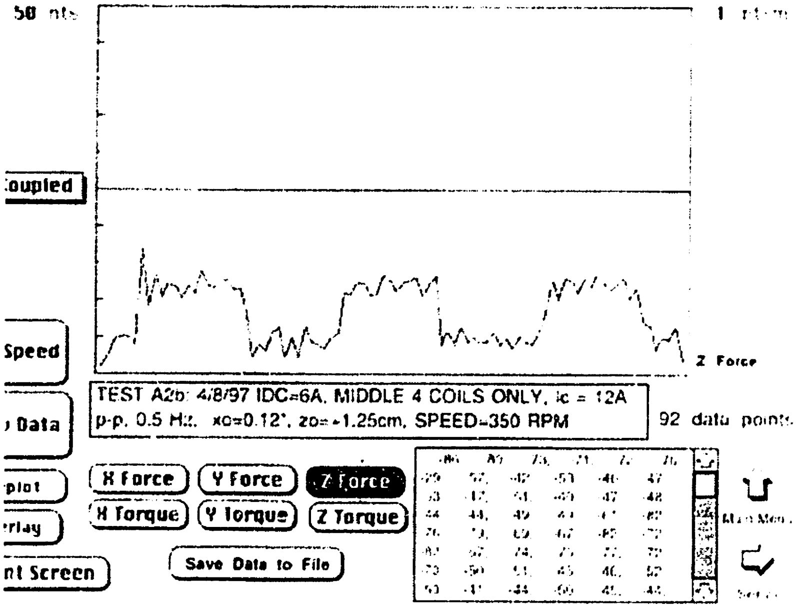

TEST A2b: 4/8/97 IDC=6A, MIDDLE 4 COILS ONLY, Ic = 12A
p-p, 0.5 Hz, xo=0.12", zo=+1.25cm, SPEED=350 RPM

92 data points

(b) Lift measurement, DC current = 6 Amps/coil, control current = 12 Amp square wave at 0.5 Hz

Figure 6-11. Differential lift measurement

In a follow-up experiment, the air bearing was energized and the magnet was allowed to bounce freely under active current excitation. The DC current for these tests was set to 5 Amperes, and a vertical resonant frequency of 1.15 Hz was measured. In *Figure 6-12a*, the differential control terminals are driven with a 12 A p-p, 0.2 Hz current signal. The bottom trace shows little motion, as the magnet is driven well below the resonant frequency.

In *Figure 6-12b*, the magnet is driven with a current at 1.1 Hz, near the measured resonant frequency. As expected, there is significant vertical deflection of the magnet.

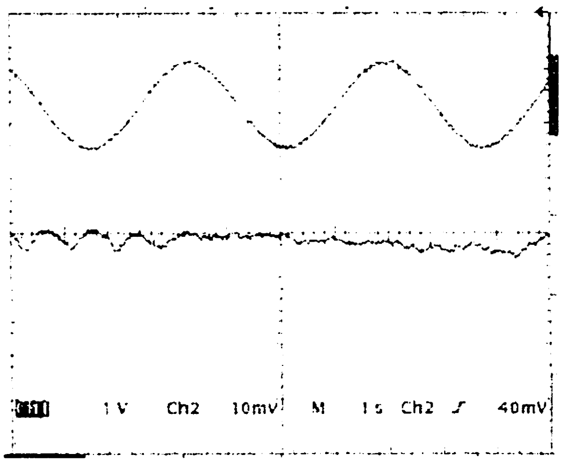

(a) Magnet driven well below resonance
Top trace: magnet current, 5 Amps/div.
Bottom trace: magnet vertical deflection, 1 cm/div.

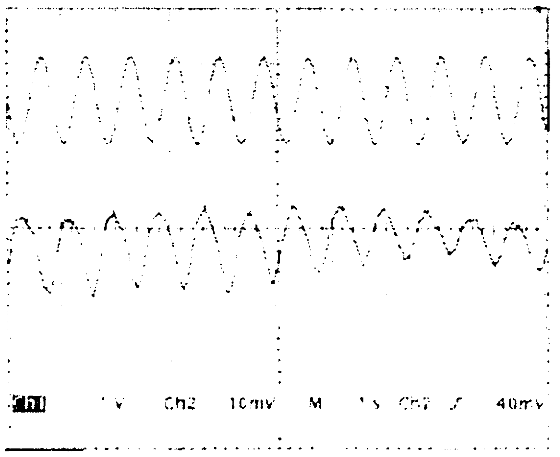

(b) Magnet driven near resonant frequency f = 1.15 Hz
Top trace: magnet current, 5 Amps/div.
Bottom trace: magnet vertical deflection, 1 cm/div.

Figure 6-12. System driven with sinusoidal current at differential drive terminals

6.4.2. Response Using Control System

In the last set of experiments, the control system was energized, with loop parameters set as follows: position gain $K_p = 1$ and velocity gain $K_v = 0.01$. These values were set based on the results of simulations. A full set of schematics for the control system is given in the Appendix (Chapter 8).

With the air bearing energized and the control system deactivated, the vertical magnet position was perturbed approximately +1 centimeter from the equilibrium position and the resultant transient decay of magnet position was observed (*Figure 6-13a*). The oscillatory behavior is at 1.15 Hz with a damping ratio of approximately 1%, corresponding to the expected underdamped EDS response.

A similar experiment was run, but with the control system energized *(Figure 6-13b)*. The resultant magnet vertical position response is much more damped ($\varsigma \sim 40\%$) showing that the control system is operating correctly. Further improvement can be made in the transient response by adjusting the loop parameters.

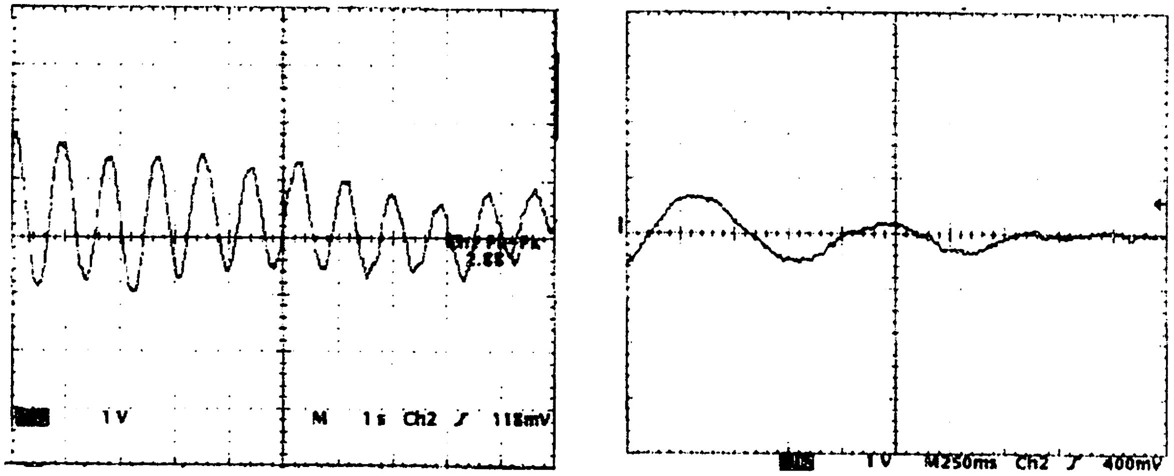

(a) Control system not operating
Initial deflection ~ 1 cm

(b) Active damping enabled
Damping ratio ~40%
(Note change in time scale)

Figure 6-13. Performance of active secondary suspension

For larger initial deflections, limit cycle behavior is possible (*Figure 6-14*) due to slew rate limiting in the current-driving amplifier and saturation limits. This could be avoided by using non-linear control.

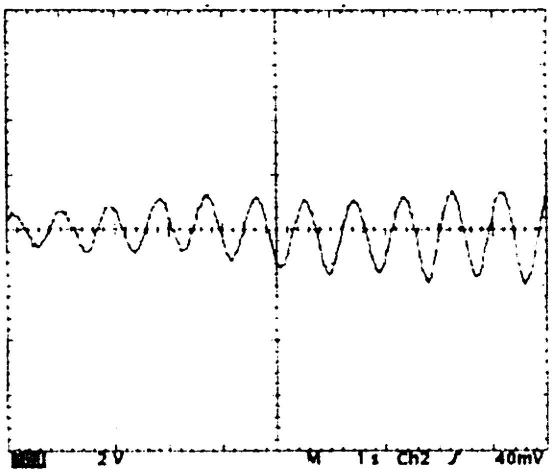

Figure 6-14. Limit cycle

6.5. Summary of Overall Maglev Test Results

Results in this section show:

- That there is good agreement between predictions based on simple circuit models with measurements taken on the test fixture for lift force, drag force, and magnetic drag peak. The models could be improved by doing additional finite-element analyses and extending the 15-coil model so that the infinitely long guideway is better approximated.
- It is possible to generate lift with AC currents using this configuration. The performance of HTSC for AC currents may make AC lift a viable alternative to low-speed mechanical suspensions. However, cooling requirements will probably limit the duration for which AC lift may be operated.
- Vertical force can be controlled by differential control of the magnet currents.
- Vertical position can be actively damped by utilizing an active magnetic secondary suspension. Use of HTSC may overcome the limitations imposed by mechanical secondary suspensions.
- Scaling laws show that the performance of an HTSC-based design at 40K may be comparable to that of low-temperature superconducting designs, with the advantage of less weight and the possibility of using AC lift for low-speed suspension.

7. Conclusions and Recommendations for Future Work

7.1. Overall Results

The successful design and test of a rotating wheel test facility for the study of Maglev electrodynamic suspensions has been demonstrated in this thesis. The 1/5-scale model suspension described is a starting point for the design of a full-scale, high-efficiency EDS suspension based on high temperature superconducting coils. Development of this model suspension has resulted in improvements and inventions for EDS Maglev, including: the use of an iron core for EDS Maglev, with its associated benefits and costs; verification of operation of the "flux-canceling" topology, including tests of lift force, drag force, and guidance force; use of differential control for controlling vertical forces; AC coil currents for the generation of lift at zero train velocity; use of an active secondary magnetic suspension for ride quality control; and development of scaling laws based on circuit models for the prediction of the performance of a full-scale Maglev system.

The test facility operates at linear peripheral speeds exceeding the Maglev drag peak with sufficient safety and mechanical tolerance. At maximum rated test wheel speed, the linear peripheral speed is 84 meters/second, significantly higher than the drag peak velocity. Therefore, both low speed and high speed tests have been done.

In Chapter 3, the mechanical design of the test facility was discussed. Of note is the design of a new low-cost guideway structure which offers good electrical performance. Although much of the guideway conductor design was driven by requirements for high strength to withstand rotating forces, the design could be suitably modified for a full-scale linear guideway where centrifugal force is not an issue.

A one degree-of-freedom air bearing was developed which allows low friction vertical motion of the Maglev magnet. The motivation for use of the air bearing was that EDS suspensions are lightly damped and in order to get meaningful test data the mechanical fixturing must have low damping.

In Chapter 4, the electrical design of the test fixture was described. A V/I curve was generated for a prototype 1/5-scale HTSC coil and it was shown that significantly less power dissipation will result from an HTSC-based design, as compared to copper, even at 77K. Significantly improved performance can result if the HTSC coil is run at intermediate temperatures of 20-40K due to improvements in critical current density.

In Chapter 5, a simple model was developed for the calculation of lift force, drag force, Maglev drag peak velocity, and lift-to-drag ratio. The calculations were based on circuit models which were calculated using geometric approximations to the actual guideway design. The goal was to generate models which offer approximate results, but are simple enough so that they may be used as a design tool for a full-scale system.

A control model was generated which predicts a lightly-damped vertical resonance. Using this model, standard P.I.D. control techniques can be used to place the closed-loop poles at more optimal locations.

Chapter 6 discussed results of the Maglev test program. First, operation of the test wheel was verified. Next, magnetic forces and moments were measured for different speeds and equilibrium magnet positions. Several important results can be inferred from these test results. First, the scale-model guideway geometry operates well with a drag peak velocity of approximately 20-25 meters per second. For a full-scale train, this drag peak velocity will be significantly lower due to scaling laws. Secondly, the guidance force for this design is significant, and it may be possible to use this in lieu of separate guidance coil windings.

A series of scaling laws for EDS Maglev was developed, based on known solutions for the inductance and resistance of simplified geometries. The same scaling laws may be used for evaluation of inductors, motors, and other magnets based on HTSC and copper designs.

AC lift tests show that it is possible to generate lift with the flux-canceling topology by using AC excitation of the magnet coils. This method may be used to achieve zero velocity "lift-off" of the EDS train. Data given for HTSC coils shows that it may be possible to take advantage of the robustness of the coils with regard to AC currents and fields in order to design an efficient zero-velocity suspension. Scaling laws were used to predict the number of Ampere-turns needed for the magnet to levitate its own weight.

Final tests were done using a novel active secondary magnetic suspension. It was shown that it is possible to actively control the magnet position to achieve good ride quality with modest power by using differential current control of the magnets. This opens up the door to the possibility of using HTSC in an active secondary suspension, to take advantage of the robustness of HTSC with regard to AC currents and background fields.

7.2. Recommendations for Future Work

During the design, construction, and testing of the Maglev test fixture it was found that several improvements could be made to the system design. The design of the guideway, which was primarily driven by electrical requirements, was modified to insure additional strength in rotation. For instance, the guideway rim was widened from what was considered to be an optimum electrical design value in order to compensate for tensile forces due to wheel rotation. It was found that the magnetic drag force did not fall off as rapidly as expected above the Maglev drag peak, perhaps to eddy currents in the widened rim.

A more detailed electrodynamic model including the effects of eddy currents in the rim and ladder rungs should be developed. The models used in this thesis were done by approximating field profiles with the aid of finite element analysis. Using a first-harmonic approximation, the excitation due to motion was predicted. This is a crude approximation at best [53] and further work is required to determine the extent of end effects. Further work could be done to further optimize the design with the use of more extensive models.

The effects of material motion are not fully accounted for in the electrodynamic models in Chapter 5. For instance, the models presented do not predict the "wake effect" [144, pp. 362] which is present in magnetic field diffusion problems with material motion.

The guidance force which was measured was larger than expected. It is unclear at this point whether the high guidance force is due to the fundamental operation of the flux-canceling suspension, or if it is a result of higher than expected eddy currents in the guideway rim. Similar circuit modeling could be done to predict performance of the guidance force.

Predictions of AC lift were based on measurements taken using the test wheel. Again, this is an approximation as the two methods of generating levitation force are not identical. Although the results given are useful for scaling test results for a full-scale system, further study is warranted.

The results of the secondary magnetic control system were very promising. Instrumentation and time limitations did not allow extensive testing of the control system. A digital controller would have been more immune to noise and drift and would allow the possibility of nonlinear control. The existing fixture could be retrofitted with the improved control system.

The air bearing worked well, but was difficult to align and was sensitive to test wheel speed, external torques, and preloading. The bearing was constructed using a frame which was used on an earlier project and was not designed with the appropriate tolerance and rigidity. A new bearing frame, made perhaps with welded non-magnetic stainless steel would be more robust.

It would be useful at this time to test the control system using a 1/5-scale HTSC magnet. The high cost of HTSC material (approximately $1000/kilogram at the time of this writing) did not allow testing with full-size coils. Given the promising results in this thesis, it would be useful to build a new cryostat operable in the 20-77K range and Bi-2223 superconducting coils. Using this fixture, power and cooling requirements could be determined using the test fixture and scaling laws could be used to more closely predict the performance of a full-scale magnet. Only time will tell if the cost of the materials will lower enough to make an HTSC suspension viable economically.

7.3. Other Concepts

Other concepts have been considered due to findings in the course of this research. Following is a potpourri of ideas, some of which may be unrealizable. It is offered as grist for thought.

One possible method for testing guideway topologies without a rotating wheel test fixture is the use of a linear section of guideway mounted to a force sensor, and a levitation magnet which is excited with AC current. As has been shown, there is a close correlation between lift forces obtained by regular Maglev interactions, and zero velocity lift using AC excitation of the magnet coils.. Using this test fixture, it would be possible to test multiple guideway geometries without the cost and complexity of a rotating test wheel. For instance, a 4 or 6-layer guideway with thinner sheets could be easily tested. Similar reasoning could be used to test linear motor concepts based on the same 2 level. An interesting idea to help fight scaling laws is to cool the resulting guideway with liquid nitrogen, thereby lowering its resistance and lowering the frequency of the Maglev drag peak.

Another interesting idea is the use of a different iron core and HTSC configuration, as shown in *Figure 7-1*. This "2 sided" suspension would be on one side of the train, with a similar magnet on the other side. The iron core wraps around the guideway. The advantage is that the magnetic gap is smaller than in conventional EDS and significantly less Ampere-turns would be needed for the same field. A modified version our magnet and test wheel could be used to test this concept. For simpler (but cruder) test results, the concept of AC lift could be used to predict lift in the full-scale train.

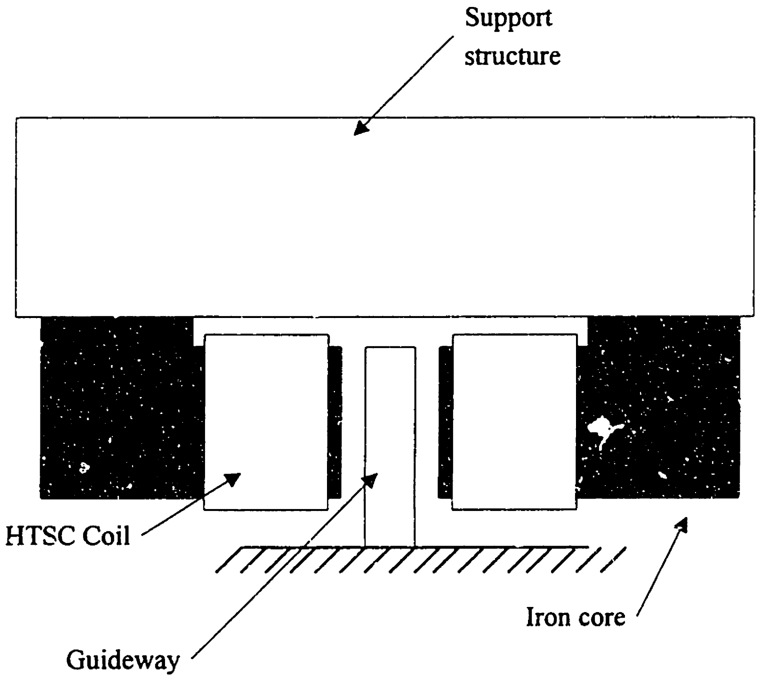

Figure 7-1. "2 Sided" EDS Maglev suspension

Another possibility for improvement of the EDS guideway us the use of powdered magnetic material in the guideway slots to help reduce AC losses. A mixture of ferrite and epoxy could be placed in the guideway slots (*Figure 7-2*); the magnetic material would help to guide the magnetic field into the gaps and away from the ladder rungs, reducing guideway losses due to eddy currents. Since the vertical ladder rungs do not contribute to lift, the lift force will not be significantly modified by the use of ferrite.

Lastly, it may be possible to design practical electromagnetic suspensions (EMS) with high-temperature superconductors. A number of studies have been performed in England [9, 10, 11, 72, 73, 123, 124] which show that it may be possible to build EMS suspensions with significant weight reduction with the use of HTSC. Current state-of-the-art EMS technology in Germany uses copper coils. It remains to be seen whether HTSC with all of its benefits and limitations is an economically-viable alternative. This deserves further study.

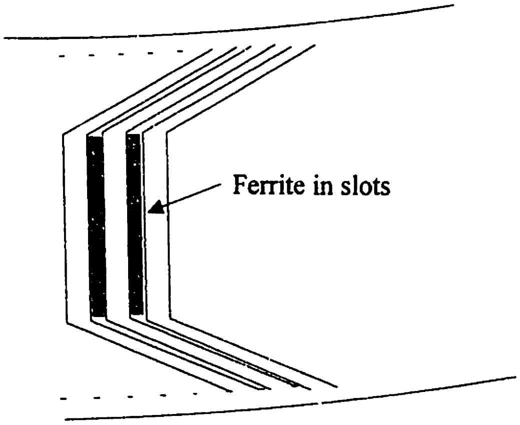

Figure 7-2. Use of ferrite in guideway slots to reduce eddy current losses

8. Appendices

8.1. Schematics

8.1.1. Control Current Source

The control current source is based on a linear H-bridge, and generates a current to a floating load under control of an input analog signal with current transfer ratio 1.0 Amps/Volt. The design specifications of the current source are as follows:

Current transfer ratio	1.0 Amps/Volt
Inductive load	< 0.2 H
Slew rate	> 2000 A/sec at supply voltage of ± 100V
Load current	± 5 Amperes
Small signal bandwidth	> 100 Hz
Circuit protection	Thermal and over-current protection
Cooling	Water cooling, heat sink < 0.05 °C/Watt
Power supply	± 100 Volts

Test results (*Figure 8-2*) show that the bandwidth and slew rate specifications are met driving the inductive load.

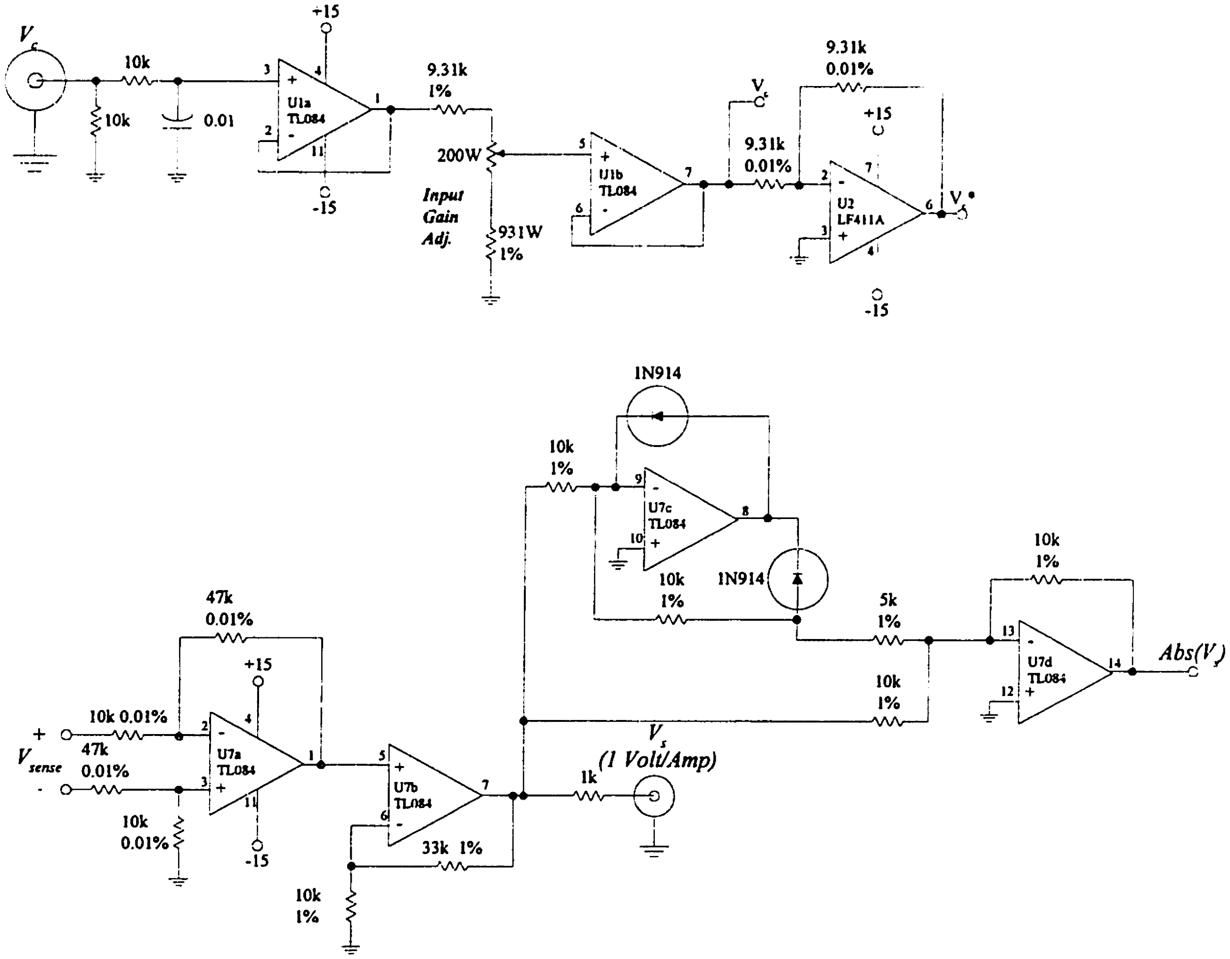

(a) Input buffering and scaling

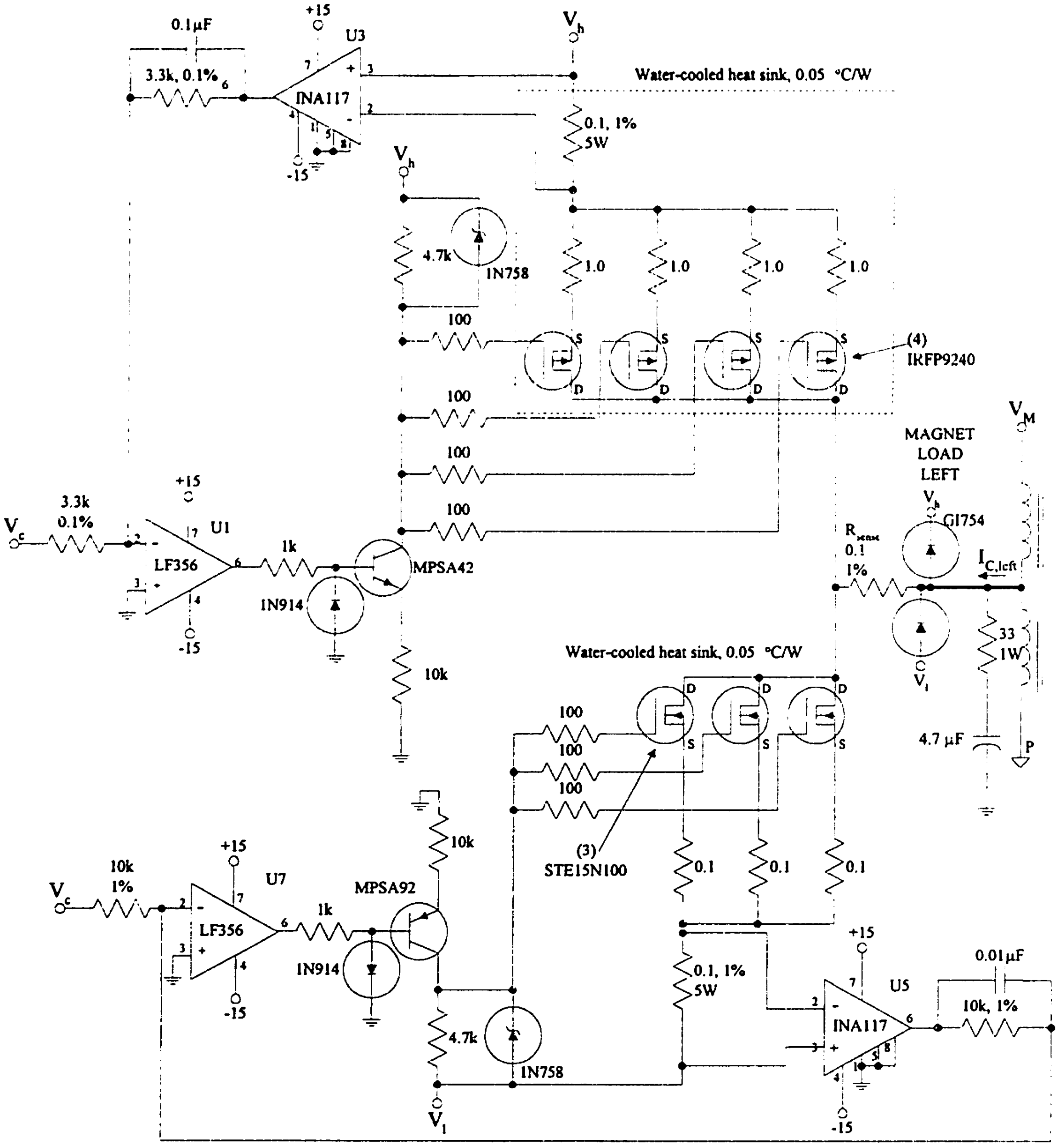

NOTES:

1. analog ground
2. power ground
3. Bypass all op-amp supplies. 0.1 µF

Maglev Current Source (Left Side)
M. Thompson 4/2/97

(b) Left side magnet driver

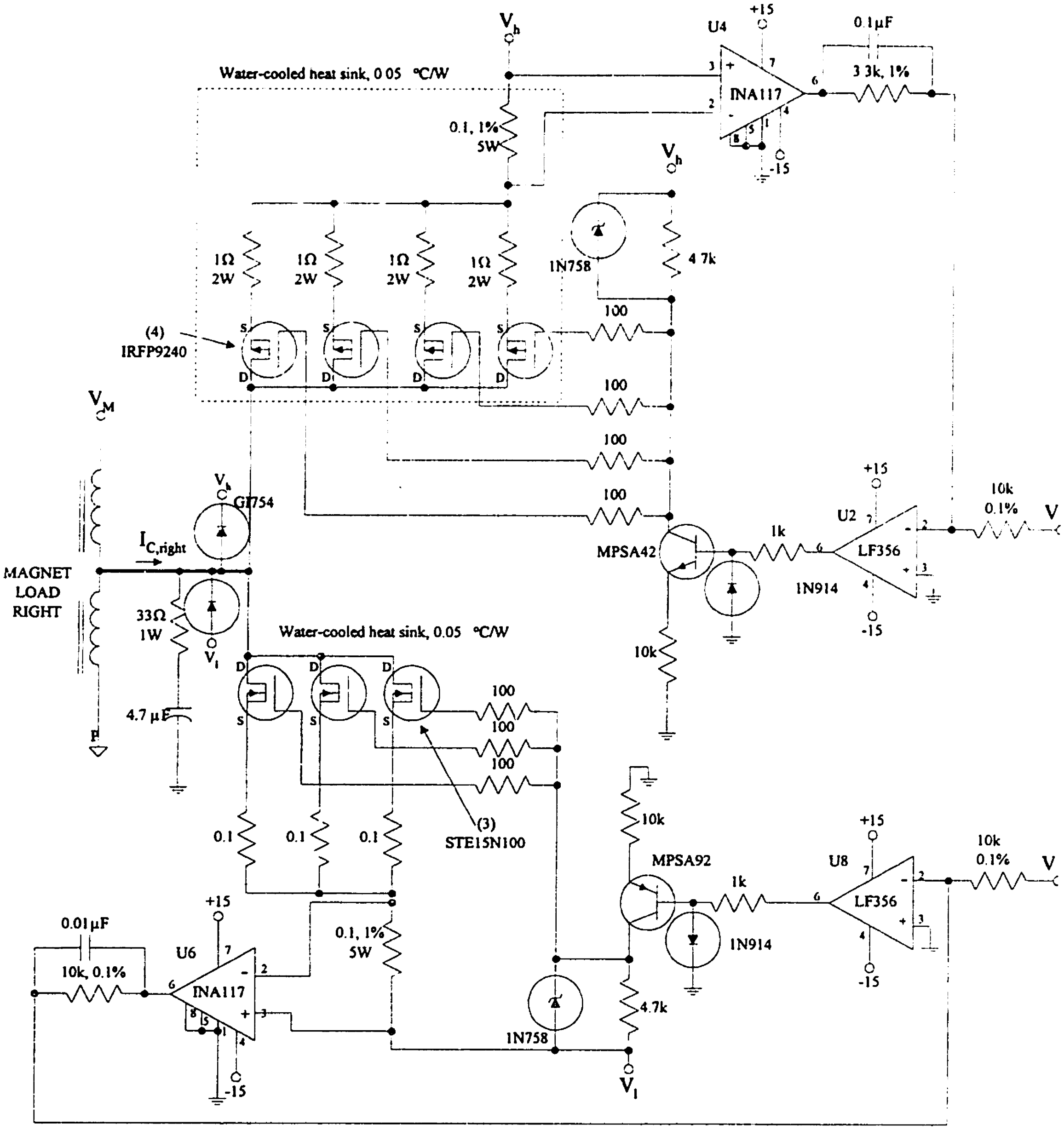

Maglev Current Source (Right Side)
M. Thompson 4/2/97

(c) Right side magnet driver

Figure 8-1. Current source schematics

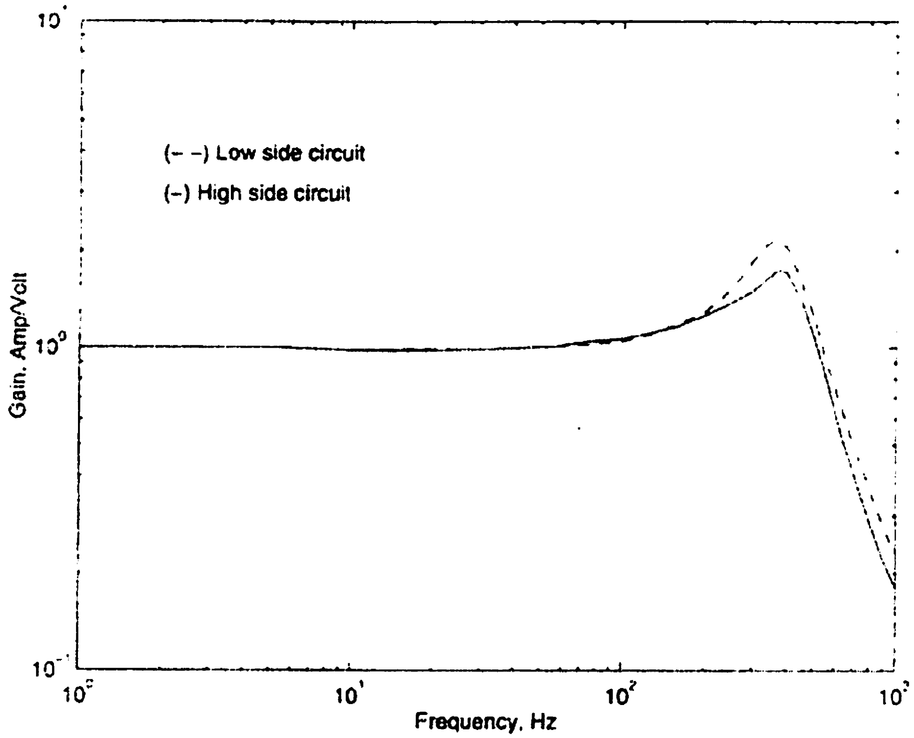

(a) Small signal bandwidth, driving 0.08 Henry load

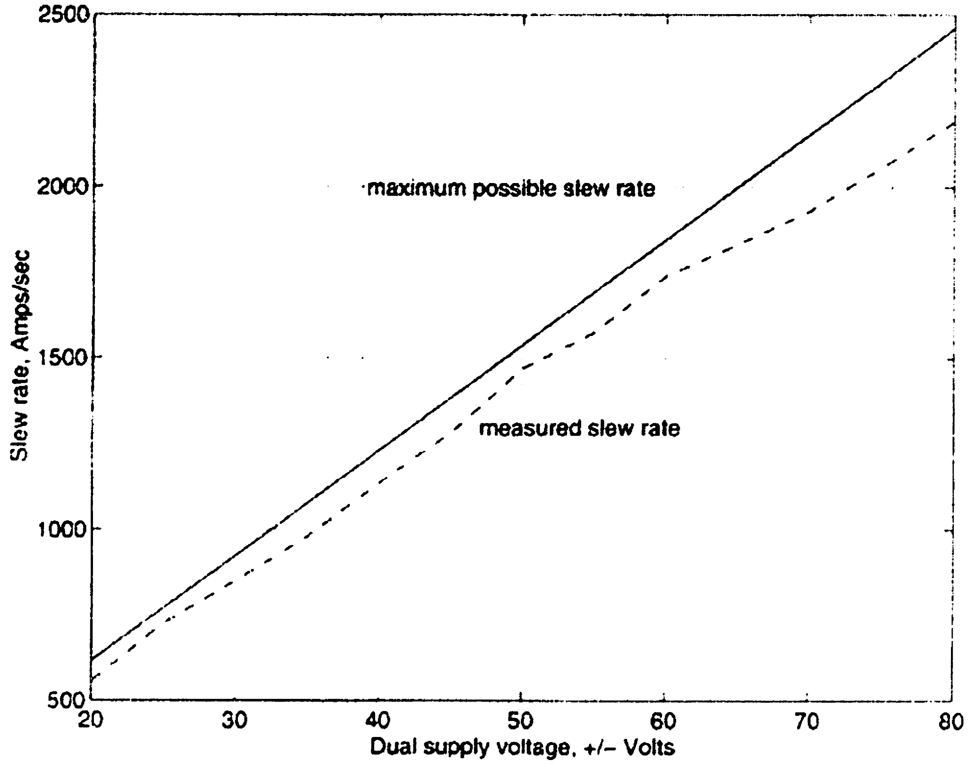

(b) Response driving 0.08 Henry load

Figure 8-2. Control current source, small signal current response

8.1.2. Accelerometer

The accelerometer module PC board (*Figure 8-3*) was mounted to the air bearing in a position optimized to reduce spurious vibrations. An Analog Devices ADXL05 module was used. This device will measure accelerations with full-scale ranges of up to ±5g with a sensitivity of 200 mV/g..The tuning and alignment procedure to compensate for amplifier voltage offsets and to null out the effects of the acceleration due to gravity is as follows:

- On the PC board are 3 switches, labeled SW1, SW2, and SW3, and 3 potentiometers labeled VR1, VR2, and VR3.
- Put all 3 switches in the UP position, and adjust VR3 until the acceleration output V_a is at 0.00 Volts. This adjustment trims the voltage offset of U2.
- Put SW2 in the DOWN position, Adjust VR1 until the the acceleration output V_a is 844 mV DC. Thes sets the sensitivity of the accelerometer to 1 Volt per g of acceleration.
- Put SW1, SW2, and SW3 in the DOWN position. Adjust VR2 until the output V_a is at 0 Volts. This adjustment nulls the effects of the Earth's gravity.
- These adjustments must be made after the accelerometer is mounted to the magnet.

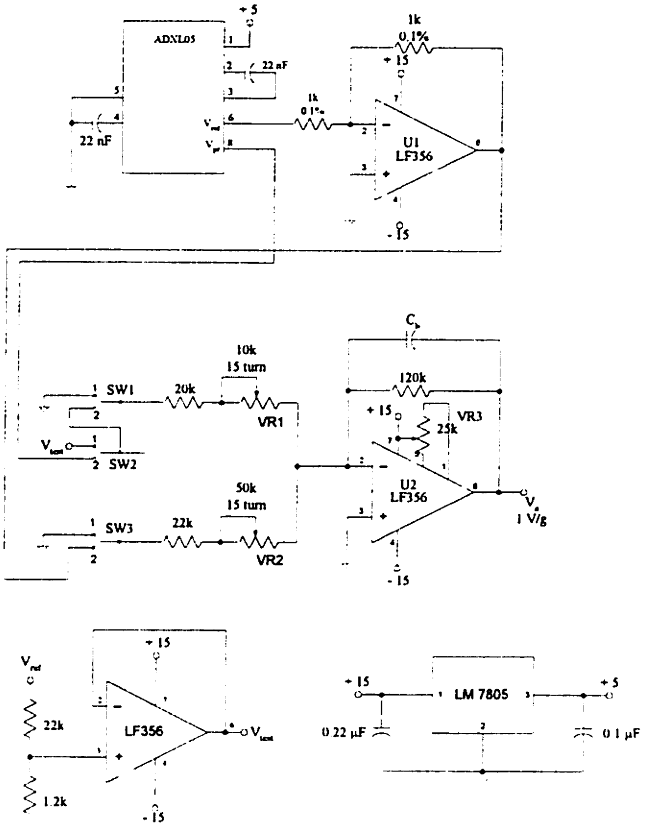

Figure 8-3. Accelerometer module

8.1.3. Position Control System

The position control system is a proportional-integral-derivative (PID) controller. The gains of the forward path gain (K_f) and velocity feedback (K_v) gains are adjustable.

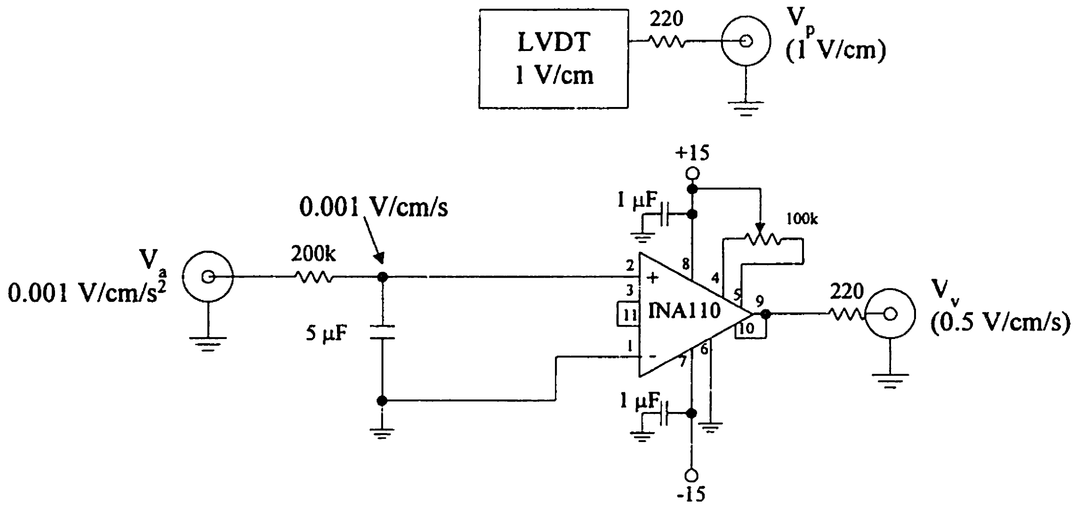

Maglev Position/Velocity/Accel. Interface
M. Thompson 4/2/97

(a) Position and velocity sensing

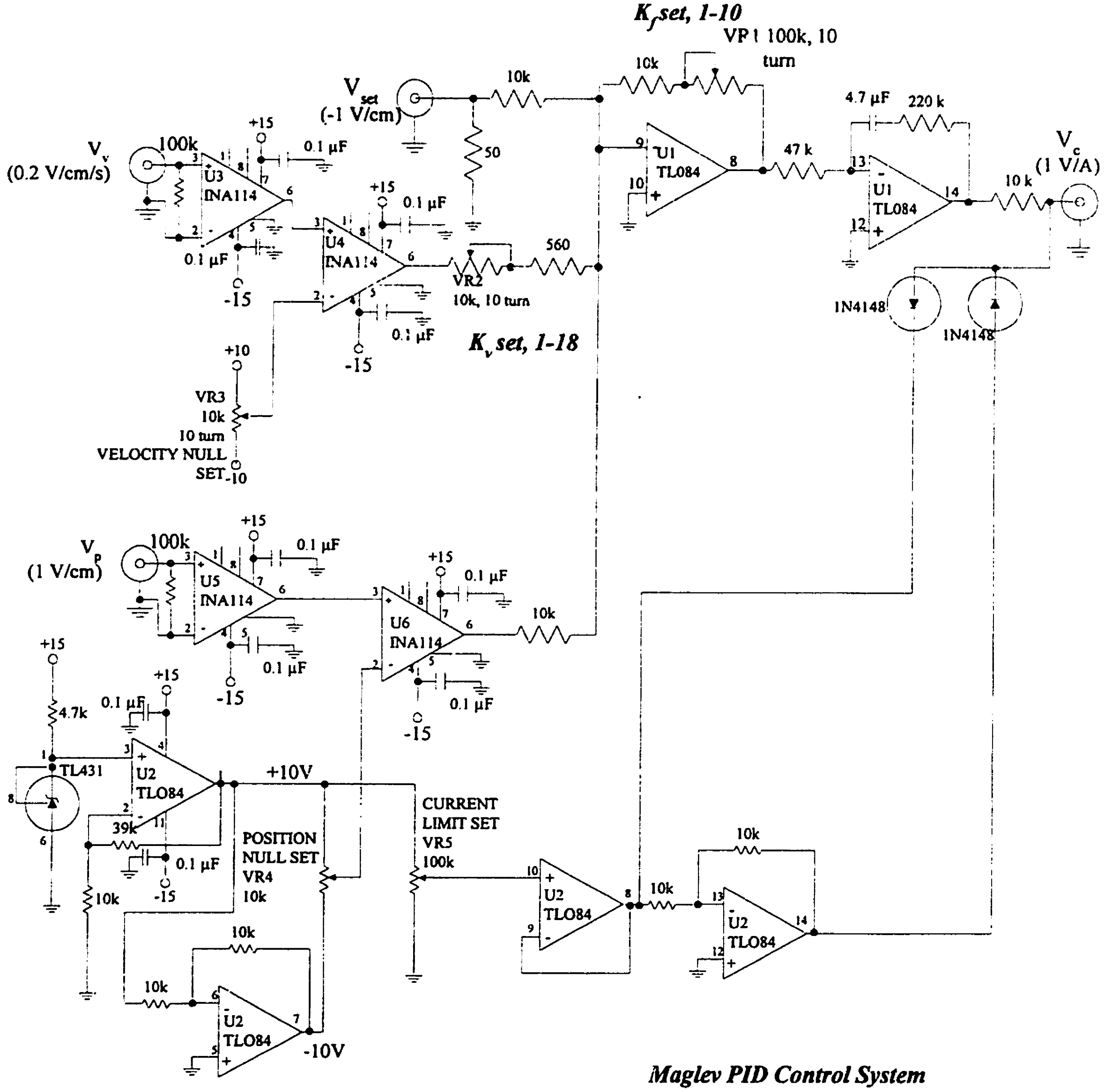

Maglev PID Control System
M. Thompson 4/2/97

(b) P.I.D. Controller

Figure 8-4. Magnet vertical position control system

8.1.4. Liquid Nitrogen Delivery System

The liquid nitrogen delivery system controls the height of nitrogen fluid in the cryostat. A surface mount resistor is mounted in the cryostat, and used as a temperature sensor. A cryogenic valve is used to control the flow into the cryostat.

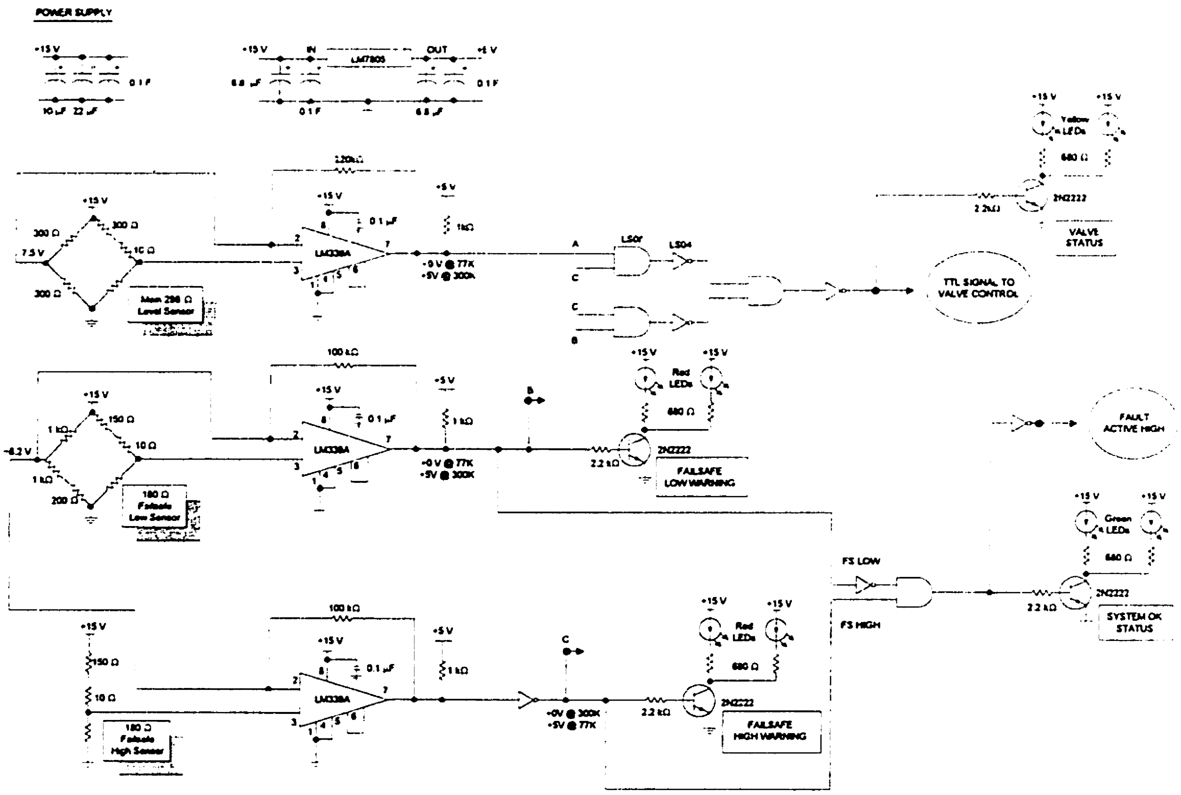

(a) Nitrogen level sensing

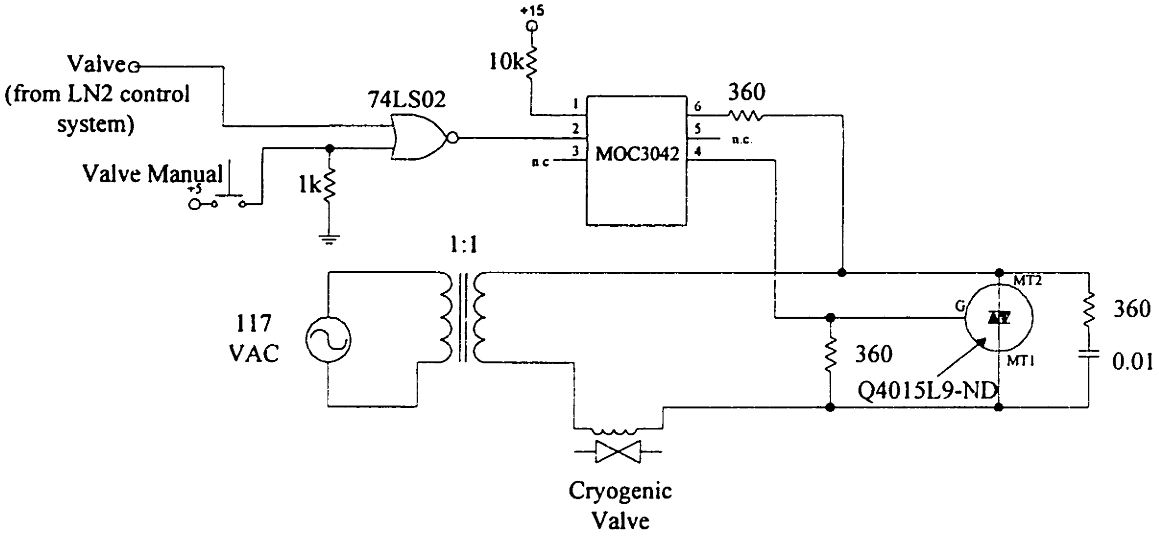

(b) Cryogenic valve control

Figure 8-5. Liquid nitrogen delivery system

8.2. Simple Magnetic Measurements for Calculation of Mutual Inductance

In lieu of finite element analysis, simple measurements were made to determine the guideway mutual inductance coupling coefficients. Two guideway loops were constructed. One loop was broken and terminals for measurements added. This coil was stationary and the other coil was allowed to slide over the top of the first coil. Inductance measurements were made at the terminals using a Hewlett Packard HP4192 impedance analyzer.

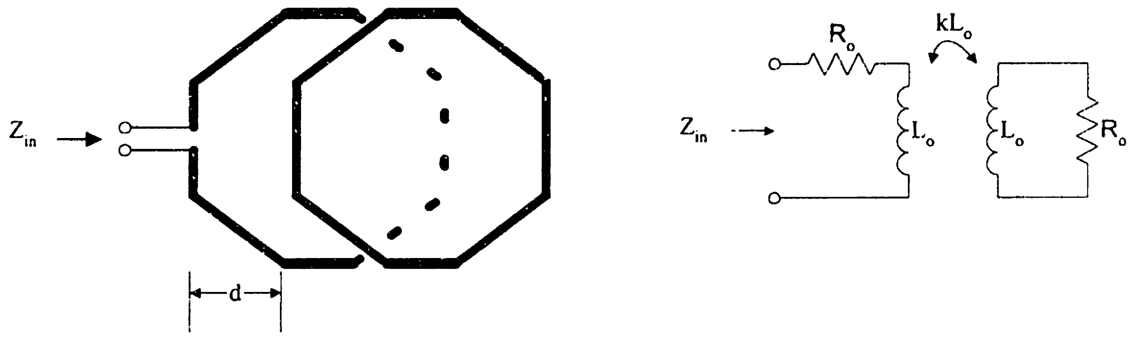

(a) Coil configuration

(b) Equivalent lumped circuit model

Figure 8-6. Experimental method for determining mutual inductance coupling coefficients

The input resistance and inductance at the terminals is [52]:

$$R_{in} = R_o\left[1 + \frac{\omega^2 (kL_o)^2}{R_p^2 + \omega^2 L_o^2}\right]$$

$$L_{in} = L_o\left[1 - \frac{\omega^2 (kL_o)^2}{R_p^2 + \omega^2 L_o^2}\right]$$

[Eq. 8-1]

If the measurement is made at a sufficiently high frequency such that $\omega L_0 >> R_0$, then the inductance measurement reduces to:

$$L_{in} \approx L_o\left[1 - k^2\right]$$

[Eq. 8-2]

For our geometry $L_0 \approx 260$ nH and Ro = 0.0007 Ω resulting in a critical frequency of ~425 Hz. Measurements were made at 10 kHz to achieve sufficient resolution.

8.3. *Material properties*

8.3.1. Material Mechanical Properties

Table 8-1. Maglev test fixture structural material parameters, T = 300 K

Material	Young's modulus, E (GPa)	Shear modulus, G (GPa)	Poisson's ratio, ν	Yield stress, σ_y (MPa) tension/shear	Density, ρ (g/cm^3)
Aluminum					
Alloy 2014	72	27	0.33	410/220	2.8
Alloy 6061	70	26	0.33	260/140	2.71
Brass	105			105/65	8.47
BSCCO	60			55	
Ceramic (alumina Al_2O_3, 99.5% pure)	372	146	0.27		3.89
Copper	118	44	0.35	260/160	8.86
Epoxy	27			~500	
Fiberglass	60	23	0.33	~1000	2.5
G-10 composite	14-18			250	~1.8
Iron					7.86
Phenolic					~1.3
Silver	71			~100	10.5
Solders					
60 Pb/40 Sn	30	19	0.3	50	8.5
96 Sn/6 Ag				100/76	
Steel	207	80	0.30	250/145	7.85
Timber	12				0.55
Titanium	110	41	0.34	~700	4.5

References:

1. D. Aized et. al., "Performance of High Temperature Superconducting Coils in High Background Fields at Different Temperatures."
2. American Society of Mechanical Engineers (ASME), 1980 Flywheel Technology Symposium
3. K. Budinski, Engineering Materials Properties and Selection, 3d ed., Prentice Hall, New Jersey
4. D. Chung, Carbon Fiber Composites, pub. by Butterworth-Heinemann, Boston 1994
5. S. Crandall, N. Dahl, and T. Lardner, An Introduction to the Mechanics of Solids
6. R. Flinn and P. Trojan, Engineering Materials and Their Applications, 3d edition, Houghton Mifflin Co., Boston, 1986 (TA403.F54)
7. Y. Iwasa, Case Studies in Superconducting Magnets, Plenum Press, 1994 (QC761.3.I9)
8. H. Manko, Solders and Soldering, McGraw-Hill, 1979, pp. 147
9. Patriot Plastics Inc., Plastics for Industry
10. M. Schwartz, Composite Materials Handbook, pub. by McGraw-Hill, New York, 1984
11. A. Ugural and S. Fenster, Advanced Strength and Applied Elasticity, 3d edition, PTR Prentice Hall, 1995
12. W. Weaver, S. Timoshenko, and D. Young, Vibration Problems in Engineering, 5th edition, John Wiley and Sons, 1990, pp. 555

Table 8-2. Material properties at liquid nitrogen temperature, T = 77 K

Material	**Young's modulus, E (GPa)**	**C_p, Specific heat, (J/kgK)**	**k, thermal cond. (W/mK)**	**Ultimate yield stress, σ_y (MPa) tension/shear**
Aluminum Alloy 6061	77	500	260	
BSCCO	60			55
Copper (1/2 hard)	77	1000		
Silver	372	146	0.27	

Reference:
Y. Iwasa, Case Studies in Superconducting Magnets, pub. by Plenum Press, New York, 1994

8.3.2. Material Thermal Properties

Table 8-3. Maglev test fixture structural material thermal parameters, 300K

Material	**Thermal cond. k (Watts/m-K)**	**Specific heat C_p (J/kg-K)**	**Coeff. of thermal expansion α ($10^{-6}/^\circ C$)**
Air, still	0.017		
Aluminum	167	900	23
Brass	116		20
BSCCO			
Ceramic (Al_2O_3)	36	880	8
Copper	393	385	17
Epoxy	0.2~1.4		~63
Fiberglass	3.2		~5-10
G-10 composite	3.2		~40
Iron	75	460	
Phenolic		1675	~40
Silver	418	234	19.5
Solder (60 Pb/40 Sn)	240		23
Steel	60	470	12
Styrofoam	~0.02		
Timber	0.15-2		4

References:
1. Burr Brown Corp., Thermal and Electrical Properties of Selected Packaging Materials," applications brief AB-030, 1991
2. Eastop and McConkey, Applied Thermodynamics, 5th ed., Songman Scientific and Technical

8.3.3. Material Electrical Properties

Table 8-4. Maglev test fixture material electrical parameters

Material	**Electrical conductivity** σ **$(\Omega\text{-m})^{-1}$ @ 77K**	**Electrical conductivity** σ **$(\Omega\text{-m})^{-1}$ @ 300K**
Aluminum		3.75×10^7
Brass		1.4×10^7
Copper	4.7×10^8	5.9×10^7
Silver		6.3×10^7
Solder (60 Pb, 40 Sn)		6.7×10^6
Solder (96 Sn, 6 Ag)		7.5×10^6
Steel, M19 transformer		2.5×10^6
Steel, stainless		9×10^5
Steel (1008)		9×10^6

Refererences:

1. Manko, Solders and Soldering, McGraw-Hill, 1979
2. J. Kassakian, M. Schlecht, G. Verghese, *Principles of Power Electronics*, Addison-Wesley 1991, pp. 601

8.3.4. Properties of Liquid Nitrogen

Table 8-5. Properties of Liquid Nitrogen at 1 Atmosphere
[291, pp. 112, 383]

T_s, Boiling Point at 1 Atm	77.4 K
h_L, Latent heat of evaporation	161 J/cm^3
q_{pk}, Peak nucleate boiling heat transfer flux	$\approx$ 15 W/cm^2
ρ_{LN2}, Density	0.8 g/cm^3

8.3.5. Approximate Cost of Materials

Table 8-6. Approximate cost of materials
(Rough estimates only)

Liquid nitrogen	\$0.10/liter
Liquid helium	\$10/liter
Aluminum	\$1/kg
Copper	\$1/kg
Magnet steel	\$0.2 - \$1/kg
Titanium	\$50/kg
Fiberglass	\$0.50/kg
NbTi	\$200/kg
Nb_3Sn	\$1500/kg
BSCCO	\$10000-15000/kg
Ag	\$200/kg

8.4. *MATLAB Scripts for MIT/Maglev Design*

8.4.1. Stresses in Flywheel

```
function wheelstr
% wheelstr.m
%calculates stress in rotating fiberglass disk
% reference, genta pp./ 65

v=0.33;                         % Poisson's ratio
E=50*10^(9);                    % Young's modulus of fiberglass

deflmax=0.001;                  % maximum allowable deflection
R=0.885;                        % outer radius
ri=0.505;                       % inner radius
rho=2250;                       % density of fiberglass
RPM=1000;                       % maximum speed, RPM
omega=RPM*2*pi/60;              % convert speed to radians/sec
r=[0.505 0.525 0.55 0.575 0.6 0.625 0.65 0.675 0.7 0.725 0.75 .775 0.8 .825 0.85 .875 0.885];
count=1;

for I=1:1:17                    % calculate shear and tensile stresses
        chi=r(count)/R;
        beta=ri/R;
        x=rho*(omega^2)*(R^2)*(3+v)/8;
        str(count)=x*(1+(beta^2)-((beta/chi)^2)-(chi^2));
        str(count)=str(count)/(10^6);
        sttheta(count)=x*(1+(beta^2)+((beta/chi)^2)-((1+3*v)/(3+v))*(chi^2));
        sttheta(count)=sttheta(count)/(10^6);
        count=count+1;
end
plot(r,str,'w--',r,sttheta,'w')
title(['Stress in test wheel, due to fiberglass alone, ',num2str(RPM), ' RPM']);
xlabel('Radial distance, meter');
ylabel('Stress, MPa')
text(0.7,2,'Shear stress'),text(0.7,13,'Tensile stress');

***************************************************************
function wheeldef
% wheeldef.m
%calculates deflection of test wheel under load
% reference, Timoshenko pp. 260

v=0.33;         % poisson's ratio
E=50*10^(9);    % young's modulus of fiberglass

F=500;          % maximum load due to sidewall magnet force
deflmax=0.001;
R=1;
b=0.8;

x=12*(1-(v^2))*F*((R^2 - b^2)^2)/(16*pi*E*deflmax*R^2);
```

```
h_meters=exp(0.33333333*log(x)) %take cube root
h_inches=h_meters/0.03937


l=0.6;
b=0.6;
x=4*F*(l^3)/(E*deflmax*b);
t_meters=exp(0.33333*log(x))
t_inches=t_meters/0.03937
```

8.4.2. Resonances in Flywheel

```
function wheelres
% wheelres.m
% Calculates lowest mode resonant frequencies of MIT test wheel
% M. Thompson 8/22/96
% Reference: Timoshenko, Vibration Problems in Engineering

dens_al=2620;            % density of Aluminum
dens_fib=2500;           % density of fiberglass
E=69*10^9;               % Young's modulus for alum.
G=26*10^9;               % Shear modulus for alum.
v=0.33                   % Poisson's ratio for alum.
Raxle=3*2.54/100;
laxle=1;                 % length of aluminum axle
lbend=6*2.54/100;        % length of bending portion of axle
raxle=3*2.54/100;        % radius of axle
rhub=20*2.54/100;        % aluminum hub radius
rwheel=35*2.54/100;      % test wheel radius
t_al=0.75*2.54/100;      % aluninum hub thickness
t_f=0.625*2.54/100;      % fiberglass thickness

%Calculate torsional resonance
        Icopper=8.67                        %inertia of copper ring
        IAl=dens_al*pi*(rhub^3)*t_al        %inertia of alum. hub
        If=dens_fib*pi*t_f*(rwheel^3-rhub^3) %inertia of fiberglass rim
        kt=pi*(Raxle^4)*G/(2*laxle);
        It=Icopper+IAl+If
        w_torsion=sqrt(kt/It);
        f_torsion=w_torsion/(2*pi)

%Calculate bending resonance
        Mcopper=27
        Mal=dens_al*pi*(rhub^2)*t_al
        Mf=dens_fib*pi*t_f*(rwheel^2-rhub^2)
        M=Mcopper+Mal+Mf
        kb=3*E*pi*(raxle^4)/(4*(lbend^3))
        w_bend=sqrt(kb/M);
        f_bend=w_bend/(2*pi)

************************************************
function discvib2
% file: discvib2.m
% calculates resonant frequencies of circular plate vibration
```

```
% for disk flexure vibration of MIT Maglev test wheel
% reference: Blevins, Formulas for Natural Frequency and Mode Shapes, pp. 240
% marc thompson, 4/1/97

table=[5.253 9.084 12.23];
a=0.89;                         % outer radius of wheel
h=((1+0.625)/2)*2.54/100;       % wheel thickness (average)
v=0.315;                        % Poisson's ratio (average)
E=60e9;                         % Young's modulus of fiberglass & Al
rho=3000;                       % average density of wheel kg/m^3
psi=rho*h;                      % mass per unit area

K=sqrt(E*(h^3)/(12*psi*(1-v^2))); % calculate 3 lowest mode frequencies
for i=1:length(table)
        lambdasq=table(i);
        freq=lambdasq*K/(2*pi*a^2)
end
```

8.4.3. HTSC Coil Calculations

```
function htsctemp
%file htsctemp.m
% compilation of various data on HTSC tapes
% plot of normalized critical current vs. operating temperature
% critical current normalized to that at 77K, 0 background field
% references:
% 1. M. Ariante, IEEE Trans. Mag. 32, #4, July 1996
% 2. B. Gamble, IEEE Trans. Mag, vol. 32, #4, July 1996
% 3. P. Haldar, IEEE Trans. Applied SC, 3, 1127-20, 1993
% 4. D. Aized, IEEE Trans. Mag, vol. 30, #4, July 1994
% 5. R. Jenkins, Applied SC Conference, October 1994

T1=[4.2 20 30 40 50 60 70];
Jc1=[7e3 4.5e3 4e3 3.5e3 2.5e3 1.5e3 8.5e2]; Jc1=Jc1./5e2;


T2=[20 35 50 64 77];
Jc2=[1.2e4 1e4 9e3 8e3 3e3]; Jc2=Jc2/3e3;

T3=[4.2 20 40 60 77 90];
Jc3=[1.5e5 1.3e5 9e4 7e4 2e4 6e3]; Jc3=Jc3./2e4

T4=[2 20 77];
Jc4=[22e3 14e3 4e3]; Jc4=Jc4/4e3;

T5=[64 68 73 77];
Ic5=[9 6 4 2]; Ic5=Ic5./2;

plot(T1,Jc1,'w',T2,Jc2,'w',T3,Jc3,'w',T4,Jc4,'w',T5,Ic5,'w')
grid
title('file:htsctemp.m; COMPILATION OF VARIOUS TESTS ON HTSC COILS, 0T BACKGROUND')
xlabel('Temperature, K')
ylabel('Normalized critical current')
```

```
****************************************************
function htscloss
%        file htscloss.m
%        Calculation of HTSC losses in Maglev HTSC Coil
%        References:
%        1. M.N. Wilson, pp. 159
%        2. Y. Iwasa, pp. 264

Jc=6200*100*100;                  % critical current at 77K, 0T
t=0.0002;                         % tape thickness
a=0.0037/2;                       % tape width/2
munot=4*pi*10^(-7);
Bp=munot*Jc*a                     % penetration field
b=0.1                             % AC field amplitude
ehy=(2/(3*munot))*(b^3/Bp)
l=30*2*(0.11+0.07);
Vol=l*a*2*t                       % volume of HTSC
cond=6*10^8;
lp=1;                             % HTSC filament winding pitch
Tcp=cond*munot*(lp^2)/(4*pi^2)    % coupling time constant
K1=(b^2)*Tcp/munot;
f=0:1:200;
for i=1:1:length(f)
        Phys(i)=ehy*f(i)*Vol;
        Peddy(i)=cond*(pi^2)*((a*b)^2)*(f(i)^2)*Vol/6;
        Pcoupling(i)=Vol*K1*(f(i)^2)/(1+(Tcp*f(i))^2);
        Ptotal(i)=Phys(i)+Peddy(i)+Pcoupling(i);

end

plot(f,Phys,'w--',f,Peddy,'w--',f,Ptotal,'w');
grid;
title('file:htscloss.m; PREDICTED AC LOSS IN HTSC COIL, Bo = 0.1 T p-p');
xlabel('Background field frequency, Hz');
ylabel('Total power dissipated, Watts');
text(30,1.5,'Hysteresis loss');
text(70,1.2,'Eddy current loss');
% text(60,0.4, 'Coupling loss');
text(50,4,'Total power')
```

8.4.4. Electrodynamic Models

8.4.4.1. Inductance Calculations

```
function appxcoil
% file appxcoil.m
% find inductance of primative Maglev guideway loop
% based on round disk coil with rectangular cross sectioin

a=5.63                  % mean radius of coil
b=0.093*2.54            % axial thickness
c=0.388                 % radial thickness
```

```
P=table26(c/(2*a))
F=table24((b/c),(c/(2*a)))

L=a*P*F

*********************************************
function F=table43(mu,x)
%values from Grover, Table 43, pp. 179

t43=[0   0 0.1  0.2   0.3   0.4   0.5   0.6   0.7   0.8    0.9    1;...
   0    1 1.3820 1.5311 1.6214 1.6220 1.4851 1.1450 0.5253 -0.4672 -1.9530 -4.053;...
   0.1  1 1.3274 1.4489 1.5139 1.4959 1.3577 1.0557 0.5505 -0.1681 -1.0231 -1.5087;...
   0.2  1 1.2780 1.3760 1.4212 1.3929 1.2641 1.0102 0.5850 0.1178  -0.3874 -0.7240;...
   0.3  1 1.2330 1.3109 1.3411 1.3085 1.1952 0.9897 0.6964 0.3489  0.0137  -0.2378;...
   0.4  1 1.1917 1.2524 1.2717 1.2390 1.1440 0.9836 0.7668 0.5246  0.2914  0.1014;...
   0.5  1 1.1536 1.1997 1.2111 1.1812 1.1052 0.9842 0.8291 0.6585  0.4938  0.3515;...
   0.6  1 1.1155 1.1517 1.1580 1.1328 1.0750 0.9876 0.8787 0.7619  0.6472  0.5441;...
   0.7  1 1.0857 1.1087 1,1112 1.0919 1.0509 0.9917 0.9200 0.8428  0.7665  0.6959;...
   0.8  1 1.0552 1.0692 1.0699 1.0568 1.0313 0.9954 0.9527 0.9070  0.8613  0.8180;...
   0.9  1 1.0267 1.0330 1.0329 1.0265 1.0146 0.9982 0.9790 0.9584  0.9376  0.9176;...
   1.0  1 1    1      1      1      1      1      1      1      1       1]
F=table2(t43,mu,x)

******************************************************
function P=table26(x)
%values from Grover, Table 26, pp. 113

t26=[   0.0 inf;...
        0.01 69.008;...
        0.02 60.299;...
        0.03 55.206;...
        0.04 51.595
        0.05 48.794;...
        0.10 40.111;...
        0.15 35.058;...
        0.20 31.500;...
        0.25 28.767;...
        0.30 26.560;...
        0.35 24.719;...
        0.40 23.150;...
        0.45 21.792;...
        0.50 20.601;...
        0.55 19.550;...
        0.60 18.614;...
        0.65 17.779;...
        0.70 17.032;...
        0.75 16.360;...
        0.80 15.759;...
        0.85 15.220;...
        0.90 14.740;...
        0.95 14.314;...
        1.0  13.939];
P=table1(t26,x)
```

```
*****************************************************
function C=table45(x)
%values from Grover, Table 45, pp. 181
% constants for equal coplanar circular filaments

t45=[   0.1 0.029766;...
        0.2 0.020681;...
        0.3 0.015073;...
        0.4 0.010840;...
        0.5 0.007334;...
        0.6 0.004272;...
        0.7 0.001506;...
        0.8 -0.001045;...
        0.9 -0.003457;...
        1.0 -0.005749;...
        1.111 -0.001886;...
        1.25  -0.001041;...
        1.4286 -0.0006160;...
        1.6667 -0.0003376;...
        2 -0.0001802];

C=table1(t45,x);

*****************************************************
function appxcoil
% calculate approximate mutual inductances of circular filamentary coils
% compare to measurements on actual coils

a=5.63;            % mean radius of coil
d=0.093*2.54;      % axial thickness
d2=5*d;
Lo=291;

ymeas=0:0.85:14*0.85;
Lomeas=259;
Lloaded=[88 125 175 203 224 234 241 247 250 252 255 256 257 258 259];
kmeas=sqrt(1-Lloaded/Lomeas)
rho=0.2*a:a/100:3*a;
for i=1:length(rho)
        x=rho(i)/(2*a);
        C(i)=table45(x);
        %r=sqrt(d^2+rho(i)^2);
        %mu=d/r;
        %kfilm(i)=table43(mu,(r/(2*a)));
        end
k=C.*a.*1000/Lo;
plot(rho,k,'w')
hold;
plot(ymeas,kmeas,'ow')
xlabel('Coil center-center axial distance, cm')
ylabel('Coupling coefficient, k')
title('file:appxmut;  MUTUAL INDUCTANCE CALCULATION')
text(4,0.4,'Measured');
text(4,-0.15,'Calculated, co-planar filamentary approximation')
```

```
grid

*****************************************************
function magloop
% plots mutual inductance of small guideway loops vs. axial spacing
% analytic results based on ANSOFT 3D finite element analysis

y=[0 8.5 17 25.5 34 42.5 51 59.5 68 76.5 85 93.5 102 110.5 119 127.5 136];
M=[160 112 78 57 42 31 21 11.2 1.32 -11.8 -18.2 -9.6 -6.14 -4.35 -3.26 -2.55 -2.03];
plot(y,M,'w');                     % calculates small loop
grid
xlabel('Axis-axis spacing, mm')
ylabel('Mutual inductance M12, nH')

% using filamentary approximate methods in F.W. Grover, pp. 177
d=0.093*2.54/100;                  % layer-layer spacing, meters
a=0.0425;                          % radius of single loop
A=d/(2*a)
f=0.0375                           % value extrapolated from Grover Table 16, pp. 83

Mo=f*a*100*1000                              % M12 with 2 coils coaxial, in nanoHenries
r=sqrt(d^2 + ((0.001.*y).*(0.001.*y)))      % r in Grover, pp. 177
B=r./(2*a)                                   %
mu=d./r                                      % cos(theta)

y2=[0 8.5 17 25.5 34 42.5 51 59.5 68];
f2=[1 1.25 1.4489 1.5 1.55 1.5 1.145 .5253 -.4672];
M2=Mo.*f2;
hold;
plot(y2,M2)
```

8.4.4.2. Drag Peak, Critical Speeds, and Force Calculation

```
function drag7
% file:drag7.m
% calc. of loop currents, forces, modal shapes
% at z = +1.45 cm, above null position

Lo=286e-9;               % self inductance of maglev loop
Ro=0.00072548;           % self-resistance of coil loop
cond=5.9e7;              % conductivity of copper
Rmmax=2*0.04/(cond*0.2*0.0254*2*0.093*0.0254);          % maximum mutual inductance
Rmmax=Rmmax/Ro;

p=0.126;                 % pole pitch
Bo=0.08;                 % magnetic field at center of pole pitch
Az=1.45/4;               % vertical distance from null position (normalized)
ncoils=15;               % number of coils modeled
n=1:1:ncoils;

%%%% Fill in the inductance matrix
k12=0.7193;k13=0.5695;k14=0.4650;k15=0.3676;k16=0.3107;
k17=0.2636;k18=0.2152;k19=0.1864;
k110=0.1644;k111=0.1243;k112=0.08;k113=0.04;k114=-0.04;k115=0;
```

```
% resistance matrix computations
R12=Rmmax;R13=Rmmax*(5/6);R14=Rmmax*(4/6);R15=Rmmax*(3/6);R16=Rmmax*(2/6);
R17=Rmmax*(1/6);R18=0.00;R19=0.00;
R110=0.00;R111=0.00;R112=0.00;R113=0;R114=0;R115=0;

L=[    1  k12 k13 k14 k15 k16 k17 k18 k19 k110 k111 k112 k113 k114 k115;...
       k12 1  k12 k13 k14 k15 k16 k17 k18 k19 k110 k111 k112 k113 k114;...
       k13 k12 1  k12 k13 k14 k15 k16 k17 k18 k19 k110 k111 k112 k113;...
       k14 k13 k12 1  k12 k13 k14 k15 k16 k17 k18 k19 k110 k111 k112;...
       k15 k14 k13 k12 1  k12 k13 k14 k15 k16 k17 k18 k19 k110 k111;...
       k16 k15 k14 k13 k12 1  k12 k13 k14 k15 k16 k17 k18 k19 k110;...
       k17 k16 k15 k14 k13 k12 1  k12 k13 k14 k15 k16 k17 k18 k19;...
       k18 k17 k16 k15 k14 k13 k12 1  k12 k13 k14 k15 k16 k17 k18;...
       k19 k18 k17 k16 k15 k14 k13 k12 1  k12 k13 k14 k15 k16 k17;...
       k110 k19 k18 k17 k16 k15 k14 k13 k12 1  k12 k13 k14 k15 k16;...
       k111 k110 k19 k18 k17 k16 k15 k14 k13 k12 1  k12 k13 k14 k15;...
       k112 k111 k110 k19 k18 k17 k16 k15 k14 k13 k12 1  k12 k13 k14;...
       k113 k112 k111 k110 k19 k18 k17 k16 k15 k14 k13 k12 1  k12 k13;...
       k114 k113 k112 k111 k110 k19 k18 k17 k16 k15 k14 k13 k12 1  k12;...
       k115 k114 k113 k112 k111 k110 k19 k18 k17 k16 k15 k14 k13 k12 1 ];
L=L.*Lo;

R=[    1  R12 R13 R14 R15 R16 R17 R18 R19 R110 R111 R112 R113 R114 R115;...
       R12 1  R12 R13 R14 R15 R16 R17 R18 R19 R110 R111 R112 R113 R114;...
       R13 R12 1  R12 R13 R14 R15 R16 R17 R18 R19 R110 R111 R112 R113;...
       R14 R13 R12 1  R12 R13 R14 R15 R16 R17 R18 R19 R110 R111 R112;...
       R15 R14 R13 R12 1  R12 R13 R14 R15 R16 R17 R18 R19 R110 R111;...
       R16 R15 R14 R13 R12 1  R12 R13 R14 R15 R16 R17 R18 R19 R110;...
       R17 R16 R15 R14 R13 R12 1  R12 R13 R14 R15 R16 R17 R18 R19;...
       R18 R17 R16 R15 R14 R13 R12 1  R12 R13 R14 R15 R16 R17 R18;...
       R19 R18 R17 R16 R15 R14 R13 R12 1  R12 R13 R14 R15 R16 R17;...
       R110 R19 R18 R17 R16 R15 R14 R13 R12 1  R12 R13 R14 R15 R16;...
       R111 R110 R19 R18 R17 R16 R15 R14 R13 R12 1  R12 R13 R14 R15;...
       R112 R111 R110 R19 R18 R17 R16 R15 R14 R13 R12 1  R12 R13 R14;...
       R113 R112 R111 R110 R19 R18 R17 R16 R15 R14 R13 R12 1  R12 R13;...
       R114 R113 R112 R111 R110 R19 R18 R17 R16 R15 R14 R13 R12 1  R12;...
       R115 R114 R113 R112 R111 R110 R19 R18 R17 R16 R15 R14 R13 R12 1];
R=R.*Ro;

% calculate natural frequencies, critical velocities, and mode shapes
wcrits=eig(R/L)
fcrits=wcrits./(2*pi)
vcrits=2*p*fcrits
RPM=vcrits*60/(2*pi*0.8)                    % test wheel speed, RPM
[Eigenvect,D]=eig(R/L)
plot((Eigenvect(:,1)./max(Eigenvect(:,1))-1),'w');hold
plot((0.5).*Eigenvect(:,2)./max(Eigenvect(:,2)),'w--')
title('Eigenvectors of 2 lowest-frequency natural modes')
text(7,0.7,'f = 96.5 Hz, v = 24.3 m/s');
text(8,0,'f = 174 Hz, v = 43.8 m/s');
xlabel('Coil #')
figure;
```

```
f=0:5:300;                                    % excitation frequencies
velocity=2*p.*f;                              % velocity
v1= [8.02 7.8 7.2 6.3 5 3.5 1.8 0 -1.8 -3.5 -5 -6.3 -7.2 -7.8 -8.02]';      % excitation mode shape, cosine
v2= [0 1.8 3.5 5 6.3 7.2 7.8 8.02 7.8 7.2 6.3 5 3.5 1.8 0]';                % sine shape
field1=(4/pi)*Bo.*cos(0.009*pi.*n./p);
field2=(4/pi)*Bo.*sin(0.009*pi.*n./p);
B1=Bo.*v1;B2=Bo.*v2;
v1=v1./8.02; v2=v2./8.02;
excshape1=v1; excshape2=v2;
LoopArea=0.0099675;
v1=((4/pi)*LoopArea*Bo*Az).*v1;  v2=((4/pi)*LoopArea*Bo*Az).*v2;

% COMPUTE LOOP CURRENTS
for i=1:length(f);
        w=2*pi*f(i);                % radians
        Zl=(j*w).*L;                % inductive reactance
        Z=Zl + R;                   % impedance matrix
        I1(:,i)=(j*w).*inv(Z)*v1;
        I2(:,i)=(j*w).*inv(Z)*v2;
end

% COMPUTE TOTAL DRAG FORCE
for i=1:length(f);
        P1=0; P2=0;
        for j=1:ncoils
                Imag1=sqrt( (real(I1(j,i))).^2+ (imag(I1(j,i))).^2); % magnitude of I
                Imag2=sqrt( (real(I2(j,i))).^2+ (imag(I2(j,i))).^2);
                Power1=(Ro/2).*Imag1.*Imag1;    % compute power in ladder
                Power2=(Ro/2).*Imag2.*Imag2;
                Prung1=(0.07*Ro/2).*Imag1.*Imag1; % compute approx. power in outer rung
                Prung2=(0.07*Ro/2).*Imag2.*Imag2;
                P1=P1+Power1+Prung1;
                P2=P2+Power2+Prung2;
        end
        fdrag1(i)=4*P1/velocity(i);
        fdrag2(i)=4*P2/velocity(i);
end

% COMPUTE TOTAL LIFT FORCE
for i=1:length(f)
        L1=0; L2=0;
        for j=1:ncoils
                Ireal1=real(I1(j,i));
                Ireal2=real(I2(j,i));
                Lift1=0.5*Ireal1*0.126*field1(j)*2;
                Lift2=0.5*Ireal2*0.126*field2(j)*2;
                L1=L1+Lift1;
                L2=L2+Lift2;
        end
        flift1(i)=4*L1;
        flift2(i)=4*L2;
end

% TEST DATA FROM MEASUREMENTS
```

```
fymax=[0 8.75 14.5 18.75 20 20 20 18.75 18 16.25 16.5 16.25]; %measured drag
fzmax=[0 3.75 12.5 20 34.4 43.75 50 57 60 62.5 65 68.75];% measured lift force
s=[0 50 100 150 200 250 300 350 400 450 500 600]; % wheel speed (RPM)
vm=s.*0.084;                                                   %velocity (m/sec)

% PLOT

subplot(2,2,1);plot(excshape1,'w');title('Excitation mode shape')
xlabel('Coil #')
subplot(2,2,2);plot(n,real(I1(:,20)),'w',n,real(I1(:,40)),'w--');
title('Real part of loop currents at 100 and 200 Hz')
ylabel('Current, Amps')
xlabel('Coil #')
subplot(2,2,3);plot(velocity,flift1,'w',vm,fzmax,'wo')
title('Lift force')
xlabel('Velocity, m/sec');ylabel('fz, Newtons');
subplot(2,2,4);plot(velocity,fdrag1,'w',vm,fymax,'wo')
title('Drag force')
xlabel('Velocity, m/sec');ylabel('fy, Newtons');

figure;
subplot(2,2,1);plot(excshape2,'w');title('Excitation mode shape')
xlabel('Coil #')
subplot(2,2,2);plot(n,real(I2(:,20)),'w',n,real(I2(:,40)),'w--');
title('Real part of loop currents at 100 and 200 Hz')
ylabel('Current, Amps')
xlabel('Coil #')
subplot(2,2,3);plot(velocity,flift2,'w',vm,fzmax,'wo')
title('Lift force')
xlabel('Velocity, m/sec');ylabel('fz, Newtons');
subplot(2,2,4);plot(velocity,fdrag2,'w',vm,fymax,'wo')
title('Drag force')
xlabel('Velocity, m/sec');ylabel('fy, Newtons');
```

8.4.5. Test Results

```
function runout
% file runout.m
% Maglev test wheel runout measurement
% Marc Thompson 3/11/97

loc=1:1:20;            % # points along circumference
xo=0.17;               % average distance, magnet-copper (inches)

% Capacitance sensor measurements, inches
s1=[.183 .196 .205 .183 .194 .187 .191 .187 .188 .173 .165 .167 .188 .195 .183 .182 .197 .181 .148 .135];
s2=[.197 .193 .193 .194 .191 .183 .180 .167 .169 .186 .198 .190 .186 .186 .176 .145 .151 .158 .205 .199];
s1=s1-xo;              % normalize spacing
s1=s1.*25.4;           % convert spacing to millimeters
s2=s2-xo;
s2=s2.*25.4;

plot(loc./20,s1,'w')
```

```
title('file:runout.m; Test wheel runout test, 3/11/97');
xlabel('Wheel position around circumference')
ylabel('Sensor-copper distance, millimeters')
grid

**********************************************************
function mar11b
% file mar11b.m
% data taken on maglev test fixture, 3/11/97

zo=-0.06;                        % distance from null position (meter)
xo=0.17*2.54/100;                % distance, magnet-copper (meter)
Io=5;                            % 5 Amps/coil
sf=0.556;                        % data scale factor
s=[0 50 100 150 200 250 300 350 400 450 500 600]; % wheel speed (RPM)
s=s.*0.084

fzmax=[0 1.25 4.00 7.50 11.25 15.00 17.50 17.50 20.00 21.00 20.00 21.50];% measured lift force (max)
fymax=[0 1.00 2.50 3.00 3.75  4.5   4.00  4.00  4.40  4.40  4.40  5.25]; %measured drag



plot(s,fzmax,'w',s,fymax,'w--')
hold;
plot(s,fzmax,'wx',s,fymax,'wo')
axis([0 60 0 25])
grid
xlabel('Linear velocity, m/sec.')
ylabel('Force, Newtons')
Title('file:mar11b.m; FORCE MEASUREMENTS: Maglev test 3/11/97; I=5A;zo=-0.6cm;xo=0.4 cm')
text(500*0.084,22,'Lift');text(500*0.084,7,'Drag')

figure
LD=fzmax./fymax;
plot(s,LD,'w',s,LD,'wx')
grid
Title('LIFT/DRAG CALCULATION: Maglev test 3/11/97; I=5A;zo=-0.6cm;xo=0.4 cm')
xlabel('Linear velocity, m/sec.')
ylabel('Lift/drag ratio')
figure

k=-fzmax./zo;
plot(s,k,'w',s,k,'wx')
Title('file:mar11b.m; SPRING CONSTANT CALCULATION: Maglev test 3/11/97; I=5A;zo=-
0.6cm;xo=0.4 cm')
xlabel('Linear velocity, m/sec.')
ylabel('Linear spring constant, N/cm')
grid

figure;
M=60;                            %MAGNET TOTAL MASS
wo=10*sqrt(k./M);
fo=wo/(2*pi);
plot(s,fo,'w',s,fo,'wx')
```

```
Title('NATURAL FREQUENCY CALCULATION:Maglev test 3/11/97; I=5A;zo=-0.6cm;xo=0.4 cm')
xlabel('Linear velocity, m/sec.')
ylabel('Magnet natural frequency, Hz')
grid
*************************************************************
 function mar12a
 % file mar12a.m
 % data taken on maglev test fixture, 3/12/97

zo=+ 1.25;                    % distance from null position (meter)
xo=0.17*2.54/100;             % distance, magnet-copper (meter)
Io=5;                         % 5 Amps/coil
sf=0.556;                     % data scale factor
s=[0 50 100 150 200 250 300 350 400 450 500 600]; % wheel speed (RPM)
speed=0.084*s;

fzmax=[0 3.75 12.5 20 34.4 43.75 50 57 60 62.5 65 68.75];% measured lift force (max)
fzmax=-1.*fzmax;
fymax=[0 8.75 14.5 18.75 20 20 20 18.75 18 16.25 16.5 16.25]; %measured drag
fx=[0 5 10 15.5 25 28.1 31.25 37.5 40.6 40.6 43.75 43.75]; %guidance force


plot(speed,fzmax,'w',speed,fymax,'w--',speed,fzmax,'wx',speed,fymax,'wo')
hold;
plot(speed,fx,'w--',speed,fx,'wo')
axis([0 50 -75 50])
grid
xlabel('Peripheral speed, meters/sec')
ylabel('Force, Newtons')
text(41.7,-60,'Lift');text(41.7,48,'Guidance');text(41.7,20,'Drag')
Title('file:mar12a.m; FORCE MEASUREMENTS: Maglev test 3/12/97; I=5A;zo=+1.25cm;xo=0.4 cm')

figure
LD=abs(fzmax./fymax);
plot(speed,LD,'w',speed,LD,'wx')
grid
Title('file:mar12a; LIFT/DRAG CALCULATION: Maglev test 3/12/97; I=5A;zo=+1.25cm;xo=0.4 cm')
xlabel('Peripheral speed, meters/sec')
ylabel('Lift/drag ratio')
figure

k=-fzmax./zo;
plot(s,k,'w',s,k,'wx')
Title('SPRING CONSTANT CALCULATION: Maglev test 3/12/97; I=5A;zo=+1.25cm;xo=0.4 cm')
xlabel('Wheel speed, RPM')
ylabel('Linear spring constant, N/cm')
grid

figure;
M=60;                         %MAGNET TOTAL MASS
wo=10*sqrt(k./M);
fo=wo/(2*pi);
plot(s,fo,'w',s,fo,'wx')
Title('NATURAL FREQUENCY CALCULATION:Maglev test 3/12/97; I=5A;zo=+1.25cm;xo=0.4 cm')
```

```
xlabel('Wheel speed, RPM')
ylabel('Magnet natural frequency, Hz')
grid

************************************************************
function mar14a
% file mar14a.m
% tests on March 14, magnet near null position

zo=+ 0.066;                     % distance from null position (meter)
xo=0.17*2.54/100;               % distance, magnet-copper (meter)
Io=5;                           % 5 Amps/coil
sf=0.556;                       % data scale factor
s=[0 50 100 150 200 250 300 350 400 450 500 600]; % wheel speed (RPM)
s=s.*0.084;

fx=[0 0 0.5 0.6 0.75 1.25 1.5 1.5 1.8 2.5 1.6 3.0];            %guidance
fy=[0 0.5 2.0 2.25 2.5 3.12 3.125 3.75 4.0 4.4 5 3.75];         %drag
fz=[0 -1.0 -3.125 -5.6 -8.0 -10.5 -11.5 -12.5 -14 -15 -15 -16]; % lift

plot(s,fz,'w',s,fy,'w--',s,fz,'wx',s,fy,'wo')
hold;
plot(s,fx,'w--',s,fx,'wo')
axis([0 600*0.084 -20 10])
grid
xlabel('Linear velocity, m/sec.')
ylabel('Force, Newtons')
text(500*0.084,-15,'Lift');text(500*0.084,2,'Guidance');text(500*0.084,6,'Drag')
Title('file:mar14a.m; FORCE MEASUREMENTS: Maglev test 3/14/97; I=5A;zo=+0.07cm;xo=0.4 cm')

figure
LD=abs(fz./fy);
plot(s,LD,'w',s,LD,'wx')
grid
Title('file:mar14a.m; LIFT/DRAG CALCULATION: Maglev test 3/14/97; I=5A;zo=+0.07cm;xo=0.4 cm')
xlabel('Linear velocity, m/sec.')
ylabel('Lift/drag ratio')

************************************************************
function mspring
% mspring.m
% calculation of kmag from 0 - 600 RPM

% reduction of data from 3/11 - 3/12

z=[-0.6 0.066 1.25];
zn=z + 0.2;

% 0 RPM
fz0 = [0 0 0];

% 50 RPM
fz50 = [1.25 -1 -3.75];
```

```
% 100 RPM
fz100 = [4.0 -3.125 -12.5];

% 150 RPM
fz150 = [7.5 -5.6 -20];

% 200 RPM
fz200 = [11.25 -8 -34.4];

% 250 RPM
fz250 = [15.0 -10.5 -43.75];

% 300 RPM
fz300 = [17.5 -11.5 -50];

% 350 RPM
fz350 = [17.5 -12.5 -57];

% 400 RPM
fz400 = [20 -14 -60];

% 450 RPM
fz450 = [21 -15 -62.5];

% 500 RPM
fz500 = [20 -15 -65];

% 600 RPM
fz600 = [21.5 -16 -68.75];


%plotting
plot(zn,fz50,'w',zn,fz100,'w--',zn,fz150,'w',zn,fz200,'w--',zn,fz250,'w',zn,fz300,'w--',zn,fz350,'w')
hold
plot(zn,fz400,'w--',zn,fz450,'w',zn,fz500,'w--',zn,fz600,'w')
axis([-0.5 1.75 -75 25]);
grid
xlabel('z - Distance from null position, cm')
ylabel('fz - Lift force, Newtons')
title('file:mspring.m; Lift force vs. displacement from null position, xo = 0.4 cm, I = 5A')
text(1.5,-3.75,'4 m/s');text(1.5,-12.5,'8 m/s');text(1.5,-20,'13 m/s');
text(1.5,-34.4,'17 m/s');text(1.5,-43.75,'21 m/s');text(1.5,-50,'25 m/s');
text(1.5,-57,'29 m/s');
text(1.5,-70,'50 m/s');

end

****************************************************************
function aclift1
% aclift1.m
% plots of AC lift force measurements, 10Hz-100Hz

k=0.1*9.81/1.6                  % spring constant of setup, N/cm
Imax=8;                         % maximum coil excitation, pp
```

```
A=(4/pi)^2+(4/(3*pi))^2;  % take care of 1st and 3rd harmonics
% A=A*(12/8)^2;

z=14.3:-1:8.3; z=z-11.3              % vertical position
I=[8 8 2.4 1.25]

%data at 10Hz
before10Hz=[14.4 13.4 12.3 11.3 10.3 9.35 8.4];
after10Hz= [14.2 12.9 12.1 11.3 10.55 9.65 8.7];
delta10Hz=before10Hz-after10Hz;
F10Hz=(k*A).*delta10Hz

%data at 20 Hz
before20Hz=[14.5 13.25 12.3 11.3 10.3 9.35 8.3];
after20Hz= [13.4 12.35 11.8 11.3 10.8 10.25 9.4];
delta20Hz=before20Hz-after20Hz;
F20Hz=(k*A).*delta20Hz

%data at 50 Hz
before50Hz=[14.4 13.3 12.25 11.3 10.25 9.4 8.3];
after50Hz =[13.95 12.7 11.95 11.3 10.6 9.95 8.9];
delta50Hz =before20Hz-after50Hz;
F50Hz=(k*A)*(8/2.4)^2.*delta50Hz;

%data at 100 Hz
before100Hz=[14.4 13.4 12.3 11.3 10.3 9.3 8.35];
after100Hz= [14.0 13 12.1 11.3 10.5 9.5 8.55];
delta100Hz=before100Hz-after100Hz;
F100Hz=(k*A)*(8/1.25)^2.*delta100Hz;

plot(z,F10Hz,'wo',z,F10Hz,'w',z,F20Hz,'wx',z,F20Hz,'w',z,F50Hz,'wo',z,F50Hz,'w')
hold
plot(z,F100Hz,'wx',z,F100Hz,'w')
xlabel('Distance from null position, cm')
ylabel('Normalized lift force, Newtons')
title('file:aclift1.m;  AC LIFT DATA, 10 - 100 Hz')
text(2,19,'100 Hz');text(2,8,'50 Hz');text(2,3,'20 Hz');text(2,-2,'10Hz')
grid
```

9. References

9.1. High-Temperature Superconducting Magnet Design

[1] D. Aized, M. D. Manlief and C. H. Joshi, “Performance of High Temperature Superconducting Coils in High Background Fields at Different Temperatures.” *IEEE Transactions on Magnetics*, vol. 30, No. 4, July 1994 pp. 2010-2013. Detail on performance of HTSC coils from 1.8 to 77K.

[2] M. Ariante, A. Matrone, E. Petrillo, A. Bonzi, P. Fabbricatore, M. Galbiati, C. Priano, L. Rossi and A. Sciutti, “Characteristics of Coils Wound with Mono and Miltifilamentary Bi-2212/Ag from 4 to 80K,” *IEEE Transactions on Magnetics*, vol. 32, no. 4, July 1996, pp. 2780-2783

[3] J. D. Edick, R. F. Schiferl, and H. E. Jordan, “High Temperature Superconductivity Applied to Electric Motors.” *IEEE Transactions on Applied Superconductivity*, vol. 2, No. 4, December 1992, pp. 189-194. Effects of HTSC on motor design.

[4] S. Foner, "New Materials --- The Road to Higher Magnetic Field Generation," *International Journal of Applied Electromagnetics in Materials*, vol. 1 (1990) pp. 111-116. Magnetic scaling laws.

[5] B. B. Gamble, G. L. Snitchler and R. E. Schwall, “Prospects for HTS Applications,” *IEEE Transactions on Magnetics*, vol. 32, no. 4, July 1996, pp. 2714-2719. HTSC cost analysis

[6] P. Haldar, J. G. Hoehn Jr., J. A. Rice, L. R. Motowidlo, U. Balachandran, C. A. Youngdahl, J. E. Tkaczyk and P. J. Bednarcqyk, “Fabrication and Properties of High-Tc Tapes and Coils Made from Silver-Clad Bi-2223 Superconductors.” *IEEE Transactions on Applied Superconductivity*, vol. 3, 1127-30 (1993)

[7] D. W. Hazelton, J. A. Rice, Y. S. Hascicek, H. W. Weijers, and S. W. Van Sciver, "Development and Test of a BSCCO-2223 HTS High Field Insert Magnet for NMR," *Proceedings of the Applied Superconductivity Conference '94*, October 1994

[8] Y. Iwasa, "Design and Operational Issues for 77-K Superconducting Magnets," *IEEE Transactions on Magnetics*, vol. 24, no. 2, March 1988, pp. 1211-1214

[9] R. G. Jenkins, H. Jones and R. M. Goodall, "Designing HTS Coils for Magnetic Circuits," *IEEE Transactions on Magnetics*, vol. 32, no. 4, July 1996, pp. 2683-2686. Iron-core HTSC coils

[10] R. G. Jenkins, H. Jones, M. Yang, M. J. Goringe and C. R. M. Grovenor, "The Construction and Performance of BSCCO 2212 Coils for Use in Liquid Nitrogen at 64K on an Iron Yoke in Demonstrator Devices," *Proceedings of the Applied Superconductivity Conference '94*, paper number LIC-2, October 1994

[11] R. G. Jenkins, H. Jones, M. Yang, I. Belenli, C. R. M. Grovenor and M. J. Goringe, "Prototype Coils wound from High-Tc Superconducting Composites," *IEEE Transactions on Magnetics*, vol. 30, no. 4, July 1994, pp. 1813-1816

[12] I. Kirschner, J. Matrai, G. Szentgyorgyi, T. Porjesz, M. Lamm, I. Milnar, Gy. Kovacs, T. Trager, P. Lukacs, T. Karman, J. Gyorgy, M. Takacs and G. Zsolt, "Construction and parameters of the first high T_c superconducting ceramic magnets for small fields," *Cryogenics*, vol. 29, no. 2, pp. 83-86, 1989

[13] S. Okada, Y. Iwahashi, and H. Mori, "A Practical Structural Stress Evaluation System for Superconducting Coils with Inner Ring Support, " *International Journal of Applied Electromagnetics in Materials*, vol. 1 (1990) pp. 99-108

[14] G. Ries, "Magnet Technology and Conductor Design with High Temperature Superconductors." *Cryogenics*, 1993 vol. 33, No. 6, pp. 609-614. Quench protection of HTSC coils; material mechanical properties of HTSC

[15] S. M. Schoenung, R. L. Bieri and T. C. Bickel, "The Advantages of Using High-Temperature Superconductors in High-Duty-Cycle Applications of SMES," IEEE Transactions on Applied Superconductivity, vol. 5, no. 2, June 1995, pp. 341-344

[16] S. M. Schoenung, W. R. Meier, R. L. Fagaly, M. Heiberger, R. B. Stephens, J. A. Leuer and R. A. Guzman, "Design, Performance, and Cost Characteristics of High Temperature Superconducting Magnetic Energy Storage," *IEEE Transactions on Energy Conversion*, vol. 8, no. 1, March 1993, pp. 33-39

[17] J. Tenbrink, M. Wilhelm, K. Heine, and H. Drauth, "Development of High-Tc Superconductor Wire for Magnet Applications." *IEEE Transactions on Magnetics*, vol. 27, No. 2, March 1991 pp. 1239-1246

[18] N. V. Vo, S. X. Dou and H. K. Liu, "Development of Bi(Pb)-2223/Ag Pancake-Shaped and Solenoidal Coils," *IEEE Transactions on Applied Superconductivity*, vol. 6, no. 2, June 1996, pp. 102-105. Recent development of HTSC coils, including detail of pancake coil designs.

9.2. High-Temperature Superconductors: Material Properties

[19] American Superconductor Corp., High-Temperature Superconductivity Seminar, 1994

[20] S. Elschner, J. Bock, G. Brommer, and P. Herrmann, "High Currents in MCP BSCCO 2212 Bulk Materials," *IEEE Transactions on Magnetics*, vol. 32, no. 4, July 1996 pp. 2724-2727

[21] B. Haken, A. Godeke, H. Schuver, and H. ten Kate, "Descriptive Model for the Critical Current as a Function of Axial Strain in Bi-2212/Ag Wires," *IEEE Transactions on Magnetics*, vol. 32, no. 4, July 1996 pp. 2720-2723

[22] P. Haldar, Intermagnetics General Corporation, personal communication, 1995

[23] D. Hazelton, Intermagnetics General Corporation, personal communication, 1995

[24] S. Kim, Y. Ueno, A. Ishiyama, H. Okada, S. Nomura, and H. Maeda, "Experiment and Numerical Analysis of Normal Zone Propagation Properties in Ag Sheathed Bi-2223 Superconducting Tapes," *IEEE Transactions on Magnetics*, vol. 32, no. 4, July 1996, pp. 2822-2825

[25] M. P. Maley, J. H. Cho, J. Y. Coulter, J. O. Willis, L. N. Bulaevskii, L. R. Motowidlo and P. Haldar, "Anisotropy of Transport Properties Normal and

Parallel to the Tape Plane in Bi-2223/Ag Tapes." *Proceedings of the Applied Superconductivity Conference '94*, Boston, October 1994

[26] G. C. Montanari, I. Ghinello, L. Gherardi and P. Caracino, "An Investigation on Aging of Multifilamentary 2223-BSCCO Specimens Under Mechanical and Environmental Stresses," *IEEE Transactions on Applied Superconductivity*, vol. 6, no. 3, September 1996, pp. 132-141

[27] M. Murakami, S. Gotoh, N. Koshizuka, S. Tanaka, T. Matsushita, S. Kambe, and K. Kitazawa, "Critical currents and flux creep in melt processed high T_c oxide superconductors," *Cryogenics*, vol. 30, pp. 390-396, May 1990

[28] R. C. Niemann, J. P. Singh, C. A. Youngdahl, W. Brockenborough and C. M. Rey, "Performance Characterizations of Bi-2223 Composite Powder-in-Tube Conductor Elements," Applied Superconductivity, vol. 3, no. 5, 1995, pp. 237-247

[29] T. P. Orlando and D. A. Delin, Foundations of Applied Superconductivity, published by Addison-Wesley, New York 1991

9.3. *Inductance Calculation Techniques*

[30] S. Butterworth, "On the Coefficients of Self and Mutual Induction of Coaxial Coils," *Philosophical Magazine*, vol.29, 1915, pp. 578-592

[31] S. Butterworth, "On the Coefficients of Mutual Induction of Eccentric Coils," *Philosophical Magazine*, series 6, vol.31, 1916, pp. 443-454. Mutual inductance calculation for filamentary coils with offset axes.

[32] A. Campbell, "On the Use of Variable Mutual Inductances," *Philosophical Magazine*, vol. 15, 6th series, 1908, pp. 155-171. Approximate technique for calculating mutual inductance of offset filamentary coils.

[33] H. B. Dwight, Electrical Coils and Conductors, McGraw-Hill, 1945

[34] F. W. Grover, Inductance Calculations: Working Formulas and Tables, Dover Publications, Inc., New York, 1946

[35] B. R. Gupta and V. K. Singh, "Inductance of Rectangular Grids," *IEEE Transactions on Power Delivery*, vol. 7, no. 3, July 1992, pp. 1218-1221

[36] W. G. Hurley and M. C. Duffy, "Calculation of Self and Mutual Impedances in Planar Magnetic Structures," *IEEE Transactions on Magnetics*, vol. 31, no. 4, July 1995, pp. 2416-2422

[37] J. V. Jones, "On the Calculation of the Coefficient of Mutual Induction of a Circle and a Coaxial Helix," *Philosophical Magazine*, vol. 27, 1889, pp. 56-62

[38] K. Kim, E. Levi, Z. Zabar, and L. Birenbaum, "Restoring Force Between Two Noncoaxial Circular Coils," *IEEE Transactions on Magnetics*, vol. 32, no. 2, March 1996, pp. 478-484

[39] T. R. Lyle, "On the Self-Inductance of Circular Coils of Rectangular Section," *Philosophical Transactions*, vol. 213A, (1913) pp. 421-435

[40] J. C. Maxwell, Electricity and Magnetism, vols. 1 and 2, Dover Publications

[41] P. N. Murgatroyd, "Some optimum shapes for toroidal inductors," *IEE Proceedings*, vol. 129, part B, no. 3, May 1982, pp. 168-176.

[42] A. Rezzoug, J. P. Caron, and F. M. Sargos, "Analytical Calculations of Flux and Induction and Forces of Thick Coils with Finite Length," *IEEE Transactions on Magnetics*, vol. 28, no. 5, September 1992, pp. 2250-2252

[43] W. T. Scott, The Physics of Electricity and Magnetism, 2d Ed., John Wiley and Sons, 1966

[44] W. R. Smythe, Static and Dynamic Electricity, 2d ed., McGraw-Hill, New York, 1950

[45] F. E. Terman, Radio Engineers' Handbook, McGraw-Hill, New York, 1943. Self inductance of rectangle of rectangular wire, pp. 53; flat rectangular coil, pp. 59

[46] H. A. Wheeler, "Formulas for the Skin Effect," *Proceedings of the I.R.E.*, September 1942, pp. 412-424

[47] M. Zahn, Electromagnetic Field Theory: A Problem Solving Approach, Krieger Publishing Company, Malabar Florida, 1987

9.4. Maglev: Circuit Modeling

[48] J. L. He and D. M. Rote, "Double-Row Loop-Coil Configuration for EDS Maglev Suspension, Guidance, and Electromagnetic Guideway Directional Switching," *IEEE Transactions on Magnetics*, vol. 29, no. 6, November 1993, pp. 2956-2958. Practical design for null-flux Maglev.

[49] J. L. He, D. M. Rote, and H. T. Coffey, "Applications of the Dynamic Circuit Theory to Maglev Suspension Systems," *IEEE Transactions on Magnetics*, vol. 29, No. 6, November 1993, pp. 4153-4164

[50] J. L. He, D. M. Rote, and H. T. Coffey, "Electrodynamic Forces of the Cross-Connected Figure-Eight Null-Flux Coil Suspension System," *MAGLEV '93, Proceedings of the 13th International Conference on Magnetically Levitated Systems and Linear Drives*, May 1993

[51] J. L. He, D. M. Rote, and H. T. Coffey, "Study of Japanese Electrodynamic-Suspension Maglev Systems," *Argonne National Laboratory report ANL/ESD-20*, April 1994

[52] Y. Iwasa, "Electromagnetic flight stability by model impedance simulation," *Journal of Applied Physics*, vol. 44, 1973, pp. 858-862

[53] O. P. Jain and B. Ooi, "The Validity and the Limitations of the AC Impedance-Modeling Technique in Electrodynamic Levitation Systems," *IEEE Transactions on Magnetics*, vol. MAG-15, no. 3, July 1979 pp. 1169-1174

[54] M. K. Mills, "Self Inductance Formulas for Multi-Turn Rectangular Loops used with Vehicle Detectors," *IEEE 1983 Vehicular Technology Conference*, pp. 65-73

[55] M. K. Mills, "Self Inductance Formulas for Quadrupole Loops used with Vehicle Detectors," *IEEE 1985 Vehicular Technology Conference*, pp. 81-87. Inductance calculations for loop guideways.

[56] M. K. Mills, "Inductive Loop System Equivalent Circuit Model," *IEEE 1989 Vehicular Technology Conference*, vol. 2, pp. 689-700

[57] E. Ohno, M. Iwamoto, and T. Yamada, "Characteristics of Superconductive Magnetic Suspension and Propulsion for High-Speed Trains," *Proceedings of the IEEE*, vol. 61, no. 5, May 1973, pp. 579-586

[58] B. Ooi, "A Dynamic Circuit Theory of the Repulsive Magnetic Levitation System," *IEEE Transactions on Power Apparatus and Systems*, vol. PAS-96, no. 4, July/August 1977, pp. 1094-1100

[59] J. Y. Wong, B. E. Mulhall and R. G. Rhodes, "The impedance modelling technique for investigating the characteristics of electrodynamic levitation systems," *Journal of Applied Physics*, vol. 8, 1975, pp. 1948-1955

9.5. Maglev: Control Systems --- Electrodynamic Suspensions (EDS)

[60] M. Abe, and H. Tsunashima, "Mechanically Controlled Permanent Magnet Levitation System for Maglev Transport Vehicle," Maglev, Society of Automotive Engineers

[61] D. L. Atherton, A. R. Eastham, and K. Sturgess, "Passive secondary magnetic damping for superconducting Maglev vehicles," *Journal of Applied Physics*, vol. 47, no. 10, October 1976, pp. 4643-4648

[62] S. Kuntz, P. Burke, and G. Slemon, "Active Damping of Maglev Vehicles Using Superconducting Linear Synchronous Motors," *Electric Machines and Electromechanics*, v. 2, (1978), pp. 371-384

[63] S. J. O. Mirzamani, G. M. Asher, and R. J. A. Paul, "Feasibility of Passive Damping from Mixed-Mu Levitation," *IEEE Transactions on Magnetics*, vol. MAG-20, no. 5, September 1984, pp. 1681-1683

[64] M. Nagai, "Recent Researches on Active Suspensions for Ground Vehicles," *JSME International Journal*, Series C, vol. 36, no. 2, 1993, pp. 161-170

[65] M. Nagai, H. Mori, and S. Nakadai, "Active Vibration Control of Electrodynamic Suspension System," *JSME International Journal*, series C, vol. 38, no. 1, 1995 pp. 48-54

[66] M. Nagai and S. Tanaka, "Study on the Dynamic Stability of Repulsive Magnetic Levitation Systems," *JSME International Journal*, series III, vol. 35, no. 1, 1992, pp. 102-108

[67] S. Nakadai and M. Nagai, "LQI optimal control of electro-dynamic suspension," *International Journal of Applied Electromagnetics in Materials*, v. 4, (1994) pp. 309-316

[68] K. Nonami, W. He, and H. Nishimura, "Robust Control of Magnetic Levitation Systems by Means of H^{∞} Control/μ-Synthesis," *JSME International Journal*, series C, vol. 37, no. 3, 1994, pp. 513-520

[69] B. Ooi and M. H. Banakar, "Passive and Active Damper Winding for the Repulsive Magnetic Levitation System," *IEEE Transactions on Magnetics*, vol. Mag-13, no. 3, September 1977, pp. 1672-1674

[70] M. Trapanese, "A Lagrangian Approach to the Electromechanical Aspects of the Superconducting Magnets for Maglev," *Proceedings of the 6th International Symposium on Superconductivity (ISS'93)* October 26-29, 1993, Hiroshima Japan

9.6. Maglev: Control Systems --- Electromagnetic Suspensions (EMS)

[71] R. D. Fruechte, R. H. Nelson, and T. A. Radomski, "Power Conditioning Systems for a Magnetically Levitated Test Vehicle," *IEEE Transactions on Vehicular Technology*, vol. VT-29, no. 1, February 1980, pp. 50-60. Control system for EMS using position-acceleration control.

[72] R. Goodall, "Dynamic characteristics in the design of Maglev suspensions," *Proc. Instn. Mech. Engrs.*, vol. 208, pp. 33-41

[73] R. M. Goodall and C. J. MacLeod, "Control Considerations Relating to the use of Superconducting Coils for Maglev," *Proc. IEEE Conf. on Control Applications (CCA95)* Albany NY, Sept. 1995, pp. 261-265

[74] E. Gottzein, B. Lange, and F. Ossenberg-Franzes, "Control System Concept for a Passenger Carrying Maglev Vehicle," *High Speed Ground Transportation Journal*, vol. 8, no. 2, 1974, found in Proceedings of the International Conference on High Speed Ground Transportation, January 1975

[75] R. J. Gran and M. Proise, "Five Degree of Freedom Analysis of the Grumman Superconducting Electromagnetic Maglev Vehicle, Control and Guideway Interaction"

[76] W. A. Hutchens, E. C. Haight, and J. L. Milner, "Analysis of the Dynamics of a Rail Car from its Response to Random Inputs," *High Speed Ground Transportation Journal*, vol. 9, no. 1, 1975, found in Proceedings of the International Conference on High Speed Ground Transportation, January 1975

[77] W. Kortum and A. Utzt, "Control Law Design and Dynamic Evaluations for a Maglev Vehicle with a Combined Lift and Guidance Suspension System," *Transactions of the ASME*, vol. 106, December 1984, pp. 286-292

[78] S. Mark, "Modeling and Control of Maglev Vehicles," M.S. Thesis, Department of Mechanical Engineering, Massachusetts Institute of Technology, May 1993

[79] T. Mizuno, "Phase-Locked Loops for the Stabilization of Active Magnetic Suspensions," *JSME International Journal*, series A, vol. 37, no. 3, 1994 pp. 499-503. Use of phase-locked loops for stabilization of EMS maglev suspensions.

[80] H. Tsunashima and M. Abe, "Dynamics of the Mechanical Levitation Control System for a Maglev Transport Vehicle," *JSME International Journal*, series C, vol. 37, no. 3, 1994, pp. 528-535

[81] A. E. Zawawi, Y. Baudon, and M. Ivanes, "Dynamic Analysis of an Electromagnetically Levitated Vehicle Using Linear Synchronous Motor," *Electric Machines and Electromechnnics*, vol. 6, pp. 129-141, 1981

9.7. Maglev: Electromechanical Stability Analysis

[82] A. Baiko, K. Voevodskii and V. Kochetkov, "Vertical unstable stability of electrodynamic suspension of high-speed ground transport," *Cryogenics*, May 1980, pp. 271-276

[83] I. Boldea, "Static and Dynamic Performance of Electrodynamic (Repulsion) Levitation Systems (EDS)," *Electric Machines and Electromechanics*, vol. 6, pp. 45-55, 1981

[84] Y. Cai and S. S. Chen, "Instability of Electrodynamic Maglev Systems," Submitted to *Journal of Sound and Vibration*, 1994

[85] S. S. Chen, S Zhu, and Y. Cai, "On Unsteady-Motion Theory of Magnetic Forces for Maglev Systems," *Journal of Sound and Vibration*, vol. 188, no. 4, pp. 529-543, 1995

[86] D. Chu and F. C. Moon, "Dynamic Instabilities in Magnetically Levitated Models," *Journal of Applied Physics*, vol. 54, no. 3, March 1983, pp. 1619-1625

[87] L. C. Davis and D. F. Wilkie, "Analysis of Motion of Magnetic Levitation Systems: Implications for High-Speed Vehicles," *Journal of Applied Physics*, vol. 42, no. 12, November 1971, pp. 4779-4793

[88] H. J. Fink and C. E. Hobrecht, "Instability of Vehicles Levitated by Eddy Current Repulsion --- Case of an Infinitely Long Current Loop," *Journal of Applied Physics*, vol. 42, no. 9, August 1971, pp. 3446-3450

[89] J. L. He, Z. Wang, D. M. Rote, and S. Winkelman, "Investigation of the Stability of AC Repulsive-Force Levitation Systems for Low-Speed Maglev," *IEEE Transactions on Magnetics*, vol. 28, no. 5, September 1992, pp. 3315-3317

[90] L. M. Holmes, "Stability of magnetic levitation," *Journal of Applied Physics*, vol. 49, no. 6, June 1978, pp. 3102-3109

[91] J. P. Howell, J. Y. Wong, R. G. Rhodes, and B. E. Mulhall, "Stability of Magnetically Levitated Vehicles Over a Split Guideway," *IEEE Transactions on Magnetics*, vol. MAG-11, no. 5, September 1975, pp. 1487-1489

[92] M. Iwamoto, T. Yamada, and E. Ohno, "Magnetic Damping Force in Electrodynamically Suspended Trains," *IEEE Transactions on Magnetics*, vol. MAG-10, (1974), pp. 458-461

[93] D. Levy, "General approach to the Stability Analysis of Maglev Systems, " *Journal of Electrical and Electronics Engineering, Australia*, vol. 10, no. 4, December 1990, pp. 255-277

[94] F. C. Moon, "Chaotic Vibrations of a Magnet Near a Superconductor," *Physics Letters A*, vol. 132, no. 5, 10 October 1988 pp. 249-252

[95] F. C. Moon, "Vibration Problems in Magnetic Levitation and Propulsion," Transport Without Wheels, E. Laithwaite Editor, Elek Science, London 1977 pp. 122-161

[96] V. Nguyen, J. Delamare, and J.-P. Yonnet, "A Passive Damper for Magnetic Suspension," *IEEE Transactions on Magnetics*, vol. 30, no. 6, November 1994, pp. 4749-4751

[97] H. Ohsaki, S. Torii, K. Higashi, and E. Masada, "Damping Characteristics of the Superconducting Maglev Vehicle," *Proceedings of the 6th International Symposium on Superconductivity (ISS'93)* October 26-29, 1993, Hiroshima Japan

[98] C. H. Woods, R. K. Cooper, V. K. Neil, and C. E. Taylor, "Stability Analysis of a Levitated Superconducting Current Ring Stabilized by Feedback and Eddy Currents," *Journal of Applied Physics*, vol. 41, no. 8, July 1970, pp. 3295-3305

[99] T. Yamada, M. Iwamoto and T. Ito, "Magnetic Damping Force in Inductive Magnetic Levitation System for High-Speed Trains, " *Electrical Engineering in Japan*, vol. 94, no. 1, 1974, pp. 80-84

9.8. Maglev: Force Calculations

[100] D. L. Atherton, A. R. Eastham, C. Fombrun, and M. Chong, "Eddy Current Distribution and Lift Force for Finite Maglev Strips," *Canadian Journal of Physics*, vol. 52, 1974, pp. 1203-1208

[101] N. Carbonari, G. Martinelli, and A. Morini, "Calculation of levitation, drag and lateral forces in EDS-MAGLEV transport systems," *Archiv fur Elektrotechnik* 71 (1988) pp. 139-148

[102] L. C. Davis, "Drag force on a magnet moving near a thin conductor, " *Journal of Applied Physics*, vol. 43, no. 10, October 1972, pp. 4256-4257

[103] R. Knowles, "Dynamic Circuit and Fourier Series Methods for Moment Calculation in Electrodynamic Repulsive Magnetic Levitation Systems," *IEEE Transactions on Magnetics*, vol. MAG-18, no. 4, July 1982 pp. 953-960

[104] J. Langerholc, "Torques and forces on a moving coil due to eddy currents," *Journal of Applied Physics*, vol. 44, no. 4, April 1973, pp. 1587-1594

[105] S. W. Lee and R. Menendez, "Forces at low and high-speed limits in magnetic levitation systems," *Journal of Applied Physics*, vol. 46, no. 1, Jan. 1975, pp. 422-425

[106] S. W. Lee and R. C. Menendez, "Force on Current Coils Moving over a Conducting Sheet with Application to Magnetic Levitation," *Proceedings of the IEEE*, vol. 62, no. 5, May 1974, pp. 567-577

[107] B. Ooi, "Levitation, Drag and Transverse Forces in Finite Width Sheet Guideways for Repulsive Magnetic Levitation," *High Speed Ground Transportation Journal*, vol. 9, no. 1, 1975, found in Proceedings of the International Conference on High Speed Ground Transportation, January 1975

[108] J. R. Reitz, "Force on Moving Magnets due to Eddy Currents," *Journal of Applied Physics*, vol. 41, No. 5, April 1970, pp. 2067-2071

[109] J. R. Reitz and L. C. Davis, "Force on a Rectangular Coil Moving above a Conducting Slab," *Journal of Applied Physics*, vol. 43, No. 4, April 1972, pp. 1547-1553

[110] T. Saitoh, N. Maki, T. Kobayashi, and M. Shibata, "Electromagnetic Force and Eddy Current Loss in Dynamic Behavior of a Superconducting Magnetically Levitated Vehicle," *IEEE Transactions on Applied Superconductivity*, vol. 3, no. 1, March 1993, pp. 417-420

[111] D. Schieber, Electromagnetic Induction Phenomena, Springer-Verlag, 1986

[112] T. Yamada, M. Iwamoto, and T. Ito, "Levitation Performance of Magnetically Suspended High Speed Trains," *IEEE Transactions on Magnetics*, Sept. 1972, pp. 634-635. Comparison of continuous sheet and ladder guideways

9.9. Maglev: Guideway Design

[113] T. Akinbiyi and P. E. Burke, "A Comparison of Ladder and Sheet Guideways for Electrodynamic Levitation of High Speed Vehicles," *IEEE Transactions of Magnetics*, vol. MAG-12, no. 6, November 1976, pp. 879-881

[114] D. L. Atherton, A. R. Eastham, and R. E. Tedford, "Joints in Strips for Electrodynamic Magnetic Levitation Systems," *IEEE Transactions on Magnetics*, vol. MAG-14, no. 2, March 1978, pp. 69-75

[115] P. E. Burke, "The Use of Stranded Conductors to Reduce Eddy Losses in Guideway Conductors of High Speed Vehicles," *IEEE Transactions on Magnetics*, vol. MAG-11, no. 5, September 1975, pp. 1501-1503

[116] P. E. Burke and T. Akinbiyi, "The Design of Flat Ladder and Coil Guideway Systems for High Speed Trains," *IEEE Transactions of Magnetics*, vol. MAG-12, no. 6, November 1976, pp. 882-884

[117] B. T. Ooi and O. P. Jain, "Force Transients at Guideway Butt Joints in Repulsive Magnetic Levitation System," *IEEE Transactions on Power Apperatus and Systems*, vol. PAS-98, no. 1, Jan./Feb. 1979, pp. 323-330

[118] R. S. Phelan, "High Performance Maglev Guideway Design," Ph.D. thesis, Department of Civil Engineering, Massachusetts Institute of Technology, 1993

[119] R. J. Ravera and J. R. Anderes, "Selection of Candidate Guideway Parameters for High Speed Tracked Levitated Vehicles," *High Speed Ground Transportation Journal*, vol. 8, no. 2, 1974, found in Proceedings of the International Conference on High Speed Ground Transportation, January 1975

[120] M. Zahn, "Power Dissipation and Magnetic forces on MAGLEV Rebars," IEEE Transactions on Magnetics, vol. 33, no. 2, part 1, pp. 1021-36, March 1997

9.10. Maglev: High Tc Magnet Design

[121] L. Bromberg, M. Sidorov, J. Bock, and S. Pourrahimi, "High Tc Monolithic Helical Magnets," *IEEE Transactions on Magnetics*, vol. 32, no. 4, July 1996 pp. 2687-2690

[122] H. Jones, R. G. Jenkins, R. M. Goodall, C. Macleod, A. A. El Abbar and A. M. Campbell, “High Temperature Superconducting Magnets with Active Control for Attractive Levitation Transport Applications,” *Proceedings of the Fourth International Symposium on Magnetic Suspension Technology*, NASA Conference Publication, pp. 535-550

[123] R. Goodall, C. MacLeod, A. El-Abbar, H. Jones, R. Jenkins and A. Campbell, "The Potential for EMS Maglev using High Temperature Superconductors," *Proc. Maglev '95*, Bremen, Nov. 1995, pp. 209-215;

[124] R. Goodall, C. MacLeod, A. El-Abbar, H. Jones, R. Jenkins and A. Campbell, “The Use of Iron-cored HTS Magnets for EMS Maglev,” *Proc. ZSS 1996*, Sapporo Japan

[125] S. S. Kalsi, "The Application of High Temperature Superconductors to Maglev Magnets," *Applied Superconductivity*, vol. 3, no. 1-3, 1995, pp. 163-168

[126] S. S. Kalsi et. al., “Iron Core Superconducting Magnet Design and Test Results for Maglev Applications,” *Proceedings of the 1994 Applied Superconductivity Conference*, Boston, Octover 1994, paper LR-3

[127] A. Senba, H. Kitahara, H. Ohsaki, and E. Masada, "Characteristics of an Electromagnetic Levitation System using a Bulk Superconductor," *IEEE Transactions on Magnetics*, vol. 32, no. 5, part 2, pp. 5049-5051, 1996

[128] E. A. Scholle and J. Schwartz, "Implications of High Temperature Superconducting Magnets on Maglev Design," submitted to *IEEE Transactions on Applied Superconductivity*

[129] S. Yokoyama, K. Shimohata, T. Inaguchi, T. Takeuchi, T. Kim, S. Nakamura, S. Miyashita, and F. Uchikawa, "A Conceptual Design of a Superconducting Magnet for MAGLEV Using a Bi-based High-Tc Tape," *Applied Superconductivity Conference '94*, paper number LLB-2, October 1994

9.11. Maglev: Magnetic Shielding

[130] W. F. Hayes, "Magnetic Field Shielding for Electrodynamic Maglev Vehicles," International Conference on Maglev and Linear Drives, Las Vegas, May 19-21, 1987 pp. 53-66

[131] Y. Iwasa, "Magnetic Shielding for Magnetically Levitated Vehicles," *Proceedings of the IEEE*, vol. 61, no. 5, May 1973, pp. 598-603

[132] S. Kikuchi and H. Kimura, "Some Considerations on the Magnetic Shielding in the Train," *IEEE Transactions on Magnetics*, vol. 31, No. 6, Nov. 1995 pp. 4256-4258

[133] T. Rikitake, Magnetic and Electromagnetic Shielding, D. Reidel Publishing Co., Boston, 1987

9.12. Maglev: Modeling

[134] D. L. Atherton and A. Eastham, "Flat guidance schemes for magnetically levitated high-speed guided ground transport," *Journal of Applied Physics*, vol. 45, 1974, pp. 1398-1405

[135] E. E. Burkhardt, J. Schwartz, and S. Nakamae, "Analysis of Superconducting Magnet (SCM)-Ground Coil Interactions for EDS Maglev Coil Configurations," *IEEE Transactions on Applied Superconductivity*, vol. 3, no. 1, March 1993, pp. 430-433. L-R modelling of null-flux suspension

[136] L. C. Davis and D. F. Wilkie, "Analysis of Motion of Magnetic Levitation Systems: Implications for High-Speed Vehicles," *Journal of Applied Physics*, vol. 42, no. 12, November 1971, pp. 4779-4793

[137] S. Fujiwara, "Characteristics of EDS Magnetic Levitation with Ground Coils for Levitation Arranged on the Side Wall," *Electrical Engineering in Japan*, vol. 108, no. 3, 1988, pp. 101-110

[138] C. A. Guderjahn, S. L. Wipf, H. J. Fink, R. W. Boom, K. E. MacKenzie, D. Williams, and T. Downey, "Magnetic Suspension and Guidance for High Speed Rockets by Superconducting Magnets," *Journal of Applied Physics*, vol. 40, no. 5, April, 1969, pp. 2133-2140

[139] S. D. Lindenbaum and M. S. Lee, "Lift, drag, and guidance forces on alternating polarity magnets, using loop guideways," *Journal of Applied Physics*, vol. 46, no. 7, July 1975, pp. 3151-3159

[140] J. R. Melcher, Continuum Electromechanics MIT Press, 1981

[141] H. Ohsaki, H. Deguchi, and E. Masada, "Dynamical Behavior Analysis of the Supercondicting Magnets for an EDS-LSM Maglev," *International Journal of Applied Electromagnetics in Materials*, vol. 2 (1991) pp. 265-273

[142] P. L. Richards and M. Tinkham, "Magnetic Suspension and Propulsion Systems for High-Speed Transportation," *Journal of Applied Physics*, vol. 43, no. 6, June 1972, pp. 2680-2691

[143] R. D. Thornton, "Flux Canceling Maglev Suspension," *MAGLEV '93, Proceedings of the 13th International Conference on Magnetically Levitated Systems and Linear Drives*, May 1993

[144] H. H. Woodson and J. R. Melcher, Electromechanical Dynamics Published by Robert E. Kreiger, Malabar, FL 1968

9.13. Maglev: Ride Comfort

[145] Y. Cai, S. S. Chen, D. M. Rote, and H. T. Coffey, "Vehicle/Guideway Interaction and Ride Comfort in Maglev Systems," submitted to *ASME J. Dynamic System, Measurement, and Control*

[146] J. J. Fearnsides, J. K. Hedrick, and H. Firouztash, "Specification of Ride Quality Criteria for Transportation Systems: The State of the Art and a New Approach," *High Speed Ground Transportation Journal*, vol. 8, no. 2, 1974, found in Proceedings of the International Conference on High Speed Ground Transportation, January 1975

[147] V. K. Garg and R. V. Dukkipati, Dynamics of Railway Vehicle Systems, Academic Press, 1984

[148] B. V. Jayawant and P. K. Sinha, "Low-Speed Vehicle Dynamics and Ride Quality Using Controlled D.C. Electromagnets," *Automatica*, vol. 13, pp. 605-610, 1977

9.14. Maglev: System Design

[149] M. Andriollo, G. Martinelli, A. Morini and A. Scuttari, “Optimization of the winding configuration in EDS-MAGLEV trains,” *IEEE Transactions on Magnetics*, vol. 32, no. 4, July 1996

[150] D. L. Atherton, "Maglev Using Permanent Magnets," *IEEE Transactions on Magnetics*, vol. MAG-16, no. 1, January 1980, pp. 146-148

[151] J. Bankuti et. al., "Design and Constructions of a Small-Scale Model of a High-Temperature Superconducting Magnetically Levitated Vehicle," *IEEE Transactions on Magnetics*, vol. 32, no. 4, July 1996 pp. 2288-2291

[152] R. H. Borcherts, “Repulsion magnetic suspension research --- US progress to date,” *Cryogenics*, July 1975, pp. 385-393

[153] R. H. Borcherts, L. C. Davis, J. R. Reitz, and D. F. Wilkie, "Baseline Specifications for a Magnetically Suspended High-Speed Vehicle," *Proceedings of the IEEE*, vol. 61, no. 5, May 1973, pp. 569-578

[154] H. T. Coffey, F. Chilton, and T. W. Barbee, Jr., "Suspension and Guidance of Vehicles by Superconducting Magnets," *Journal of Applied Physics*, vol. 40, no. 5, April 1969, pp. 2161

[155] A. R. Eastham and W. F. Hayes, "Maglev Systems Development Status," *IEEE AES Magazine*, January 1988, pp. 20-21

[156] T. Fujimoto and S. Fujiwara, “Electrodynamic Characteristics of MLU002,” *Quarterly Report of the RTRI*, vol. 32, no. 2, June 1991, pp. 50-58

[157] S. Fujiwara, “Characteristics of EDS Maglev Having Levitation Coils on the Side Wall of the Guideway,” *Quarterly Report of the RTRI*, vol. 29, no. 4, Nov. 1988, pp. 157-163

[158] C. A. Guderjahn and S. L. Wipf, “Magnetic Suspension and Guidance for High-Speed Trains by Means of Superconducting Magnets and Eddy Currents,” *Proceedings of the 1969 Cryogenic Engineering Conference*, UCLA, June 16-18, 1969, found in Advances in Cryogenic Engineering, vol. 15, pp. 117-123

[159] C. A. Guderjahn and S. L. Wipf, “Magnetically levitated transportation,” *Cryogenics*, June 1971, pp. 171-178.

[160] A. G. Hammitt, "Special Aerodynamic Problems of High Speed Ground Transportation Systems," *High Speed Ground Transportation Journal*, vol. 8, no. 2, 1974, found in Proceedings of the International Conference on High Speed Ground Transportation, January 1975

[161] H. Ichikawa and H. Ogiwara, "Design Considerations of Superconducting Magnets as a Maglev Pad," *IEEE Transactions on Magnetics*, vol. MAG-10, no. 4, December 1974, pp. 1099-1103

[162] B. V. Jayawant, "Electromagnetic suspension and levitation," *Reports on Progress in Physics*, vol. 44, 1981, pp. 411-472

[163] Y. Kyotani, "Recent Progress on JNR on Maglev. " *IEEE Transactions on Magnetics*, vol. MAG-24, No. 2, March 1988 pp. 804-807

[164] E. Leung, M. Dew, G. Samavedam, and B. Gamble, "A Study of Two Distinct Coil Designs for a Maglev EDS Application," *IEEE Transactions on Magnetics*, vol. 30, no. 4, July 1994, pp. 2379-2382

[165] F. C. Moon, Superconducting Levitation, John Wiley, New York, 1994

[166] S. Nakamura, "Devolopent of High Speed Surface Transport System (HSST)," *IEEE Transactions on Magnetics*, vol. Mag-15, no. 6, November 1979, pp. 1428-1433

[167] H. Nakashima, "The Superconducting Magnet for the Maglev Transport System. " *IEEE Transactions on Magnetics*, vol. 30, No. 4, July 1994 pp. 1572-1578

[168] J. R. Powell and G. R. Danby, "High speed transport by magnetically levitated trains," *ASME Winter Annual Meeting*, New York, paper 66-WA/RR-5, 1966;

[169] J. R. Powell and G. R. Danby, "Magnetically Suspended Trains for Very High Speed Transport," *Proceedings of the Fourth Intersociety Energy Conversion Engineering Conference*, Sept. 22-26, 1969, Washington, pp. 953-963

[170] J. R. Powell and G. R. Danby, "Magnetically suspended trains: the application of superconductivity to high-speed transport," *Cryogenics and Industrial Gases*, vol. 4, October 1969, pp. 19-24

[171] J. R. Powell and G. R. Danby, "Magnetically Suspended Trains for Very High Speed Transport," *Proceedings of the Fourth Intersociety Energy Conversion Engineering Conference*, Sept. 22-26, 1969, Washington, pp. 953-963"Magnetic suspension for levitated tracked vehicles," *C.yogenics*, June 1971, pp. 192-204

[172] K. Sawada, "Development of magnetically levitated high speed transport system in Japan," *IEEE Transactions on Magnetics*, vol. 32, no. 4, July 1996 pp. 2230-2235

[173] M. Shibata, N. Maki, T. Saito, and T. Kobayashi, "Levitation Coil Length Optimization of a Magnetically Levitated Train," *Electrical Engineering in Japan*, vol. 113, no. 2, 1993, pp. 112-120

[174] R. D. Thornton, "Magnetic Levitation and Propulsion, 1975," *IEEE Transactions on Magnetics*, vol. MAG-11, no. 4, July 1975, pp. 981-995

[175] R. D. Thornton, "Design Principles for Magnetic Levitation," *Proceedings of the IEEE*, vol. 61, no. 5, May 1973, pp. 586-598

[176] R. D. Thornton, D. Perreault, T. Clark, "Linear Synchronous Motors for Maglev," *U.S. Dept. of Transportation, Federal Railroad Administration Report DOT/FRA/NMI-92/13*, January 1993

[177] Y. Tzeng and T. Wang, "Optimal Design of the Electromagnetic Levitation with Permanent and Electro Magnets," *IEEE Transactions on Magnetics*, vol. 30, no. 6, November 1994, pp. 4731-4733

[178] U. S. Department of Transportation, Federal Railroad Administration, "Compendium of Executive Summaries from the Maglev System Concept

Definition Final Reports," prepared by the National Maglev Initiative, Washington D.C., Spetember 30, 1992

[179] S. Yamamura, "Magnetic Levitation Technology of Tracked Vehicles. Present Status and Prospects," *IEEE Transactions on Magnetics*, vol. 12, no. 6, November 1976, pp. 874-878

9.15. Maglev: Test Results

[180] D. L. Atherton, A. R. Eastham, B. Ooi, and O. P. Jain, "Forces and Moments for Electrodynamic Levitation Systems --- Large-Scale Test Results and Theory," *IEEE Transactions on Magnetics*, vol. MAG-14, no. 2, March 1978, pp. 59-68

[181] J. Bankuti, I. Vajda, L. Mohacsi, A. Szalay, I. Kotsis and M. Enisz, "Design and Construction of a Small-Scale Model of a High-Temperature Superconducting Magnetically Levitated Vehicle, " *IEEE Transactions on Magnetics*, vol. 32, no. 4, July 1996, pp. 2288-2291

[182] R. H. Borcherts and L. C. Davis, "Force on a Coil Moving over a Conducting Surface Including Edge and Channel Effects," *Journal of Applied Physics*, vol. 43, no. 5, May 1972, pp. 2418-2427

[183] W. S. Brown, "A 1/25 Scale Magneplane," Ph.D. Thesis, Department of Electrical Engineering and Computer Science, Massachusetts Institute of Technology, October 1975

[184] N. D. Fintescu and J. P. Pascal, "Test Results of Full-Scale 1 MW Linear Induction Motor ("U-LIM-AS") with PWM Inverter, " *1986 IEEE International Conference on Maglev and Linear Drives*, May 14-16, Vancouver, pp. 165-170

[185] H. Hieronymus, J. Miericke, F. Pawlitschek, and R. Rudel, "Experimental Study of Magnetic Forces on Normal and Null Flux Coil Arrangements in the Inductive Levitation System," *Applied Physics* 3, (1974) pp. 359-366

[186] Y. Hikasa and Y. Takeuchi, "Detail and Experimental Results of Ferromagnetic Levitation System of Japan Air Lines HSST-01/-02 Vehicles, " *IEEE Transactions on Vehicular Technology*, vol. VT-29, no. 1, February 1980, pp. 35-40

[187] T. Iwahana, "Study of Superconducting Magnetic Suspension and Guidance Characteristics on Loop Tracks," *IEEE Transactions on Magnetics*, vol. MAG-11, no. 6, November 1975, pp. 1704-1711

[188] Y. Iwasa, W. S. Brown, and C. B. Wallace, "An Operational 1/25-scale Magneplane System with Superconducting Coils," *IEEE Transactions on Magnetics*, vol. MAG-11, no. 5, September 1975, pp. 1490-1492

[189] H. H. Kolm, R. D. Thornton, Y. Iwasa, and W. Brown, "The magneplane system," *Cryogenics*, July 1975, pp. 377-384

[190] A. Kondoleon, D. Seltzer, R. D. Thornton, and M. T. Thompson, "Development of a Large Scale High Speed Wheel Test Facility," *Proceedings of the Third International Symposium on Magnetic Suspension Technology*, NASA Conference Publication 3336, part 2, pp. 523-534, Dec. 13-15, 1995

[191] J. L. Mahtani and R. G. Rhodes, "Electrodynamic Force Characteristics of the Split-Track Maglev System," *Journal de Physique*, vol. 45, January 1984, pp. C1-747 - C1-751

[192] T. M. Mulcahy, J. He, D. M. Rote, and T. D. Rossing, "Forces on a Magnet Moving Past Figure-Eight Coils," *IEEE Transactions on Magnetics*, vol. 29, no. 6, November 1993, pp. 2947-2949

[193] K. Oka and T. Higuchi, "A Three-Degrees-of-Freedom Maglev System with Actuators and Permanent Magnets," *Electrical Engineering in Japan*, vol. 116, no. 5, 1996, pp. 138-147

[194] R. G. Rhodes and B. E. Mulhall, "A superconducting maglev test facility for high speed transport," *Proceedings of the Sixth International Cryogenic Engineering Conference*, 1976, pp. 489-491

[195] K. Sawada, "Development of Magnetically Levitated High Speed Transport System in Japan," *IEEE Transactions on Magnetics*, vol. 32, no. 4, July 1996, pp. 2230-2235

9.16. Maglev: Thermal Stability Analysis

[196] J. Lue, M. Lubell, D. Aized, J. Campbell, and R. Schwall, "Spontaneous Quenches of a High Temperature Superconducting Pancake Coil," *IEEE Transactions on Magnetics*, vol. 32, no. 4, July 1996 pp. 2613-2616

[197] H. Miyomoto, S. Nishijima, T. Kushida, and T. Okada, "Instability of Impregnated Superconducting Windings Induced by Mechanical Disturbances," *IEEE Transactions on Magnetics*, vol. 32, no. 4, July 1996 pp. 3008-3011

[198] A. Ninomiya et. al., "Monitoring of Superconducting Magnets Using Acoustic Resonance," *IEEE Transactions on Magnetics*, vol. 24, No. 2, March 1988 pp. 1215-1218

[199] S. Ohashi, K. Higashi, H. Ohsaki, and E. Masada, "Influence of Magnet Quench on the Superconducting Magnetically Levitated Bogie, " *IEEE Transactions on Magnetics*, vol. 32, no. 5, part 2, pp. 5046-5048, 1996

[200] E. A. Scholle and J. Schwartz, "Power Dissipation Due to Vibration-Induced Disturbances in maglev Superconducting Magnets," *IEEE Transactions on Applied Superconductivity*, vol. 4, no. 4, pp. 205-210, 1994

[201] E. A. Scholle and J. Schwartz, "Thermal Stability of MAGLEV SCMs with Vibration-Induced Disturbances." *Proceedings of the Applied Superconductivity Conference '94*, Boston, October 1994

[202] K. Seo, M. Morita, S. Nakamura, T. Yamada, and Y. Jizo, "Minimum Quench Energy Measurments for Superconducting Wires," *IEEE Transactions on Magnetics*, vol. 32, no. 4, July 1996 pp. 3089-3093

[203] C. M. Srivastava and C. Srinivasan, Science of Engineering Materials, Wiley Eastern Limited, New Delhi, 1987

[204] E. Suzuki, "Heating Phenomena in the Vibrating Superconducting Magnet on Maglev," *IEICE Transactions on Electronics*, vol. E78-C, No. 55, May 1995, pp. 549-555

9.17. Magnetic Levitation: Elementary Theory

[205] A. H. Boerdijk, "Technical Aspects of Levitation," *Philips Research Reports*, vol. 11, 1956, pp. 45-56

[206] R. Frazier, P. Gilinson, Jr., and G. Oberbeck, Magnetic and Electric Suspensions, MIT Press, Cambridge MA 1974

[207] R. M. Goodall, “The Theory of Electromagnetic Levitation,” *Physics in Technology*, v. 16, no. 5, 1985, pp. 207-213

[208] R. J. Hill, "Teaching Electrodynamic Levitation Theory," *IEEE Transactions on Education*, vol. 33, no. 4, November 1990, pp. 346-354

[209] F. Holmes, "Axial Magnetic Suspensions," *Review of Scientific Instruments*, November 1937, pp. 444-447

[210] B. V. Jayawant, “Magnetic and electrostatic suspension techniques,” *The New Zealand Electrical Journal*, 25 March, 1972, pp. 32-36

[211] J. Miericke and L. Urankar, "Theory of Electrodynamic Levitation with a Continuous Sheet Track --- Part I," *Applied Physics*, vol. 2, 1973, pp. 201-211.

[212] J. Miericke and L. Urankar, "Theory of Electrodynamic Levitation with a Continuous Sheet Track --- Part II," *Applied Physics*, vol. 3, 1974, pp. 67-76

[213] W. M. Saslow, "Maxwell's theory of eddy currents in thin conducting sheets, and applications to electromagnetic shielding and MAGLEV," *American Journal of Physics*, vol. 60, no. 8, August 1992

9.18. Magnetic Levitation System Concepts

[214] P. J. Geary, Magnetic and Electric Suspensions, British Scientific Instrument Research Association, 1964

[215] B. V. Jayawant, Electromagnetic Levitation and Suspension Techniques, Edward Arnold, Ltd., London 1981

[216] E. Laithwaite, editor, Transport Without Wheels, pub. by Elek Science, London, 1977

[217] R. G. Rhodes and B. E. Mulhall, Magnetic Levitation for Rail Transport, Clarendon Press, Oxford, 1981

[218] P. Sinha, Electromagnetic Suspension Dynamics and Control, pub. by. Peter Peregrinus Ltd., 1987. Multiple-D.O.F. Maglev models.

[219] Society of Automotive Engineers, Inc., Maglev, technical report SP-926, 1992

[220] R. D. Thornton, editor, *Proceedings of the IEEE*, Special Issue on Ground Transportion for the Eighties, vol. 61, no. 5, May 1973

9.19. Magnetic Levitation: Other Applications

[221] J. Beams, "High Rotational Speeds," *Journal of Applied Physics*, vol. 8, Dec. 1937, pp. 795-806

[222] F. C. Moon, "Magnetic Forces in High-Tc Superconducting Bearings," *Applied Electromagnetics in Materials*, vol. 1 (1990) pp. 29-35

[223] W. G. Pfann and D. W. Hagelbarger, "Electromagnetic Suspension of a Molten Zone, " *Journal of Applied Physics*, vol. 27, no. 1, January 1956, pp. 12-18

[224] M. Sarma and A. Yamamura, "Nonlinear Analysis of Magnetic Bearings for Space Technology," *IEEE Transactions on Aerospace and Electronic Systems*, vol. AES-15, no. 1, January 1979, pp. 134-140

[225] G. Schweitzer, editor, Magnetic Bearings, *Proceedings of the First International Symposium* Zurich, 1988. Pub. by. Springer Verlag, 1989

[226] K. Sivier, "A One-Component, Magnetic Support-and-Balance System," *Journal of Aircraft*, vol. 6, no. 5, 1969

[227] Z. Xia, Q. Y. Chen, K. B. Ma, C. K. McMichael, M. Lamb, R. S. Cooley, P. C. Fowler, and W. K. Chu, "Design of Superconducting Magnetic Bearings with High Levitating Force for Flywheel Energy Storage Systems," *IEEE Transactions on Applied Superconductivity*, vol. 5, no. 2, June 1995, pp. 622-625

9.20. Materials: Properties, Strength, etc.

[228] K. Budinski, Engineering Materials Properties and Selection, 3d ed., Prentice Hall, New Jersey, 1989

[229] D. Chung, Carbon Fiber Composites, pub. by Butterworth-Heinemann, Boston 1994

[230] S. H. Crandall, N. Dahl, and T. Lardner, An Introduction to the Mechanics of Solids, McGraw-Hill, Inc. New York, 1978

[231] R. Flinn and P. Trojan, Engineering Materials and Their Applications, 3d edition, Houghton Mifflin Co., Boston 1986

[232] Handy & Harman Co., Inc., The Brazing Book, 1983

[233] E. Hearn, Mechanics of Materials, pub. by Pergamon Press, New York, 1977

[234] Patriot Plastics, Inc., Plastics for Industry, compilation of datasheets on various plastic products

[235] M. Schwartz, Composite Materials Handbook, pub. by McGraw-Hill, New York, 1984

[236] A. Ugural and S. Fenster, Advanced Strength and Applied Elasticity, 3d edition, PTR Prentice Hall, 1995

[237] ______, "Basics of Design Engineering: Materials," *Machine Design*, February 9, 1995, pp. 79-124. Review of practical engineering materials and applications.

9.21. *Miscellaneous References*

[238] M. Chiu, "Low-Cost, Highly-Damped, Precision Linear Motion Using Porous Carbon Air Bearings and Epoxy Replication," Master's Thesis, Massachusetts Institute of Technology, Department of Mechanical Engineering, 1994. Ceramic alumina specifications, pp. 32

[239] Emerson & Cuming, Inc., Stycast 2850-GT datasheet

[240] E. Fong, "Design and Analysis of a Liquid Nitrogen Delivery System for Cooling a High Temperature Superconducting Magnet for MAGLEV," B.S. Mechanical Engineering Thesis, Massachusetts Institute of Technology, June, 1995

[241] J. Kassakan, M. Schlecht, and G. Verghese, Principles of Power Electronics, Addison-Wesley, 1991

[242] D. Megna, (A): "A Linear, H-Bridge 1 kW Current Source Design," *M.I.T. 6.100 Lab Report*, January 15, 1997. (B): "High Voltage Test Results for the Current Source at the MAGLEV Test Fixture," *M.I.T. 6.100 Lab Report*, February 2, 1997.

[243] J. W. Roblee, "Design of Externally Pressurized Gas Bearings for Dynamic Applications," Lawrence Livermore National Laboratory report UCRL-53643, September 30, 1985

9.22. *Rotordynamics*

[244] American Society of Mechanical Engineers (ASME), 1980 Flywheel Technology Symposium

[245] R. D. Blevins, Formulas for Natural Frequency and Mode Shapes, R. E. Krieger, Malabar Florida, 1984

[246] D. Childs, Turbomachinery Rotordynamics, John Wiley, 1993

[247] F. Ehrich, editor, Handbook of Rotordynamics, McGraw-Hill, New York, 1992

[248] G. Genta, Kinetic Energy Storage Theory and Practice of Advanced Flywheel Systems, pub. by Butterworths, London 1985. Flywheel stress profiles, exotic geometries, etc.

[249] C. Harris and C. Crede, editors, Shock and Vibration Handbook, 2d edition, McGraw-Hill, New York, 1976

[250] J. Den Hartog, Mechanical Vibrations, 4th ed., Dover Publications, Inc. New York, 1985. Critical speeds of flywheel, pp. 225; dynamic balancing, pp. 233.

[251] M. Larkin, Design and Optimization of a Motor/Generator for Use in a Satellite Flywheel Energy Storage System, M.S.M.E. Thesis, Massachusetts Institute of Technology, September, 1985

[252] O. Mahrenholtz, editor, Dynamics of Rotors: Stability and System Identification, Springer-Verlag, Wien, Germany, 1984

[253] J. Mitchell, An Introduction to Machinery Analysis and Monitoring, PennWell Books, Tulsa OK, 1981

[254] S. Rao, Mechanical Vibrations, 3d edition, Addison-Wesley, Reading MA 1995

[255] S. Timoshenko, and D. Young, Vibration Problems in Engineering, 3rd edition, D. Van Nostrand Company, Inc., Princeton, 1955

[256] J. Williams, Fundamentals of Applied Dynamics, John Wiley & Sons, New York, 1996

9.23. Structural Stress and Deflection Analysis for Systems

[257] B. Allen, Soldering Handbook, Iliffe Books Lts., London, 1969

[258] G. A. Cuccuru, F. Ginesu, B. Picasso and P. Priolo, "Characterization of Composite Materials for Filament Wound Flywheels," *Journal of Composite Materials*, vol. 14, (Jan. 1980) pp. 31-41

[259] D. H. Curtiss, P. P. Mongeau, and R. L. Puterbaugh, "Advanced Composite Flywheel Structural Design for a Pulsed Disk Alternator," *IEEE Transactions on Magnetics*, vol. 31, no. 1, January 1995, pp. 28-31. Discussion of flywheel with imbedded conductors in periphery.

[260] E. L. Danfelt, S. A. Hewes, and T. W. Chou, "Optimization of Composite Flywheel Design," *International Journal of Mechanical Science*, vol. 19, 1977, pp. 69-78. Material properties of composite materials: fiberglass, Kevlar, etc.

[261] J. C. Georgian, "Optimum Design of Variable Composite Flywheel," *Journal of Composite Materials*, vol. 23, January 1989, pp. 2-10

[262] M. Iremonger, Basic Stress Analysis, Butterworth Scientific, London, 1982

[263] H. Manko, Solders and Soldering, 2d edition, McGraw-Hill, New York, 1979

[264] R. Roark, Formulas for Stress and Strain, McGraw-Hill, New York, 1965

[265] S. Timoshenko, Theory of Plates and Shells, McGraw-Hill, New York, 1940

9.24. Superconductors: AC Applications and Loss Measurements

[266] S. P. Ashworth, M. Ciszek, A. M. Campbell, W. Y. Liang, and B. A. Glowacki, "AC Losses in Silver Clad High T_c Superconducting Tapes," *Chinese Journal of Physics*, vol. 34, no. 2-II, April 1996, pp. 232-242

[267] S. A. Boggs, E. W. Collings and M. V. Parish, "AC Losses in HTSC Conductor Elements." *IEEE Transactions on Applied Superconductivity*, vol. 2, No. 3, Sept. 1992 pp. 117-121

[268] M. Ciszek, B. Glowacki, S. Ashworth, A. Campbell, and J. Evetts, "AC Losses of Ag-(Bi,Pb)SrCaCuO-2223 Tapes in Combination of Transverse External Magnetic Field and Transport Current," *IEEE Transactions on Applied Superconductivity*, vol. 5, no. 2, June 1995, pp. 709-712

[269] M. Dragomirecky, J. V. Minervini, J. W. Ekin, R. B. Goldfarb and A. F. Clark, "Losses in Nb-Ti Superconductor as Functions of AC Field Amplitude and DC Transport Current," *Proceedings of the Eleventh International Cryogenic Engineering Conference*, 1986, pp. 746-750

[270] R. F. Giese, T. P. Sheahen, A. M. Wolsky and D. K. Sharma, "High Temperature Superconductors: Their Potential for Utility Applications." *IEEE Transactions on Energy Conversion*, vol. 7, No. 3, September 1992, pp. 589-597

[271] F. Gomery, "Measurement of Magnetization Curves and Losses in Superconducting Magnets at Pulse Durations of 1 s." *Cryogenics* 26, pp. 273, 1986

[272] F. Gomery and L. Cesnak, "Loss and Magnetization Measurement of Superconducting Magnets Pulsed at Very Low Ramp Rates." *Cryogenics*, 25, pp. 375, 1985

[273] P. F. Herrmann, C. Cottevieille, A. Leriche, and S. Elschner, "Refrigeration Load Calculation of a HTSC Current Lead under AC Conditions," *IEEE Transactions on Magnetics*, vol. 32, no. 4, July 1996, pp. 2574-2577

[274] I. Hlasnik and D. Ito, "AC Applications of Superconductors at 50/60 Hz Frequency," vol. 28, no. 8, 1993, pp. 128-150

[275] M. Janocko and D. Deis, "An apparatus for the measurement of ac losses in superconductors," *Cryogenics*, vol. 14, no. 7, July 1974, pp. 391-394. Calirometric methods.

[276] H. Kanetaka et. al. "Experimental Evaluation of AC Losses in Superconducting Multifilamentary Wires for 50/60 Hz use Exposed to a Magnetic Field with Arbitrary Angle with the Wire Axis." *Proceedings of the Applied Superconductivity Conference '94*, Boston, October 1994

[277] W. Knaak and H. Reiss, "High-temperature superconductors for a.c. applications," *Materials and Design*, vol. 14, no. 2, 1993, pp. 115-121

[278] J. Kokavec, I. Hlasnik, and S. Fukui, "Very Sensitive Electric Method for AC Loss Measurement in SC Coils," *IEEE Transactions on Applied Superconductivity*, vol. 3, no. 1, March 1993, pp. 153-155

[279] E. J. Lucas, W. F. B. Punchard, P. M. G. Margosian and D. S. Beard, "Design and Use of an Electronic Loss Measurement Apparatus for Superconducting Coils." *IEEE Transactions on Magnetics*, vol. MAG-13, No. 1, January 1977 pp. 538-541

[280] R. Mints, A. Akhmetov and A. Devred, "Enhanced Quench Propagation Velocity," *IEEE Transactions on Applied Superconductivity*, vol. 3, no. 1, March 1993, pp. 654-657

[281] T. Mower and Y. Iwasa, "Experimental investigation of a.c. losses in cabled superconductors," *Cryogenics*, 1986, vol. 26, May pp. 281-292

[282] J. Paasi, and A. Tuohimaa, "Hysteresis Losses in Bi-2223 Superconductors," *IEEE Transactions on Magnetics*, vol. 32, no. 4, July 1996, pp. 2796-2799

[283] J. Paasi, M. Polak, P. Kottman, D. Suchon, M. Lahtinen and J. Kokavec, "Electric Field and Losses in BSCCO-2223/Ag Tapes Carrying AC Transport Current." *Proceedings of the Applied Superconductivity Conference '94*, Boston, October 1994

[284] J. Paasi, M. Lahtinen, D. Aized, S. Fleshler, G. Snitchler and A. P. Malezemoff, "AC Losses in Multifilamentary Bi-2223/Ag Superconducting Tapes," *IEEE Transactions on Magnetics*, vol. 32, no. 4, July 1996, pp. 2792-2795

[285] P. Penczynski, "Measurement of 50 Hz Alternationg Current Losses on Superconducting Niobium Cylinders," *Siemens Forschungs - und Entwicklungsberichte*, vol. 2, no. 5, pp. 296-306 (1973)

[286] K. M. Reilly and G. H. Morgan, "A Digital Technique for the Measurement of Power Losses in High Temperature Superconductors, " *IEEE Transactions on Applied Superconductivity*, vol. 2, no. 3, September 1992, pp. 181-183

[287] Y. Yasukawa, K. Takita, H. Hiue, I. Itoh, M. Mimura, K. Iwashita, Y. Tanaka, M. Iwakuma, K. Funaki, M. Takeo, and K. Yamafuji, "Development of 2 kA High-Temperature Superconducting Current Lead System for AC Applications, " *IEEE Transactions on Magnetics*, vol. 32, no. 4, July 1996, pp. 2671-2674

9.25. Superconducting Magnet Design --- General

[288] M. Ariante, A. Matrone, E. Petrillo, A. Bonzi, P. Fabbricatore, M. Galbiati, C. Priano, L. Rossin and A. Scutti, "Characteristics of Coils Wound with Mono and Multifilamentary Bi-2212/Ag from 4 to 80K," *IEEE Transactions on Magnetics*, vol. 32, no. 4, July 1996, pp. 2780-2783. Discussion of latest research on HTSC in round wire geometry.

[289] A. M. Dawson and D. B. Montgomery, "A Data Base of Magnet Failures and Its Relevance to Magnet Design," *IEEE Transactions on Magnetics*, vol. 32, no. 4, July 1996, pp. 2974-2977

[290] S. Foner and B. Schwartz, editors, Superconductor Materials Science: Metallurgy, Fabrication, and Applications, pub. by Plenum Press, New York, 1981. Thermal stability of low-Tc materials, pp. 84; lap joint analysis, pp. 125; strain effects in low-Tc materials, pp. 455; large superconducting machines, pp. 757;

[291] Y. Iwasa, Case Studies in Superconducting Magnets, pub. by Plenum Press, New York, 1994

[292] C. Levillain and P. Therond, "Minimal Performances of High Tc Wires for Cost Effective SMES Compared With Low Tc's," *IEEE Transactions on Magnetics*, vol. 32, no. 4, July 1996, pp. 2308-2311

[293] D. Montgomery, Solenoid Magnet Design, Wiley-Interscience, 1969

[294] K. Seo, M. Morita, S. Nakamura, T. Yamada, and Y. Jizo, "Minimum Quench Energy Measurement for Superconducting Wires," *IEEE Transactions on Magnetics*, vol. 32, no. 4, July 1996, pp. 3089-3093

[295] M. Wilson, Superconducting Magnets, Clarendon Press, Oxford, 1983

9.26. Thermal System Design

[296] Burr Brown Corp., "Thermal and Electrical Properties of Selected Packaging Materials," applications brief AB-030, 1991

[297] Eastop and McConkey, Applied Thermodynamics, 5th ed., Longman Scientific and Technical

[298] General Electric Corp., SCR Manual, Prentice-Hall, New Jersey, 1979

[299] International Rectifier Corp., Power Modules Designer's Manual, 1991

[300] R. Resnick and D. Halliday, Physics, Part 1. Publ. by John Wiley & Sons, New York 1977

[301] SGS-Thomson, Inc. Designers' Guide to Power Products: Applications Manual

Marc T. Thompson

Marc T. Thompson was born in Vinalhaven, Maine, in 1963. He received the B.S.E.E. degree from the Massachusetts Institute of Technology (M.I.T.) in 1985, the M.S.E.E. in 1992, the Electrical Engineer's degree in 1994 and the Ph.D. degree in May 1997.

From 1987-1993 he worked at Polaroid Corporation, specializing in high speed analog design, including modulators of high-power semiconductor diode lasers. Since then, he has worked as a consultant in analog and magnetics design, and holds 2 patents. His research areas at MIT included design of superconducting suspensions, applications of magnetic fluids, and stability analysis and use of scaling laws for magnetic structures.